amU
Aix Marseille Université

NNT : 2025AIXM0050

THÈSE DE DOCTORAT

Soutenue à AMU — Aix-Marseille Université
le 13 mars 2025 par

Vincent DURET

Cosmological constraints by tomographic galaxy clustering with Euclid data

Discipline
Physique et Sciences de la Matière

Spécialité
Astrophysique et Cosmologie

École doctorale
ED352

Laboratoire
Centre de Physique des Particules de Marseille

Composition du jury

Alain BLANCHARD IRAP, Toulouse	Président du jury, Rapporteur
Etienne BURTIN CEA, Paris-Saclay	Rapporteur
Micol BOLZONELLA INAF, Bologna	Examinatrice
Ariel SANCHEZ MPE, Garching bei München	Examinateur
Stéphanie ESCOFFIER CPPM, Marseille	Directrice de thèse
William GILLARD CPPM, Marseille	Co-directeur de thèse

CENTRE DE PHYSIQUE DES PARTICULES DE MARSEILLE
CPPM

Affidavit

I, undersigned, Vincent Duret, hereby declare that the work presented in this manuscript is my own work, carried out under the scientific supervision of Stéphanie Escoffier and William Gillard, in accordance with the principles of honesty, integrity and responsibility inherent to the research mission. The research work and the writing of this manuscript have been carried out in compliance with both the french national charter for Research Integrity and the Aix-Marseille University charter on the fight against plagiarism.

This work has not been submitted previously either in this country or in another country in the same or in a similar version to any other examination body.

At Marseille, April 4 2025



This work is licensed under Creative Commons Attribution-NonCommercial-NoDerivatives 4.0 International Public License

Liste de publications et participation aux conférences

Liste des publications et/ou brevets réalisées dans le cadre du projet de thèse :

1. EUCLID COLLABORATION : DURET et al. (2025), Euclid preparation. BAO analysis of photometric galaxy clustering in configuration space
   Auteurs principaux : Vincent Duret, Stéphanie Escoffier, William Gillard, Isaac Tutusaus, Stefano Camera, Nicolas Tessore, Francisco Javier Castander.
   Soumis au journal A&A.

Participation aux conférences et écoles d'été au cours de la période de thèse :

1. Colloque national Action Dark Energy 2022, 17-18 novembre 2021
   https://indico.in2p3.fr/event/27399/
2. *Euclid* annual meeting Oslo, 25-29 avril 2022, distanciel,
   https://www.mn.uio.no/astro/english/research/news-and-events/events/conferences/ECmeeting2022/
3. Ecole *Euclid* Rodolphe Clédassou cycle 1, 15-27 août 2022,
   https://ecole-euclid.cnrs.fr/
4. Symposium *Euclid* France 2022, 1-2 décembre 2022,
   https://euclid-fr2022.sciencesconf.org/
5. Meeting *Euclid* GC SWG Milan, 20-24 février 2023,
   Flash talk on Cosmological parameters from full-shape analysis of the two-point angular correlation function with the Flagship simulation,
   https://indico.ict.inaf.it/event/2269/overview
6. Ecole *Euclid* Rodolphe Clédassou cycle 2, 15-30 août 2023,
   Talk on Tomographic analysis of photometric galaxy clustering with Flagship 2.1,
   https://ecole-euclid.cnrs.fr/
7. *Euclid* annual meeting Copenhague, 19-23 juin 2023,
   https://euclid2023.org/

8. Colloque national Action Dark Energy 2023, 5-8 novembre 2023,
   https://indico.in2p3.fr/event/29646/
9. Symposium *Euclid* France 2023, 24-26 janvier 2024, flash talk on BAO with configuration space observables,
   https://euclid-fr2023.sciencesconf.org
10. Meeting *Euclid* GC SWG Marseille, 29 janvier-2 février 2024 ,
    Flash talk on BAO with configuration space observables and photometric galaxy clustering systematic uncertainties
11. *Euclid* annual meeting Rome, 17-21 juin 2024.

Résumé et mots clés [1]

Nous sommes actuellement à l'aube de l'ère des relevés cosmologiques de niveau IV, qui a débuté avec le programme principal du Dark Energy Spectroscopic Instrument (DESI) en mai 2021. Le relevé nominal de la mission *Euclid* a débuté le 14 février 2024. Il est dédié à l'étude de l'énergie sombre et de la matière noire, les deux constituants principaux mais invisibles de notre Univers, en cartographiant la distribution des galaxies en tant que traceurs de la matière. L'étude du regroupement des galaxies établit les propriétés des structures aux grandes échelles à travers diverses approches condensant l'information de cette distribution en une observable comme la fonction de corrélation. Le cadre théorique développé depuis l'établissement de la théorie de la relativité générale a évolué vers le modèle standard de la cosmologie appelé ΛCDM mais aussi vers une myriade de modèles alternatifs créés pour pallier à ses échecs. Confronter ces modèles aux observations avec des méthodes bayésiennes ou fréquentistes contraint leurs paramètres. Dans le chapitre 1, j'introduis les notions de base de cosmologie, à travers les équations d'Einstein, pour comprendre les relations entre l'Univers, son évolution et son contenu puis je présente le modèle ΛCDM et ses extensions comme les modèles d'énergie sombre. Le relevé *Euclid* est présenté pour comprendre le contexte de ce travail, avant d'aborder le sujet des principales analyses de cette thèse, les oscillations baryoniques acoustiques (BAO). Comme j'utilise des redshifts [2] photométriques plutôt que spectroscopiques pour déterminer les distances des galaxies et étudier leur regroupement, j'explore dans le chapitre 2 des méthodes récentes développées pour améliorer l'estimation des redshifts photométriques grâce au deep learning, tout d'abord avec les observations du Sloan Digital Sky Survey puis avec des simulations *Euclid*. Le chapitre 3 est consacré à l'analyse du regroupement des galaxies photométriques. De la théorie de la fonction de corrélation angulaire à deux points à son estimateur et aux données de la simulation Flagship d'*Euclid*, je présente ensuite les mesures obtenues dans plusieurs configurations, avec l'aire totale de la simulation, 5157 deg^2, ou 2500 deg^2 comme attendu au moment de la publication DR1 de données *Euclid*. Comme c'est une analyse tomographique, l'effet du type de bin est considéré, soit équipeuplé, soit équidistant. L'effet de choix d'analyses variés est étudié, comme la taille ou la résolution angulaire du catalogue de points aléatoires, le nombre d'échantillons jackknife utilisés pour calculer la covariance empirique. Les covariances empirique et analytique sont introduites et comparées. Les analyses BAO effectuées avec ces données sont présentées dans le chapitre 4, avec différentes approches : analyse sur les bins de redshift individuels ou analyse jointe,

1. Cette thèse est basée sur, ou contient des documents non-publics du consortium Euclid ou des résultats qui n'ont pas encore été approuvés par le consortium Euclid.
2. Redshift : décalage vers le rouge

covariance empirique ou analytique, vecteur de données mesuré ou synthétique, MCMC ou profil de vraisemblance. Avec les contraintes obtenues dans chaque bin, je montre que l'on peut contraindre l'évolution de l'expansion de l'Univers. Avec l'analyse jointe, je démontre le potentiel du regroupement des galaxies photométriques avec *Euclid* avec des contraintes trois fois plus fortes qu'avec le relevé photométrique Dark Energy Survey. Une analyse détaillée de la robustesse des résultats obtenus est fournie, à propos des bins de redshift inclus dans l'analyse, la cosmologie fiducielle, la forme fonctionnelle utilisée pour extraire le signal BAO, les distorsions de l'espace des redshifts, la sélection des échelles utilisées, la définition des bins de redshifts ou la covariance utilisée. Je conclus par une étude préliminaire des pistes d'améliorations de ces analyses BAO pour de futurs travaux. Le dernier chapitre est une analyse full-shape de $w(\theta)$ dans le contexte de la Data Release 1 *Euclid* pour contraindre les paramètres du modèle ΛCDM. Je quantifie le décalage de ces paramètres créé par un biais ou élargissement de la distribution en redshift utilisée pour calculé le modèle théorique de $w(\theta)$.

Mots clés : Cosmologie, Galaxy clustering, Oscillations acoustiques baryoniques, Euclid, Tomographie, Deep learning

Abstract and keywords[1]

We are currently at the dawn of the era of stage IV cosmological surveys, initiated with the Dark Energy Spectroscopic Instrument main program in May 2021. The nominal survey of the *Euclid* satellite started in February 2024 and it is dedicated to the study of dark energy and dark matter, the two principal but invisible components of our Universe, by mapping the distribution of galaxies as tracers of matter. Galaxy clustering establishes the properties of large scale structures, through different approaches like field-level inference or summary statistics which condense the information into observables like the correlation function. The theoretical framework built since the theory of General Relativity was established evolved towards the standard model of Cosmology called ΛCDM which currently explains most observations, but also a myriad of alternative models created to explain its failures. Confronting these models to observations with Bayesian or frequentist methods constrains their parameters. Having a detailed understanding of the influence of the choices made to obtain constraints is necessary. Making the most of the very large amount of data that *Euclid* will provide is also very important to me, which is why I study baryonic acoustic oscillations (BAO) with photometric galaxy clustering in my thesis. The first part of this thesis is dedicated to the required notions of Cosmology, the ΛCDM model, but also an introduction to *Euclid* and BAO. In the second part, I explore the use of deep learning methods to improve photometric redshift estimates with both observations and simulations. Different architectures of neural networks are compared in order to quantify the improvement given by the use of images with respect to photometry alone. The use of hybrid architectures with both images and photometry is also tested to further increase performance. The third part of this work describes photometric galaxy clustering through the two-point angular correlation function, from its theory to the way it is measured. The data from the *Euclid* Flagship simulation will be introduced along with the various measurements obtained. A study of various analysis choices is provided to understand their effect over the observable. The empirical and analytical covariances are introduced at the end of this third chapter. The fourth chapter is a set of tomographic analyses of BAO with photometric galaxy clustering. We extract and constrain the BAO signal as a function of redshift to constrain the expansion of the Universe and cosmological parameters, but we also constrain the BAO signal in a joint analysis of all redshift bins. A detailed study of various effects is presented, including the weight of each redshift bin, the choice of fiducial cosmology, the template used to extract the signal, scale cuts, redshift space distortions, the choice of redshift binning scheme and the covariance. I conclude with a preliminary study

1. This thesis is based on, or contains non-public Euclid Consortium material or results that have not yet been endorsed by the Euclid Consortium.

of how these constraints from BAO can be improved in the future. The last chapter is a full-shape analysis of $w(\theta)$ in a *Euclid* Data Release 1-like setting to constrain the cosmological parameters of the ΛCDM model. We quantify the shift of these parameters induced by an eventual bias and broadening of the redshift distributions used to compute the theoretical model of $w(\theta)$.

Keywords: Cosmology, Galaxy clustering, Baryon acoustic oscillations, Euclid, Tomography, Deep learning

Résumé en français

Introduction

La cosmologie est la science de l'étude de l'Univers, de son origine à son évolution passée et future. Un des objectifs majeurs en cosmologie moderne est donc de quantifier précisément quelle fraction du contenu de l'Univers chacun de ses éléments représente. La théorie de la relativité générale établie par Albert Einstein a permis le développement d'un cadre formel pour étudier les lois régissant le contenu de l'Univers, leurs interactions et l'évolution de l'Univers dans sa globalité. Confronter nos observations à une théorie permet de mieux déterminer les paramètres de ses équations ou même de la réfuter en cas d'incompatibilité. Ainsi, les observations font progresser la théorie et de la même manière, la théorie guide les observations en proposant des objectifs à atteindre pour contraindre ses modèles. Ces objectifs peuvent être d'observer un grand nombre de galaxies sur une grande surface du ciel pour mieux caractériser leur distribution aux grandes échelles, là où les grandes tendances de l'évolution globale de l'Univers se font le plus sentir. La fin du XX^{e} et le début du XXI^{e} siècle ont ainsi vu plusieurs programmes naître pour réaliser des sondages de galaxies, multipliant leur taille à chaque progrès technologique. Nous sommes actuellement à l'aube de l'ère des relevés cosmologiques de niveau IV, commencée par le programme principal du Dark Energy Spectroscopic Instrument en mai 2021 (DESI). Le relevé nominal de la mission *Euclid* a débuté le 14 février 2024. Il est dédié à l'étude de l'énergie sombre et de la matière noire, les deux constituants principaux mais invisibles de notre Univers, en cartographiant la distribution des galaxies en tant que traceurs de la matière. L'étude statistique du regroupement des galaxies (galaxy clustering) détermine les propriétés des structures aux grandes échelles, par exemple à travers l'utilisation de statistiques condensant l'information de cette distribution en une observable comme la fonction de corrélation. Le cadre théorique développé depuis l'établissement de la théorie de la relativité générale a évolué vers le modèle standard de la cosmologie appelé ΛCDM mais aussi vers une myriade de modèles alternatifs créés pour pallier à ses échecs. La confrontation de ces modèles aux observations pour contraindre leurs paramètres passe par des méthodes bayésiennes comme la méthode de Monte Carlo par chaînes de Markov (MCMC) ou fréquentistes comme la vraisemblance profilée.

Cosmologie à l'aube des relevés cosmologiques de niveau IV

Les avancées technologiques ayant permis d'observer l'Univers lointain sont relativement récentes. Les premiers relevés cosmologiques observant une grande partie du ciel le sont encore plus mais ont déjà permis des découvertes majeures. Le spectre de la première lumière émise par le fond diffus cosmologique a été observé pour la première fois en 1996, spectre dont l'analyse prouve que l'Univers était plus chaud et dense dans le passé. Associée au travail de George Lemaître et de Edwin Hubble qui ont montré que les galaxies s'éloignent de nous à une vitesse proportionnelle à leur distance et donc qu'elles étaient autrefois plus proches, cette découverte a renforcé les bases du modèle du Big Bang qui stipule que l'Univers observable était initialement infiniment petit, chaud et dense et s'est étendu depuis. Les relevés du 2-degree Field Galaxy Redshift Survey et du Sloan Digital Sky Survey (SDSS) ont cartographié la distribution des galaxies sur une large fraction du ciel en en relevant la position et distance, cette dernière étant mesurée via le décalage vers le rouge (redshift) du spectre observé par un spectrographe. Le signal des oscillations baryoniques acoustiques, une faible surdensité présente à une échelle fixe dans la distribution des galaxies, a été détecté pour la première fois grâce à ces observations. Pour illustrer l'accélération des prouesses techniques dans le domaine observationnel, on peut citer le fait qu'après une année d'observations, le premier relevé cosmologique de niveau IV, DESI, compte déjà 5.7 millions de galaxies et les meilleurs contraintes sur l'échelle des BAO, 3 fois plus que SDSS en 20 ans. Ces avancées sont parallèles au développement de la théorie qui a connu une révolution avec la théorie de la relativité générale d'Einstein en 1915 dans laquelle la gravitation est dérivée du principe d'équivalence. Le lien entre la courbure de l'espace-temps et son contenu est donné par l'équation d'Einstein dont la conséquence directe est que les objets massifs déforment l'espace-temps.

Le principe cosmologique est l'hypothèse selon laquelle l'Univers est statistiquement homogène et isotrope. Friedmann et Lemaître ont dérivé les équations décrivant cet univers en expansion, tandis que Robertson et Walker ont établi la forme générale de la métrique dite FLRW satisfaisant ce principe. En injectant la métrique FLRW dans l'équation d'Einstein, les équations de Friedman sont dérivées, décrivant l'évolution du facteur d'échelle a et donc l'expansion de l'Univers comme une fonction des paramètres de densité d'énergie du rayonnement Ω_r, de la matière Ω_m, de la courbure de l'Univers Ω_k et de la constante cosmologique Ω_Λ. L'évolution temporelle de ces paramètres définit une succession d'ères de domination, d'abord par le rayonnement, puis par la matière et aujourd'hui, par la constante cosmologique Λ. Le nom de modèle ΛCDM vient de cette domination de Λ et dans une moindre mesure, de la matière noire froide (cold dark matter). Ce modèle est souvent paramétré en fonction de la constante de Hubble réduite h, la densité physique baryonique $\omega_\mathrm{b} = \Omega_\mathrm{b} h^2$ et celle de la matière noire froide ω_cdm, la profondeur optique de la réionisation τ, de l'amplitude du spectre de puissance primordial A_s et son indice spectral n_s. Bien qu'étant actuellement le modèle standard de la cosmologie, le modèle ΛCDM n'explique pas tout.

Le problème d'ajustement fin correspond à la nécessité d'avoir une valeur initiale de Ω_k très précise et extrêmement faible pour expliquer les observations actuelles de $\Omega_k < 0.0016$. L'extrême homogénéité du fond diffus cosmologique est également inattendue car certaines régions impliquées étaient trop éloignées pour que la lumière ait eu le temps de les connecter. Ces deux premiers problèmes peuvent être expliqués si l'on introduit une phase d'inflation, une expansion extrêmement rapide et importante aux débuts de l'Univers. Un autre problème du modèle ΛCDM est l'incompatibilité des mesures de la constante de Hubble obtenues par analyse des BAO et par analyse des supernovæ de type Ia, avec une très grande importance statistique ($\sim 5\sigma$). Enfin, ce modèle n'explique pas l'écart extraordinaire entre la valeur de Λ mesurée en cosmologie et sa valeur théorique prédite par la mécanique quantique. Ces problèmes motivent l'étude de modèles alternatifs, comme les modèles d'énergie sombre. Certains introduisent une dépendance temporelle dans le paramètre d'équation d'état w, par exemple avec la paramétrisation CPL $w = w_0 + \frac{z}{1+z} w_a$.

Le relevé *Euclid* repose sur l'observation simultanée en spectroscopie et en photométrie d'un champ commun de 0.54 deg^2. La technique de spectroscopie sans fente utilisée par l'instrument NISP-S disperse la lumière de toutes les sources observées à la fois avec un grisme. En observant les mêmes sources avec des grismes d'orientations variées, il est possible de distinguer et extraire le spectre de chacune des sources dont le flux H_α est supérieur à $2 \times 10^{-16}\,\mathrm{erg\,cm^{-2}\,s^{-1}}$. Environ 35 millions de spectres sont attendus entre $z = 0.84$ et $z = 1.88$ en 6 années d'observations. Pour la photométrie, l'instrument VIS couvre la bande I_E alors que le photomètre NISP-P observe les bandes H_E, J_E et Y_E (voir Fig.1.4). L'échantillon de galaxies s'étendra de $z = 0.2$ à $z = 2.5$ et devrait compter 1.5 milliard de galaxies. L'étude du lentillage gravitationnel via la distorsion apparente de la morphologie des galaxies est permise par la résolution du VIS et l'association des bandes du NISP-P avec les relevés extérieurs sera nécessaire pour déterminer la distance de ces galaxies via leur redshift photométrique (z_{ph}).

Les BAO sont des fluctuations du champ de densité de baryons expliquées par l'opposition entre les forces de gravitation qui regroupent la matière et la force de pression du rayonnement qui l'éloigne dans le fluide primordial de baryons couplés aux photons. Les oscillations qui en découlent se propagent dans la matière, jusqu'au moment où l'Univers est suffisamment froid pour que photons et baryons se découplent et que la force de pression du rayonnement cesse. La taille de ces oscillations à l'époque du découplage, r_d a donc été fixée et depuis, n'augmente plus que sous l'effet de l'expansion de l'Univers. Mesurer la taille apparente des BAO θ_{BAO} à différentes époques revient donc à mesurer l'expansion de l'Univers à travers la distance de diamètre angulaire D_A, ce qui nous permet de contraindre entre autres h, Ω_b et Ω_{cdm}.

Redshifts photométriques

Dans ce chapitre, nous étudions les z_{ph} et plusieurs méthodes récentes développées pour les améliorer grâce à l'apprentissage profond (deep learning), tout d'abord avec les observations du Sloan Digital Sky Survey puis avec des simulations *Euclid*.

Pour estimer le redshift d'une galaxie, la méthode traditionnelle d'ajustement de distributions spectrales d'énergie (SED fitting) minimise le khi carré par rapport au redshift, le khi carré étant calculé entre les magnitudes observées dans les bandes photométriques et des modèles théoriques de SED convolués à la réponse instrumentale. Cependant, les nombreux calculs d'intégrales rendent cette méthode difficile à appliquer à l'échelle des grands relevés cosmologiques actuels. Cette méthode nécessite aussi la production d'une librairie de modèles de SED représentative de l'échantillon auquel la méthode sera appliquée. De la même manière, les méthodes d'apprentissage automatique requièrent un échantillon de données d'entraînement représentatif. Ces dernières sont très variées et incluent les forêts d'arbres décisionnels, éventuellement améliorées par les méthodes comme `Adaboost` ou la descente de gradient mais aussi des méthodes comme les k plus proches voisins, les modèles linéaires généralisés, les processus gaussiens, les machines à vecteurs de support, les cartes autoadaptatives ou cartes de Kohonen, ou encore les réseaux de neurones. Quand il est supervisé, l'entraînement vise à minimiser la valeur d'une fonction de perte telle que l'erreur quadratique moyenne, calculée entre la valeur prédite par le réseau de neurones et la valeur de l'échantillon d'entraînement considérée comme vraie. La rétropropagation du gradient de la fonction de perte par rapport aux poids des neurones permet une mise à jour des paramètres et donc une optimisation itérative.

Pour aller au-delà des estimations de $z_{\rm ph}$ obtenues avec un réseau où tous les neurones sont connectés (perceptron multi-couche ou MLP) n'utilisant que les magnitudes des galaxies comme information, j'évalue l'apport de l'utilisation de l'image de la galaxie entière pour prédire $z_{\rm ph}$. Pour cela, j'utilise des réseaux de neurones à convolution (CNN) basés sur des couches qui convoluent les images avec des filtres pour en extraire les propriétés importantes. Un avantage majeur de ces réseaux est la préservation des propriétés spatiales de l'image, contrairement aux réseaux de neurones denses comme les MLP où tous les neurones sont reliés entre eux. Un deuxième avantage majeur est la réduction significative du nombre de paramètres à entraîner à nombre de neurones égal. En particulier, je compare les réseaux CNN séquentiels aux CNN à inception, basés sur des blocs regroupant des couches de convolutions de diverses tailles organisées de manière à optimiser l'extraction de l'information. Une autre comparaison est effectuée avec le réseau à résidus ResNet34. Je considère également des versions alternatives de ces réseaux dans lesquelles un réseau de neurones denses MLP est concaténé au CNN pour traiter les magnitudes en parallèle. Enfin, des fonctions de densité de probabilité (PDF) de $z_{\rm ph}$ sont produites en prédisant les valeurs de probabilités pour que $z_{\rm ph}$ soit dans chacune des fines classes de redshift de largeur 2.5×10^{-3} entre le redshift minimum et maximum de l'échantillon au lieu de prédire une valeur unique de $z_{\rm ph}$. Je caractérise les performances des prédictions des valeurs scalaires de $z_{\rm ph}$ via le biais moyen δz, l'écart-type, la déviation absolue médiane normalisée $\sigma_{\rm NMAD}$ robuste aux valeurs extrêmes et les fractions de valeurs aberrantes $\eta_{0.15}$, $\eta_{0.10}$ et $\eta_{0.05}$ définies dans la section 2.1.3. La qualité des PDF produites est caractérisée par l'histogramme des valeurs de PIT calculé via Eq. (2.7). De plus, les métriques précédentes sont calculées avec une estimation ponctuelle de $z_{\rm ph}$ calculée comme l'espérance de la PDF.

Avec les données de la Data Release 12 de SDSS, le MLP a déjà des performances intéressantes avec des $z_{\rm ph}$ qui suivent la relation 1 :1 avec les redshifts spectroscopiques $z_{\rm spec}$, avec $\delta z = 0.037$, $\sigma_{\rm NMAD} = 0.043$ et $\eta_{0.15} = 0.027$. Néanmoins, le CNN à inception réduit δz et les fractions d'outliers d'un facteur 1.3. Le ResNet34 est encore meilleur dans ce cas, avec un facteur d'amélioration qui atteint 1.7 sur $\eta_{0.15}$ et $\eta_{0.10}$ par rapport au MLP. Cependant, son nombre de paramètres 15 fois plus grand le rend beaucoup plus lent lors de l'entraînement et de l'inférence. J'ai effectué une étude des performances en variant la taille de l'échantillon d'entraînement. Il est intéressant de noter que les performances ne sont dégradées qu'au maximum d'un facteur 1.66 selon la métrique considérée quand on utilise 40 fois moins de galaxies pour entraîner le CNN à inception. Si l'on considère les modèles en mode classification pour prédire une PDF de $z_{\rm ph}$ au lieu de $z_{\rm ph}$, on trouve que le CNN à inception produit 1.4 fois moins de valeurs aberrantes qu'un CNN séquentiel. Les performances sont même améliorées par rapport au même modèle en mode régression. L'histogramme des valeurs de PIT est plat et présente une pente positive très limitée, gage de qualité des PDF calculées.

Les images de galaxies simulées pour le Science Challenge 8 (SC8) *Euclid* ont été utilisées pour constituer un échantillon d'entraînement visant à estimer les performances atteignables avec les méthodes de deep learning sur images avec *Euclid* seul, sans relevé de galaxies extérieur. Cependant, des problèmes de sous-estimation du flux H_α et des artéfacts dans les spectres 1D ont causé des erreurs importantes dans l'extraction des $z_{\rm spec}$ de ces galaxies simulées, empêchant leur exploitation. J'ai donc simulé un catalogue de $z_{\rm spec}$ qui correspond à ce qui aurait dû être mesuré grâce à un modèle développé au sein du consortium avec le code `FastSpec`. `FastSpec` simule les spectres 1D mesurés par *Euclid* à partir d'un catalogue de vrais redshifts et de flux, spectres dont le $z_{\rm spec}$ est ensuite extrait, permettant la construction du modèle reliant directement le catalogue à $z_{\rm spec}$. Ce catalogue d'entraînement est cependant très bruité avec $\eta_{0.15} = 0.626$. Idéalement, de multiples réalisations de ce catalogue auraient été créées et les entraînements et inférences répétés autant de fois pour moyenner les résultats. Comme le modèle utilisé n'est pas construit avec la dernière version des codes utilisés par *Euclid*, j'ai décidé de créer un seul catalogue et de considérer l'évolution des métriques d'un réseau de neurones à un autre plutôt que les valeurs elles-mêmes. Avec ces données, le CNN à inception améliore Δz, $\sigma_{\rm NMAD}$, $\eta_{0.15}$, $\eta_{0.10}$ et $\eta_{0.05}$ d'un facteur 1.4 à 1.5 par rapport au MLP. De la même manière, la combinaison CNN à inception + MLP obtient d'encore meilleures performances par rapport au MLP avec un facteur 1.5 sur Δz, 2.1 sur $\sigma_{\rm NMAD}$, 4.0 sur $\eta_{0.15}$, 2.7 sur $\eta_{0.10}$ et 1.6 sur $\eta_{0.05}$. Ces améliorations sont un argument fort pour l'utilisation des images en plus de la photométrie extraite avec ces architectures CNN à inception combinées au MLP pour améliorer la qualité des photo-z utilisés dans des études comme celles présentées dans les chapitres suivants.

Regroupement des galaxies photométriques

Ce chapitre 3 est consacré à l'analyse du galaxy clustering photométrique (GCph). Il s'agit de l'étude de la manière dont les galaxies se regroupent sous l'effet de la gravitation et j'utilise la fonction de corrélation angulaire à deux points $w(\theta)$ pour cela. Cette fonction mesure l'amplitude du clustering en fonction de la séparation angulaire θ entre les galaxies. Ainsi, l'excès créé par les BAO dans la distribution de matière se traduit par un pic dans $w(\theta)$ à la séparation angulaire $\theta_{\rm BAO}$. Le GCph est une sonde très importante pour *Euclid* car elle sera utilisée dans l'analyse 3×2-points en combinaison avec la fonction de corrélation du lentillage gravitationnel et la corrélation croisée du GCph et du lentillage gravitationnel. Cette observable sera utilisée en considérant la forme entière de la fonction de corrélation dans une analyse dite full-shape pour contraindre les paramètres du modèle ΛCDM et de son extension à l'énergie sombre avec les paramètres de l'équation d'état w_0 et $w_{\rm a}$ de la paramétrisation CPL. La mission *Euclid* vise à contraindre ces deux paramètres avec une figure de mérite de 400. Néanmoins, le travail présenté dans cette thèse porte sur une analyse différente qui met à profit le très grand nombre de galaxies observées en photométrie pour contraindre le signal BAO d'une manière indépendante de l'analyse spectroscopique des BAO. En 2024, le relevé Dark Energy Survey (DES) a obtenu une contrainte à 2.1% sur la position du pic BAO et on peut espérer une amélioration importante avec *Euclid*, comme je le montrerai dans le chapitre suivant. Cette analyse nécessite cependant une bonne compréhension de $w(\theta)$, ce pourquoi on étudie à la fois la construction du modèle théorique de $w(\theta)$ et l'influence de plusieurs choix sur la mesure. Dans l'étude du modèle théorique, je montre que les distorsions de l'espace des redshifts (RSD) augmentent l'amplitude de $w(\theta)$ aux grandes séparations angulaire θ et surtout à bas redshift. L'effet des échelles considérées avec les valeurs maximales du nombre d'onde $k_{\rm max}$ et du multipôle $\ell_{\rm max}$ est étudié, ainsi que l'approximation de Limber pour laquelle on constate une variation de $w(\theta)$ qui n'est pas du tout négligeable aux θ considérés dans l'analyse BAO, ce pourquoi on ne l'utilisera qu'aux échelles où son effet est inférieur à 1 %. Pour la mesure de $w(\theta)$, l'estimateur de Landy–Szalay est utilisé avec le code `TreeCorr`, évaluant ainsi le contraste entre la distribution de galaxies et une distribution aléatoire uniforme. Cette mesure est effectuée sur le catalogue de galaxies Flagship v.2.1.10 créé à partir d'une simulation à N corps de 4×10^{12} particules, de côté $3.6\,{\rm h}^{-1}\,{\rm Gpc}$ et couvrant les redshifts entre $z=0$ et $z=2.5$. Dans ce catalogue, une sélection des galaxies dont la magnitude $I_{\rm E}$ est inférieure à 24.5 est faite. Je retire également les galaxies dont le $z_{\rm ph}$ présente un avertissement de fiabilité donné par le code utilisé pour calculer $z_{\rm ph}$. Au total, la simulation couvre 5157 $\deg^2$, un huitième du ciel. L'échantillon de galaxies est divisé en 13 tranches (bins) de redshift équipeuplées avec 34.8 millions de galaxies par bin et 30 fois plus de points dans le catalogue aléatoire uniforme. La mesure de $w(\theta)$ est présentée dans la figure 3.8 pour les autocorrélations mais les cross-corrélations sont également mesurées et présentées dans la figure 3.10. On constate qu'avec *Euclid*, les cross-corrélations des bins adjacents ne sont pas négligeables et ont une amplitude allant jusqu'à plus de 60 % de l'autocorrélation associée. La mesure de $w(\theta)$ est aussi effectuée et com-

parée avec 13 bins équidistants. Deux mesures sont également effectuées avec des configurations envisagées pour la première grande publication de données *Euclid* (Data Release 1 ou DR1) avec une aire de 2500 deg^2 et deux sélections $I_E \leq 22.25$ et $I_E \leq 23.5$. L'effet de la taille ou résolution angulaire du catalogue de points aléatoires, du nombre d'échantillons jackknife utilisés pour calculer la covariance empirique, de l'approximation b_s du code `TreeCorr`, du type de z_{ph} utilisé (médiane ou premier mode de la PDF de z_{ph}, code utilisé pour le calculer) est mesuré et quantifié. Les covariances empiriques (jackknife) et analytiques sont introduites, avec les contributions gaussienne et super relevé (super sample covariance, SSC).

Une analyse tomographique des BAO avec le galaxy clustering photométrique

Les analyses BAO effectuées avec ces données sont présentées dans le chapitre 4, avec différentes approches : analyse sur les bins de redshift individuels ou analyse jointe, covariance empirique ou analytique, vecteur de données mesuré ou synthétique, méthode bayésienne avec MCMC ou fréquentiste avec le profil de vraisemblance. L'analyse BAO repose sur la forme fonctionnelle

$$T(\alpha,\theta) = B\, w(\alpha\theta) + A_0 + \frac{A_1}{\theta} + \frac{A_2}{\theta^2} \tag{0.1}$$

dans laquelle α est le paramètre Alcock-Paczynski transverse qui quantifie un décalage éventuel du pic BAO entre $w(\theta)$ mesuré et le modèle théorique $w_{fid}(\theta)$ calculé pour la cosmologie fiducielle de la simulation Flagship. Les paramètres de nuisance B, A_0, A_1, et A_2 sont nécessaires pour compenser d'éventuels effets résiduels non linéaires qui n'affectent pas la position du pic BAO. L'analyse de chaque bins, fournit 13 valeurs de α proches de 1 comme attendu, la cosmologie fiducielle étant identique à celle de la simulation. Dans le premier bin de redshift, là où le pic BAO est large et dilué du fait de l'évolution gravitationnelle non linéaire des grandes structures, l'incertitude sur α obtenue par la méthode MCMC avec la covariance de jackknife vaut 0.131, alors qu'elle atteint 0.024 dans le bin le mieux contraint. Les variations constatées sont compatibles avec $\alpha = 1$ dans tous les bins sauf le 11^e où un décalage de $1.3\,\sigma$ est trouvé. Je vérifie que ces biais disparaissent lorsque le vecteur de données $w(\theta)$ mesuré est remplacé par un vecteur synthétique calculé comme le modèle théorique (cas idéal sans bruit). Les contraintes obtenues par profil de vraisemblance sont équivalentes dans les bins où le signal BAO est bien défini. Avec les contraintes obtenues dans chaque bin, je montre que l'on peut contraindre l'évolution de l'expansion de l'Univers. En effet, comme α dépend de h, Ω_b et Ω_{cdm}, on peut contraindre ces paramètres. Avec une probabilité a priori de Planck 2015 sur le produit $\Omega_b\, h^2$, on obtient $h = 0.669 \pm 0.003$, $\Omega_b \times 10^2 = 4.921^{+0.044}_{-0.046}$ et $\Omega_{cdm} = 0.293^{+0.023}_{-0.022}$. Les biais sur h, Ω_b et Ω_{cdm} sont réduits de 0.4, 0.4, et 0.9 σ avec $w(\theta)$ mesuré à 0.1, 0.1, et 0.3 σ avec le vecteur de données synthétique. Dans les deux cas, on quantifie le poids de chaque bin de redshift en les

retirant successivement de l'analyse. On constate que le bin 11, celui dont la valeur de α est 1.3σ supérieure à 1, explique les biais observés avec des biais réduits de 0.4, 0.4, et 0.9 σ à 0.3, 0.2, et 0.4 σ.

Avec l'analyse jointe, un unique paramètre α est utilisé pour tous les bins de redshift. Cela augmente la puissance de contrainte de l'analyse mais ne donne plus l'évolution en fonction du redshift. Je démontre le potentiel du GCph avec *Euclid* avec des contraintes sur ce α joint trois fois plus fortes que celles obtenues par le Dark Energy Survey en 2024. De la même manière que pour les contraintes sur les paramètres cosmologiques, je vérifie le poids de chaque bin dans l'analyse jointe. Je mets en garde sur l'utilisation de cette analyse dans le contexte d'*Euclid* car l'analyse jointe n'est pertinente que dans l'approximation d'une cosmologie fiducielle choisie proche de la cosmologie réelle, inconnue dans le cadre de l'Univers. En cas de différence, la variation de α par rapport à la valeur de référence dépend du redshift et étant donné la puissance de contrainte de l'analyse jointe avec *Euclid*, cet effet peut devenir non négligeable, contrairement aux analyses de relevés précédents qui couvrent un intervalle de redshift beaucoup plus restreint comme DES, en plus d'avoir une puissance de contrainte inférieure.

Une analyse détaillée de la robustesse des résultats obtenues est fournie, au-delà du poids des bins de redshift inclus dans l'analyse. L'effet de la cosmologie fiducielle est vérifié et inférieur à 0.1σ pour des variations de $\Omega_{\rm cdm}$ large de $\pm 5\sigma_{Planck}$. La forme fonctionnelle utilisée pour extraire α donnée par Eq. (0.1) est arbitraire et l'ordre du polynôme peut être modifié. Je teste 10 variations du polynôme. En retirant le terme en θ^{-2}, un biais allant jusqu'à 0.4σ apparaît sur α mesuré dans les premiers bins de redshift. L'incertitude est également sous-estimée d'environ 10% dans ce cas. En revanche, augmenter l'ordre du polynôme n'améliore ni les contraintes, ni la robustesse vis-à-vis du choix de cosmologie fiducielle. L'influence des distorsions de l'espace des redshifts est évaluée. Elles sont inclues dans le modèle théorique par défaut mais si elles sont retirées, les paramètres de nuisance compensent efficacement la variation d'amplitude de $w(\theta)$.

L'effet de la sélection en séparations angulaires $[\theta_{\rm min}, \theta_{\rm max}]$ appliquée à $w(\theta)$ dans l'analyse bayésienne est étudié. Je montre qu'il est important de considérer ce point car $\theta_{\rm BAO}$ varie de 1.6°à 7°et exclure $\theta \leq 1°$ semble biaiser α, du moins dans l'analyse réalisée avec une approche d'estimation du maximum de vraisemblance. Une grille de limites $[\theta_{\rm min}, \theta_{\rm max}]$ restreinte et choisie suite aux résultats de l'analyse précédente est ensuite utilisée dans une analyse MCMC. Cette dernière montre que cette fois-ci, les contraintes sont robustes à la fois au niveau de α dans chaque bin de redshift et au niveau des contraintes cosmologiques sur h, $\Omega_{\rm b}$ et $\Omega_{\rm cdm}$. La définition des bins de redshifts, équipeuplés ou équidistants, est importante pour les contraintes cosmologiques. En effet, le pic BAO est mieux défini dans un plus grand nombre de bins, ce qui améliore les contraintes sur $\Omega_{\rm cdm}$ de 36.4%. De plus, les biais précédemment constatés sur h, $\Omega_{\rm b}$ et $\Omega_{\rm cdm}$ avec le binning équipeuplé sont réduits de 0.3, 0.5 et 1.0σ à 0.09, 0.1 et 0.24σ. L'effet de la covariance utilisée est également quantifié sur les analyses individuelles et jointes. La covariance de jackknife surestime l'incertitude de $w(\theta)$ par rapport à la covariance analytique, ce qui explique l'incertitude en moyenne

39% plus grande sur α, avec un maximum de 99% à haut redshift. Avec un vecteur $w(\theta)$ synthétique, cet effet est moins marqué, avec une incertitude en moyenne 28% plus grande et avec un maximum de 55%. On constate aussi un biais de α par rapport à 1 qui est plus faible avec la covariance analytique. En revanche, la contribution de la SSC à la covariance analytique est complètement négligeable avec un décalage maximal de $0.04\,\sigma$ sur α. Pour l'analyse jointe, je constate que l'analyse MCMC avec `emcee` souffre de problèmes d'exploration de l'espace des paramètres pour α lorsque la covariance analytique est utilisée et j'explique pourquoi. Je conclus ce chapitre par une étude préliminaire des pistes d'améliorations de ces analyses BAO pour de futurs travaux suggérant qu'utiliser 15 bins équidistants plutôt que 13 équipeuplés peut améliorer la figure de mérite de h, Ω_b et Ω_cdm d'un facteur 1.5, avec une amélioration de 32% sur la contrainte de Ω_cdm.

Une analyse tomographique full-shape avec le galaxy clustering photométrique

Ce chapitre 5 est dédié à l'étude tomographique dite full-shape de $w(\theta)$, utilisant sa forme entière plutôt que la seule position du pic BAO. La mesure de $w(\theta)$ réalisée avec 6 bins de redshift et une sélection d'échantillon de galaxies à $I_\mathrm{E} \leq 22.25$ est utilisée, de manière similaire à l'analyse prévue pour la DR1 d'*Euclid*. Ce travail a été réalisé en collaboration avec Klara Bertmann dans le contexte du groupe de travail du GCph *Euclid*. Alors qu'elle a effectué une analyse 3×2-points avec des vecteurs de données synthétiques, je me suis concentré sur le GCph avec les mesures effectuées sur la simulation Flagship. L'analyse MCMC pour le full-shape échantillonne les paramètres cosmologiques du modèle ΛCDM plutôt qu'un template comme dans l'analyse des BAO. Je fournis les contraintes obtenues tout en me focalisant sur les biais observés en fonction de différents choix, comme celui de la covariance, analytique ou empirique, ou bien en fonction des échelles angulaires utilisées. La comparaison des biais est réalisée au niveau du modèle théorique de $w(\theta)$ mais aussi au niveau des contraintes cosmologiques. Je constate notamment des écarts dans l'amplitude de $w(\theta)$ aux échelles $\theta \geq 100'$ qui occasionnent des biais supérieurs à $2\,\sigma$ sur les paramètres cosmologiques si ces échelles ne sont pas exclues.

Dans un second temps, je quantifie l'effet d'erreurs liées aux distributions de redshift dans le modèle théorique de $w(\theta)$. En effet, ces distributions sont estimées à partir des données et donc sujettes à erreurs. Ces erreurs sont paramétrées en un paramètre de biais et un paramètre d'élargissement des distributions. Un biais continu et multiplicatif B$= 0.002\,(1+z)$ et un biais discret et additif dont l'amplitude dépend du redshift moyen du bin B$= 0.002\,(1+z_{\mathrm{moyen},i})$ sont considérés, tandis qu'un étirement des distributions d'un facteur W$= 1.02$ est envisagé, seul ou en combinaison avec le biais. Je constate que les deux biais ont un effet très nettement inférieur à l'étirement avec des biais qui n'excèdent pas $0.1\,\sigma$ sur σ_8. En revanche, l'étirement biaise σ_8 de $0.44\,\sigma$ à lui tout seul et de $0.49\,\sigma$ s'il est associé au biais. Ces résultats sont susceptibles de changer en fonction de la quantité de données disponibles à la DR1. Il sera donc

important de vérifier ces conclusions une fois l'échantillon DR1 mieux connu.

Conclusion

Dans cette thèse, j'étudie la sonde du GCph pour exploiter au mieux les observations de la mission *Euclid*. L'application de méthodes de deep learning pour calculer les photo-z nécessaires au GCph est proposée dans le chapitre 2. J'ai montré que les tendances observées sur un ensemble de données du relevé SDSS DR12 sont retrouvée avec des données *Euclid* simulées, bien que les bandes photométriques soient différentes : utiliser des réseaux CNN à inception pour exploiter l'image des galaxies améliore les prédictions des $z_{\rm ph}$ et combiner image et magnitudes avec des architectures hybrides est encore plus efficace. De plus, je montre qu'il est possible d'utiliser ces réseaux pour prédire des PDF de $z_{\rm ph}$ sans dégrader les performances. Le chapitre 3 décrit le modèle théorique de $w(\theta)$ et l'importance d'éléments comme les RSD ou l'approximation de Limber. J'ai réalisé différentes mesures de $w(\theta)$ avec les données de la simulation *Euclid* Flagship, à la fois pour d'autres analyses et pour étudier les conséquences de nombreux choix dans la mesure, montrant l'importance du type de $z_{\rm ph}$, de la taille ou de la résolution angulaire du catalogue de points aléatoires, avant d'introduire les covariances empirique et analytique. Dans le chapitre 4, mon analyse tomographique des BAO avec ces données fournit des résultats présentant des progrès significatifs pour contraindre α à la fois en fonction du redshift et avec une analyse jointe des bins de redshifts. J'ai obtenu des contraintes sur les paramètres cosmologiques h, $\Omega_{\rm b}$ et $\Omega_{\rm cdm}$ à partir des valeurs de α, montrant les capacités du GCph avec *Euclid*. L'étude de nombreux choix d'analyse a aussi révélé le fait que malgré la robustesse des BAO vis-à-vis de nombreux effets comme le choix de la cosmologie fiducielle, de la forme fonctionnelle utilisée pour extraire le signal ou bien vis-à-vis des RSD, il est nécessaire d'être prudent et d'étudier en détail le poids de chacun des bins de redshift dans les contraintes obtenues, le choix de la sélection en séparations angulaires ou encore de la covariance. Enfin, je fournis des pistes d'améliorations pour les futures analyses BAO avec le GCph et *Euclid* en étudiant l'effet du nombre de bins de redshift, de leur type (équipeuplé ou équidistant) et du choix de magnitude limite de l'échantillon de galaxies. Une analyse full-shape a été présentée dans le chapitre 5 pour estimer les contraintes cosmologiques sur $\Omega_{\rm m}$, σ_8 et S_8 possibles avec le GCph au moment de la DR1 d'*Euclid*. J'ai également quantifié l'importance d'un biais et d'un étirement des distributions de redshift des galaxies utilisées dans le modèle théorique de $w(\theta)$. Il sera donc important d'utiliser des paramètres de nuisance pour éviter ces biais, malgré la détérioration des contraintes cosmologiques liée à la marginalisation d'un plus grand nombre de paramètres. Quand les données *Euclid* le permettront, le code développé durant cette thèse permettra une étude complète depuis la production des photo-z à partir des images de galaxies et avec des modèles de deep learning, jusqu'aux contraintes cosmologiques avec à la fois les études des BAO et full-shape du galaxy clustering photométrique tomographique.

Acknowledgements

I would like to thank my thesis advisors Stéphanie Escoffier and William Gillard who gave me this unique opportunity to work on a subject I love within the context of the preparation of the *Euclid* mission, its launch and first 20 months of observations. Your questions and feedback during our regular meetings helped me improve my work throughout these years and this is invaluable.

I would also like to thank Alain Blanchard and Etienne Burtin for reviewing my thesis as well as Micol Bolzonella and Ariel Sánchez for accepting to be part of my thesis committee, for your comments and questions.

I am grateful to Dominique Fouchez as head of the Renoir Cosmology group during most of my thesis at CPPM. The Renoir meetings have always been interesting and I appreciate that you invited so many researchers to give talks. For our discussions on BAO and also for taking part in the organization of the Renoir meetings, I give my thanks to Julian Bautista. Your investment in the group and your positivity is always a pleasure to see. For welcoming me at CPPM and our discussions, I am grateful to the Renoir Cosmology group with Benjamin, Smaïn, Fabrice, Marie-Claude, Charling, Alice, Nicolas, Aurélia and Frédéric. I thank all the PhD and post-doctoral students I had the chance to interact with : Sébastien, Tyann, Jean, Vincent, Lucas, Simone, Pauline, Philippe and Marie.

I would like to express my gratitude to Isaac Tutusaus and Stefano Camera for their advice as leads of the *Euclid* Photometric Galaxy Clustering Work Package of the Galaxy Clustering Science Working Group. The feedback and suggestions you gave me since the beginning of my thesis were precious.

For all the help with the DEC cluster and providing 3 GPU to train my deep learning models, I want to give special thanks to Julien Zoubian and Adrien Rivière.

I would like to thank Ben Henghes for our exchanges on deep learning and for sharing his data set.

Many thanks to Sylvain de la Torre for sharing his calibrated bypass model of *Euclid* spectroscopic redshifts.

For the help with their `PySSC` code, I would like to thank Sylvain Gouyou-Beauchamps and Fabien Lacasa.

Thank you to the *Euclid* Collaboration, it was a real pleasure to work within such a scientifically rich environment.

I would like to thank Paolo Bianchini and Jonathan Chardin who offered me my first internship in Astrophysics at the Strasbourg Astronomical Observatory and helped me start in this field as I wanted to since so many years.

To my parents and my brother, thank you. I cannot express the extent of my gratitude. For raising me, being role models, giving me my passion for science and books,

encouraging my curiosity and answering my questions, for providing me with a great education, for your continuous support, thank you again.

Contents

Affidavit 2

Liste de publications et participation aux conférences 3

Résumé et mots clés 5

Abstract and keywords 7

Résumé en français 9

Acknowledgements 19

Contents 21

List of Figures 24

List of Tables 29

Introduction 31

1. Cosmology at the dawn of stage IV surveys 33
- 1.1. The LCDM model . . . 33
  - 1.1.1. Observational cosmology . . . 33
  - 1.1.2. General relativity and metric . . . 36
  - 1.1.3. Content of the Universe . . . 39
  - 1.1.4. The LCDM model parameters . . . 41
  - 1.1.5. Dark energy models . . . 43
- 1.2. The Euclid survey . . . 44
  - 1.2.1. Spectroscopy with Euclid . . . 44
  - 1.2.2. Photometry with Euclid . . . 46
- 1.3. What are BAO . . . 47

2. Photometric redshifts 51
- 2.1. Data-driven methods . . . 52
  - 2.1.1. State of the art of data-driven methods for photo-z . . . 52
  - 2.1.2. Convolutional neural networks . . . 55
  - 2.1.3. Metrics . . . 58
- 2.2. Deep learning for photometric redshifts with SDSS DR12 . . . 59
  - 2.2.1. Data . . . 59
  - 2.2.2. Results with SDSS DR12 . . . 60

2.3. Photometric redshifts with the Euclid Science Challenge 8 66
2.3.1. Data and mock spectroscopic redshifts 66
2.3.2. Results with Euclid SC8 70

3. Photometric galaxy clustering **75**
3.1. A complementary probe for Euclid 75
3.2. The two-point angular correlation function 77
3.2.1. Theory 77
3.2.2. Estimator 82
3.3. The Euclid Flagship simulation 82
3.4. Measurements of the two-point correlation function 86
3.4.1. Two-point angular correlation function with the equipopulated binning 86
3.4.2. Two-point angular correlation function with the equidistant binning 88
3.4.3. Two-point angular correlation function with a DR1 setting . . . 92
3.4.4. Effect of the photometric redshift choice 92
3.4.5. Effect of the random sample angular resolution $N_{\rm side}$ 96
3.4.6. The `TreeCorr` bin_slop approximation 97
3.4.7. Jackknife resampling, effect of $N_{\rm jack}$ 101
3.4.8. Effect of the ratio $N_{\rm rand}/N_{\rm galaxies}$ 101
3.5. Covariances 103

4. A tomographic BAO analysis of photometric galaxy clustering **112**
4.1. Constraints on the BAO scale as a function of redshift 113
4.1.1. Methodology for the analysis of individual redshift bins 113
4.1.2. Results of the individual redshift bins baseline analysis 115
4.2. Cosmological constraints from BAO 121
4.2.1. Methodology of the inference of cosmological parameters from BAO 121
4.2.2. Cosmological parameters infered from BAO 123
4.3. Constraints on alpha from a joint analysis 127
4.3.1. Methodology for the joint analysis 127
4.3.2. Results with the baseline joint analysis 127
4.4. BAO, a robust probe 130
4.4.1. Influence of the fiducial cosmology 130
4.4.2. Influence of the template 130
4.4.3. Influence of redshift space distortions 132
4.4.4. Influence of the scale cuts 133
4.4.5. Influence of the redshift binning scheme 136
4.4.6. Influence of the covariance 140
4.4.7. Optimization of the sample selection and redshift binning scheme 146

5. A tomographic full-shape analysis of photometric galaxy clustering 150
5.1. Methodology of the full-shape analysis 150
5.2. Constraints on the ΛCDM model 152
5.3. Impact of redshift uncertainties on cosmological constraints 154

Conclusion 161

Bibliography 164

Appendices 181

A. Architectures of deep learning models 182
A.1. Multi-layer perceptron 182
A.2. Sequential CNN 183
A.3. Inception CNN 184
A.4. Multi-input inception CNN+MLP 186
A.5. ResNet34 189

B. Optimization for the BAO analysis 193

List of Figures

1.1. Hubble diagram of galaxy velocities 35
1.2. Evolution of the density of radiation, matter and cosmological constant as a function of the scale factor 40
1.3. Evolution of the scale factor as a function of Ω_m and Ω_Λ 42
1.4. Transmission of the *Euclid* filters as a function of the wavelength 46

2.1. 2D convolutional layer : Hadamard product 56
2.2. Inception block architecture 57
2.3. SDSS DR12 redshift distribution of galaxies in the training sample with photometry in all u, g , r , i , and z passbands 60
2.4. 2D histogram of z_{ph} estimates against z_{spec} with the random forest algorithm 61
2.5. 2D histogram of z_{ph} estimates against z_{spec} with the ResNet34 model . 62
2.6. 2D histogram of z_{ph} estimates against z_{spec} with the inception CNN model 63
2.7. Evolution of the ratio of the metrics M for various training sample sizes over their respective values measured with the entire data set 64
2.8. Random examples of photo-z PDF predicted with the inception CNN . 65
2.9. Histogram of the PIT values of the photo-z PDF predicted with the inception CNN. 65
2.10. Galaxy images in the H_E passband with the associated z_{spec} measured by the SGS pipeline during the *Euclid* SC8. 67
2.11. Spectroscopic redshifts measured by the SGS pipeline during the *Euclid* SC8 against the true redshifts, which range between $z = 0$ and $z = 2.3$. . 67
2.12. Fraction of right redshifts in orange, noise interlopers in blue, and different kind of line interlopers as a function of the true redshift, for a H_α flux of 0.5×10^{-16} erg/s/cm^2. 69
2.13. Probability of measuring a redshift z_m with the spectroscopic pipeline as a function of the true redshift z_t for various H_α flux thresholds. . . . 70
2.14. Simulated spectroscopic redshifts as a function the true redshifts. . . . 71
2.15. Photometric redshifts as a function of spectroscopic redshifts with a MLP 71
2.16. Photometric redshifts as a function of spectroscopic redshifts with a sequential CNN 72
2.17. Photometric redshifts as a function of spectroscopic redshifts with an inception CNN 73
2.18. Photometric redshifts as a function of spectroscopic redshifts with a multi-input inception CNN 74

3.1. Theoretical $w(\theta)$ computed with and without RSD using the redshift distributions of 4 redshift bins from the Flagship simulation shown in Fig. 3.6. 78
3.2. Effect of $k_{\max}$ in Mpc^{-1} over the theoretical model of $w(\theta)$ computed in 4 of the 13 redshift bins using the redshift distribution from the Flagship simulation 79
3.3. Effect of $\ell_{\max}$ over the theoretical model of $w(\theta)$ computed in 4 of the 13 redshift bins using the redshift distribution from the Flagship simulation. 80
3.4. Angular power spectrum C_ℓ computed with and without Limber approximation 81
3.5. Effect of the Limber approximation over the theoretical model of $w(\theta)$ computed in 4 of the 13 redshift bins using the redshift distribution from the Flagship simulation. 81
3.6. Normalised redshift distributions of galaxies in Flagship 2.1.10. The sample is divided into 13 equipopulated photometric redshift bins. . . 84
3.7. Normalised redshift distributions of galaxies in Flagship 2.1.10. The sample is divided into 13 equidistant photometric redshift bins. 84
3.8. Two-point angular correlation function measured on the Flagship simulation in 13 equipopulated redshift bins 86
3.9. Galaxy bias measured with equidistant and equipopulated redshift bins on Flagship 2.1 87
3.10. Two-point angular correlation function measured on the Flagship simulation in 13 equipopulated redshift bins with their 78 cross-correlations 89
3.11. For each redshift bin i, ratios of the associated cross-correlations (i,j) with bin j with respect to the autocorrelation (i,i) 90
3.12. Two-point angular correlation function jackknife error measured on the Flagship simulation in 13 equidistant and equipopulated redshift bins. 90
3.13. Two-point angular correlation function measured on the Flagship simulation in 13 equidistant redshift bins 91
3.14. Normalised redshift distributions of galaxies in Flagship 2.1.10. The sample is divided into 6 equipopulated photometric redshift bins. . . . 92
3.15. Two-point angular correlation function measured on the Flagship simulation in 6 equipopulated redshift bins with $I_{\mathrm{E}} \leq 23.5$ 93
3.16. Two-point angular correlation function measured on the 2500 deg^2 of the Flagship simulation in 6 equipopulated redshift bins with a DR1-like setting 93
3.17. Shift of $w(\theta)$ measured with the first mode photo-z with respect to the reference $w(\theta)$ measured with the median photo-z 94
3.18. Two-point angular correlation function measured with photo-z either computed with `NNPZ` or `DeepZ` on the full Flagship simulation in 12 equidistant redshift bins 95
3.19. Influence of the angular resolution of the HealPix mask N_{side} used to compute the catalogue of random points with DES 96

3.20. Influence of the angular resolution of the HealPix mask $N_{\rm side}$ used to compute the catalogue of random points with Flagship 97
3.21. Comparison of $w(\theta)$ measured in the first redshift bin of the Flagship simulation with $b_{\rm s} \in (0.3, 0.6, 1.0)$ 99
3.22. Comparison of the effect of $b_{\rm s}$ in all redshift bins for $b_{\rm s} = 1$ (version 4.3.2) and $b_{\rm s} = 0.01$ (version 4.3.3) 100
3.23. Computation time as a function of the number of galaxies and random points for $w(\theta)$ on the Flagship simulation 13 equidistant bins. 100
3.24. Comparison of the jackknife error measured on the Flagship simulation with a resampling of $w(\theta)$ in $N_{\rm jack} \in (30, 60, 90, 210, 500)$ patches 102
3.25. Comparison of the jackknife error measured in the last four redshift bins on the Flagship simulation with a resampling of $w(\theta)$ in 500 or 1000 patches 102
3.26. Comparison of the shot noise measured on the Flagship simulation in the first redshift bin for $N_{\rm rand}/N_{\rm galaxies} \in [10, 20, 30, 40, 50]$. 103
3.27. Comparison of $w(\theta)$ measured on the Flagship simulation in the first redshift bin for $N_{\rm rand}/N_{\rm galaxies} \in [10, 20, 30, 40, 50]$. 103
3.28. Full jackknife covariance matrix of $w(\theta)$ in the 13 redshift bins, cross-correlations included 105
3.29. $S_{i,j,k,l}$ matrix computed with the PySSC code and the $p_i(z)$ measured on Flagship 2.1.10. 108
3.30. SSC covariance matrix computed with the PySSC code and the $p_i(z)$ measured on Flagship 2.1.10. 109
3.31. Full Gaussian+SSC analytical covariance matrix of $w(\theta)$ in the 13 redshift bins, cross-correlations included 110
3.32. Ratio of the diagonal terms of the autocorrelations blocks of the Gaussian and jackknife covariance matrices. 111
3.33. Ratio of the diagonal terms of the autocorrelations blocks of the Gaussian+SSC and Gaussian covariance matrices. 111

4.1. Comparison of the α_i obtained by MCMC analysis and profile likelihood on the data vector measured in the 13 redshift bins of Flagship. 117
4.2. Comparison of the constraints on the ratio $D_{\rm A}/r_{\rm d}$ obtained with BOSS DR12, DES Y6, and Flagship 2.1 118
4.3. Comparison of the α_i obtained by MCMC analysis with template fitting of $w(\theta)$ measured on Flagship and computed as a synthetic noise-free data vector 119
4.4. Comparison of the α_i obtained by MCMC analysis and profile likelihood on the synthetic data vector computed in the 13 redshift bins. 120
4.5. Evolution of the ratio $D_{\rm A}/r_{\rm d}$ as a function of redshift. 123
4.6. Constraints on h, $\Omega_{\rm b}$, and $\Omega_{\rm cdm}$ with *Planck* priors. 124
4.7. Comparison of cosmological parameters obtained when one or several redshift bins are removed from the analysis 125

4.8. Constraints on h, Ω_b, and Ω_{cdm} without *Planck* priors and large uniform priors . . . 126
4.9. Constraints on h, Ω_b, and Ω_{cdm} without *Planck* priors and smaller uniform priors . . . 126
4.10. Profile likelihood of α from a joint analysis . . . 128
4.11. Comparison of α from a joint analysis in which redshift bins are successively removed . . . 129
4.12. Effect of the fiducial cosmology on α in all redshift bins for three variations 131
4.13. Comparison of templates for BAO fitting as a function of redshift bin . 132
4.14. Comparison of templates 1 and 6 for BAO fitting at the level of cosmological parameters . . . 133
4.15. Comparison of the constraints on α with and without RSD in the theoretical model for the redshift bin $1.048 < z < 1.190$ . . . 134
4.16. Bias on α as a function of minimum and maximum scales in the 13 redshift bins . . . 135
4.17. Comparison of the constraints obtained for α in bin 2 when the scale cuts applied to the data vector are varied in a grid . . . 136
4.18. Comparison of the constraints obtained for α in bin 13 when the scale cuts applied to the data vector are varied in a grid . . . 137
4.19. Comparison of the constraints on h, Ω_b, and Ω_{cdm} obtained from BAO when the scale cuts applied to the data vector are varied in a grid . . . 139
4.20. Comparison of the constraints on α_i for the equidistant and equipopulated redshift binning schemes, in blue and orange respectively. . . . 139
4.21. Comparison of the constraints on cosmological parameters obtained with an equidistant and equipopulated redshift binning schemes, in blue and orange respectively. . . . 140
4.22. Comparison of the constraints on α_i changing the covariance from jackknife to Gaussian+SSC. . . . 141
4.23. Comparison of the constraints on α_i changing the covariance from jackknife to Gaussian+SSC, with a synthetic data vector. . . . 141
4.24. Comparison of the constraints on α_i changing the covariance from Gaussian to Gaussian+SSC, with a synthetic data vector. . . . 142
4.25. Result of the profile likelihood $\Delta\chi^2(\alpha)$ for the joint analysis . . . 143
4.26. 1 to 5σ contours of α against the first nuisance parameter B_0 obtained with the MCMC analysis of the measured $w(\theta)$, analytical covariance and with a large initialization . . . 146
4.27. Evolution of the synthetic $w(\theta)$ with 9 redshift bins as a function of the binning scheme and magnitude cut in the I_E band . . . 147
4.28. For various numbers of bins, I_E magnitude cuts and binning schemes, ratio of the FoM of h, Ω_b, and Ω_{cdm} over the FoM of the baseline with 13 equipopulated bins with $I_E \leq 24.5$. . . . 149

5.1. Comparison of the constraints on Ω_m, σ_8 and S_8 for the simulated and measured $w(\theta)$ with the full-shape analysis in a DR1-like setting. . . . 152

5.2. Measurement of $w(\theta)$ on the Flagship simulation with 6 redshift bins and comparison with the theoretical model simulated while varying the redshift distribution, galaxy bias and neutrino mass. 154
5.3. Comparison of the constraints on Ω_m, σ_8 and S_8 for the full-shape analysis, varying the redshift distribution, galaxy bias and neutrino mass used to compute the theoretical model. 155
5.4. Comparison of the redshift distributions used in the full-shape analysis with and without multiplicative bias in a DR1-like setting. 156
5.5. Comparison of the redshift distributions used in the full-shape analysis with and without stretch in a DR1-like setting. 157
5.6. Comparison of the theoretical model of $w(\theta)$ used in the full-shape analysis with and without bias and stretch in a DR1-like setting. 159
5.7. Comparison of the constraints on Ω_m, σ_8 and S_8 for the full-shape analysis with and without bias and stretch in a DR1-like setting. 160
5.8. Comparison of the constraints on Ω_m, σ_8 and S_8 for the full-shape analysis with and without bias and stretch in a DR1-like setting with b_g fitted between $6'$ and $60'$. 160

A.1. Inception CNN architecture. 188

List of Tables

2.1. Statistics of the neural networks trained to predict photo-z point-estimates on the sample of SDSS DR12 galaxies up to $z_{\rm spec} = 7$. 61
2.2. Statistics of the neural networks trained to predict photo-z PDF on the sample of SDSS DR12 galaxies up to $z_{\rm spec} = 7$. The point-estimates used in the metrics are computed from the PDF as the expected value. . . . 64
2.3. Statistics of the neural networks trained to predict photo-z point-estimates on the SC8 sample. 72

3.1. Statistics of the 13 redshift bins for the Flagship 2.1.10 galaxy mock catalogue with two different redshift binning schemes 85

4.1. Priors used for the template fitting parameters 114
4.2. α with its uncertainty at 68 % extracted from the MCMC analysis and its detection level in each redshift bin 116
4.3. Measurement of α in the 13 redshift bins, its positive and negative uncertainties determined by the $16^{\rm th}$ and $84^{\rm th}$ quantiles for MCMC and INS, and the positive and negative roots of $\Delta\chi^2(\alpha) - 1 = 0$ for profile likelihood (PL). 117
4.4. α with its uncertainty extracted from the MCMC analysis in each redshift bin using a noise-free synthetic data vector. 119
4.5. Measurement of α in the 13 redshift bins as in Table 4.3 for the validation synthetic data vector. 120
4.6. α with its uncertainty extracted from the MCMC analysis in a DR1-like setting and its detection level in 6 equipopulated redshift bins 121
4.7. α obtained with the reference template 1 and templates including higher polynomial orders using a fiducial cosmology which differs from the simulation cosmology 134
4.8. α with its uncertainty extracted from the MCMC analysis and its detection level in each equidistant redshift bin 138
4.9. Constraints on α from various joint analyses, varying the covariance used, data vector, analysis method 145

5.1. Galaxy bias measured by fitting $w(\theta)$ following the approach detailed in Sect. 3.4.1 with two different choice of scale cuts. 151

5.2. Constraints on the parameters of the ΛCDM model with the full-shape analysis in a DR1-like setting. The first setting uses the simulated $w(\theta)$ and the analytical covariance while setting 2 uses the measured $w(\theta)$ and the analytical covariance and setting 3 uses the measured $w(\theta)$ and jackknife covariance. 153
5.3. Constraints on the parameters of the ΛCDM model with the full-shape analysis in a DR1-like setting, varying the redshift distribution, galaxy bias and neutrino mass used to compute the theoretical model. 156
5.4. Constraints on the parameters of the ΛCDM model with the full-shape analysis in a DR1-like setting, varying the multiplicative bias B= 0.002(1+ z) and stretch W = 1.02 of the redshift distributions. The galaxy bias is fitted with $30' \leq \theta \leq 240'$. 158
5.5. Constraints on the parameters of the ΛCDM model with the full-shape analysis in a DR1-like setting, varying the redshift-dependent additive bias B = $0.002\left(1+z_{\mathrm{mean},i}\right)$ and stretch W = 1.02 of the redshift distributions. The galaxy bias is fitted with $6' \leq \theta \leq 60'$. 158

A.1. Properties of the layers of the MLP model 182
A.2. Properties of the layers of the sequential CNN model 183
A.3. Properties of the layers of the inception CNN model 184
A.4. Properties of the layers of the inception CNN+MLP model 186
A.5. Properties of the layers of the ResNet model 189

B.1. Cosmological constraints on h, Ω_{b}, and Ω_{cdm} obtained from BAO with between 9 and 15 bins, a cut in the I_{E} band varying between 22 and 25, and an equipopulated or equidistant binning scheme. 193

Introduction

Cosmology is the science which aims at studying the Universe and its evolution. One of the main goals of modern Cosmology is to quantify precisely which fraction of the content of the Universe each of its components represents. The theory of General Relativity established by Albert Einstein in 1915 allowed the development of a formal theoretical framework to study the laws governing the components of the Universe, their interactions and the way they affect the evolution of the entire Universe. This is a complex challenge which allows us to understand the origin of what we observe and to answer questions which used to be limited to philosophy or beliefs. To take on this challenge requires a theoretical work to create a model representing the Universe through a set of laws and equations but also a meticulous work of observation to study the behaviour of matter at cosmological scales. Confronting observations with theory is key to setting the parameters of these equations or to refute them if they are not compatible. Thus, observations help theory progress by excluding some cosmological models and guide the research work to try and explain observations which seem contradictory at first sight. In the same manner, theory guides observations by suggesting goals to attain in order to constrain its models. These goals can be to observe a large number of galaxies over a large sky area to better characterize their distribution on large scales, where the trends of the global evolution of the Universe are the strongest. Another example would be to reach a given spatial resolution to better quantify the distortion of these galaxies by the field of matter between the telescope and the galaxies, thus mapping the distribution of matter. The end of the 20th century and the beginning of the 21st have seen the birth of several galaxy surveys of increasing size, multiplying their performances with every technological advance. We are currently at the dawn of the era of stage IV cosmological surveys, initiated by the main program of the Dark Energy Spectroscopic Instrument in May 2021 (DESI). The Large Synoptic Space Telescope program will start at the end of 2025 while the nominal survey of the *Euclid* satellite started on 14 February 2024. It is dedicated to the study of dark energy and dark matter, the two main but invisible components of the Universe, by mapping the distribution of galaxies as tracers of matter. The statistical study of galaxy clustering determines the properties of large scale structures through various approaches like field-level inference to directly estimate theoretical model parameters from the galaxy distribution, another approach being summary statistics which condense the information of this distribution into an observable like the correlation function or its counterpart, the power spectrum. The theoretical framework developed since 1915 lead to the current standard model of Cosmology called ΛCDM, but also many other models to explain its failures.

In Chapter 1, I introduce basic notions of Cosmology from an observational and

theoretical point of view, in particular through Einstein's equations, to understand the relations between the Universe, its evolution and its content, as it is intimately linked to the birth of the ΛCDM model and other extensions like dark energy models. The *Euclid* survey is presented to understand the context of this work before taking a closer look into baryonic acoustic oscillations (BAO), the subject of the main analyses in this thesis. However, since I use photometric redshifts instead of spectroscopic redshifts to determine galaxy distances and study their clustering, I explore in Chapter 2 recent approaches developed to obtain better estimates of photometric redshifts through deep learning, first with Sloan Digital Sky Survey observations and then with *Euclid* simulations.

Chapter 3 is dedicated to the photometric galaxy clustering analysis. Starting from the theory of the observable used, the two-point angular correlation function, to its estimator and the *Euclid* Flagship simulation data, I then present the data vectors obtained in different configurations, with either the full 5157 deg^2 of the simulation or a restriction to an area of 2500 deg^2 expected at the time of the first *Euclid* public Data Release (DR1). Since it is a tomographic analysis, the effect of the redshift binning scheme used, equipopulated or equidistant, is considered. The effect of various analysis choices is studied, like the size and angular resolution of the catalogue of random points, or the number of jackknife samples to build an empirical covariance of the measured data vector. The empirical and analytical covariances are introduced from their theoretical standpoint and compared.

I present the BAO analyses performed with this data in Chapter 4, with several approaches : analysis on individual redshift bins and joint analysis, empirical or analytical covariance, measured or synthetic data vector, MCMC or profile likelihood. With the constraints obtained from individual redshift bins, I show that we can in turn constrain the expansion history of the Universe. With the joint analysis, I show the potential of photometric galaxy clustering with *Euclid* with a three-fold improvement with respect to the latest constraints obtained with the same probe in the Dark Energy Survey. A detailed analysis of the robustness of the results obtained is provided, with respect to the redshifts bins included in the analysis, the fiducial cosmology, the template used to extract the BAO signal, redshift space distortions, the scale cuts applied to the data vector, the redshift binning scheme, or the covariance used. I conclude the presentation of these BAO analyses with a preliminary study of how they can be improved in the future. A different analysis is presented in Chapter 5, where I study the full shape of $w(\theta)$ measured in a *Euclid* DR1-like setting to constrain the ΛCDM model cosmological parameters. These results are affected by the bias and broadening of the redshift distributions used to compute the theoretical model of $w(\theta)$ and we quantify this effect.

1. Cosmology at the dawn of stage IV surveys

Summary

1.1. The LCDM model 33
1.1.1. Observational cosmology 33
1.1.2. General relativity and metric 36
1.1.3. Content of the Universe 39
1.1.4. The LCDM model parameters 41
1.1.5. Dark energy models 43
1.2. The Euclid survey 44
1.2.1. Spectroscopy with Euclid 44
1.2.2. Photometry with Euclid 46
1.3. What are BAO 47

In this chapter, we present the context of this work, from the notions required to describe our Universe to the *Euclid* mission. The standard model of cosmology is introduced in Sect. 1.1. The *Euclid* mission will be introduced in Sect. 1.2 as one of the main stage IV surveys which will provide data to the scientific community for the next 6 years. Finally, as the main cosmological probe used in this thesis, baryonic acoustic oscillations (BAO) will be introduced in Sect. 1.3.

1.1. The ΛCDM model

Cosmology is the science which aims at studying the Universe, from its origin to its past and future evolutions. This study relies on the description of the content of the Universe and the laws governing the interactions of the various elements composing the Universe. This entails that we need to observe the Universe and have a theoretical framework with which these observations can be confronted.

1.1.1. Observational cosmology

While we have observed planets of the Solar system, stars of the Milky Way or close galaxies like Andromeda for centuries, only recently has technology improved to the point where surveys can span a large fraction of the sky. This lead to major discoveries

in the field of cosmology like the measurement of the cosmic microwave background radiation spectrum (CMB) in 1996 by the FIRAS instrument, on the COBE satellite (Mather et al., 1999). The CMB light is the first emitted after the recombination of electrons with hydrogen or helium atoms which were previously ionised in an opaque plasma, around 13.8 billion years ago. The recombination made the interaction rate of photons and electrons by Thomson scattering much smaller and allowed their propagation on long distances. The mean free path of photons is now larger than the observable Universe. The fact that the spectrum of this first light from 380 000 years after the Big Bang follows a black body distribution of temperature $T_{\rm CMB} = 2.725\,\mathrm{K}$ entails that the photons of the CMB were in thermal equilibrium with the primordial plasma before the Universe reached a temperature of about 2940 K, at the time these photons were last scattered. Showing that the Universe was hotter and denser in the past is a strong argument to further confirm that our Universe is in expansion. It was a confirmation rather than a discovery because the expansion was already known thanks to the work of several astronomers at the beginning of the 20th century. Henrietta Leavitt discovered the relation between the period of variation of the luminosity of Cepheid stars and their intrinsic luminosity which enabled the estimate of their distance (Leavitt et al., 1912). Edwin Hubble used this relation to estimate the distance of galaxies, thought to be extragalactic nebulae at this time, and publish the result of his observations with Milton Hamuson at Mount Wilson in Hubble (1929), showing the linearity of the relation between the distance of the observed source and its redshift z defined as

$$z \equiv \frac{\lambda_{\rm r} - \lambda_{\rm e}}{\lambda_{\rm e}}\,, \tag{1.1}$$

with $\lambda_{\rm e,r}$ the respective wavelength of the radiation emitted by the source and received by the observer. The linear relation Edwin Hubble published is

$$c\,z = H_0\,d\,, \tag{1.2}$$

where $c\,z$ is the speed of the object in the non-relativistic limit $v \ll c$ or $z \ll 1$ so that the Doppler effect gives the redshift z, d being the distance of the observed source and H_0 the Hubble constant in $\mathrm{km\,s^{-1}\,Mpc^{-1}}$. As one can see in Fig. 1.1, this relation entails that the further an object is, the faster it moves away from the observer, which suggests that the Universe is expanding since in the past, objects were closer. The measurements shown in Fig. 1.1 yield either a slope of $H_0 = 465 \pm 50\,\mathrm{km\,s^{-1}\,Mpc^{-1}}$ if all 24 galaxies are considered individually or $513 \pm 60\,\mathrm{km\,s^{-1}\,Mpc^{-1}}$ if they are grouped in 9 groups depending on their distance and direction, about which Edwin Hubble says that "For such scanty material, so poorly distributed, the results are fairly definite". The large difference with the value $H_0 \sim 70\,\mathrm{km\,s^{-1}\,Mpc^{-1}}$ measured today is explained by the fact that the distances estimated by Edwin Hubble were about 7 times smaller than the truth. Only because all distances were affected by the same factor was he able to find this relation. Since this relation was first discovered by George Lemaître in Lemaître (1927), this relation is now called the Hubble–Lemaître law. This discovery later lead to the development of the Big Bang theory which describes the observable

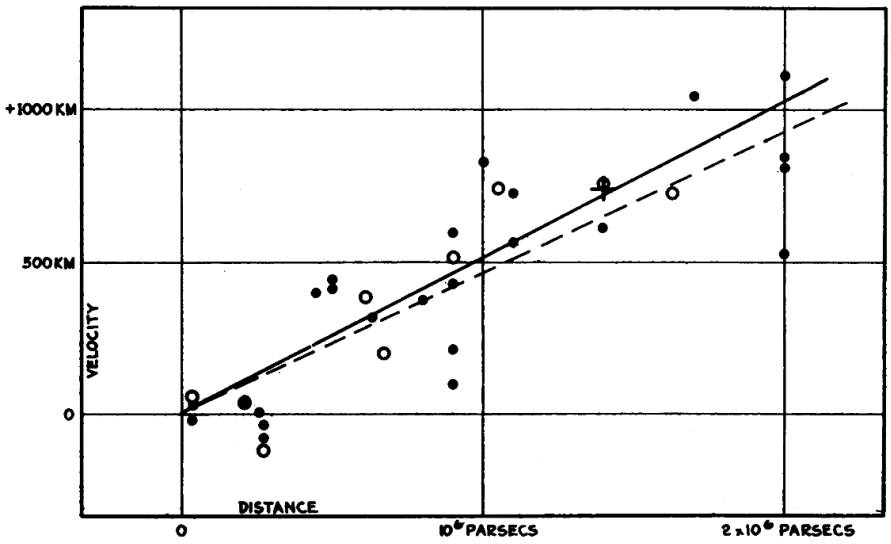


Figure 1.1. – Velocity of galaxies in $\mathrm{km\,s^{-1}}$ (the axis legend in kilometers is a mistake from the author) as a function of the distance in Mpc. These measurement yield a slope of $H_0 \sim 500\,\mathrm{km\,s^{-1}\,Mpc^{-1}}$ while improved distance measurements will later show that the value of the Hubble constant is closer to $70\,\mathrm{km\,s^{-1}\,Mpc^{-1}}$. Figure taken from Hubble (1929).

Universe as initially infinitely small, with all its content condensed at extremely high temperature and density, and expanded since then. The scales involved explain that the theoretical framework of the Big Bang is strongly linked to the field of particle physics. Note that the expansion of the Universe implies that as time goes, objects of fixed coordinates will maintain their comoving distance, defined as the distance between their coordinates, while their physical distance will increase with time. At this point, we define the scale factor a

$$a = \frac{1}{1+z} \tag{1.3}$$

as a quantity which is a function of time, corresponds to the ratio $\frac{r(t)}{r_0}$ between the physical and comoving distances, and describes the expansion of the Universe. The Hubble constant is the present value of the Hubble parameter defined as

$$H(t) \equiv \frac{\dot{a}(t)}{a(t)}. \tag{1.4}$$

On the opposite side of the spectrum of scales, surveys which map the position of galaxies on a large fraction of the sky like the Sloan Digital Sky Survey (SDSS, Eisenstein, Zehavi, et al., 2005) and the 2-degree Field Galaxy Redshift Survey (2dFGRS, Percival et al., 2001; Cole et al., 2005) allowed the observation of large scale structures and lead to a second major discovery which is the observation of the baryon acoustic

oscillations signal (BAO), seen as a small overdensity in the distribution of galaxies. The scale at which this overdensity exists is fixed in comoving coordinates and only changes in proper coordinates under the effect of the expansion of the Universe. BAO will be presented in more detail in Sect. 1.3. Cepheids which are far from us are not bright enough to measure their distances and then probe the evolution of the expansion on a long period of time. Supernovae of type Ia (SNIa), whose luminosity curve can be standardized to infer their distance, are brighter than Cepheids and can extend to higher redshifts the direct measurement of the expansion rate through the Hubble constant. This direct method is however also limited by the brightness and is usually used for redshifts $z < 1$. On the other hand, the BAO approach is sometimes called an indirect method as it probes the rate of expansion through a scale measured statistically from the observed distribution of galaxies and fixed at the drag epoch $z_{\rm drag} \sim 1060$. These two examples of observational cosmology successes are less than 30 years old. Since then, the speed at which technology progressed increased, so much so that the recent Dark Energy Spectroscopic Instrument (DESI) survey acquired in one year the largest sample of galaxy redshifts for its BAO analysis with 5.7 million galaxies (DESI Collaboration: Adame et al., 2024), about 3 times as large as the Data Release 16 of the SDSS survey (DR16) which spanned two decades (Alam, Aubert, et al., 2021).

1.1.2. General relativity and metric

In parallel of this observational aspect of cosmology, the theoretical field has also been growing since the beginning of the 20th century. While the theory of gravitation as established by Isaac Newton in his Philosophiae Naturalis Principia Mathematica (Newton, 1687) was a major step to explain interactions between massive objects, the work from Albert Einstein on the theory of General Relativity published in Einstein (1915) is the foundation of the theoretical framework required for cosmology. In his work, the gravitational force, which is dominant at cosmological scales, is described as the effect of mass and energy over the curvature of spacetime. The following explanations are mainly based on the Webb et al. (2023) book. This result on the gravitational force was derived from the equivalence principle which states that for any point of a gravitational field and at any time, one can always find a free-falling reference frame where the laws of physics are locally identical to the ones observed in a Galilean reference frame which is free from gravitational force. A geometrical analogy with the Gauss postulate is helpful in understanding the consequences of the equivalence principle over gravitation and the curvature of space. This postulate states that a curved surface can be locally described by a Euclidean geometry which entails that for a small displacement $\mathrm{d}M$ between two points, one can write the separation as $\mathrm{d}s^2 = \mathrm{d}\xi_x^2 + \mathrm{d}\xi_y^2$ where ξ_x and ξ_y are the locally Euclidean coordinates associated with the x and y coordinates of the curved surface. Gauss proved that the geometry of the surface is entirely described through the change of coordinates $\xi \rightarrow x$. The analogy can be done between the locally Euclidean coordinate system and the locally Galilean and free from gravitational force reference frame to help find a mathematical

expression of the equivalence principle. Generalizing this to one time coordinate and three spatial dimensions in a Galilean reference frame, we can write

$$\mathrm{d}s^2 = c^2\mathrm{d}t^2 - \mathrm{d}\xi_x^2 - \mathrm{d}\xi_y^2 - \mathrm{d}\xi_z^2 = \mathrm{d}\xi^\mu \eta_{\mu\nu}\mathrm{d}\xi^\nu\,, \tag{1.5}$$

where μ and $\nu \in [0,3]$ and the sum over repeated indices is implicit. The Minkowski metric $\eta_{\mu\nu}$ is a diagonal matrix of terms $[1,-1,-1,-1]$. A change of coordinate system can then be done through the relation

$$\mathrm{d}\xi^\mu = \frac{\partial \xi^\mu}{\partial x^\rho}\mathrm{d}x^\rho \tag{1.6}$$

to obtain

$$\mathrm{d}s^2 = \mathrm{d}x^\rho g_{\rho\sigma}\mathrm{d}x^\sigma\,, \tag{1.7}$$

with the metric

$$g_{\rho\sigma} = \frac{\partial \xi^\mu}{\partial x^\rho}\frac{\partial \xi^\nu}{\partial x^\sigma}\eta_{\mu\nu}\,. \tag{1.8}$$

This result can be used to derive the equations of motion for a particle under the effect of the gravitational force. The equivalence principle allows us to chose a free-falling reference frame locally free from any gravitational force of coordinate system ξ^α which entails that

$$\frac{\mathrm{d}^2\xi^\alpha}{\mathrm{d}\tau^2} = 0\,. \tag{1.9}$$

This can be rewritten using Eq. (1.6):

$$\frac{\partial \xi^\alpha}{\partial x^\mu}\frac{\mathrm{d}^2 x^\mu}{\mathrm{d}\tau^2} + \frac{\partial \xi^\alpha}{\partial x^\nu \partial x^\mu}\frac{\mathrm{d}x^\nu}{\mathrm{d}\tau}\frac{\mathrm{d}x^\mu}{\mathrm{d}\tau} = 0 \tag{1.10}$$

to obtain, after multiplying by $\frac{\partial x^\lambda}{\partial \xi^\alpha}$ and summing over α, the generic form of the equation of motion otherwise known as the geodesic equation

$$\frac{\mathrm{d}^2 x^\lambda}{\mathrm{d}\tau^2} + \Gamma^\lambda_{\mu\nu}\frac{\mathrm{d}x^\nu}{\mathrm{d}\tau}\frac{\mathrm{d}x^\mu}{\mathrm{d}\tau} = 0\,, \tag{1.11}$$

where the Christoffel symbol is

$$\Gamma^\lambda_{\mu\nu} = \frac{\partial^2 \xi^\alpha}{\partial x^\nu \partial x^\mu}\frac{\partial x^\lambda}{\partial \xi^\alpha} = \frac{1}{2}g^{\lambda\beta}\left(\partial_\mu g_{\beta\nu} + \partial_\nu g_{\mu\beta} - \partial_\beta g_{\mu\nu}\right), \tag{1.12}$$

with $g^{\lambda\beta}$ the inverse of $g_{\lambda\beta}$ and ∂_μ the contracted notation of the partial derivative $\frac{\partial}{\partial x^\mu}$. Thanks to this result, we understand the link between the gravitational force and the metric.

The relation between the spacetime curvature and its content is given by Einstein's

equation (Einstein, 1917) for a metric $g_{\mu\nu}$

$$G_{\mu\nu} + g_{\mu\nu}\Lambda = -\frac{8\pi G}{c^4} T_{\mu\nu}\,, \tag{1.13}$$

where $G_{\mu\nu}$ is the Einstein tensor, Λ is the cosmological constant, G is the Newton constant, and $T_{\mu\nu}$ is the energy-momentum tensor. The Einstein tensor is

$$G_{\mu\nu} = R_{\mu\nu} - \frac{1}{2} g_{\mu\nu} R\,, \tag{1.14}$$

with $R_{\mu\nu}$ the Ricci tensor

$$R_{\mu\nu} = \partial_\mu \Gamma^\sigma_{\mu\sigma} - \partial_\sigma \Gamma^\sigma_{\mu\nu} + \Gamma^\rho_{\mu\sigma}\Gamma^\sigma_{\rho\nu} - \Gamma^\rho_{\mu\nu}\Gamma^\sigma_{\rho\sigma}\,. \tag{1.15}$$

and the scalar curvature R, defined as the trace of the Ricci tensor

$$R = g^{\mu\nu} R_{\mu\nu}\,. \tag{1.16}$$

The energy-momentum tensor for a homogeneous and isotropic perfect fluid is

$$T_{\mu\nu} = \left(\rho + \frac{p}{c^2}\right) u_\mu u_\nu - p g_{\mu\nu}\,, \tag{1.17}$$

where ρ is the energy density, p the pressure, and u the four-velocity. $T_{\mu\nu}$ is a tensor of order 2 and so it is a 4×4 matrix. If the fluid is at rest, then we have $u_\mu = u_\nu = (1,0,0,0)$ and we find that $T_{00} = \rho c^2$, $T_{0i} = 0$ and $T_{ij} = p\delta_{ij}$ where Latin indices i and j runs between 1 and 3. The cosmological constant Λ is homegeneous to a curvature with its dimension $[L^{-2}]$. As first suggested by George Lemaître in Lemaître (1934), the associated term can also be included in the right-hand side of Einstein's equation Eq. (1.13) under the form $T^{(\text{vacuum})}_{\mu\nu} = \frac{\Lambda c^4}{8\pi G} g_{\mu\nu}$. Current cosmological constraints estimate $\Lambda \approx 10^{-52}\,\text{m}^{-2}$ (Alam, Aubert, et al., 2021).

The cosmological principle is the assumption that the Universe is statistically homogeneous and isotropic, which is only true at cosmological scales. However, this assumption is important when building a metric. The most general form of the metric satisfying this principle was established by Alexandre Friedmann, Georges Lemaître, Howard Percy Robertson and Arthur Geoffrey Walker (FLRW) for the different cases of a closed, flat or open Universe between 1922 and 1935. They also proved the unicity of this metric for an homogeneous and isotropic spacetime. In a spherical system of coordinates x, θ, ϕ, Eq. (1.8) becomes

$$\mathrm{d}s^2 = -c^2\mathrm{d}t^2 + R^2 a^2(t)\left(\frac{\mathrm{d}x^2}{1-kx^2} + x^2(\mathrm{d}\theta^2 + \sin^2\theta\mathrm{d}\phi^2)\right) \tag{1.18}$$

with a the scale factor, function of the time coordinate t, x is a dimensionless spatial coordinate, and k the sign of the curvature of the Universe. If the curvature $k = -1$ then the Universe geometry is hyperbolic, if $k = 1$ then it is spherical, and if $k = 0$ then

it is flat.

1.1.3. Content of the Universe

Injecting the metric from Eq. (1.18) into Eq. (1.13), one can derive the Friedmann–Lemaître equations (Friedmann, 1922; Friedmann, 1924; Lemaître, 1927) to link the evolution of the scale factor a i.e. the expansion of the Universe to the content of the Universe through p and ρ. The first equation

$$\left[\frac{\dot{a}(t)}{a(t)}\right]^2 = \frac{8\pi G\rho(t)}{3c^2} + \frac{\Lambda c^2}{3} - \frac{kc^2}{R^2 a^2(t)} \tag{1.19}$$

is derived from the temporal component (0,0) of Einstein's equation while the second equation

$$\frac{\ddot{a}(t)}{a(t)} = -\frac{4\pi G}{3c^2}\left[\rho(t) + 3p(t)\right] + \frac{\Lambda c^2}{3} \tag{1.20}$$

is derived from the spatial component (i, j) of Einstein's equation.

A natural definition of a critical energy density ρ_c can be derived from Eq. (1.19) for the case $\Lambda = 0$ and in the absence of curvature $k = 0$

$$\rho_c \equiv \frac{3c^2 H^2}{8\pi G}. \tag{1.21}$$

We can now split the energy density into 4 different components : radiation, matter, curvature and the cosmological constant to define the respective dimensionless energy density parameters of the Universe Ω_r, Ω_m, Ω_k, and Ω_Λ

$$\Omega_r \equiv \frac{\rho_r}{\rho_c}, \tag{1.22}$$

$$\Omega_m \equiv \frac{\rho_m}{\rho_c}, \tag{1.23}$$

$$\Omega_k \equiv -\frac{3}{8\pi G\rho_c}\frac{kc^2}{R^2}, \tag{1.24}$$

$$\Omega_\Lambda \equiv \frac{3}{8\pi G\rho_c}\frac{\Lambda c^2}{3}, \tag{1.25}$$

whose sum $\Omega_r + \Omega_m + \Omega_k + \Omega_\Lambda = 1$. These various components are caracterized by their equation of state

$$p = w\rho \tag{1.26}$$

where w is the equation of state parameter. Radiation includes photons and ultra-relativistic fluids, characterized by $w = \frac{1}{3}$. Matter includes non-relativistic fluids like bayonic matter (15%) and dark matter (85 %), characterized by $w = 0$ (pressure-less). As it is non-relativistic, it is usually refered to as cold dark matter (CDM). Dark matter is the denomination of non-baryonic matter, first introduced by Fritz Zwicky in Zwicky

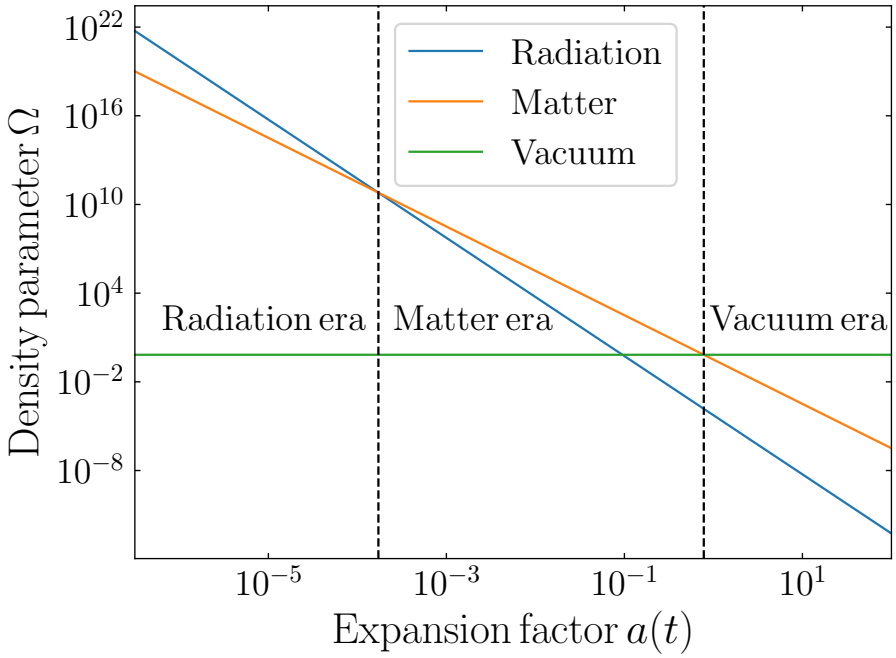


Figure 1.2. – Evolution of the density of radiation, matter and cosmological constant as a function of the scale factor. This evolution defines three domination eras in the history of the Universe : the radiation era, the matter era and vacuum era. The first transition happened at the equivalence otherwise known as the matter-radiation equality around 49 000 years after the Big Bang for a *Planck* 2018 cosmology. The second transition happened around 10.4 Gyr after the Big Bang.

(1933), republished in English in Zwicky (2009) to explain the discrepancy between the measured galaxy velocity dispersion in the Coma cluster and the dispersion expected from the mass of the observed galaxies. By definition, Ω_k takes into account the effect of the curvature of the Universe on its expansion. It is characterized by $w = -\frac{1}{3}$. Finally, the cosmological constant, which can be interpreted as the vacuum energy, has an equation of state parameter $w = -1$. These equations of state give the associated evolutions of the densities ρ_r, ρ_m, ρ_k, and ρ_Λ as

$$\rho = \rho^0 \, a^{-3(1+w)} \tag{1.27}$$

where the index 0 stands for the present value of the density. The evolution of the density of the various components as a function of the scale factor is shown in Fig. 1.2. This evolution defines three domination eras in the history of the Universe : the radiation era, the matter era and vacuum era. The first transition happened at the equivalence otherwise known as the matter-radiation equality around 49 000 years after the Big Bang, at a redshift $z_{eq} = 3411$ (Planck Collaboration : Aghanim et al., 2020). The second transition from matter to vacuum-dominated era has no specific name and happened around 10.4 Gyr after the Big Bang, at $z \approx 0.3$.

The first Friedmann–Lemaître equation Eq. (1.19) can be rewritten with the density of the different components of the Universe

$$H^2 = \frac{8\pi G}{3c^2}\left[\rho_\mathrm{r} + \rho_\mathrm{m} + \rho_\mathrm{k} + \rho_\Lambda\right] = H_0^2\left[\Omega_\mathrm{r}^0 a^{-4} + \Omega_\mathrm{m}^0 a^{-3} + \Omega_\mathrm{k}^0 a^{-2} + \Omega_\Lambda^0\right] \tag{1.28}$$

and so the variation of the scale factor with time is given by

$$\frac{\mathrm{d}a}{\mathrm{d}t} = \pm H_0\sqrt{\Omega_\mathrm{r}^0 a^{-2} + \Omega_\mathrm{m}^0 a^{-1} + \Omega_\mathrm{k}^0 + \Omega_\Lambda^0 a^2} \tag{1.29}$$

the sign being positive in an expanding Universe. The effect of Ω_m and Ω_Λ over the scale factor as a function of time is shown in Fig. 1.3. The origin $t = 0\,\mathrm{Gyr}$ is taken at the present time, for which $a(t=0) = 1$. The first cosmology considered is similar to the one measured by the *Planck* experiment , with $h = 0.67$, $\Omega_\mathrm{m} = 32$, and $\Omega_\Lambda = 0.68$. In this case, we find that integrating the second Friedmann–Lemaître equation Eq. (1.20) with $\Omega_\mathrm{r} = \Omega_\mathrm{k} = 0$ yields

$$a(t) = \left(\frac{\Omega_\mathrm{m}}{\Omega_\Lambda}\right)^{\frac{1}{3}} \sinh^{\frac{2}{3}}\left(\frac{3H_0\, t\sqrt{\Omega_\Lambda}}{2}\right), \tag{1.30}$$

and the Universe is currently 13.8 Gyr old. The second cosmology is radiation-dominated with $\Omega_\mathrm{r} = 1$, $\Omega_\mathrm{m} = \Omega_\Lambda = \Omega_\mathrm{k} = 0$. In this case, we find that

$$a(t) = \sqrt{2H_0\, t}, \tag{1.31}$$

which is useful to describe the first moments after the Big Bang. The third cosmology corresponds to an Einstein–de Sitter Universe, only filled with matter, for which the scale factor evolves as

$$a(t) = \left(\frac{3H_0}{2}\, t\right)^{\frac{2}{3}}, \tag{1.32}$$

The last cosmology is vacuum-dominated (de Sitter Universe) with $\Omega_\Lambda = 1$. The analytical solution for the scale factor is

$$a(t) = a_0 e^{H_0(t-t_0)}, \tag{1.33}$$

where $a_0 = a(t_0)$, t_0 being the time at which we start integrating the Friedmann–Lemaître equation to avoid the divergence in $a = 0$. This describes the present domination era of our Universe, now in an exponentially accelerated expansion.

1.1.4. The ΛCDM model parameters

Because the Universe is currently dominated by the effect of the cosmological constant and, to a lesser extent, cold dark matter, the current standard model of cosmology is named ΛCDM. The parameters of the ΛCDM model are often given under the form of the dimensionless Hubble constant $h \equiv H_0/100\,\mathrm{km\,s^{-1}\,Mpc^{-1}}$, phys-

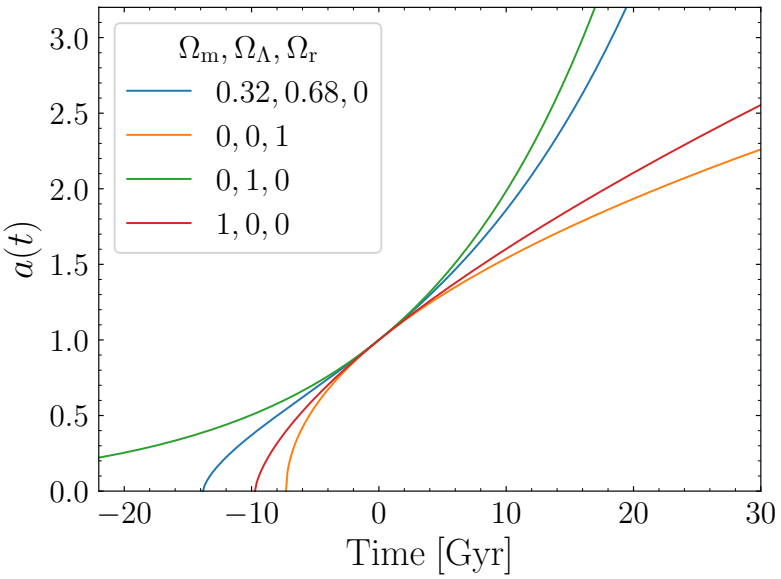


Figure 1.3. – Evolution of the scale factor as a function of Ω_m and Ω_Λ. The origin $t = 0\,\mathrm{Gyr}$ is taken at the present time, for which $a(t = 0) = 1$. The first cosmology considered is similar to the one measured by *Planck* in 2018, while the second one is radiation-dominated, the third one corresponds to an Einstein–de Sitter Universe, only filled with matter, and the last one is vacuum-dominated (de Sitter Universe).

ical baryonic and cold dark matter densities $\omega_b \equiv \Omega_b h^2$ and $\omega_{cdm} \equiv \Omega_{cdm} h^2$. To build the complete model, four additional parameters are needed. We mentionned earlier that the CMB follows a black body distribution of temperature $T_{CMB} = 2.7\,\mathrm{K}$. This temperature is one of the parameters of the ΛCDM model. However, most of the time, it is left fixed due to the level of precision of the constraint at 0.02% $T_{CMB} = 2.72548 \pm 0.00057$ that was obtained in Fixsen (2009). The anisotropies of the CMB, though small, are due to the fluctuations of the density field which grow progressively. Following the dark ages which last between the recombination 380 000 years after the Big Bang and about 300 Myr after, stars and galaxies start to form from these overdensities during the cosmic dawn. The ultraviolet light of these stars initiated the reionization of the mostly neutral hydrogen in the Universe during the epoch of reionization, between $z \sim 12$ and $z \sim 6$. The Thomson scattering optical depth τ quantifies the opacity of the reionized medium to CMB radiation and impacts measurements of the CMB anisotropies. The last two parameters are the amplitude A_s and the slope n_s of the primordial matter power spectrum. The parameters of the ΛCDM model are tightly constrained by the final data release PR4 of the *Planck* CMB experiment combined with BAO (Tristram et al., 2024), yielding $h = 0.6781 \pm 0.0038\,\mathrm{km\,s^{-1}\,Mpc^{-1}}$, $\omega_b = 0.02229 \pm 0.00012$, $\omega_{cdm} = 0.1186 \pm 0.0009$, $\log\left(10^{10} A_s\right) = 3.048 \pm 0.012$, $n_s = 0.9690 \pm 0.0035$, and $\tau = 0.0605 \pm 0.0059$. While the ΛCDM model assumes a flat Universe, it can be extended to include a curvature with Ω_k, as seen previously. In the same work, the constraint $\Omega_k = 0.0000 \pm 0.0016$ is given,

in agreement with a flat Universe.

Nevertheless, ΛCDM model suffers from a few issues, despite the fact that it is favoured by most observations. The fine-tuning problem stems in the fact that the flatness of the Universe observed today $\Omega_k < 0.0016$ at 1σ and the evolution of Ω_k given by the Friedmann–Lemaître equations entails that at very high redshift, Ω_k had to be 5×10^{50} times smaller at the Planck time, 7.624×10^{-44} s after the Big Bang, time before which the laws of physics as we know them are no longer valid. Moreover, the homogeneity of the CMB temperature and anisotropies at large scales cannot be explained by the ΛCDM model alone since these scales should have never been causally connected since it involves distances larger than what light had time to travel. The theory of inflation was proposed in Guth (1981) to explain both of these issues by introducing a phase of exponential expansion of the early Universe, with a growth of 60 orders of magnitude (e-folds) for the size of the Universe, about 10^{-35} s after the Big Bang. Another problem lies in the difference between the value of H_0 inferred from CMB+BAO and low-z SNIa, at a $\sim 5\sigma$ level of disagreement. The study of systematic effects in the processus of standardization of SNIa, prone to shift the value of H_0, discards more and more effects to explain this tension. The last problem that we will mention here is the discrepancy between the value of the cosmological constant inferred from cosmological observations and the vacuum energy predicted by the quantum field theory which varies between 10^{50} and 10^{120} depending on the assumptions made. The cosmological constant problem, the H_0 tension and the fact that the nature of dark energy is still unknown motivate the study of new cosmological models, especially time-evolving parametrisations of the dark energy equation of state parameter to replace the cosmological constant.

1.1.5. Dark energy models

Initially introduced by Einstein to have a static Universe, the cosmological constant Λ was considered to be null after the discovery of the expansion of the Universe, following the work of Edwin Hubble and George Lemaître. The observations of SNIa by the High-Z Supernova Search Team lead by Adam Riess and the Supernova Cosmology Project lead by S Perlmutter were the first to put significant constraints on $\Omega_\Lambda > 0$ (confidence level of 99%) and prove that the expansion of the Universe is accelerating (Riess et al., 1998; Perlmutter et al., 1999). As we have seen in Fig. 1.2, the expansion of the Universe is dominated by the effect of the cosmological constant since about 3.4 Gyr which corresponds to $z \sim 0.3$. However, we have seen in Sect. 1.1.2 that the cosmological constant can be treated as the vacuum energy. Given the cosmological principle problem, we generalize this notion and call dark energy any fluid characterized by $w < -\frac{1}{3}$, causing the accelerated expansion. It is perfectly possible to assume that the equation of state parameter $w = w_0 \neq -1$. Another interesting option to study eventual deviations of w from -1 is to use the Chevallier–Polarski–Linder parametrisation (CPL, Chevallier et al., 2001; Linder et al., 2003)

$$w = w_0 + \frac{z}{1+z} w_a \,. \tag{1.34}$$

This choice of parametrisation probes deviations from the cosmological constant at low redshift and only constrain the behaviour of dark energy, no physical model of the associated fluid is considered. Quintessence models introduce a time-varying scalar field ϕ in the energy-momentum tensor $T_{\mu\nu}$ of Eq. (1.13), with an associated potential energy which explains the accelerated expansion without strongly affecting the clustering (Peebles et al., 1988; Wetterich, 1988; Caldwell et al., 1998; Sahni et al., 2000). In quintessence models, the equation of state parameter w varies between -1 and 1. On the other hand, theories of modified gravity change how gravity itself behaves, rather than changing the energy-momentum tensor. The theories usually affect gravity at cosmological scales while keeping its behaviour at smaller scales through a screening mechanism to explain local observations, general relativity being very well constrained in the Solar System (Vainshtein, 1972). Many other models have been proposed to explain dark energy. A non-exhaustive list could include k-essence (Armendariz-Picon et al., 2000; Armendariz-Picon et al., 2001), kinetic gravity braiding (Deffayet et al., 2010; Kobayashi et al., 2010; Pujolàs et al., 2011), galileon cosmology (Chow et al., 2009), Brans–Dicke (Brans et al., 1961; Boisseau et al., 2000), and f(Gauss-Bonnet) (Nojiri et al., 2005; Carroll et al., 2005; de Felice et al., 2010; Kobayashi et al., 2011).

1.2. The Euclid survey

As a stage-IV survey, *Euclid* (Euclid Collaboration: Mellier et al., 2024) is a mission from the European Space Agency primarily designed to constrain dark energy with two main probes: weak lensing and spectroscopic galaxy clustering. The former will make use of galaxy shapes observed with the Visible Camera (VIS, Euclid Collaboration: Cropper et al., 2024) and their photometric redshifts obtained with the photometer of the Near-Infrared Spectrometer and Photometer (NISP-S and NISP-P respectively, Euclid Collaboration: Jahnke et al., 2024) together with ground-based observations. *Euclid* will provide a photometric sample of about 1.5 billion galaxies which can be used not only for weak lensing, but also for many other probes like photometric galaxy clustering (see chapter 3). The combination of weak gravitational lensing with photometric galaxy clustering will provide strong cosmological constraints (Euclid Collaboration: Blanchard et al., 2020; Tutusaus et al., 2020). Launched on 1 July 2023, *Euclid* reached the Sun-Earth Lagrange point L2 and after its commissioning and performance verification, the nominal survey started on 14 February 2024. Over six years, the Euclid Wide Survey (EWS, Euclid Collaboration: Scaramella et al., 2022) will covery 14 000 deg^2 while the Euclid Deep Survey (EDS) will cover 53 deg^2 divided into 3 fields (Euclid Deep Field North and South, and Euclid Deep Fornax).

1.2.1. Spectroscopy with Euclid

We explained in Sect. 1.1.1 that galaxy surveys like SDSS or 2dFGRS have played a fundamental role in the development of cosmology by probing large scale struc-

tures. This is indeed necessary in order to constrain theoretical models describing the Universe. However, several issues arise when such surveys are performed. The determination of the galaxy redshift is one of the main ones. Spectroscopy is ideal to determine the shift of spectral lines characteristic of the stars present in galaxies, like the H_α, O_{II}, O_{III}, S_{II}, or N_{II} lines or the shift of specific features like the Balmer break through Eq. 1.1. This method allows for a precise and accurate determination of galaxy distances. However, traditional spectroscopy only allows for the observation of one galaxy at a time, which explains the small number of galaxies observed in the 20th century. In 1979, thanks to the development of optical fibers and the first observation of a galaxy spectrum through one in early 1978 (Hubbard et al., 1979), the first fiber multi-object spectroscopic instrument Medusa was built at the Steward Observatory (Hill et al., 1980; Hill, 1988), allowing the observation of 32 galaxy spectra at once. The optical fibers were fixed in holes made in a plate to observe specific galaxies and observing a different field required the preparation of another plate. The 2dFGRS used this technology with 400 optical fibers to observe a sample of 221 414 galaxy spectra across 1500 deg^2 in 5 years. The SDSS used two spectrographs of 320 fibers each (later upgraded to 500) observed more than 4 million spectra in 20 years among which 2.25 million were used in the galaxy clustering analyses (Alam, Aubert, et al., 2021). Automation techniques were developed to overcome the limitations entailed by the use of field-specific plates which had to be produced beforehand and then changed between observations. Instead of manually changing plates and positioning optical fibers to the holes, robots have been designed to do this which simplifies the procedure and significantly decrease the time needed. For example, DESI uses a focal plane system which updates the position of its 5020 optical fibers every 10 to 20 minutes in 2 minutes (Silber et al., 2023), while manually placing this many fibers between each observation would be much much slower, decrease the number of observations and be unfeasible given the duration of the survey. Nevertheless, while this is possible in ground-based spectrographs, this is not the case for the *Euclid* spectrograph, in space.

For this reason, the NISP-S (Euclid Collaboration: Jahnke et al., 2024) uses a different technology called slitless grism spectroscopy. In the 0.54 deg^2 field of view, the light from all sources is dispersed by a grism and projected onto the detector. It is then possible to detect the position of emission lines through a careful deblending of the 2D-spectrograms made possible by the 4 spectrograms measured with different orientations. One red grism of passband 1206–1892 nm has a dispersion direction of 0° while the second one has a dispersion direction of 180°. An additional rotation of ±4° is added with the wheel on which the grisms are positionned to have a total of four orientations −4°, 0°, 180°, and 184°. The resolution of the red grisms $\mathscr{R} > 480$ will allow a high precision for the spectroscopic redshifts of H_α galaxies with $\sigma_z = 0.001\,(1+z)$ between $z = 0.84$ and $z = 1.88$ (Euclid Collaboration: Mellier et al., 2024). This sample will be divided into 4 equidistant redshift bins for spectroscopic galaxy clustering analyses. The sensitivity of NISP-S reaches a signal-to-noise ratio S/N = 3.5 for fluxes down to $2 \times 10^{-16}\,\mathrm{erg\,cm^{-2}\,s^{-1}}$, below which the probability of detection decreases. A blue grism is used in the EDS to detect H_α emitters down to $z = 0.41$ and to reach

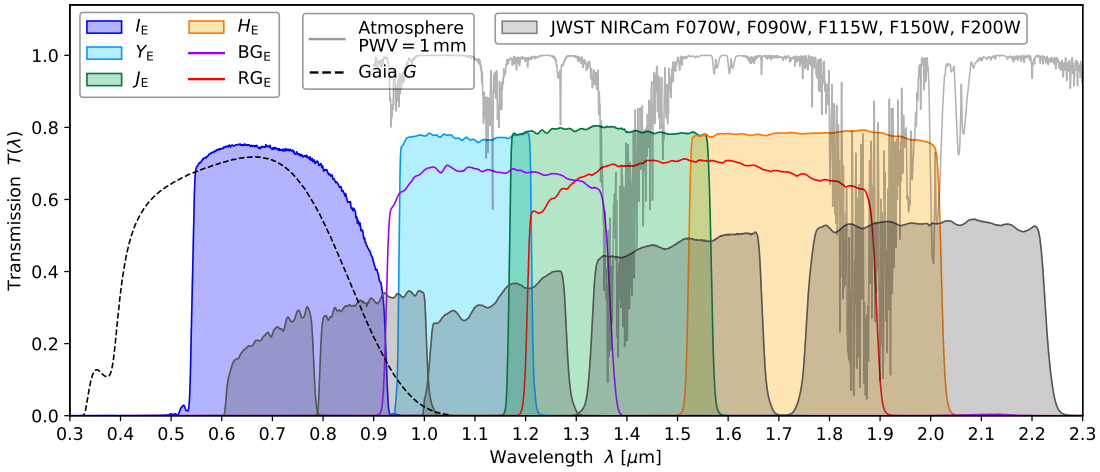


Figure 1.4. – Transmission of the *Euclid* filters as a function of the wavelength for the VIS I_E passband, for the NISP-P Y_E, J_E, and H_E passbands as well as for the NISP-S red and blue grisms. Figure taken from Euclid Collaboration: Mellier et al. (2024).

the goal of 99% purity and completeness for the EDS. Thanks to the use of slitless spectroscopy, about 35 million galaxy spectra are expected by the end of the mission.

1.2.2. Photometry with Euclid

The VIS instrument will measure fluxes in one large passband I_E between 530 and 920 nm, sampling at 0,1″ pixel^{-1} the same field of view as the NISP down to AB magnitudes of 24.5 at S/N ≥ 10 (Euclid Collaboration: Cropper et al., 2024). The NISP-P will measure fluxes in three passbands Y_E between 950 nm and 1212 nm, J_E between 1168 nm and 1567 nm, and H_E between 1522 and 2021 nm (Euclid Collaboration: Jahnke et al., 2024). The NISP-P samples the field of view at 0,3″ pixel^{-1} . As for the limiting magnitude, the instrument reaches 24.5 AB mag with S/N = 5, which exceeds its requirement by 0.5 AB mag. All passbands are shown in Fig. 1.4 with the associated transmission of the Euclid filters, including the red and blue grisms from the NISP-S. About 1.5 billion galaxies are expected in the photometric sample, between $z = 0.2$ and $z = 2.5$. The observations of the VIS will allow the determination of the shapes and ellipticities of these sources while the fluxes in the Y_E, J_E, and H_E bands will enable the computation of photometric redshifts. Ground-based observations from the Dark Energy Survey (DES, Abbott, Abdalla, and Allam, 2018) for the first data releases, the Legacy Survey of Space and Time (LSST, Ivezić et al., 2019) and the Ultraviolet Near Infrared Optical Northern Survey (UNIONS) will be used to complete the three NISP-P bands. The UNIONS survey is composed of the observations from the Canada-France-Hawaii Telescope (CFHT, Ibata et al., 2017), the Panchromatic Survey Telescope and Rapid Response System (Pan-STARRS Chambers et al., 2016), observations from Hyper Suprime-Cam (Aihara et al., 2018; Miyazaki et al., 2018) by the Wide Imaging with

Subaru-Hyper Suprime-Cam Euclid Sky (WISHES) group, and from the Waterloo-Hawaii-IfA g-band Survey (WHIGS). The expected precision of these photometric redshifts $\sigma_z = 0.05\,(1+z)$ is explained by the much scarcer information with respect to the spectra from NISP-S. Photometric galaxy clustering analyses will divide this large sample into 13 equipopulated redshift bins between $z = 0.2$ and $z = 2.5$.

1.3. What are BAO

Baryon acoustic oscillations are fluctuations of the baryon density field and originate from the opposing forces of gravitation and radiation pressure in the primeval Universe, when photons and baryons were still coupled. This coupling is due to the very efficient Thomson scattering of photons in the dense plasma, limiting their mean free path and causing constant interactions, creating what is called a baryon-photon fluid. In this context, primordial perturbations of the matter density field grow under the effect of gravitation. Thomson scattering increases with density and so as matter fall towards overdensities, the radiation pressure of photons increases until it becomes strong enough to counteract the gravitational force. The baryon-photon fluid is pushed away from the overdensity and cools down while it expands. This creates acoustic oscillations of the baryon-photon fluid which continue to propagate until photons decouple from baryons. This happens at a redshift $z_* \sim 1090$ called recombination redshift, when the Universe becomes cold enough to limit Thomson scattering and allow electrons and protons to combine into the first neutral hydrogen atoms, under 3000 K. Due to their number density smaller by a factor 5×10^{10}, baryons decouple from photons at an ulterior redshift $z_{\rm drag} \sim 1060$ called the drag epoch, about 18000 years later. At this time, the baryon acoustic oscillations completely stop propagating and freeze, creating shells of matter of radius $r_{\rm d} \simeq 100\,h^{-1}\,$Mpc, a distance known as the sound horizon at drag epoch determined by the speed of the acoustic waves in plasma $c_{\rm s}$ through the following relation :

$$r_{\rm d} = \int_{z_{\rm drag}}^{+\infty} {\rm d}z' \frac{c_{\rm s}}{H(z)} \tag{1.35}$$

The speed of the acoustic waves depends of the baryons and photons energy densities $\rho_{\rm b}$ and ρ_γ. It is defined by

$$c_{\rm s} = 3\left(1 + \frac{3\rho_{\rm b}}{4\rho_\gamma}\right)^{-\frac{1}{2}} \tag{1.36}$$

In our analysis, we compute $r_{\rm drag}$ following the fast approximations from Eisenstein and Hu, 1998 Eqs. (2) to (6) in which we updated the CMB temperature to its value reported in the final FIRAS CMB results Mather et al., 1999 $T_{\rm CMB} = 2.725$ K. We report here the expressions used for the redshift $z_{\rm eq}$ and wavenumber of the particle horizon $k_{\rm eq}$ at the matter-radiation equality, in which $\Theta_{2.7} = \frac{T_{\rm CMB}}{2.7}$ as well as the expression

used for $z_{\rm drag}$:

$$\begin{aligned}
z_{\rm eq} &= 2.5\times10^4\,\omega_{\rm m}\Theta_{2.7}^{-4}-1\\
k_{\rm eq} &= 0.0746\,\omega_{\rm m}\Theta_{2.7}^{-2}\\
z_{\rm drag,b1} &= 0.313\,\omega_{\rm m}^{-0.419}\left(1+0.607\,\omega_{\rm m}^{0.674}\right)\\
z_{\rm drag,b2} &= 0.238\,\omega_{\rm m}^{0.223}\\
z_{\rm drag} &= 1345\,\frac{\omega_{\rm m}^{0.251}}{1+0.659\,\omega_{\rm m}^{0.828}}\left(1+z_{\rm drag,b1}\Omega_{\rm b}^{z_{\rm drag,b2}}\right)
\end{aligned} \tag{1.37}$$

Then we compute the distance $r_{\rm drag}$ as :

$$\begin{aligned}
R_{\rm drag} &\equiv \frac{3\rho_{\rm b}(z_{\rm drag})}{4\rho_\gamma(z_{\rm drag})} = 31.5\,\Omega_{\rm b}\Theta_{CMB}^{-4}\frac{1000}{1+z_{\rm drag}}\\
R_{\rm eq} &\equiv \frac{3\rho_{\rm b}(z_{\rm eq})}{4\rho_\gamma(z_{\rm eq})} = 31.5\,\Omega_{\rm b}\Theta_{CMB}^{-4}\frac{1000}{1+z_{\rm eq}}\\
r_{\rm drag} &= \frac{2}{3k_{\rm eq}}\sqrt{\frac{6}{R_{\rm eq}}}\ln\left(\frac{\sqrt{1+R_{\rm drag}}+\sqrt{R_{\rm drag}+R_{\rm eq}}}{1+\sqrt{R_{\rm eq}}}\right)
\end{aligned} \tag{1.38}$$

where $R_{\rm drag}$ and $R_{\rm eq}$ are the ratio of the baryon to photon momentum density evaluated respectively at the drag epoch and at the epoch of matter-radiation equality. The prefactor 1345 was taken from Hu et al., 1996 Eq. (E-2) rather than 1291 used in Eisenstein and Hu, 1998 because we find a significantly better agreement with the results from the Boltzmann code `CAMB` Lewis et al., 2000 (same with `CLASS`, Blas et al., 2011). Varying h, $\Omega_{\rm b}$ or $\Omega_{\rm m}$ in [0.6,0.8], [0.039,0.059], and [0.17,0.37] respectively while fixing the other parameters to the fiducial values of the *Euclid* Flagship simulation (Euclid Collaboration: Castander et al., 2024), we find an average relative difference $\frac{r_{\rm drag,HS}}{r_{\rm drag,CAMB}}-1$ of -0.04 %, 0.01 %, and 0.03 % using 1345 as a prefactor against $\frac{r_{\rm drag,EH}}{r_{\rm drag,CAMB}}-1$ of 2.7 %, 2.7 %, and 2.6 % using 1291.

The sound horizon $r_{\rm d}$ is by definition constant in comoving space. As such, it can be used as a standard ruler, it is a characteristic length of our Universe. In configuration space, its apparent size increases as the Universe expands. Since acoustic oscillations were created from not one but a multitude of overdensities, it cannot be observed as a single shell but statistically, as a matter overdensity found at a specific scale therefore called the BAO scale. It appears as a single peak in the correlation function or a succession of peaks in the power spectrum. To constrain the angular size of the BAO $\theta_{\rm BAO}$ at a given redshift, that is, the angular separation of the peak in the two-point angular correlation function of a sample of given effective redshift, we constrain the angular diameter distance $D_{\rm A}(z_{\rm eff})$, computed as

$$D_{\rm A}(z) = \frac{r_{\rm d}}{\theta_{\rm BAO}(1+z)} \tag{1.39}$$

From a theoretical point of view, we can derive the expected $r_{\rm d}$ and $D_{\rm A}$ for a given

cosmology in a possibly curved Universe. We first derive the comoving distance and angular diameter distance. The FLRW metric in spherical coordinates is given by Eq. (1.18). It is useful to rewrite the FLRW metric by the successive changes of variables $x \to \sin(\chi)$ and $R\chi \to r$ to obtain

$$\mathrm{d}s^2 = -c^2\mathrm{d}t^2 + a(t)^2\left(\mathrm{d}r^2 + S_\mathrm{k}^2(r)\left(\mathrm{d}\theta^2 + \sin^2\theta\mathrm{d}\phi^2\right)\right) \tag{1.40}$$

with

$$S_\mathrm{k}(r) = \begin{cases} R\sin\frac{r}{R} & \text{if } k = 1 \\ r & \text{if } k = 0 \\ R\sinh\frac{r}{R} & \text{if } k = -1 \end{cases} \tag{1.41}$$

where R is the curvature of the Universe which is linked with the curvature energy density parameter and the Hubble parameter through Eq. (1.24) and Eq. (1.21)

$$\Omega_\mathrm{k} = -\frac{k}{H^2R^2}\,. \tag{1.42}$$

Given two comoving points, one at the origin of the frame of reference, the other one being at the position $\{r_0, \theta_0 = 0, \phi_0 = 0\}$. For a photon emitted in r_0, the fact that it has no mass entails that $\mathrm{d}s = 0$, it moves on null geodesics. If we consider photons moving radially, which entails $\mathrm{d}\theta = \mathrm{d}\phi = 0$, Eq. (1.40) becomes

$$\mathrm{d}s^2 = -c^2\mathrm{d}t^2 + a^2(t)\mathrm{d}r^2 = 0 \tag{1.43}$$

hence $c\mathrm{d}t = -a(t)\mathrm{d}r$.

Using Eq. (1.29), we can now write the comoving coordinate distance as a function of the energy densities and the Hubble constant :

$$\mathrm{d}r = -\frac{c}{H_0}\frac{\mathrm{d}a}{\sqrt{\Omega_\mathrm{r}^0 + \Omega_\mathrm{m}^0 a + \Omega_\mathrm{k}^0 a^2 + \Omega_\Lambda^0 a^4}} \tag{1.44}$$

and after changing from scale factor to redshift and integration, the comoving distance is given by

$$r = \frac{c}{H_0}\int_0^z \frac{\mathrm{d}z}{\sqrt{\Omega_\mathrm{r}^0(1+z)^4 + \Omega_\mathrm{m}^0(1+z)^3 + \Omega_\mathrm{k}^0(1+z)^2 + \Omega_\Lambda^0}} \tag{1.45}$$

The angular diameter distance of an object of proper length L and subtended angle θ_L is by definition

$$D_\mathrm{A} = \frac{L}{\theta_\mathrm{L}} \tag{1.46}$$

We consider an object with no radial extent ($\mathrm{d}r = 0$), with an orientation along θ only ($\mathrm{d}\phi = 0$), and at a constant time $\mathrm{d}t = 0$. From this, Eq. (1.40) simplifies into

$$\mathrm{d}s = a(t)S_\mathrm{k}(r)\mathrm{d}\theta \tag{1.47}$$

which after integration yields

$$S = a(t) S_{\mathrm{k}}(r) \theta_{\mathrm{L}} \tag{1.48}$$

This expression can be directly linked to the definition of Eq. (1.46) to identify $D_{\mathrm{A}} = a(t) S_{\mathrm{k}}(r)$. This gives us the following definition of D_{A} for any curvature :

$$D_{\mathrm{A}}(z) = \begin{cases} \frac{c}{(1+z) H_0 \sqrt{|\Omega_{\mathrm{k}}|}} \sin\left(H_0 \sqrt{|\Omega_{\mathrm{k}}^0|} r \right) & \text{if } \Omega_{\mathrm{k}} < 0 \\ \frac{r}{1+z} & \text{if } \Omega_{\mathrm{k}} = 0 \\ \frac{c}{(1+z) H_0 \sqrt{\Omega_{\mathrm{k}}}} \sinh\left(H_0 \sqrt{\Omega_{\mathrm{k}}^0} r \right) & \text{if } \Omega_{\mathrm{k}} > 0 \end{cases} \tag{1.49}$$

Through these observables, it becomes possible to compare theory and observations in order to constrain the cosmological parameters of our Universe. However, this requires a careful extraction of the BAO scale which will be discussed in chapter 4.

2. Photometric redshifts

Summary

2.1. Data-driven methods 52
2.1.1. State of the art of data-driven methods for photo-z 52
2.1.2. Convolutional neural networks 55
2.1.3. Metrics 58
2.2. Deep learning for photometric redshifts with SDSS DR12 59
2.2.1. Data 59
2.2.2. Results with SDSS DR12 60
2.3. Photometric redshifts with the Euclid Science Challenge 8 66
2.3.1. Data and mock spectroscopic redshifts 66
2.3.2. Results with Euclid SC8 70

In this chapter, we discuss photometric redshifts (photo-z or $z_{\rm ph}$) and their computation in the context of large galaxy surveys. As explained in Sect. 1.2.2, we call photo-z redshifts inferred from the photometry of a source rather than from its spectrum. They are necessary in weak lensing and 3×2-point analyses which use the 1.5 billion sources from the photometric survey since spectroscopic redshifts are not available for all of them. Using photometric galaxy clustering also prevents any correlation of the weak lensing analysis with the selection biases of spectroscopic galaxy clustering. The historical method to compute photometric redshifts is template fitting. Based on star and galaxy evolution models, spectral energy distributions (SED) templates are produced for typical galaxies, convolved with the instrument response, and shifted to a different redshift. A maximum likelihood approach is then utilized to minimize the chi-square between the observed photometry and the library of templates, and infer the redshift this way. We list here some of the codes developed with this template-fitting approach and the associated references without delving into their respective specificities since this approach was not used in this work : `HyperZ` (Bolzonella et al., 2000), `BPZ` (Bayesian photo-z, Benitez, 2000; Benítez et al., 2004), `Le Phare` (Arnouts et al., 2002; Ilbert et al., 2006), `ZPEG` (Le Borgne et al., 2002), `ZEBRA` (Zurich Extragalactic Bayesian Redshift Analyzer, Feldmann et al., 2006), `EAzY` (Brammer et al., 2008), `LRT` (Low-Resolution Spectral Templates, Assef et al., 2010), `Photo-z-SQL` (Beck, Dobos, Budavári, A. Szalay, et al., 2017), `CPz` (Classification-aided photo-z, Fotopoulou et al., 2018), `BCNz` (Eriksen et al., 2019), and `Phosphoros` (Euclid Collaboration: Tucci et al., 2025). A comparison of the performances of some of these codes can be found

in Abdalla et al. (2011) and Euclid Collaboration: Desprez et al. (2020).

However, this method requires a SED library which includes all types of galaxies in order to be representative of the photometric sample. Another issue which arose with the development of very large surveys is that this method requires the integration of the templates over the passbands of the instrument shown in Fig. 1.4 to compute the theoretical photometric points and this is too slow to realistically compute 1.5 billion photo-z in a reasonable amount of time. For example, the `Phosphoros` algorithm takes about 0.8 second to infer the redshift of one galaxy (Euclid Collaboration: Enia et al., 2024), which means that the inference of 1.5 billion photo-z would require 5.4 years on one core. Data-driven algorithms are a faster alternative which we will present in Sect. 2.1. As a comparison with template fitting, the inference is between 53 and 800 times faster depending on the neural network considered among the ones used in this work. Moreover, neural networks can efficiently benefit from GPU acceleration, potentially increasing the inference speed by 10 or 100 depending on the hardware. In Sect. 2.2, we will present our results using data from the 12^{th} data release of SDSS (DR12) and Sect. 2.3 will be dedicated to the results obtained with the *Euclid* science challenge 8 (SC8).

2.1. Data-driven methods

Data-driven methods use a training sample of galaxies to train an algorithm to predict the redshift of a galaxy given some input information which is, most of the time, its photometry. It can be supervised or non-supervised, depending on whether labels are available for this training. In the supervised case, labels can either be the true redshifts of the training sample of galaxies in the case of simulations, or spectroscopic redshifts when they are available. A last option are high-quality photo-z, for example from the Pau survey which counts so many thin photometric passbands that the resulting photo-z are qualified of quasi-spectroscopic. The training consists in minimizing the error between the predicted photo-z and the redshift label so that the algorithm can then be used to infer photo-z when spectroscopy is unavailable. On the contrary, unsupervised methods are used to train an algorithm when labels are not available. In this case, the algorithm learns by minimizing a distance between galaxy properties and can either find similarities to group galaxies in classes (clustering) or reduce dimensionality. In this work, only supervised methods are considered.

2.1.1. State of the art of data-driven methods for photo-z

Data-driven methods use a wide variety of techniques to learn to predict photo-z from a given input. One of the first method to be explored was decision trees. Decision trees successively divide the initial training sample into subsamples according to criteria which are optimized during the training in order to group galaxies according to their features (e.g., magnitudes). The final subsamples or leaves at the end of these branches of decisions either correspond to a class label when the decision tree is a

classifier or a discrete value when it is a regressor (regression tree). In the former case, the optimization often use the entropy or the Gini index (Gini, 1921) which measures the impurity of the data sets resulting of each decision split to optimize the training while the mean square error (MSE) or mean absolute error (MAE) is usually chosen for regression. The uncertainty of photo-z can be obtained by predicting many times a point-estimate while perturbing the input magnitudes within their respective errors. The combination of a multitude of decision trees is called a random forest and use a majority vote to determine the final output photo-z. Each tree does not hold a strong predictive power but their combination does. In addition, combining them decrease the risk of overfitting the training sample and help generalization to other data. The implementation of random forest regressor from the `scikit-learn` library has been used in Euclid Collaboration: Desprez et al. (2020) to predict photo-z. The `TPZ` code is another implementation of the random forest which predicts photo-z uncertainties through out-of-bag samples which are left unused in each tree (Carrasco Kind et al., 2013). Random forest successively create decision trees in order to grow. This growth can be controlled to compensate for the errors of previous decision trees and iteratively decrease the number of failures in the forest. This adaptive boosting has been implemented in `Adaboost` (Freund et al., 1997) and uses a multitude of shallow decision trees with only one or few decision nodes to rapidly strengthen the random forest, which improves the predictions of photo-z with respect to the simple random forest algorithm (Hoyle et al., 2015; Euclid Collaboration: Desprez et al., 2020). The `ArborZ` code specifically implements this method for photo-z inference (Gerdes et al., 2010). Gradient boosted regression trees combine this boosting approach with gradient descent to further improve performances (`GBRT`, Euclid Collaboration: Desprez et al., 2020).

A second class of algorithms use variants of the nearest-neighbour technique to group galaxies according to their position in the multi-dimensional space of colours and then identify their redshift using a reference sample of spectroscopic redshifts. The k-nearest neighbours algorithm `NNPZ` (Tanaka et al., 2018) matches galaxy magnitudes and colours to a reference sample whose photo-z probability density function (PDF) is known. The photo-z PDF is then infered as a weighted average of the neighbours, the weight being either the Euclidean distance in magnitude and colour space or alternatively, a chi-square metric. The Directional Neighbourhood Fitting code `DNF` introduced a new neighbourhood function in De Vicente et al. (2016), defined as the product of the Euclidean and angular neighbourhoods. This neighbourhood is fitted to find the link between redshift and magnitudes and then infer the photo-z of galaxies which are not in the training sample.

Among other approaches, we can cite `CosmoPhotoZ` which uses generalized linear models (GLMs, Nelder et al., 1972) to compute an estimate of photo-z which may not be as precise or accurate than other codes but has advantages : it is not a black box system and it can still reach an outlier fraction as small as 1% after a training of a few minutes (Elliott et al., 2015). The `GPz` code (Almosallam, M. J. Jarvis, et al., 2016; Almosallam, Lindsay, et al., 2016) uses gaussian processes in a Bayesian approach to fit the training sample and predict the photo-z PDF after taking into account

both input colours uncertainties and training data density. Support vector machine (SVM) classification is applied to photo-z inference with SPIDERz (SuPport vector classification for IDEntifying Redshifts, Jones et al., 2017), recently adapted from the IDL environment to Python with SpyderZ (Agarwal et al., 2024). Self-organizing maps (SOM, Kohonen, 1982) are exploited in SOMz to map galaxy photometric features from the training sample to a space of lower dimension (typically, two) which preserves the topology such that galaxies with similar properties are clustered (Carrasco Kind et al., 2014). For a new galaxy, its photometry is mapped in the trained SOM and a photo-z PDF is computed from the redshifts of a random atlas of training galaxies whose properties are similar to the new one.

Artificial neural networks are another kind of algorithm used to learn to predict photo-z. A neural network is built as a succession of layers, each layer being composed of neurons. A neuron is a linear system characterized by its matrix of weights $\boldsymbol{W}$ and a linear bias b which takes multiple inputs in a vector $\boldsymbol{x}$ and returns a value $\boldsymbol{W}.\boldsymbol{x}+b$. As a consequence, a layer returns several values which are the inputs of the next layer. Any layer which is not the input of the network or its output is usually called a hidden layer. Non-linearities are introduced through activation functions like the hyperbolic tangent, the sigmoid $f(x) = (1+e^{-x})^{-1}$, exponential linear unit (ELU) $f(x) = \alpha(\exp(x)-1)$ if $x < 0$ else $f(x) = x$, with α an hyperparameter chosen to be 1 in this work, rectified linear unit (ReLU) $f(x) = \max(0,x)$, or leaky ReLU $f(x) = \epsilon x + (1-\epsilon)\max(0,x)$ where x is the output of one neuron and ϵ is an hyperparameter. When it is supervised, the training aims at finding a set of weights and biases which allows the output of the network to be as close as possible from the label by minimizing a metric like the MSE or MAE. This minimization is performed iteratively through the backpropagation of the gradient of the loss function, computed between the output of the network and the label, with respect to the weights. An optimization scheme like gradient descent is used to update the weights using the gradient of the loss function and then perform a new forward pass of the training input data in the updated network. The amplitude of the update depends on the gradient and a factor λ called learning rate, another hyperparameter of the training. Typically, the update of the weights is done once a small subset called batch of the training sample has passed through the network. Once the whole training sample has been used in the training, one epoch is done. Depending on the network architecture, the complexity of the training task and the data, a complete training requires from a few tens to hundreds of thousands epochs. To prevent overfitting the training sample, an independent validation sample is often used to compute the validation loss at the end of each epoch and check if the model is overfitting the training data. A third independent test sample is sometimes used to compute the loss of the fully trained model.

The Machine-learning Estimation Tool for Accurate PHOtometric Redshifts code (METAPHOR, Amaro et al., 2019; Cavuoti et al., 2017) trains a multi-layer perceptron (MLP), a type of neural network where all neurons of a given layer send their output to all the neurons of the next layer, otherwise known as dense layers. It can either infer a point-estimate of photo-z or a PDF, computed as the distribution of point-estimates obtained by perturbing the input photometry according to the uncertainties of the

magnitudes. ANNz2, described in Sadeh et al. (2016), utilizes a different approach by training several machine learning estimators like boosted regression trees or artificial neural networks to obtain a point-estimate of photo-z and its PDF. The PDF includes both the uncertainty from the input photometry and the machine learning estimator itself. For the effect due to the input uncertainty of a given galaxy, it is estimated as the 68th percentile of the distribution of the photo-z bias $z_{\rm ph} - z_{\rm spec}$ from the K nearest neighbours in the magnitude or colour space of the training sample. The uncertainty of the estimator is obtained by training different machine learning methods, ranking them by bias, scatter, and outlier fraction, selecting the best one for the point-estimate before computing the PDF using the weighted solutions from all estimators. Another possibility is to use classification with many small redshift bins to estimate the photo-z PDF.

All of these data-driven methods and codes focus on learning to estimate photo-z from extracted galaxy magnitudes or colours. However, the development of a new kind of neural network called convolutional neural networks (CNN) and their use to automate the treatment and analysis of images has progressed since the work from Yannick Lecun in Lecun et al. (1998). It is now possible to use the networks to estimate photo-z from multi-passband galaxy images rather than extracted photometry, which circumvents limitations like the choice of aperture size and adds information like variations of the colours in the galaxy, its morphology, orientation or background. This comes at a computational cost which is important since the information treated, from typically 4 or 5 magnitudes, jumps to 14 400 pixels with galaxy images of size 60×60 in the g, r, i, and z passbands in the first works using CNN for photo-z estimate (Hoyle, 2016; D'Isanto, A. et al., 2018), or 20 480 pixels in Pasquet et al. (2019) with 64×64 images and the addition of the u passband, with 400 000 images in the training sample. The development of algorithms to train neural networks on graphic processing units (GPU) allowed for a significant speed-up by a factor of several hundreds.

2.1.2. Convolutional neural networks

In this work, we have exploited several deep learning architectures to study if using galaxy images can improve photo-z estimates with respect to flux-based estimates obtained with a multi-layer perceptron of 6 fully-connected layers whose details are given in Table A.1. The first model used was a sequential convolutional neural network. Its architecture is based on a succession of convolutional layers. These layers where introduced to make up for the loss of spatial information with fully-connected neuron layers, where an image would have been flattened to a vector $\boldsymbol{x}$. Moreover, traditional fully-connected networks would see their number of parameters explode (weights and biases). Indeed, treating one 64×64 image in 5 channels with one layer of 128 neurons yields $(64 \times 64 \times 5 + 1) \times 128 \approx 2.6 \times 10^6$ parameters which should be multiplied by a few layers, knowing that even if these image sizes are usual in works on photo-z estimation, other fields may use R, G, B images of millions of pixels and more than 1000 neurons per layer, easily exceeding 10^9 parameters per layer. Convolutional layers use a set of kernels or filters whose number and size are hyperparameters chosen when building

the architecture of the network, typically between 8 and 64 kernels of size 3×3 or 5×5. The kernels span the input image $\boldsymbol{x}$ by strides of 1 pixel or more and the output is the convolution of each kernel $\boldsymbol{\omega}$ of size $m \times n$ with the input, computed with the Hadamard product

$$\tilde{\boldsymbol{y}} = \sum_{i=1}^{m} \sum_{j=1}^{n} \tilde{\boldsymbol{x}}_{i,j} \omega_{i,j} \,, \tag{2.1}$$

where $\tilde{\boldsymbol{x}}$ is the part of the image $\boldsymbol{x}$ covered by the $m \times n$ kernel at each stride. This operation is illustrated for a single-channel image with one kernel in Fig. 2.1. Note that unless a padding of zeros is applied around the input image, this operation reduces the spatial dimension of the image. This is wanted in most cases since we want to extract features from the image and, layer by layer, reduce it to a single value which is the photo-z. As this operation is repeated with each kernel, the depth of the output will be increased accordingly, producing as many images as the number of kernels in the layer. These images are called feature maps because each kernel has its own set of weights and extract different features from the input. The size of the kernel is indicative of the size of the features which can be extracted : a large kernel will be inadequate for small features. The result of an input image of size $64 \times 64 \times 5$ which went through a convolutional layers with 16 kernels of size 4×4, with a stride of 2 and a padding of 0 will be 16 feature maps of side $(64 + 2 \times 0 - 4)/2) + 1 = 31$. The number of parameters for this layer is $5 \times 4 \times 4 \times 16 = 1280$, which is much more reasonable than with fully-connected layers.

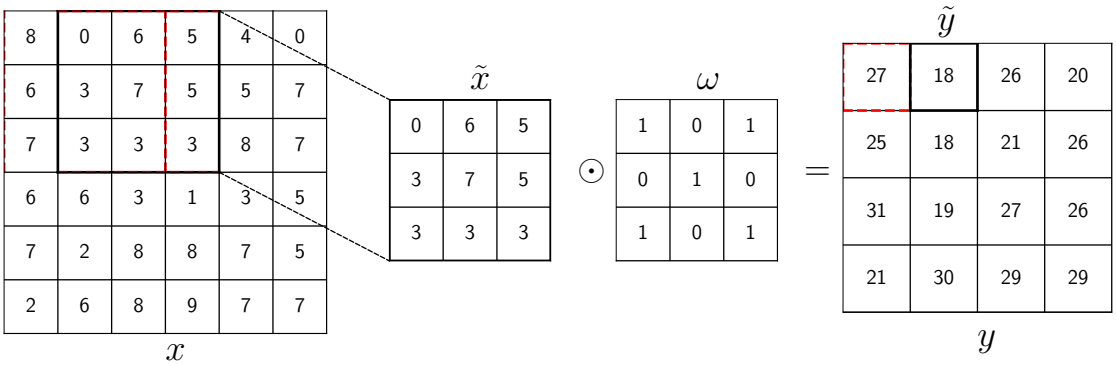


Figure 2.1. – 2D convolutional layer : Hadamard product of a 6×6 input image x by a 3×3 kernel ω without padding and a stride of 1.

Batch normalization is an operation first introduced in Ioffe et al. (2015) which can be performed after the convolution to normalize the output of the layer so that the mean and the standard deviation stay close to 0 and 1. This makes the training of the neural network quicker and more stable. The activation function can be applied on the output of the convolutional layers or after the batch normalization depending on the architecture and application. Max pooling can be added after the normalization by downsampling the feature maps in a moving window which, like the convolutional kernels, has a given size, stride and eventual padding. Max pooling further decreases the spatial dimension of the feature maps, concentrates the information with the largest

weight, decreases the number of operations in the following layers, and decrease the risk of overfitting the data by removing small details or noise. This downsampling can also be done by average pooling instead of max pooling.

In a sequential CNN, a succession of convolutional layers is used before flattening all feature maps into a single vector which is then fed in a succession of fully-connected layers of decreasing number of neurons, the output of the last layer being the estimate of photo-z. The complete detail of the architecture can be found in Table A.2. It is implemented in `Tensorflow` with the `Keras` API (Abadi et al., 2015; Chollet, 2015). With 3 convolutional layers and 5 fully connected layers, the model has a total of 529 409 parameters. We use the ReLU activation function after each convolutional and fully-connected layers, except for the output layer which uses the linear activation function $f(x) = x$. The padding used preserves the input image dimension. The term sequential stems from the fact that one can implement other branches in the architecture. For example, in a multi-input architecture, one input can go through some layers (the first branch) and the second input goes through different layers (the second branch) before a concatenation and a common part of fully-connected layers. Multi-output architectures are also possible but will not be considered in this work as we either estimate a point-estimate of photo-z or its PDF.

The inception CNN architecture was introduced for the first time in Szegedy et al. (2015). Fig. 2.2 shows the organization of the inception blocks used as components of inception CNN architectures. The goal of this block is to make the extraction of information from the image more efficient by probing several scales with convolutions of different kernel sizes applied on the same input. Moreover, decreasing the number of kernels (depth) before the 3×3 and 5×5 convolutions thanks to the addition of convolutions with a 1×1 kernel allows a significant decrease of the number of parameters. In the architectures presented in Table A.3 and A.4 for the multi-input version with MLP, the models have 1 451 001 and 7 826 353 parameters respectively. We also include a more visual summary of the inception architecture in Fig. A.1.

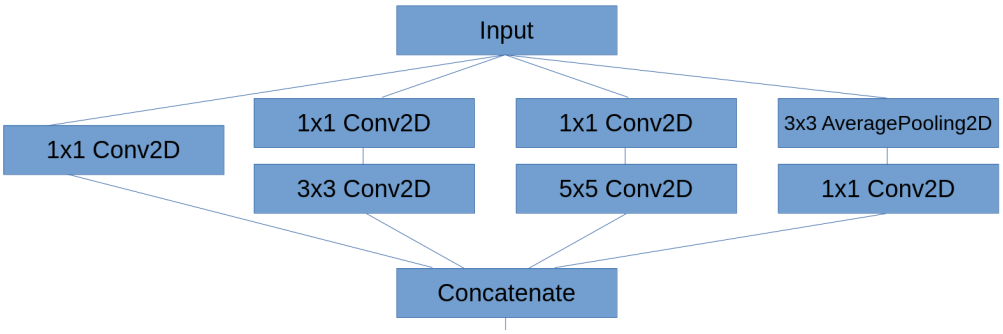


Figure 2.2. – Inception block architecture

As a comparison point, we also use the residual network ResNet34 architecture, widely used in computer vision problems since its introduction in He et al., 2016 and described in Table A.5. This larger model (21 576 065 parameters) uses residual connections otherwise known as skip connections which add the output of some

layers to the output 2 convolutional layers deeper in the architecture. Skip connections prevent gradients from vanishing to values close to 0 during the backpropagation, leading to very small updates of the weights and a training which stagnates. This typically happens when the number of layers is large and when the activation function returns values between 0 and 1, like the hyperbolic tangent or the sigmoid function.

To predict the PDF of photo-z, we adopt the approach of Pasquet et al. (2019) and change this regression problem into a classification one, where the model returns the probabilities of photo-z being in redshift intervals defined by a thin binning between the minimum and maximum redshifts of the sample. This is implemented by changing the last layer of the model to return as many values as there are classification bins, fixing the PDF resolution in redshift. In the same time, the activation function of the last layer is changed from the linear or identity function to the softmax function

$$f(x_i) = \frac{e^{x_i}}{\sum_{k=1}^{n_{\text{class}}} e^{x_k}}, \tag{2.2}$$

with n_{class} the number of classification bins and x_i the value of the input vector x in the i^{th} bin. The sum of the denominator is 1 so the output of this function is akin to a probability. Unlike in regression mode, the label is no longer z_{spec}. Instead, we use the number of the classification bin corresponding to z_{spec}.

2.1.3. Metrics

These networks are trained in regression mode to predict a point-estimate of photo-z with the mean-squared error (MSE) as a loss function. The MSE is defined for a label $z_{\text{spec},i}$ and the prediction by the model $z_{\text{ph},i}$ as

$$MSE(z_{\text{spec}}, z_{\text{ph}}) = \frac{1}{n}\sum_{i=1}^{n}(z_{\text{spec},i} - z_{\text{ph},i})^2, \tag{2.3}$$

where n stands for the size of the sample considered (training, validation or test sample). We train our deep learning models with an early stopping callback from the `Keras` library so that the training stops when the loss function computed on the validation sample reaches a plateau for more than 15 epochs. In this work, this plateau is defined by an absence of improvement of the validation loss during these 15 epochs. The model is saved at each epoch where the validation loss is improved and we then select the model whose validation loss is the lowest to predict the photo-z of the test sample and compute the associated metrics.

We consider several metrics to characterize the performance of the models. The mean bias $\delta z = \langle z_{\text{ph}} - z_{\text{spec}} \rangle$, its standard deviation σ and the mean scaled bias

$$\Delta z = \left\langle \frac{z_{\text{ph}} - z_{\text{spec}}}{1 + z_{\text{spec}}} \right\rangle \tag{2.4}$$

which includes a $1 + z_{\text{spec}}$ scaling are often used in the literature but we will also cite

the normalized median absolute deviation (NMAD)

$$\sigma_{\rm NMAD} = 1.4826 \times \text{median}\left(|\Delta z - \text{median}\left(\Delta z\right)|\right) , \tag{2.5}$$

which is more robust to outliers than σ. We also report the fractions of outliers $\eta_{0.15}$, $\eta_{0.10}$, and $\eta_{0.05}$, respectively defined as the fraction of samples for which Δz exceeds 0.15, 0.10, or 0.05.

In the case of classification for PDF estimation, the loss function is changed from MSE to sparse categorical cross entropy. For a given training label which is the classification bin number k and an output vector of values denoted $\hat{y}_j$ with $j \in [1, n_{\rm class}]$, the loss is $-\log\left(\hat{y}_k\right)$. The loss of a training, validation or test sample is then taken as the average of the losses of all predictions. With the photo-z PDF, we compute the same metrics using the expected value of the PDF $P(z)$ as a point-estimate

$$z_{\rm ph} = \sum_{k=1}^{n_{\rm bins}} z_k \, P(z_k) \tag{2.6}$$

with z_k the midpoint of bin k. We use classification bins of width 2.5×10^{-3} between $z = 0$ and $z = 7$.

We characterize the quality of the photo-z PDF by the histogram of the probability integral transform (PIT) values which are defined for each galaxy of redshift $z_{{\rm spec},i}$ and PDF $P_i(z)$ as

$$\text{PIT}\left(z_{{\rm spec},i}\right) = \int_0^{z_{{\rm spec},i}} P_i(z) \mathrm{d}z \tag{2.7}$$

A positive or negative slope in the histogram of PIT values indicates a systematic underestimation or overestimation of $z_{\rm ph}$, respectively. A concave PIT distribution, with an excess of values close to 0 and 1, means that the PDF tend to be too narrow and $z_{\rm spec}$ is either missed or in the tail of the PDF. On the contrary, a convex PIT distribution is a symptom of PDF which are too wide and will always include $z_{\rm spec}$.

2.2. Deep learning for photometric redshifts with SDSS DR12

2.2.1. Data

We use galaxy images and Petrosian magnitudes in the u, g, r, i, and z passbands from the SDSS 12th data release (Alam, Albareti, et al., 2015), along with the associated spectroscopic redshifts which are used as labels to compute the loss of the training. Only galaxies for which the 5 passbands are available are kept. Galaxy cutouts have a side of 32 pixels. The sample is similar to the one used in Henghes et al. (2022), at the difference that we don't exclude galaxies at $z > 1$ to check if the low number of galaxies beyond $z = 1$ affects the performance of the deep learning method. We adopt a training strategy which consists in keeping 20% of the total sample of galaxies for the

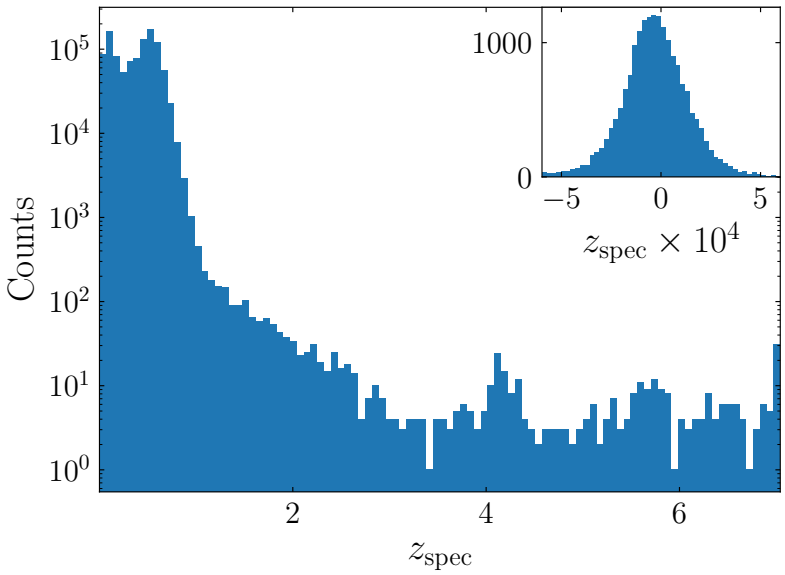


Figure 2.3. – SDSS DR12 redshift distribution of galaxies in the training sample with photometry in all u, g, r, i, and z passbands. A zoom is shown in the top right panel to show the redshift distribution at very low redshifts.

test sample while the rest is divided into the training and validation samples with 80% and 20% of the galaxies respectively. In the end, the training sample counts 678 193 galaxies, the validation sample has 169 549 galaxies while the test sample is composed of 211 936 galaxies. The distribution of spectroscopic redshifts in the training sample is shown in Fig. 2.3. Galaxies beyond $z = 1$ account for 0.2% of the sample. The two peaks observed in the redshift distribution around $z = 0.1$ and $z = 0.5$ correspond respectively to the combined main galaxy sample and luminous red galaxies sample (MGS+LRG) and the Baryon Oscillation Spectroscopic Survey (BOSS) whose respective distributions are described in Beck, Dobos, Budavári, A. S. Szalay, et al. (2016). We observe an excess of spectroscopic redshifts at $z < 0.005$ almost centered around $z = 0$, whose distribution is shown in the top right panel of the figure.

2.2.2. Results with SDSS DR12

We first present our results on photo-z point-estimates obtained using only magnitudes with the random forest algorithm from the `scikit-learn` library. The random forest has 60 decision trees, a minimum of 2 splits per tree, a maximum depth of 25, and the training uses the MAE loss. Fig. 2.4 shows the 2D histogram of the predicted $z_{\rm ph}$ against $z_{\rm spec}$.

We see in the central panel that the one-to-one relation, shown as a red line, is followed with a bias $\delta z = 0.037$, a NMAD $\sigma_{\rm NMAD} = 0.043$, and an outlier fraction $\eta_{0.15} = 0.027$. The limits $\delta z \leq 0.15$ are shown as the area between the black dashed lines around the one-to-one red line. A larger fraction of outliers is visible around $z_{\rm spec} = 0.3$, explained by the lower number of galaxies at this redshift in the training

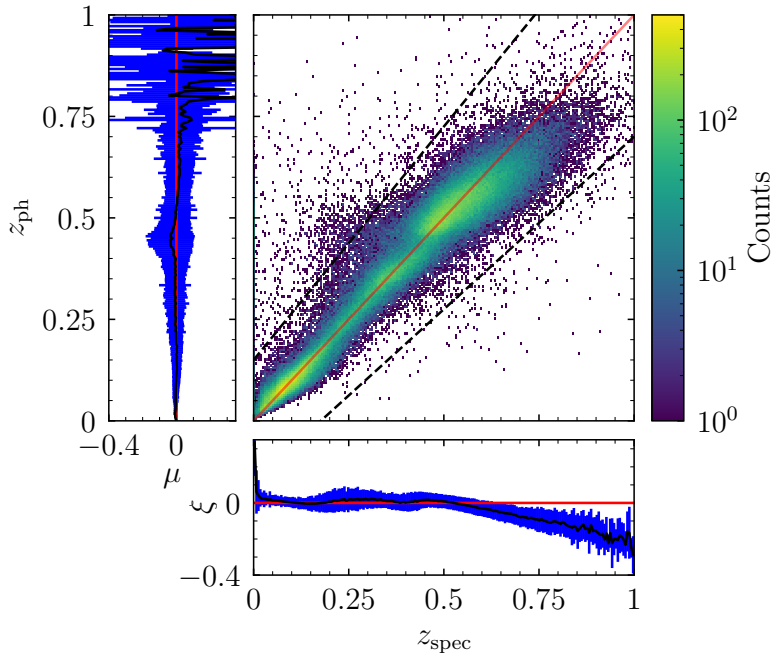


Figure 2.4. – 2D histogram of $z_{\rm ph}$ estimates against $z_{\rm spec}$, considered as the true redshift to train the random forest algorithm. In the central panel, the one-to-one relation is shown as a red line.

Table 2.1. – Statistics of the neural networks trained to predict photo-z point-estimates on the sample of SDSS DR12 galaxies up to $z_{\rm spec} = 7$.

Model	δz	$\sigma_{\rm NMAD}$	σ	$\eta_{0.15}$	$\eta_{0.10}$	$\eta_{0.05}$
RF	0.037	0.043	0.131	0.027	0.048	0.176
ResNet34	0.029	0.034	0.116	0.016	0.029	0.118
Inception CNN	0.028	0.038	0.117	0.021	0.038	0.139

sample. We restrict the interval of redshifts shown to $z \in [0,1]$ because the largest fraction of galaxies lies below $z = 1$. However, the metrics are computed on all galaxies up to $z = 7$. Overall, galaxies beyond $z = 1$ have an increasingly large bias towards lower values. All metrics are grouped in Table 2.1.

The bottom panel of Fig. 2.4 shows in black the learning error $\xi = p\left(z_{\rm ph} - z_{\rm spec} \,|\, z_{\rm spec}\right)$ computed as the mean bias $z_{{\rm ph},k} - z_k$ and in blue the associated standard deviation, where z_k is the midpoint of each bin of the 2D histogram and $z_{{\rm ph},k}$ is the set of $z_{\rm ph}$ falling into the $k^{\rm th}$ bin. In the panel on the left, the recovery uncertainty $\mu = p\left(z_{\rm ph} - z_{\rm spec} \,|\, z_{\rm ph}\right)$ is computed similarly, as the mean of $z_{{\rm spec},k} - z_k$ where $z_{{\rm spec},k}$ is the set of $z_{\rm spec}$ falling into the $k^{\rm th}$ bin. We find that ξ is biased towards low values at $z_{\rm spec} > 0.5$ and shows a positive bias with a very large uncertainty at very small $z_{\rm spec}$, which is explained by the excess seen in Fig. 2.3 around 0. For these $z_{\rm spec}$, the predicted values of $z_{\rm ph}$ tend to be overestimated, similarly to the underestimation of redshifts at the other extreme, close to $z = 1$.

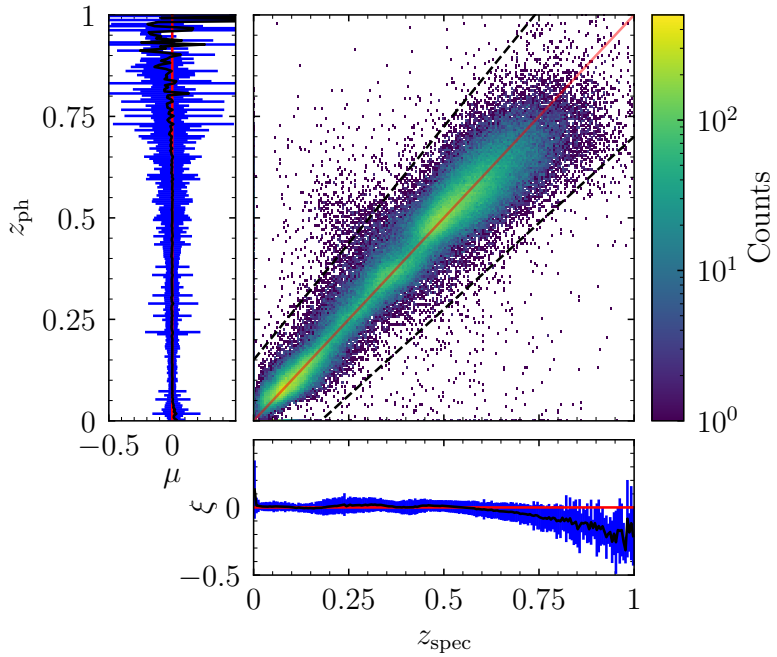


Figure 2.5. – 2D histogram of $z_{\rm ph}$ estimates against $z_{\rm spec}$, considered as the true redshift to train the ResNet34 model. In the central panel, the one-to-one relation is shown as a red line.

As a comparison, we show in Fig. 2.5 the same plot obtained with the ResNet34 architecture, using galaxy images in the 5 flux passbands instead of the magnitudes. Deep learning models are trained on a set of 3 Nvidia 2080Ti GPU and one Nvidia RTX A3000 Laptop GPU. After some tests to determine the hyperparameter values which yield the best performances, we decided to use a cyclical learning rate (Smith, 2017) with λ varying between 1×10^{-6} and 1×10^{-3} with an exponential decay on the upper limit, a batch size of 64, and ELU activation function with $\alpha = 1$. The outliers observed around $z_{\rm spec} = 0.3$ and at $z_{\rm spec} > 0.6$ with the random forest are reduced by a factor 1.7 to reach $\eta_{0.15} = 0.016$. The performances on the bias and NMAD are improved by a factor 1.3 and 1.5, respectively. The learning error ξ deviates from 0 beyond a higher redshift than with the random forest, at $z_{\rm spec} > 0.6$. The bias observed at very low redshifts is smaller than before. The improvements are explained by the use of a more complex model, with about 21.6×10^6 parameters, but also by the gain of information in galaxy images with respect to photometry alone. However, we also note the apparition of an horizontal line of $z_{\rm ph} \approx 0$ values in the central panel for various $z_{\rm spec}$ values, mostly at $z_{\rm spec} < 0.2$, which means that this model completely fails to properly estimate the photo-z of these galaxies.

With the inception CNN architecture (trained with a larger batch size of 1024), we find that the performances are slightly worse than with ResNet34 (see Table 2.1), with a NMAD and outlier fraction $\eta_{0.15}$ which are 12 %, and 30% larger, respectively. The 2D histogram shown in Fig. 2.6 is similar to the one obtained with the ResNet34 model predictions in terms of distribution of the outliers. However, there is no line of $z_{\rm ph} \approx 0$

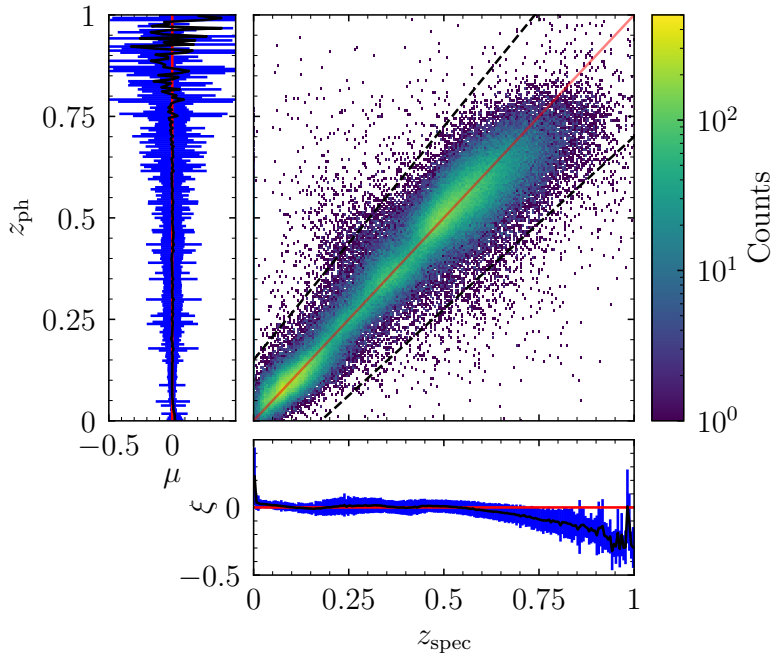


Figure 2.6. – 2D histogram of $z_{\rm ph}$ estimates against $z_{\rm spec}$, considered as the true redshift to train the inception CNN model. In the central panel, the one-to-one relation is shown as a red line.

values for $z_{\rm spec} \in [0, 0.2]$ like with ResNet34. This entails that there is a part of the sample for which the inception CNN extracts the properties adequatly to predict $z_{\rm ph}$ while the ResNet34 model fails.

About the scaling of the performance as a function of the size of the training data set, we trained the inception CNN model with fractions of the previous training sample ranging from 0.025 to 1. The results of this study are grouped in Fig. 2.7, with the variation of the metrics as a function of training sample size. Apart from the bias and dispersion, we find that all metrics shown in this figure decrease when the training sample size increases, which is expected given that the model has more examples on which to learn. The metrics measured with the entire data set are improved by up to 1.66 times with respect to a training with 40 times less galaxies. Note that this comparison is done at equal hyperparameters while the performance at small training sample size could be optimized by varying the hyperparameters.

If we now consider the classifier models where a PDF is predicted instead of photo-z point-estimates, we find that the metrics are not degraded when we switch from point-estimates directly predicted by the model to point-estimates computed from the photo-z PDF predicted by the model. With a CNN classifier, we report $\delta z = 0.031$, $\sigma_{\rm NMAD} = 0.031$, and an outlier fraction $\eta_{0.15} = 0.021$ (see Table 2.2). The inception CNN model yields an interesting improvement of the results with $\delta z = 0.030$, a NMAD $\sigma_{\rm NMAD} = 0.027$, and an outlier fraction $\eta_{0.15} = 0.015$, 40 % smaller.

We show 4 random examples of the predicted photo-z PDF in Fig. 2.8 with the associated r passband galaxy image given as input to the inception CNN classifier

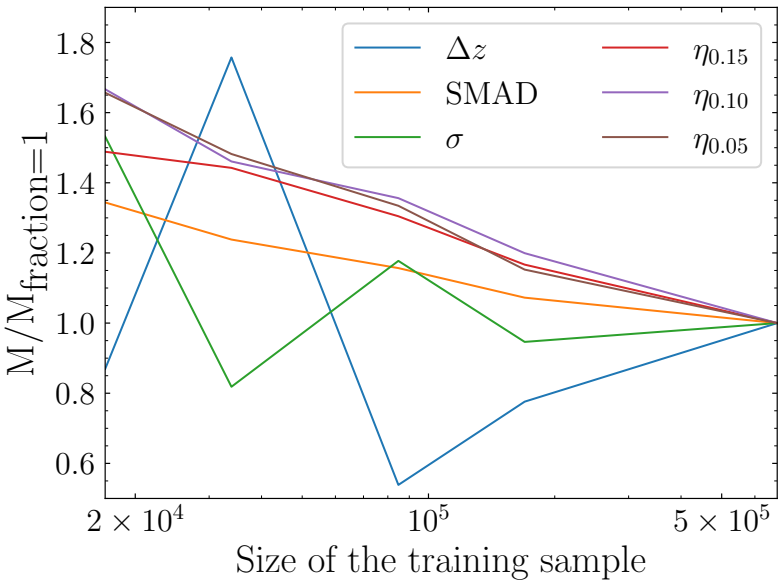


Figure 2.7. – Evolution of the ratio of the metrics M for various training sample sizes over their respective values measured with the entire data set. The fractions tested in this study are 0.025, 0.05, 0.125, 0.25 and 1. Apart from the bias and dispersion, all metrics show a clear improvement when the size of the training sample increases.

Table 2.2. – Statistics of the neural networks trained to predict photo-z PDF on the sample of SDSS DR12 galaxies up to $z_{\mathrm{spec}} = 7$. The point-estimates used in the metrics are computed from the PDF as the expected value.

Model	δz	σ_{NMAD}	σ	$\eta_{0.15}$	$\eta_{0.10}$	$\eta_{0.05}$
CNN classifier	0.031	0.031	0.125	0.021	0.034	0.121
Inception CNN classifier	0.030	0.027	0.118	0.015	0.025	0.086

neural network.

The histogram of the PIT values of the photo-z PDF is presented in Fig. 2.9 for the inception CNN model. We find that the distribution is close to 1 and almost flat, which means that most the PDF predicted represent adequatly the uncertainties of photo-z. The expected PIT distribution in the case of PDF which are on average 20 % too narrow would reach a relative frequency of about 0.3 for PIT values of 0 and 1 and a relative frequency of 1.2 at PIT values of 0.5 (Pasquet et al., 2019). In our case, we can say that the PIT distribution of Fig. 2.9 is flat and that the width of our PDF estimates is adequate.

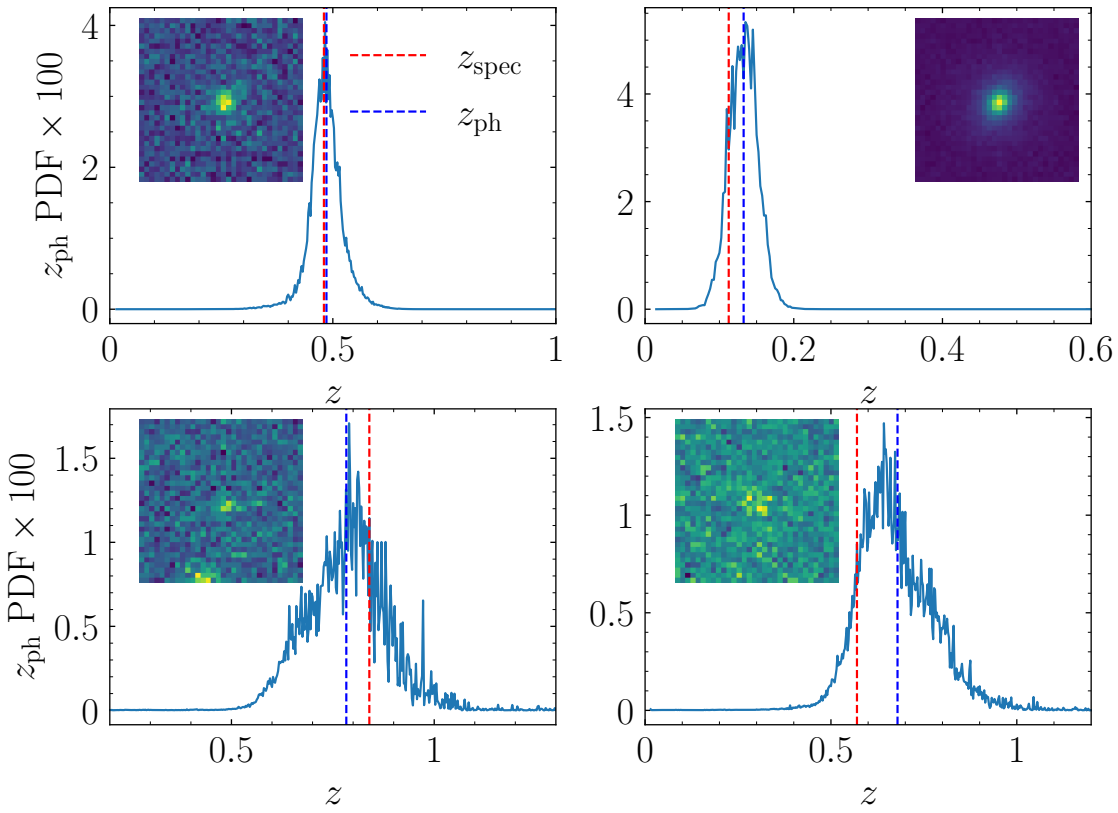


Figure 2.8. – Random examples of photo-z PDF predicted with the inception CNN. The galaxy cutouts shown are in the r passband.

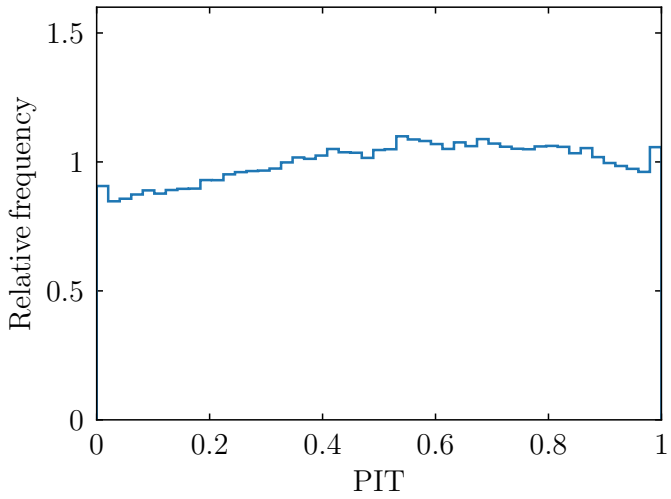


Figure 2.9. – Histogram of the PIT values of the photo-z PDF predicted with the inception CNN.

2.3. Photometric redshifts with the Euclid Science Challenge 8

In this section, we introduce the *Euclid* SC8 images used in this work, the model used to simulate *Euclid* $z_{\rm spec}$ measurements associated with these images, and the results obtained for photo-z estimates.

2.3.1. Data and mock spectroscopic redshifts

The *Euclid* SC8 (Euclid Collaboration: Serrano et al., 2024) is a large-scale validation exercise performed by the *Euclid* Science Ground Segment (SGS), the pipeline which processes all the data observed by *Euclid*. The goal of this exercise was to validate on simulations the entire pipeline of the SGS and ensure that the data received will be processed properly, yielding the expected products while respecting the time and computing resources available. The SC8 data set was built in several main steps. The large cosmological N-body simulation called Flagship was produced to build a galaxy mock catalogue. A catalogue of stars was built and merged with Flagship into the True Universe catalogue, with a selection of galaxies with a magnitude cut at $I_{\rm E} \leq 26$ for 165 deg^2 of the *Euclid* Wide Survey and $I_{\rm E} \leq 28$ for 1 deg^2 of the Deep Survey. Then, the instrumental models of the VIS and NISP instruments were applied to the True Universe catalogue to simulate observations from *Euclid*. These simulations have been processed by the SGS pipeline to create the expected products. In this work, we used the simulated galaxy images from the $I_{\rm E}$, $Y_{\rm E}$, $J_{\rm E}$, and $H_{\rm E}$ passbands (see Fig. 1.4), the photometry measured by the SGS pipeline on these images, and the spectroscopic redshifts extracted from the simulated spectrograms. We show in Fig. 2.10 16 examples of galaxies simulated in the $H_{\rm E}$ passband with their respective redshifts as measured by the SGS pipeline. Various levels of noise are observed in the images, noise from physical, environmental and instrumental effects introduced in the simulations to make them more realistic. A very large amount of data was generated during the SC8 with 10.2 terabytes for the VIS and NISP-P exposures. We chose to use a data set of size similar to the one used previously, with 493 921 galaxies to build our training, validation and test samples.

An issue encountered at this point was the fact that the majority of the extracted $z_{\rm spec}$ were not valid due to a failure during the SC8. An underestimation of the H_α flux measured in the pipeline with respect to the True Universe flux lead to a negative continuum for many galaxy spectra. Moreover, some artefacts like wiggles in 1D spectra also polluted the extraction of redshifts. The flag supposed to give the reliability of these measurements was also affected, making a cleaning of this sample through quality cuts difficult. The resulting $z_{\rm spec}$ measured by the SGS pipeline are shown in Fig. 2.11. While the true redshifts lie between $z = 0$ and $z = 2.3$, the measured $z_{\rm spec}$ ranges from $z = 0.3$ to $z = 5$. The mean bias Δz is 0.743 and the fraction of outliers is $\eta_{0.15} = 0.836$. For this reason, it was impossible to use these spectroscopic redshifts as a training sample.

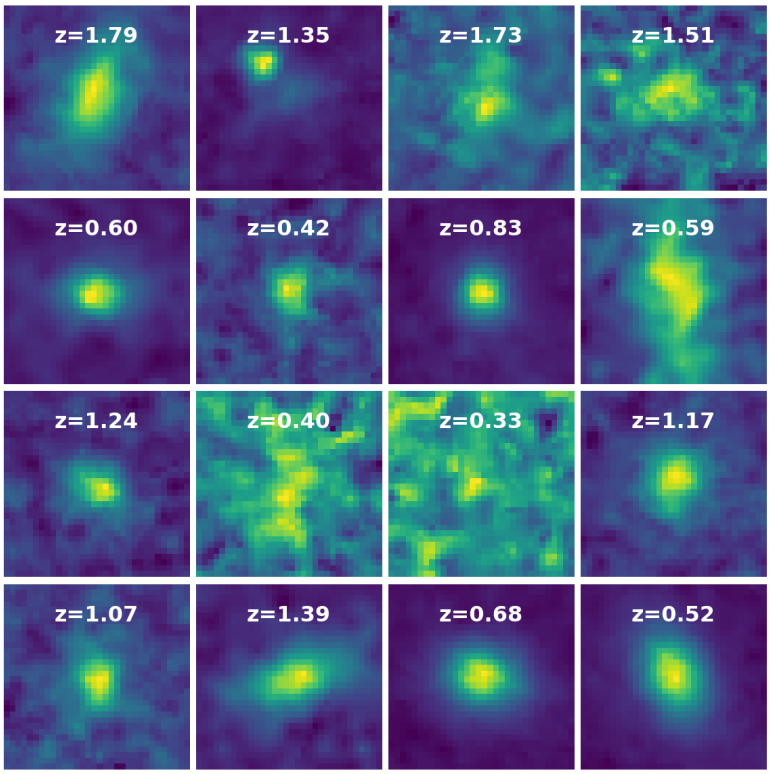


Figure 2.10. – Galaxy images in the H_E passband with the associated z_{spec} measured by the SGS pipeline during the *Euclid* SC8.

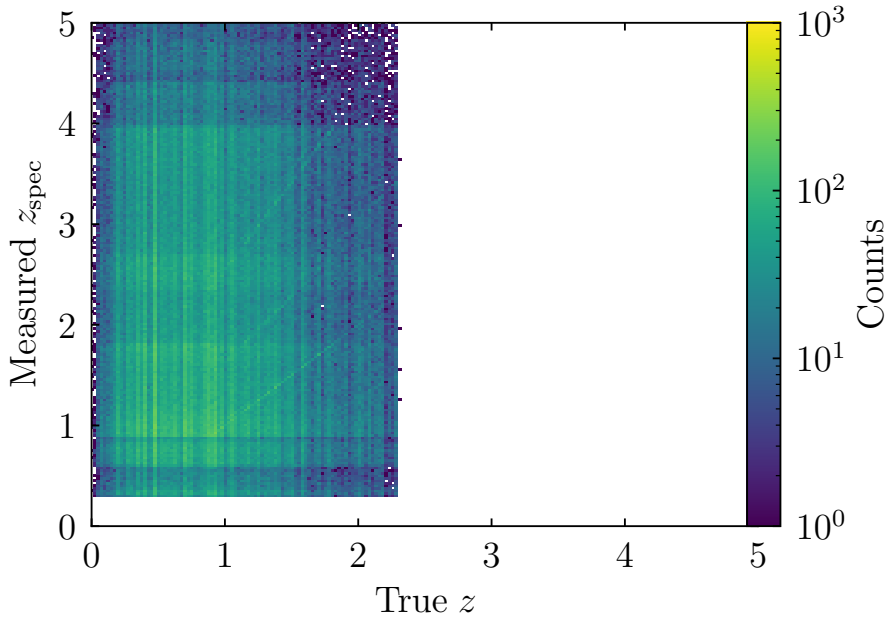


Figure 2.11. – Spectroscopic redshifts measured by the SGS pipeline during the *Euclid* SC8 against the true redshifts, which range between $z = 0$ and $z = 2.3$.

The first approach considered was to use the true redshifts as labels. With this very optimistic approach, we find that the deep learning models efficiently learn the relationship between the input images and $z_{\rm ph}$. For example, the inception CNN+MLP classifier estimate $z_{\rm ph}$ with a bias $\Delta z = 1.25 \times 10^{-6}$, $\sigma = 0.020$, and $\eta_{0.15} = 0.0008$. In order to build a more realistic training set, we simulated mock $z_{\rm spec}$ measurements with a model used by the End-to-End Work Package of the Galaxy Clustering Science Working Group (de la Torre et al, in prep.). In this work package, bypass codes were created in order to study the effect of different analysis choices on the outputs of the SGS pipeline without effectively running the whole pipeline since it takes a long time and requires significant computing resources. One of this bypass codes called `FastSpec` directly computes galaxy spectra from a catalogue. It was used in association with the pipeline of $z_{\rm spec}$ measurement from spectra to build a model which enables the simulation of a sample of $z_{\rm spec}$ given the true redshift and the associated Hα input flux. This model samples distributions calibrated to give the probability of measuring either the target redshift of the galaxy within a given uncertainty or a wrong redshift which can either be a line interloper or a noise interloper. A line interloper is observed when the spectral line used to determine the redshift of a galaxy is mistaken for another line, for example O_{II} and H_α. For a true redshift $z_{\rm t}$, the measured resdhift is given by

$$z_{\rm interloper} = \frac{\lambda_{\rm emit,true}\,(1+z_{\rm t})}{\lambda_{\rm emit,assumed}} - 1\,. \tag{2.8}$$

Line interlopers are sometimes obtained when the noise of the galaxy spectrum mimics an emission line. Unlike line interlopers, noise interlopers have no specific relation to the true redshift. The conditional probability of measuring a given $z_{\rm spec}$ $P(z_{\rm spec}|z_{\rm true})$ depends on the probability of measuring $z_{\rm spec}$, the probability of measuring a noise interloper and the probability of line interlopers. The fraction of right redshifts (target sample), noise or line interlopers is calibrated on the EL-Cosmos simulation catalogue of emission lines for various thresholds of H_α flux at 0.5, 1, 2, 3, 4, 5, 7, and 10×10^{-16} erg/s/cm^2. For example, with a flux of 0.5×10^{-16} erg/s/cm^2, the calibrated fractions f are shown in Fig. 2.12. As expected from a flux which is 4 times smaller than the threshold of the *Euclid* nominal survey, the fraction of noise interlopers is high. When the flux is larger, the noise fraction $f_{\rm noise}$ decreases while the fraction of correct redshifts increases.

The probability of noise interlopers $p_{\rm noise}$ is computed as

$$\frac{p_{\rm noise}}{f_{\rm noise}} = \frac{p[0]\left(z_t^{p[1]} + z_t^{(p[1]*p[2])} + z_t^{p[5]}\right)}{\left(z_t^{p[2]} + p[3] + z_t^{p[4]}\right)} \times e^{(-z_t^2/4)} + p[6]\left(\mathrm{erf}(\frac{z_t - p[7]}{p[8]}) + \left(1 - \mathrm{erf}(\frac{z_t - p[9]}{p[10]})\right) - 1\right), \tag{2.9}$$

with p a list of coefficients calibrated for each flux threshold. For line interlopers, the

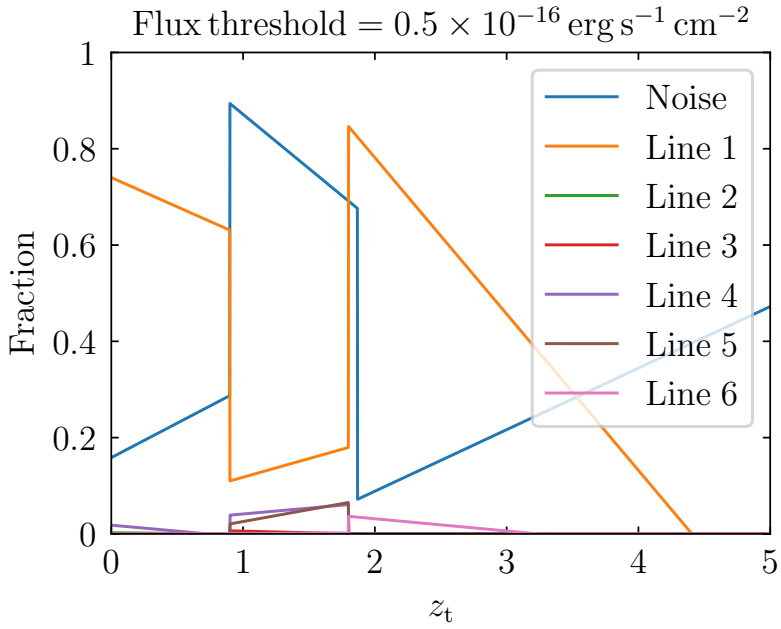


Figure 2.12. – Fraction of right redshifts in orange, noise interlopers in blue, and different kind of line interlopers as a function of the true redshift, for a H_α flux of 0.5×10^{-16} erg/s/cm^2.

probability p_{line} is computed from the previous fractions f as

$$p_{\text{line}} = \frac{f}{\sqrt{2\pi}} e^{\left(\frac{-\left(z_t - z_{\text{interloper}}\right)^2}{2\sigma^2_{\text{interloper}}}\right)} \tag{2.10}$$

where $\sigma_{\text{interloper}} = 0.001$ or 0.002 depending on the lines involved in the interloper. The probability of measuring z_{spec} is shown in Fig. 2.13 as a function of the true reshift. The probability of measuring z_{m} is higher between $0.9 < z < 1.8$ because it is the range of redshifts for which the NISP instrument is designed. It should be noted that the calibration and the model used in this work correspond to its version 1.0. With this model, a mock catalogue of z_{spec} was created from the True Universe catalogue to replace the defective z_{spec} from SC8. An important caveat to the work of the following section is that given the statistical nature of the creation of the mock z_{spec} data set, the analysis would be more robust if several mock catalogues were created. In this case, training the deep learning models and averaging their performances over the different mock realizations would have been profitable. For this reason, we warn that the performances found in the following section should not be considered as a reference or a forecast of what could be obtained with observed *Euclid* data but as a comparative study of the different deep learning models instead. For two main reasons, it was decided to work with only one mock realization. The first reason is that the version 1.0 of the model was only adequate to simulate the performance of the *Euclid* SGS z_{spec} extraction pipeline as of December 2022, performance which improved since

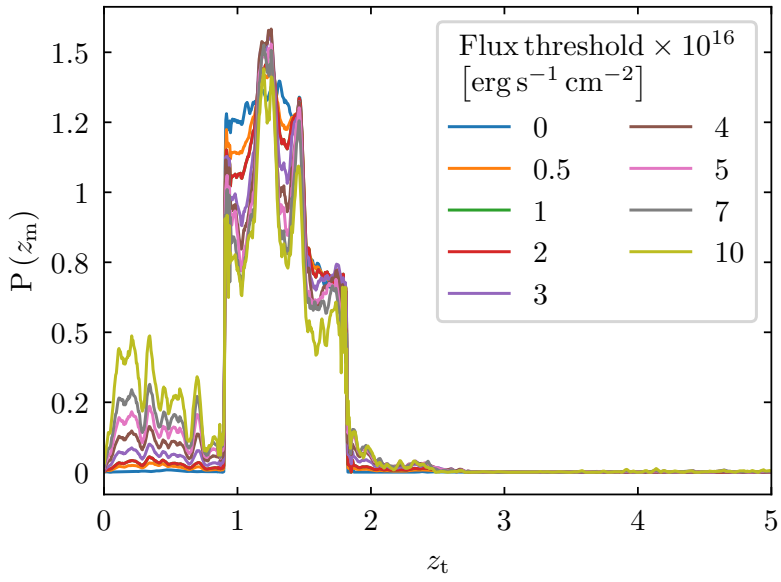


Figure 2.13. – Probability of measuring a redshift z_m with the spectroscopic pipeline as a function of the true redshift z_t for various H_α flux thresholds.

then. The second reason is that the Third Small Performance Verification exercise plan (SPV3) included the generation of new, improved and updated pixel-level simulations which would be processed by a version of the SGS pipeline in which the issues found in the SC8 exercise were fixed. Thanks to SPV3, it would have been unnecessary to simulate z_{spec}. However, these simulations were cancelled and the next pixel-level simulations are planned for the end of 2025, making once again the mock z_{spec} the only option to perform this study, despite its caveats. The distribution of the mock sample of z_{spec} as a function of z_{true} is given in Fig. 2.14.

The one-to-one relation shown with the red line is followed by part of the sample, with line interlopers visible as secondary skewed lines between $z_{spec} = 0.9$ and $z_{spec} = 1.8$. Using the same metrics as before, we find $\Delta z = 0.234$, $\sigma_{NMAD} = 0.317$, $\sigma = 0.569$, and $\eta_{0.15} = 0.626$. Given the fraction of outliers, this is a pessimistic scenario for the training. The data set counts 493 921 galaxies divided into a training sample of 400 075 galaxies, a validation sample of 44 453 galaxies and a test sample of 49 393 galaxies.

2.3.2. Results with Euclid SC8

We now present our results obtained with the SC8 simulated images and mock z_{spec}. Figure 2.15 shows the z_{ph} estimates as a function of the simulated z_{spec} with a significant bias of $\Delta z = 0.0172$, dispersion $\sigma_{NMAD} = 0.109$, and fraction of outliers $\eta_{0.15} = 0.290$. In particular, we observe a large population of outliers with a positive bias between $z_{spec} = 0.2$ and $z_{spec} = 0.5$ and a second group of outliers with a negative bias at $z_{spec} \geq 1$. All metrics of the trainings done on this sample can be found in Table 2.3.

These performances are expected from the quality of the training sample but unlike

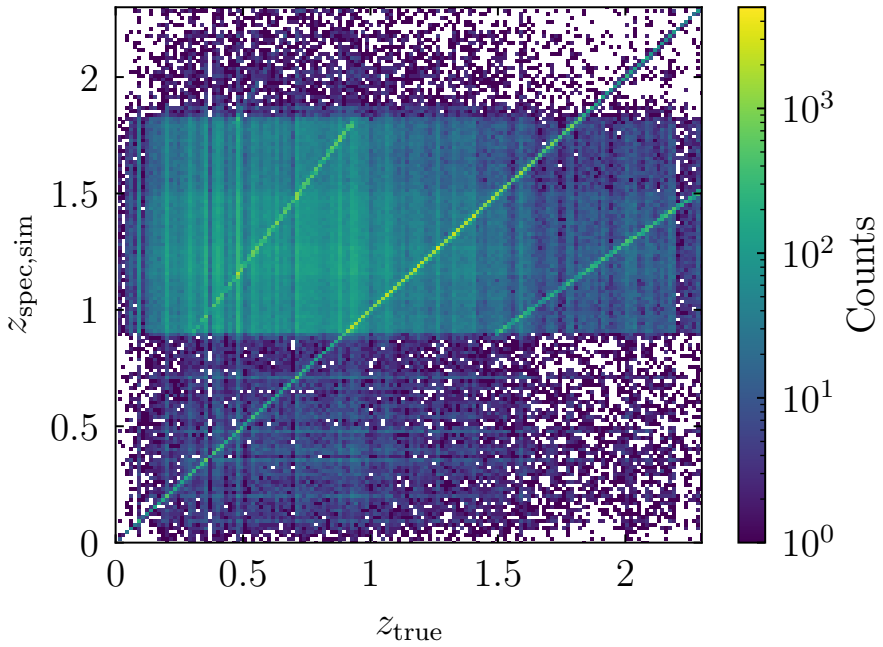


Figure 2.14. – Simulated spectroscopic redshifts as a function the true redshifts.

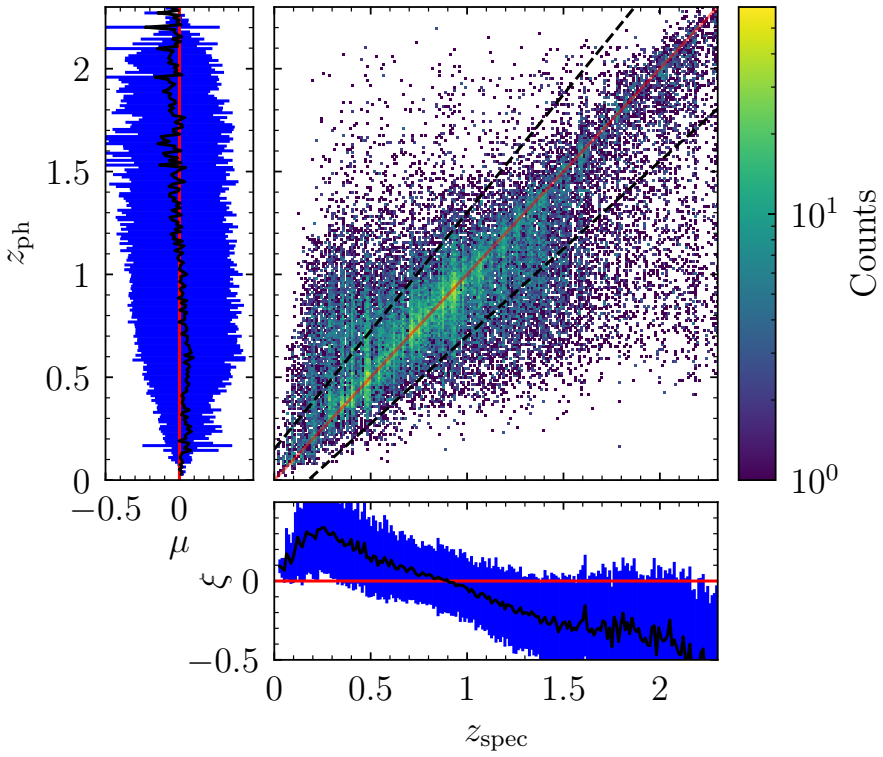


Figure 2.15. – Photometric redshifts as a function of spectroscopic redshifts with a MLP. Only galaxy magnitudes are used as inputs of this neural network.

Table 2.3. – Statistics of the neural networks trained to predict photo-z point-estimates on the SC8 sample.

Model	Δz	$\sigma_{\rm NMAD}$	σ	$\eta_{0.15}$	$\eta_{0.10}$	$\eta_{0.05}$
MLP	0.0172	0.109	0.334	0.290	0.411	0.602
CNN	0.0258	0.099	0.237	0.194	0.337	0.602
Inception CNN	0.0127	0.076	0.267	0.189	0.300	0.506
Inception CNN+MLP	0.0114	0.052	0.147	0.072	0.155	0.368

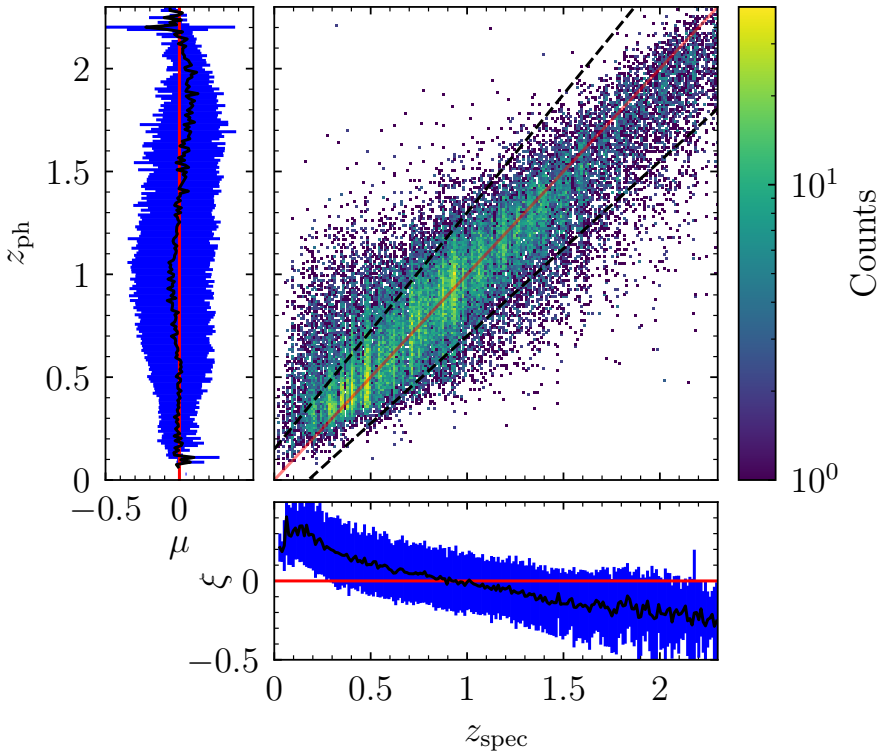


Figure 2.16. – Photometric redshifts as a function of spectroscopic redshifts with a sequential CNN. Only galaxy images are used as inputs of this neural network.

the results obtained with the pure sample of true redshifts, this pessimistic scenario is closer to what can be expected from the early data of the *Euclid* survey. We find that with galaxy images instead of photometry and using a sequential CNN instead of a MLP already improves these performances (Fig. 2.16).The outlier populations are reduced with a fraction $\eta_{0.15}$ which is decreased by 50 %. However, the bias is also increased by 50 % and only the fractions of outliers $\eta_{0.15}$ and $\eta_{0.10}$ are decreased, while $\eta_{0.05}$ isn't.

With the inception CNN (Fig. 2.17), the bias $\Delta z = 0.0127$ is twice as small as with the CNN and the NMAD is improved by a factor 1.3. Even if there is a similar fraction of large outliers $\eta_{0.15}$, both $\eta_{0.10}$ and $\eta_{0.05}$ are improved by a factor 1.2 and 1.4 with

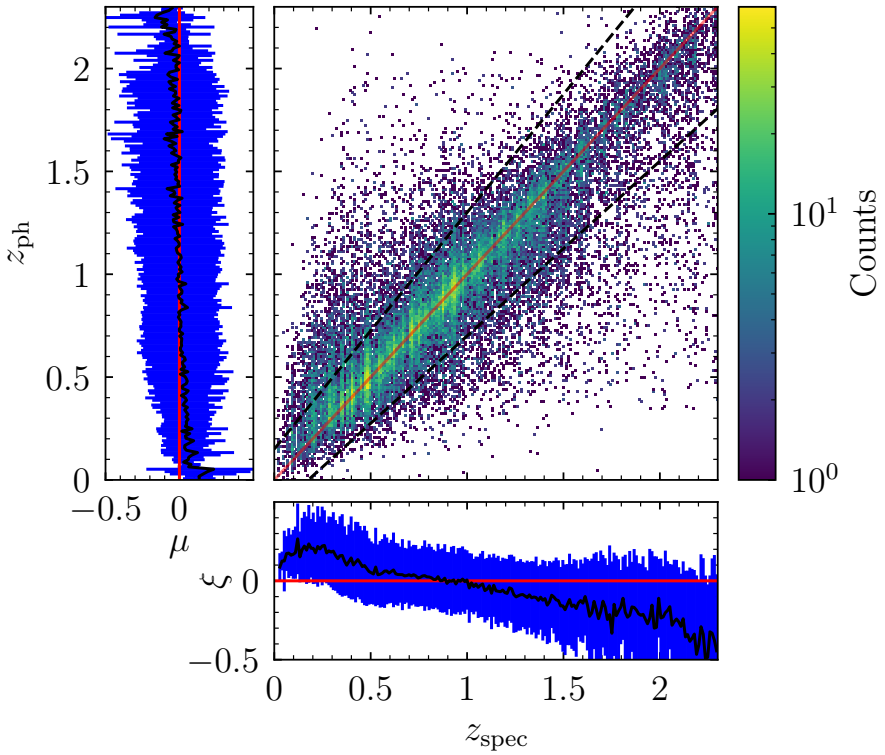


Figure 2.17. – Photometric redshifts as a function of spectroscopic redshifts with an inception CNN. Only galaxy images are used as inputs of this neural network.

respect to the MLP. Despite this evident superiority of the inception architecture over MLP or CNN models for $z_{\rm ph}$ estimates, the extraction of the photometric information is not perfect, which is expected from the finite number of parameters in the neural networks. The multi-input architecture combining inception CNN and MLP to process both images and magnitudes helps the training and this is obvious with the results of Fig. 2.18. With respect to the inception CNN and images alone, Δz, $\sigma_{\rm NMAD}$, $\eta_{0.15}$, $\eta_{0.10}$, and $\eta_{0.05}$ are further decreased by a factor 1.1, 1.5, 2.6, 1.9, and 1.4, respectively. With respect to the MLP and magnitudes alone, the improvement on the same metrics is even larger with the following factors : 1.5, 2.1, 4.0, 2.7, and 1.6 for Δz, $\sigma_{\rm NMAD}$, $\eta_{0.15}$, $\eta_{0.10}$, and $\eta_{0.05}$, respectively. These results are strong arguments to use the combination of images and magnitudes to improve photo-z estimates for analyses which do not use both photo-z and galaxy morphology extracted from the images, like weak lensing. For example, it would be beneficial to photometric galaxy clustering analyses such as the ones presented in Chapters 3 and 4.

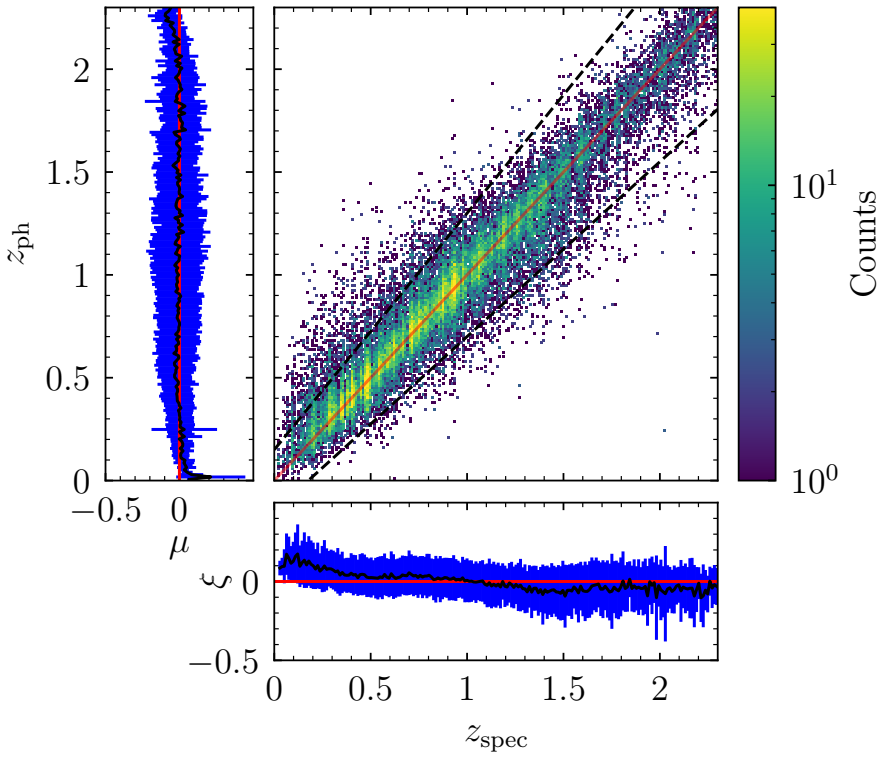


Figure 2.18. – Photometric redshifts as a function of spectroscopic redshifts with a multi-input inception CNN. Both galaxy images and magnitudes are used as inputs of this neural network.

3. Photometric galaxy clustering

Summary

3.1. A complementary probe for Euclid . . . 75
3.2. The two-point angular correlation function . . . 77
3.2.1. Theory . . . 77
3.2.2. Estimator . . . 82
3.3. The Euclid Flagship simulation . . . 82
3.4. Measurements of the two-point correlation function . . . 86
3.4.1. Two-point angular correlation function with the equipopulated binning . . . 86
3.4.2. Two-point angular correlation function with the equidistant binning . . . 88
3.4.3. Two-point angular correlation function with a DR1 setting . . . 92
3.4.4. Effect of the photometric redshift choice . . . 92
3.4.5. Effect of the random sample angular resolution $N_{\rm side}$ . . . 96
3.4.6. The `TreeCorr` *bin_slop* approximation . . . 97
3.4.7. Jackknife resampling, effect of $N_{\rm jack}$ . . . 101
3.4.8. Effect of the ratio $N_{\rm rand}/N_{\rm galaxies}$ . . . 101
3.5. Covariances . . . 103

This chapter is dedicated to the presentation of the study of galaxy clustering with photometric redshifts, in particular through one observable, the two-point angular correlation function $w(\theta)$. We describe how this probe meshes with the *Euclid* Collaboration scientific goals, the theoretical model of $w(\theta)$, its estimator and measurement on the *Euclid* Flagship simulation along with an investigation of the influence of different choices in the way we measure $w(\theta)$. The theoretical background on the computation of covariance matrices is given in the last section of this chapter.

3.1. A complementary probe for Euclid

The *Euclid* mission was designed to use two main probes for its core science, BAO and weak gravitational lensing. The first one aims at extracting the signal left by BAO in the distribution of galaxies by measuring spectroscopic redshifts with a precision of $\sigma_z = 0.001\,(1+z)$ with the slitless spectrograph of the NISP instrument (Euclid Collaboration: Jahnke et al., 2024). This way, we can precisely map galaxies in the

Universe and compare how they cluster under the effect of gravity and expansion to theoretical models describing the distribution of matter in the Universe in order to constrain the BAO scale. On the other hand, weak gravitational lensing will measure the correlation of the ellipticities of 1.5 billion galaxies. The ellipticity of galaxies is the result of the perturbation of the propagation of photons through a Universe filled with matter and for the main part, dark matter. Their shape measurements allow us to map the distribution of matter in the Universe which distorts the image of distant galaxies. However, the distances of 1.5 billion galaxies cannot be provided by spectroscopic measurement. Even if slitless spectroscopy speeds up significantly obtaining the redshifts with respect to spectrographs which use optical fibers, it is restricted by the limiting flux of $2 \times 10^{-16}\,\mathrm{erg\,cm^{-2}\,s^{-1}}$, the value for which *Euclid* is capable of reliably detecting emission line resulting from the mission optimisation (Euclid Collaboration: Mellier et al., 2024). As a consequence, photometric redshifts (photo-z) will be used instead. From this very large number of photo-z, one can also study galaxy clustering in a similar manner to what is done in spectroscopic galaxy clustering. In this case, the very large statistical sample of photo-z compensates the lower precision $\sigma_z = 0.05\,(1 + z_{\rm ph})$ of these redshifts with respect to spectroscopic ones. The main way this photometric galaxy clustering is used is in combination with weak lensing, through the study of the autocorrelations of galaxy lensing and galaxy clustering and their cross-correlation. This is commonly called the 3×2-point analysis. One of the main objective of the mission is to put stringent constraints on the parameters of the dark energy equation of state $w(a) = w_0 + w_{\rm a}(1 - a)$, with a goal of reaching uncertainties of $\Delta w_0 = 0.02$ and $\Delta w_a = 0.1$. The quality of these constraints is usually quantified in the figure of merit

$$\mathrm{FoM} = \frac{1}{\sqrt{\det \mathrm{Cov}(w_0, w_{\rm a})}}\,. \tag{3.1}$$

It increases when the dark energy parameters are better constrained and *Euclid* aims at reaching a FoM of a least 400 (Euclid Collaboration: Blanchard et al., 2020). The combination of probes through this 3×2-point analysis is the way *Euclid* plans to achieve such a high FoM. In the 3×2-point analysis, the full shape of the photometric galaxy clustering correlations is used, unlike the BAO analysis which is focused on the position of the BAO peak. In this full-shape analysis, one kind of systematic effect which can plague the results is model misspecifications. Compared to the observed data, the theoretical model of an observable is computed assuming a number of parameters, one of them being the redshift distribution of galaxies as a function of redshift $p(z)$. As the true $p(z)$ of the Universe is unknown, we can only estimate this distribution from our observations, an estimate which is subject to biases. In Chapter 5 Sect. 5.3, we study this effect. However, it is also perfectly possible to exploit this huge amount of photo-z to constrain the BAO signal in an independent manner from the main spectroscopic BAO analysis. This is what was done with the Dark Energy Survey which recently constrained the BAO signal at the 2.1 % level (Abbott, Adamow, et al., 2024) by combining three different two-point statistics through the measure-

ment of the angular correlation function $w(\theta)$, the angular power spectrum C_ℓ and the projected correlation function $\xi_{\rm p}(s_\perp)$. The three share a very large amount of information but their combination actually tightens slightly the constraints obtained from each of them (respectively 2.4 %, 2.3 % and 2.1 %). In this work, we focus on the observable in configuration space, the two-point angular correlation function $w(\theta)$ which will be introduced in the following Sect. 3.2. There are two reasons for the use of this two-dimensional correlation function rather than a three-dimensional one. First of all, as explained previously, the accuracy of photo-z is too poor to properly measure three-dimensional correlation functions. However, using this tomographic approach with one measurement of $w(\theta)$ in each bin of redshift also prevents the need to convert redshifts to distances, needed to compute the 3D correlation function. This conversion introduces the assumption of a cosmology in the measurement itself. Even though careful analyses of the dependence of the results with respect to this assumed cosmology are usually undertaken, we prefer using the model-independent tomographic approach in this work, both for the full-shape and BAO analyses. Regarding the latter, it is also mandatory to use redshift bins to increase the strength of the BAO signal. Indeed, since the BAO peak is found at different scales in configuration space when redshift changes, it will be diluted if the correlation function is measured on galaxies from very different redshifts. There is a compromise to be found between the size of the redshift bins and the number density of galaxies in order to have a sharp peak without increasing too much the size of the correlation function error bars.

3.2. The two-point angular correlation function

In this section we describe the observable relevant to galaxy clustering with the photometric survey that has been considered in this analysis: the galaxy two-point angular correlation function. We also present its estimator and its covariance.

3.2.1. Theory

As we process information projected into bins of redshift, we consider the galaxy two-point angular correlation function $w(\theta)$, defined as (e.g., Crocce et al., 2011):

$$w(\theta) = \sum_{\ell \geq 0} \frac{2\ell+1}{4\pi} C(\ell)\, P_\ell \cos(\theta)\,, \tag{3.2}$$

with P_ℓ being the Legendre polynomial and $C(\ell)$ the angular power spectrum defined as

$$C(\ell) = 4\pi \int_0^\infty \frac{\mathrm{d}k}{k}\, \mathscr{P}_\Phi(k)\, \Delta_\ell^2(k)\,. \tag{3.3}$$

In Eq. (3.3), k is the wavenumber and $\mathscr{P}_\Phi$ stands for the dimensionless power spectrum of the primordial curvature perturbations $\Phi(k)$ that we model with `HMCode` (Mead et al., 2021) as implemented in the Boltzmann code `CAMB` (Challinor et al., 2011). The term Δ_ℓ is the sum of the transfer function of number counts for the galaxy density

field $\Delta_\ell^{\rm D}$ and the linear RSD contribution $\Delta_\ell^{\rm RSD}$ (Chisari et al., 2019):

$$\Delta_\ell(k) = \Delta_\ell^{\rm D}(k) + \Delta_\ell^{\rm RSD}(k)\,, \tag{3.4}$$

where the two terms are respectively defined as:

$$\Delta_\ell^{\rm D}(k) := \int_0^{z_{\rm max}} {\rm d}z\; p(z)\; b(z)\; T_\delta(k,z)\; j_\ell\,(kr)) \tag{3.5}$$

and

$$\Delta_\ell^{\rm RSD}(k) := \int_0^{z_{\rm max}} {\rm d}z\; \frac{(1+z)\,p(z)}{H(z)}\, T_\theta(k,z)\; j_\ell''\,(kr)\,, \tag{3.6}$$

where $p(z)$ is the normalized galaxy redshift distribution, $b(z)$ is the linear galaxy bias, $z_{\rm max}$ is the maximum redshift of the survey that we fix to 3 for practical purposes, j_ℓ is the spherical Bessel function of order ℓ, j_ℓ'' its second derivative, and $r(z)$ is the comoving radial distance. In Eqs. (3.5) and (3.6), the transfer function $T_{\rm X}(k,z)$ of a quantity X is defined as the ratio $X(k,z)/\Phi(k)$ so that T_δ is the transfer function of the matter overdensity $\delta(k,z)$ and T_θ is the transfer function of the divergence of the comoving velocity field. The effect of including the RSD term $\Delta_\ell^{\rm RSD}$ in the theoretical model is shown in Fig. 3.1. Without shifting the position of the BAO peak, it increases the amplitude of $w(\theta)$ at large scales, especially at low redshift. This is the Kaiser effect, explained by the infall of galaxies towards overdensities, which is stronger at low redshift (Kaiser, 1987). Note that in Eq. (3.3), we compute $C(\ell)$ for

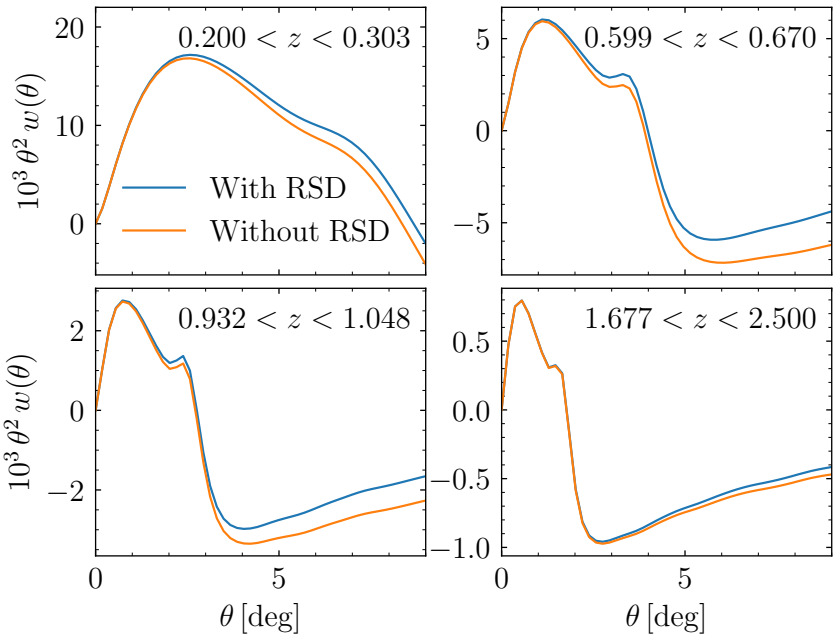


Figure 3.1. – Theoretical $w(\theta)$ computed with and without RSD using the redshift distributions of 4 redshift bins from the Flagship simulation shown in Fig. 3.6.

autocorrelations. In the case of cross-correlations between two redshift bins, Δ_ℓ^2 is replaced by the product of Δ_ℓ computed for each redshift bin ($p(z)$ is bin-specific). In the computation of the theoretical model, we fix $k_{\rm max} = 20\,{\rm Mpc}^{-1}$ for the integrals computed in `CAMB` and $\ell_{\rm max} = 10\,000$. The effect of $k_{\rm max}$ and $\ell_{\rm max}$ is shown in Fig. 3.2 and Fig. 3.3 respectively. We show that $k_{\rm max} = 5\,{\rm Mpc}^{-1}$ already provides an absolute relative error below 0.17% with respect to $100\,{\rm Mpc}^{-1}$ for the $w(\theta)$ theoretical model but we choose to use $k_{\rm max} = 20\,{\rm Mpc}^{-1}$ with an absolute relative error below 0.02% at all redshifts and angular separations. On average, the absolute relative errors with 5 and $20\,{\rm Mpc}^{-1}$ is of the order of 10^{-4} and 10^{-5} respectively. As for $\ell_{\rm max}$, we find that only using $\ell_{\rm max} = 10\,000$ or larger values can have the maximum absolute relative error with respect to $\ell_{\rm max} = 50\,000$ drop below 0.4% at high redshift, though the average absolute relative error is much smaller with 0.05%.

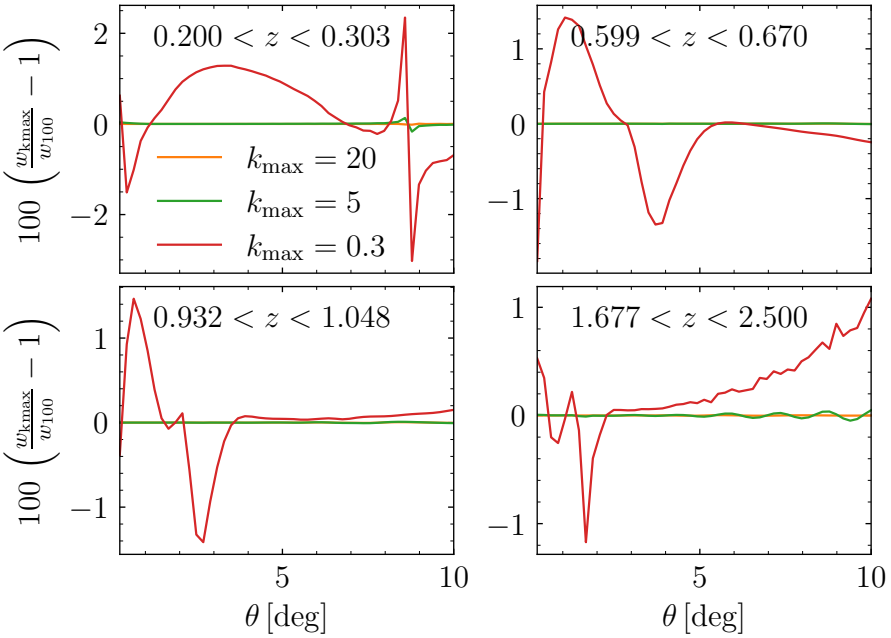


Figure 3.2. – Effect of $k_{\rm max}$ in ${\rm Mpc}^{-1}$ over the theoretical model of $w(\theta)$ computed in 4 of the 13 redshift bins using the redshift distribution from the Flagship simulation. The orange curve for $k_{\rm max} = 20\,{\rm Mpc}^{-1}$ is under the green curve of $k_{\rm max} = 5\,{\rm Mpc}^{-1}$.

Gravitational lenses can increase the observed flux of background sources. When a magnitude cut is applied to a sample, this increase changes the number of galaxies selected. This effect called magnification bias affects galaxy clustering. Discussed in Lepori et al., 2022 regarding full-shape analyses of photometric galaxy clustering, we checked that the effect of magnification bias over α is smaller than $0.2\,\sigma$ in most redshift bins, which is why no $\Delta_\ell^{\rm M}(k)$ term as defined in Eq. (26) of Chisari et al., 2019 is included in the model. Other relativistic effects are completely sub-dominant and not included either (Alonso et al., 2015).

While the fast Limber approximation described in Kaiser (1992) is used at $\ell \in$

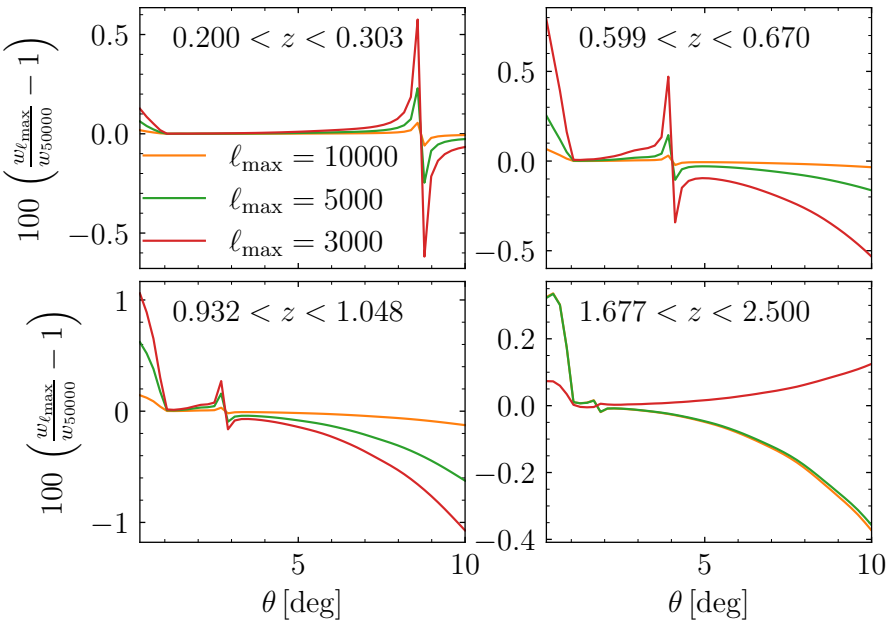


Figure 3.3. – Effect of $\ell_{\rm max}$ over the theoretical model of $w(\theta)$ computed in 4 of the 13 redshift bins using the redshift distribution from the Flagship simulation.

[220, 10000], to accurately model large scales at $\ell < 220$ needed for BAO analysis, non-Limber integrals are computed using the Fang–Krause–Eifler–MacCrann (FKEM) method described in Fang, Krause, et al. (2020). The FKEM method divides the power spectrum in its non-linear and linear components. The non-linear component is only important at small scales, where the Limber approximation is accurate and can be used. The linear matter power spectrum is factorized to to write $P_{\rm lin}(k, z_1, z_2) = D(z_1)\, D(z_2)\, P_{\rm lin}(k, z = 0)$. This factorization allows the computation of Eq. (3.3) without the double-Bessel integral which appears when the integral is expanded. We checked in Fig. 3.4 that the effect of the Limber approximation over $C(\ell)$ is smaller than 1% in this range of ℓ. We find in Fig. 3.5 that the effect of this approximation is absolutely non negligible at the scales considered in a BAO analysis. Only a full-shape analysis restricted to small scales can use the Limber approximation without introducing a large error in the model.

Throughout this work, the theoretical $w(\theta)$ is computed using the Core Cosmology Library (Chisari et al., 2019). We refer to $w_{\rm fid}(\theta)$ when the theoretical $w(\theta)$ is computed with the fiducial cosmological parameters defined in Eq. (4.5).

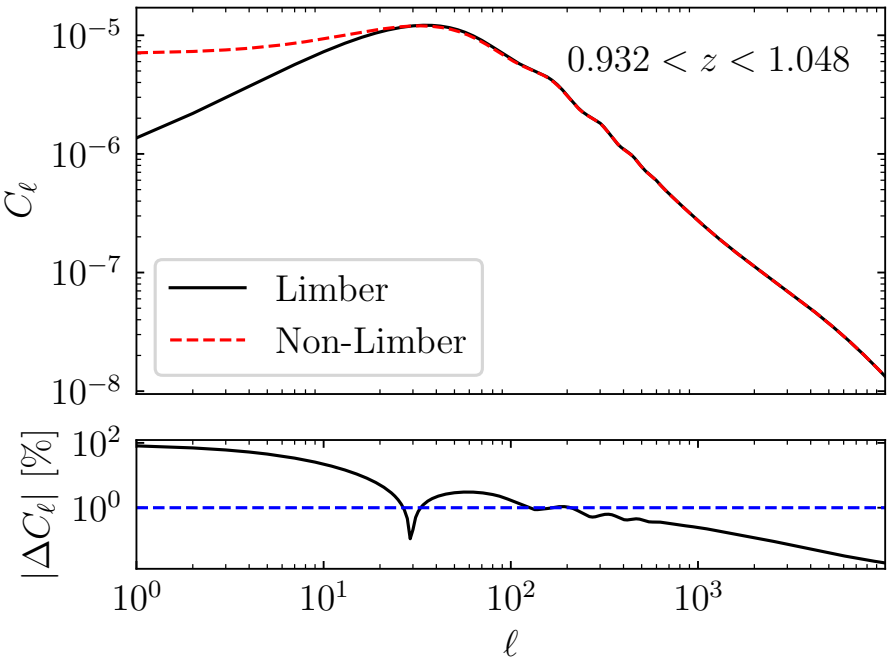


Figure 3.4. – Angular power spectrum C_ℓ computed with and without Limber approximation (top panel) and error induced by the approximation (bottom panel).

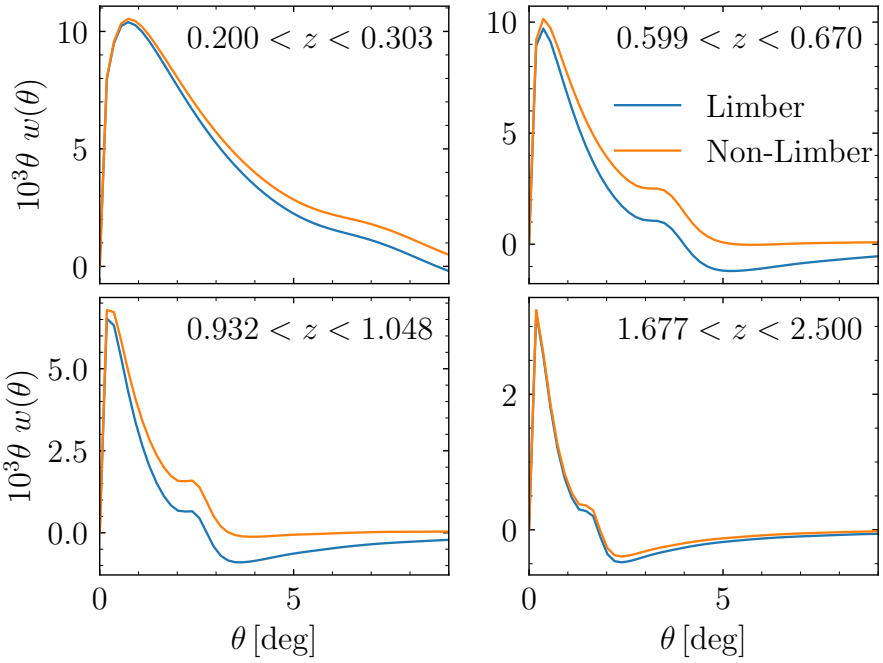


Figure 3.5. – Effect of the Limber approximation over the theoretical model of $w(\theta)$ computed in 4 of the 13 redshift bins using the redshift distribution from the Flagship simulation.

3.2.2. Estimator

The two-point angular correlation function is computed from the Flagship Mock Galaxy Catalogue with the Landy–Szalay estimator (Landy et al., 1993):

$$w(\theta) = \frac{N_{\rm DD} - N_{\rm DR} - N_{\rm RD} + N_{\rm RR}}{N_{\rm RR}}, \tag{3.7}$$

where $N_{\rm DD}$, $N_{\rm DR}$, $N_{\rm RD}$, and $N_{\rm RR}$ are the pair counts where D stands for the data i.e. galaxy pairs in a given redshift bin and R for a random point. Autocorrelations are computed for each redshift bin with $N_{\rm DR}$= $N_{\rm RD}$ while cross-correlations use the respective galaxy and random point pairs measured in two different redshift bins so that $N_{\rm DR} \neq N_{\rm RD}$. These random points are created by sampling the footprint of the Flagship simulation defined by a `HEALPix` mask of $N_{\rm side} = 4096$, which is equivalent to an angular resolution of 0.014°. We use 30 times as many random points as galaxies, yielding 1.04×10^9 random points per redshift bin. The angular binning has a resolution of 0.1° and spans between $\theta_{\rm min} = 0.12°$ and $\theta_{\rm max} = \theta_{\rm BAO} + 2.5°$ where $\theta_{\rm BAO}$ is the expected position of the BAO peak in the fiducial cosmology

$$\theta_{\rm BAO} = \frac{r_{\rm s,\,drag,\,fid}}{(1+z_{\rm eff})\, D_{\rm A,\,fid}(z_{\rm eff})}, \tag{3.8}$$

where $r_{\rm s,\,drag,\,fid}$ and $D_{\rm A,\,fid}$ are the sound horizon at the drag epoch and the angular diameter distance computed at the mean redshift of each bin $z_{\rm eff}$ with the cosmology of the simulation given in Sect. 3.3. The measurement of $w(\theta)$ is performed with the code `TreeCorr`[1] (M. Jarvis et al., 2004) and errors are estimated by a jackknife resampling of 500 patches.

3.3. The Euclid Flagship simulation

In the various analyses of this work, we use the Flagship v.2.1.10 galaxy mock sample (Euclid Collaboration: Castander et al., 2024) available to the *Euclid* Consortium on CosmoHub[2] (Tallada et al., 2020; Carretero, Tallada, et al., 2017) created from the Flagship N-body dark matter simulation (Potter et al., 2017). This simulation uses a flat ΛCDM cosmology : matter density parameter $\Omega_{\rm m} = 0.319$ which is the sum of the cold dark matter, baryons and neutrinos contributions , baryon density parameter $\Omega_{\rm b} = 0.049$, dark energy density parameter $\Omega_\Lambda = 0.681 - \Omega_{\rm r} - \Omega_\nu$, with a radiation density parameter $\Omega_{\rm r} = 0.00005509$ and $\Omega_\nu = 0.00140343$ for massive neutrinos, dark energy equation of state parameter $w_{\rm de} = -1.0$, reduced Hubble constant $h = 0.67$, spectral index of the primordial power spectrum $n_{\rm s} = 0.96$, and its amplitude $A_{\rm s} = 2.1 \times 10^{-9}$ at $k = 0.05\,{\rm Mpc}^{-1}$. This simulation box of 4×10^{12} particles of mass $10^9\, h^{-1} M_\odot$ has a side of $3.6\,{\rm h}^{-1}\,{\rm Gpc}$. The main output of this simulation is a light-cone that spans redshifts between 0 and 3, from which dark matter haloes are then

1. https://github.com/rmjarvis/TreeCorr
2. https://cosmohub.pic.es/

identified down to $10^{10}\,h^{-1}\,M_\odot$ with ROCKSTAR (Behroozi et al., 2013). These haloes were then populated with galaxies with halo abundance matching and halo occupation distribution techniques following Carretero, Castander, et al. (2015). Galaxy luminosities have been calibrated with a combination of the luminosity functions from Blanton, Hogg, et al. (2003), Blanton, Lupton, et al. (2005), and Dahlen et al. (2005). Galaxy clustering measurements were calibrated as a function of colour and luminosity following Zehavi et al. (2011) and the colour-magnitude diagram from Blanton, Lupton, et al. (2005) was used as a reference.

A cut in magnitude is applied at $I_\mathrm{E} \leq 24.5$ in the VIS I_E band. This cut removes faint galaxies, most of them at high redshift, and for which the photometric redshift quality is the most likely to be poor. This sample covers one octant of the sky between right ascension $145° \leq \mathrm{RA} < 235°$ and declination $0° < \delta < 90°$ for a total area of $5157\,\mathrm{deg}^2$. Following Euclid Collaboration: Mellier et al. (2024), the sample is divided into 13 equipopulated redshift bins according to the galaxy photometric redshifts, whose normalized redshift distributions $p_i(z)$ are shown in Fig. 3.6. This division yields a large number of galaxies, with about 34.8 million galaxies per redshift bin. Another redshift binning scheme will be used in Sect. 4.4.5 as a comparison to this one, with 13 equidistant bins of width $\Delta z = 0.177$ and for which Fig. 3.7 shows the associated normalized $p_i(z)$. The galaxy surface density $\bar{n}$ of the selected sample is 24.3 galaxies per arcmin^2. With the equipopulated redshift binning scheme, this leads to a constant surface density per bin of about $\bar{n}_i = 1.87$ galaxies per arcmin^2 in each redshift bin. With the equidistant redshift bins, the density increases from 2.74 galaxies per arcmin^2 in the first bin to 4.08 in the third one and decreases to 0.16 in the last bin. Despite its significantly smaller surface density, the last bin still counts almost 2.9×10^6 galaxies. The effective redshifts and surface densities per bin are grouped in Table 3.1, with the effective redshift of bin i is defined as:

$$z_{\mathrm{eff,i}} = \int_0^3 \mathrm{d}z\, z\, p_i(z)\,, \tag{3.9}$$

where $p_i(z)$ is the normalized distribution of photometric redshifts shown in Fig. 3.6 or Fig. 3.7. For each redshift bin, one can define its effective volume from the comoving volume V_0 and non-linear power spectrum P_nl as :

$$V_\mathrm{eff} = V_0 \left[\frac{\bar{n}_i\, P_\mathrm{nl}(k_\mathrm{BAO}, z_\mathrm{eff})}{1 + \bar{n}_i\, P_\mathrm{nl}(k_\mathrm{BAO}, z_\mathrm{eff})} \right]^2 \tag{3.10}$$

where $V_0 = 4\pi\, f_\mathrm{sky}/3\, \left(r(z_\mathrm{max})^3 - r(z_\mathrm{min})^3\right)$ with r the comoving distance and $z_\mathrm{min,max}$ the limits of the redshift bin. The wavemode associated with the BAO scale is computed as $k_\mathrm{BAO} = 2\pi / r_{\mathrm{s,drag,fid}} = 0.0427\,\mathrm{Mpc}^{-1}$. The effective volume gives an idea of the amount of information contained in a given redshift bin i.e. a larger effective volume entails a larger constraining power, in theory. In the case of the equipopulated binning, the constant number density associated with larger and larger effective volumes when redshift increase should lead to a significant increase in constraining power when comparing first and last redshift bins. This is the general trend observed in the results

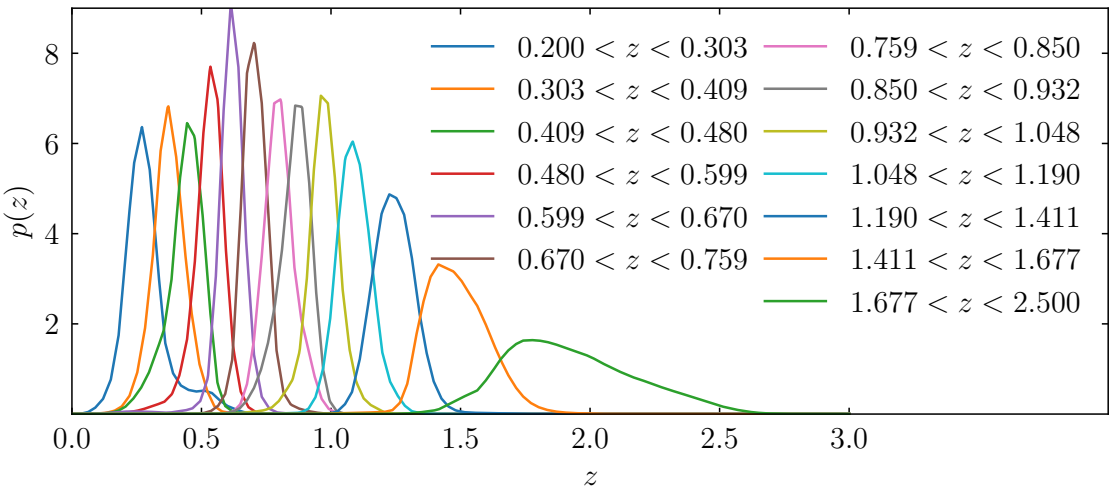


Figure 3.6. – Normalised redshift distributions of galaxies in Flagship 2.1.10. The sample is divided into 13 equipopulated photometric redshift bins.

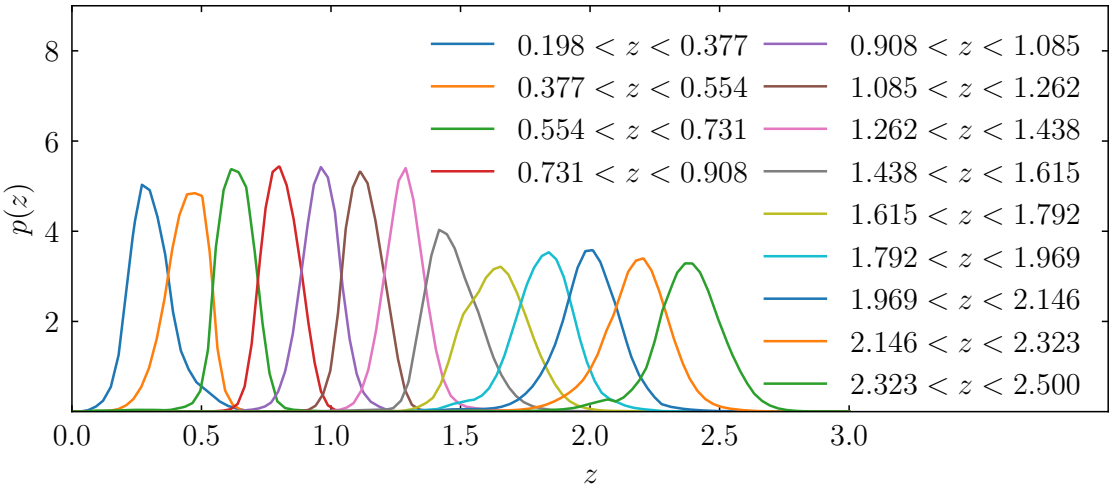


Figure 3.7. – Normalised redshift distributions of galaxies in Flagship 2.1.10. The sample is divided into 13 equidistant photometric redshift bins.

of Table 4.4 obtained with a synthetic data vector. However, as one can see in Table 4.2 obtained with the measured data vector, there is a degradation of the constraints in the last redshift bins which is actually explained by the fact that the quality of the data degrades at high redshift. In particular, photometric redshifts have larger scatter with respect to the true redshift in the last two bins.

The photometric redshifts from the Flagship mock galaxy catalogue used in this work are defined as the first mode of the probability density functions (PDF) obtained with the k-nearest neighbours algorithm `NNPZ` (Tanaka et al., 2018) by matching galaxy magnitudes and colours to a reference sample of 2 million galaxies simulated up to the depth of the *Euclid* calibration field $I_E = 29.4$ and whose PDF are obtained using the template-fitting code `Phosphoros` (Euclid Collaboration: Tucci et al., 2025). The

Table 3.1. – Statistics of the 13 redshift bins for the Flagship 2.1.10 galaxy mock catalogue with two different redshift binning schemes, given the selection of $I_E \leq 24.5$ and `phz_flags = 0`. The "1" subscript stands for the equipopulated scheme while "2" stands for the equidistant one. The effective redshift is defined in Eq. (3.9), $\bar{n}_i$ is the galaxy surface density of bin i in galaxies per arcmin^2 and $V_{\rm eff}$, the effective volume in Gpc^3 is defined in Eq. (3.10). The difference of 0.002 in $z_{\rm min,1/2}$ is caused by the quantile-based discretization function used to compute the limits of the equipopulated bins, there are actually no galaxy of $z < 0.2$ in the sample.

Bin	$z_{\rm min,1}$	$z_{\rm max,1}$	$z_{\rm eff,1}$	$\bar{n}_{i,1}$	$V_{\rm eff,1}$	$z_{\rm min,2}$	$z_{\rm max,2}$	$z_{\rm eff,2}$	$\bar{n}_{i,2}$	$V_{\rm eff,2}$
1	0.200	0.303	0.290	1.876	0.7	0.198	0.377	0.311	2.737	1.6
2	0.303	0.409	0.374	1.874	1.3	0.377	0.554	0.442	3.974	3.2
3	0.409	0.480	0.436	1.875	1.2	0.554	0.731	0.630	4.077	5.0
4	0.480	0.599	0.527	1.871	2.7	0.731	0.908	0.806	3.547	6.6
5	0.599	0.670	0.613	1.874	2.0	0.908	1.085	0.961	2.910	8.0
6	0.670	0.759	0.705	1.874	2.9	1.085	1.262	1.126	2.117	9.1
7	0.759	0.850	0.802	1.873	3.3	1.262	1.438	1.286	1.453	10.0
8	0.850	0.932	0.858	1.874	3.4	1.438	1.615	1.474	1.292	10.6
9	0.932	1.048	0.972	1.874	5.2	1.615	1.792	1.641	0.894	11.0
10	1.048	1.190	1.090	1.874	7.1	1.792	1.969	1.820	0.496	11.4
11	1.190	1.411	1.245	1.873	12.1	1.969	2.146	1.993	0.446	11.6
12	1.411	1.677	1.488	1.874	16.0	2.146	2.323	2.174	0.275	11.7
13	1.677	2.500	1.922	1.874	53.5	2.323	2.500	2.365	0.156	11.7

photometric redshift PDF of each galaxy is computed as a weighted average of the PDF of the neighbours found by `NNPZ`, the weight being the inverse of the χ^2 distance computed between the photometry of each galaxy and its neighbours. The constraint `phz_flags = 0` ensures that the galaxy had enough neighbours found to properly derive the photo-z when `NNPZ` was applied. The quality of these photo-z is optimistic because the computation assumes that the exquisite photometry from LSST is available for all galaxies. In practice, this will not be true for all galaxies or some band might be missing, especially in the beginning of the *Euclid* survey, leading to a degraded photo-z estimate. The redshift distributions $p(z)$ are computed by binning these first mode photometric redshifts against the observed redshift `observed_redshift_gal` in the Flagship galaxy mock catalogue, defined as the redshift observed with a S/N which is infinite. The observed redshift differs from the true redshift from the simulation by including the contribution from the peculiar velocity of the galaxy.

3.4. Measurements of the two-point correlation function

In this section, the methodology and code used to obtain the two-point correlation are described before showing the measurement themselves for the equipopulated and equidistant redshift binning schemes. We also study the effect of the photometric redshift definition (first mode or median of the PDF), the effect of the angular resolution of the catalogue of random points, the effect of one approximation of the `TreeCorr` code used, the effect of the number of jackknife samples used to estimate errors and the effect of the ratio between the numbers of random points and galaxies.

3.4.1. Two-point angular correlation function with the equipopulated binning

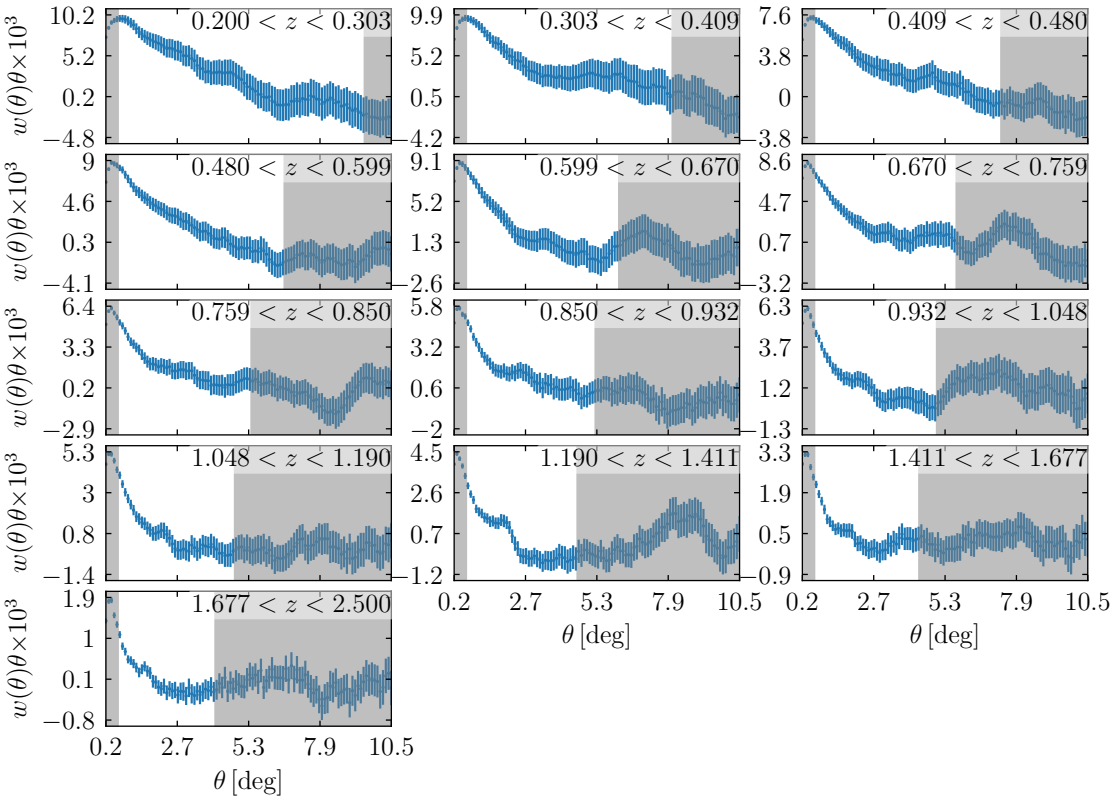


Figure 3.8. – Two-point angular correlation function measured on the Flagship simulation in 13 equipopulated redshift bins. The errors come from the jackknife covariance presented in Sect. 3.5. Scale cuts of the BAO analysis are shown as grey bands and are defined as $\theta_{\rm min} = 0.6°$, $\theta_{\rm max} = \theta_{\rm BAO} + 2.5°$

In Fig. 3.8, we show the measurement of $w(\theta)$ in the thirteen redshift bins in blue. The grey areas represent the scale cuts used for the baseline analysis of the BAO

further described in Sect. 4.4.4. The error bars represented are computed from a jackknife resampling of $N_{\rm jack} = 500$ patches. We can see that the position of the BAO peak is found at larger angles as redshift decreases, varying from 1.6° in the last one to 7° in the first redshift bin. At high redshift, the peak is the most visible and well defined and as it shifts to larger scales at low redshift, following the expansion of the Universe, it becomes smeared and wide under the effect of gravitation, which is a non linear evolution of the large scale structures. Large scales also show some large statistical fluctuations of the signal, which are typically discarded with scale cuts. These fluctuations are however exaggerated by the representation in $w(\theta) \times \theta$ usually chosen to better highlight the BAO peak than with $w(\theta)$. The jackknife error ranges from about $\sigma(w) = 9.5 \times 10^{-4}$ to 2.0×10^{-4} between $\theta = 0.12°$ and 10.5° in the first of the equipopulated redshift bins down to $\sigma(w) = 3.5 \times 10^{-4}$ to 0.4×10^{-4} in the last bin.

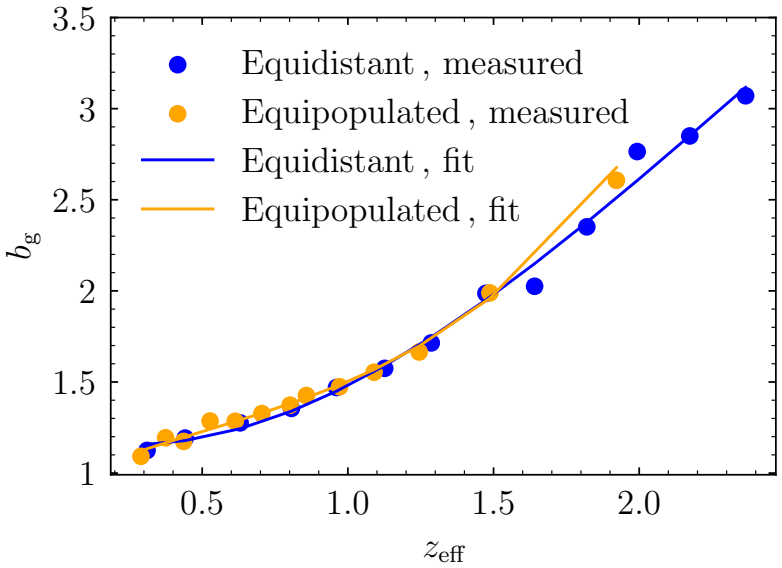


Figure 3.9. – Galaxy bias measured with equidistant and equipopulated redshift bins on Flagship 2.1 between 0.5 and 4.0°with the associated polynomial fits.

A fit of the linear galaxy bias $b(z)$ is performed in each redshift bin with the residuals $w(\theta) - b^2 w_{\rm fid,b=1}(\theta)$ and the jackknife covariance, where $w_{\rm fid,b=1}$ denotes the theoretical angular correlation function of matter defined in Eq. (3.2) computed with the Flagship cosmology and a galaxy bias $b = 1$. We use scales between 0.5° and 4° in this full shape fit. A third order polynomial is then fitted to the result :

$$b(z) = b_3 z^3 + b_2 z^2 + b_1 z + b_0\,, \tag{3.11}$$

which is then used in Eq. (3.5) to compute the theoretical model of the two-point angular correlation function. We report the estimate of the linear galaxy bias, shown in orange in Fig. 3.9 with the best fit obtained for $b_3 = 0.268$, $b_2 = -0.409$, $b_1 = 0.694$, and $b_0 = 0.949$ as the coefficients of Eq. (3.11) for the equipopulated bins. It is then used to compute the theoretical model of $w(\theta)$ in Eq. (3.5).

The full measurement is shown in Fig. 3.10, including the 78 cross-correlations of the 13 redshift bins. As expected from the theory in Eq.(3.3), we find that the amplitude of cross-correlations decreases when the difference in redshift of the bins increases. However, cross-correlations with adjacent or next-to-adjacent bins are not negligible with respect to the autocorrelations, which is expected given the large overlap of the redshift distributions visible in Fig. 3.6. The ratios at small scales $\theta < 2°$ are shown in Fig. 3.11. In the first three redshift bins, at $z < 0.48$, the amplitude of the cross-correlation with the adjacent bin is around half of the amplitude of the autocorrelation. This ratio decreases to 25 % at higher redshifts. Cross-correlations with the next-to-adjacent redshift bin are close to 25 % and 10 % of the amplitude of the aucorrelation signal in the first and second redshift bins. Otherwise, the ratio for cross-correlations with more distant redshift bins ranges between 0 and 10 %. When *Euclid* will have gathered enough data, it will be interesting to see if the amplitude of cross-correlations is similar, larger or smaller. Depending on the case, it could be interesting to include adjacent and eventually next-to-adjacent cross-correlations in photometric galaxy clustering analyses, though the high level of correlation will limit the information gain.

3.4.2. Two-point angular correlation function with the equidistant binning

In the case of the equidistant binning scheme, the measurement of Fig. 3.13 shows peaked BAO signals in more redshift bins than with the equipopulated binning scheme because of the associated redshifts are larger. However, the jackknife error bars $\sigma(w(\theta))$ shown in Fig. 3.12 are also smaller in all equidistant redshift bins but the last three of the equipopulated bins, where the number of galaxies is significantly smaller. With the equidistant bins, $\sigma(w(\theta))$ varies between 7.5×10^{-4} and 2×10^{-4} when θ varies between 0° and 10° in the first redshift bin and it decreases to values between 4.5×10^{-4} and 1×10^{-4} at $z_{\rm eff} = 0.806$. Beyond this redshift, $\sigma(w(\theta))$ stagnates at similar values. With the equipopulated redshift bins, $\sigma(w(\theta))$ is 1.2 times as large as with the equidistant redshift bins in the first redshift bin when averaging over θ but this factor increases to 1.7 in the redshift bins 2 to 10 and then decreases down to 0.7 in the last bin. This will be useful to understand the constraining power of the two redshift binning schemes studied in Sect. 4.1.

We report the estimate of the linear galaxy bias with the equidistant binning, shown in blue in Fig. 3.9 with the best fit obtained for $b_3 = -0.106$, $b_2 = 0.747$, $b_1 = -0.362$, and $b_0 = 1.202$ as the coefficients of Eq. (3.11), used to compute the fiducial $w_{\rm fid}(\theta)$ that will be injected in the template of Eq. (4.1). The galaxy bias estimate is very similar to the equipopulated binning result, as expected.

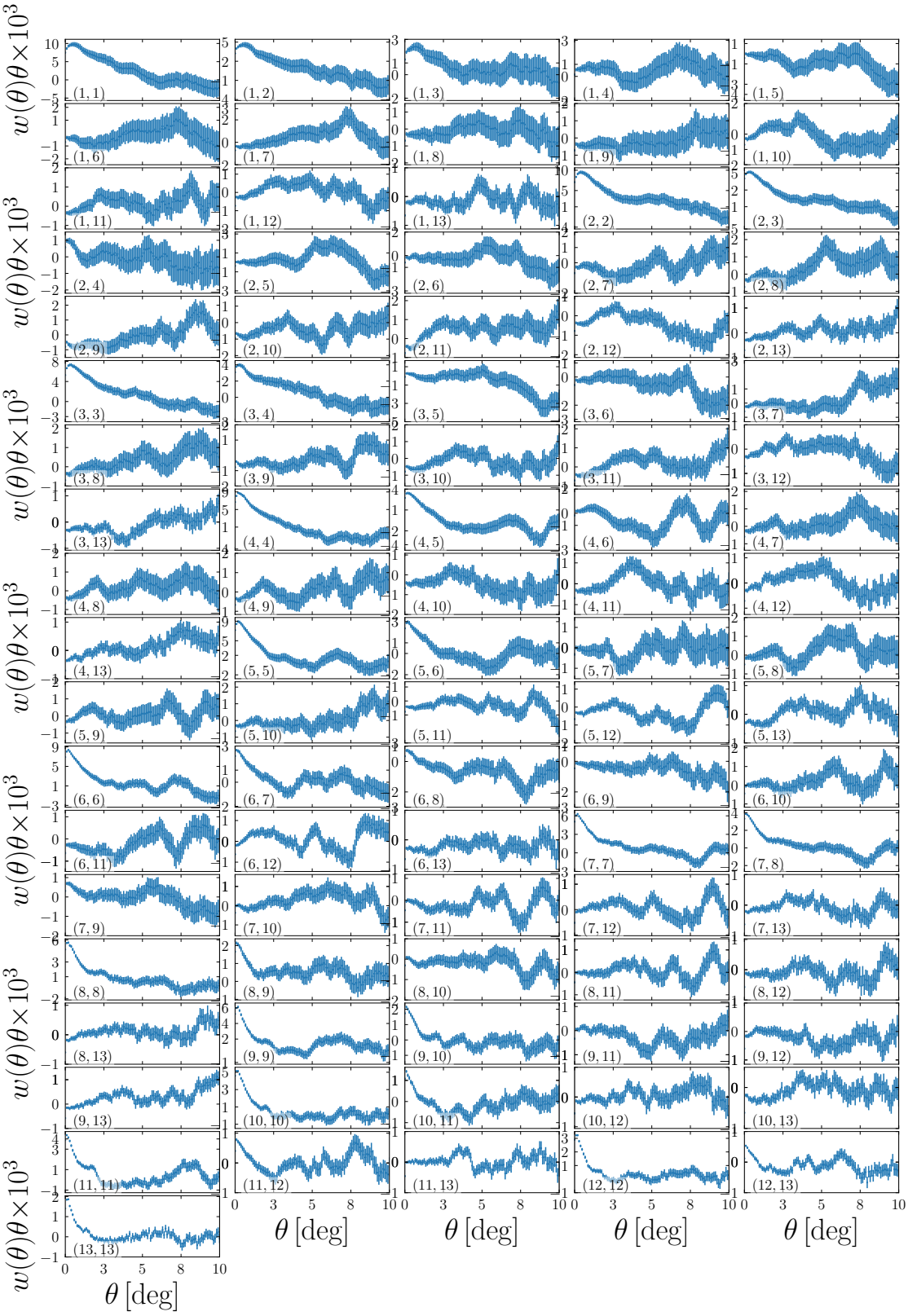


Figure 3.10. – Two-point angular correlation function measured on the Flagship simulation in 13 equipopulated redshift bins with their 78 cross-correlations. In each panel, the two redshift bins involved in the autocorrelation or cross-correlation are indicated by their respective indices (i,j). The errors come from the analytical covariance presented in Sect. 3.5.

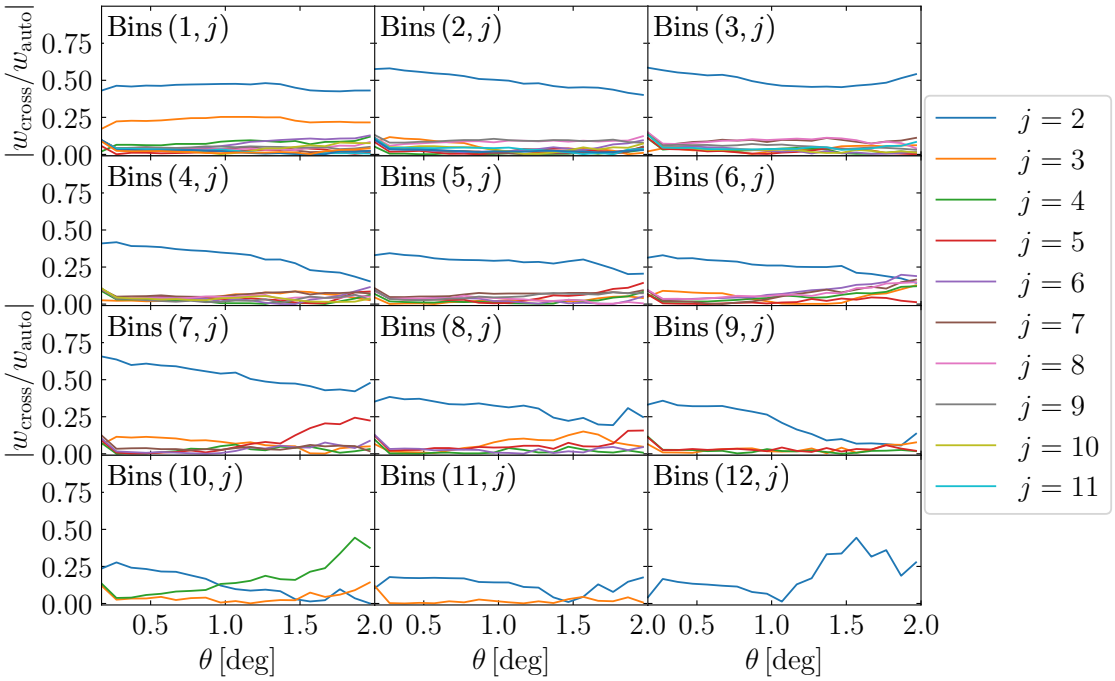


Figure 3.11. – For each redshift bin i, ratios of the associated cross-correlations (i,j) with bin j with respect to the autocorrelation (i,i) at small scales $\theta < 2°$.

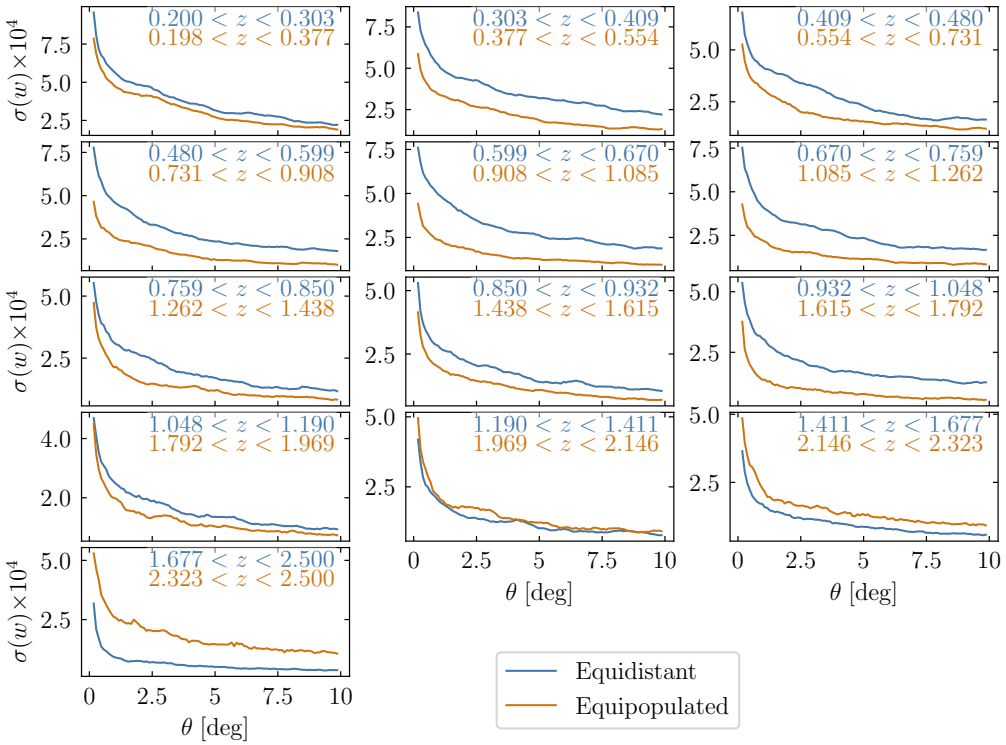


Figure 3.12. – Two-point angular correlation function jackknife error measured on the Flagship simulation in 13 equidistant and equipopulated redshift bins.

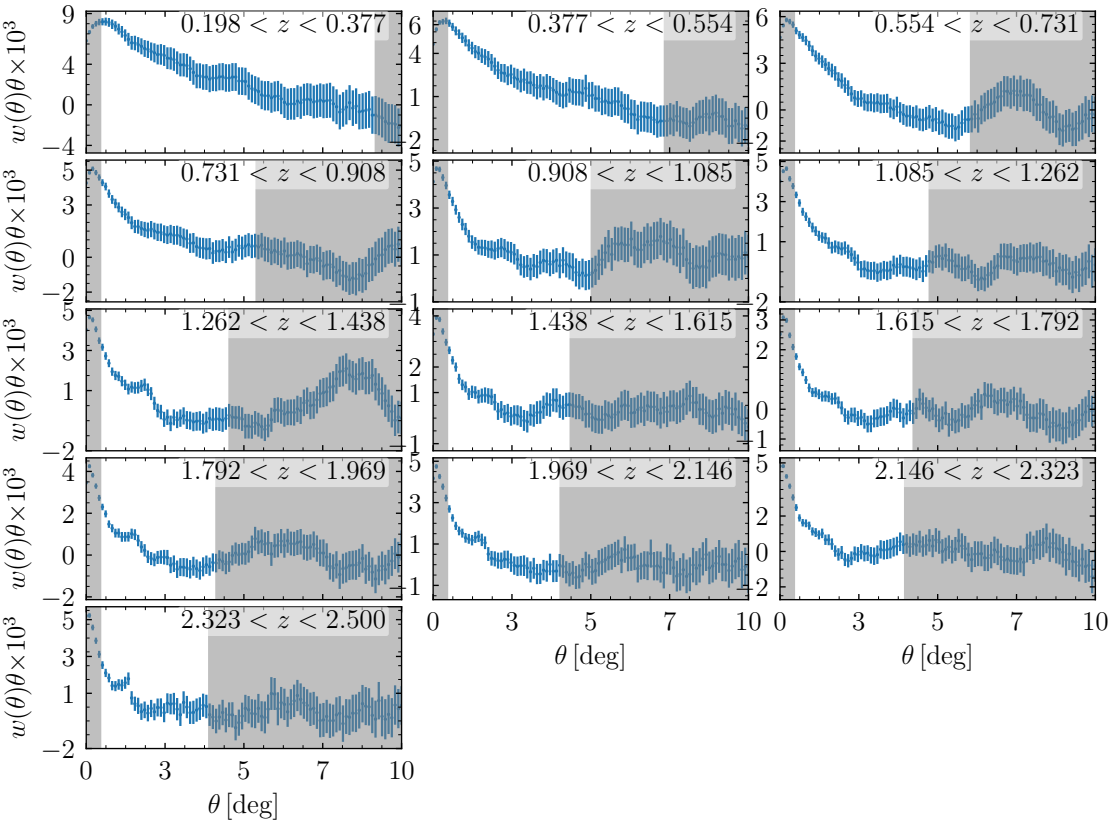


Figure 3.13. – Two-point angular correlation function measured on the Flagship simulation in 13 equidistant redshift bins. Scale cuts of the BAO analysis are shown as grey bands and are defined as $\theta_{\rm min} = 0.6°$, $\theta_{\rm max} = \theta_{\rm BAO} + 2.5°$. The errors come from the jackknife covariance presented in Sect. 3.5.

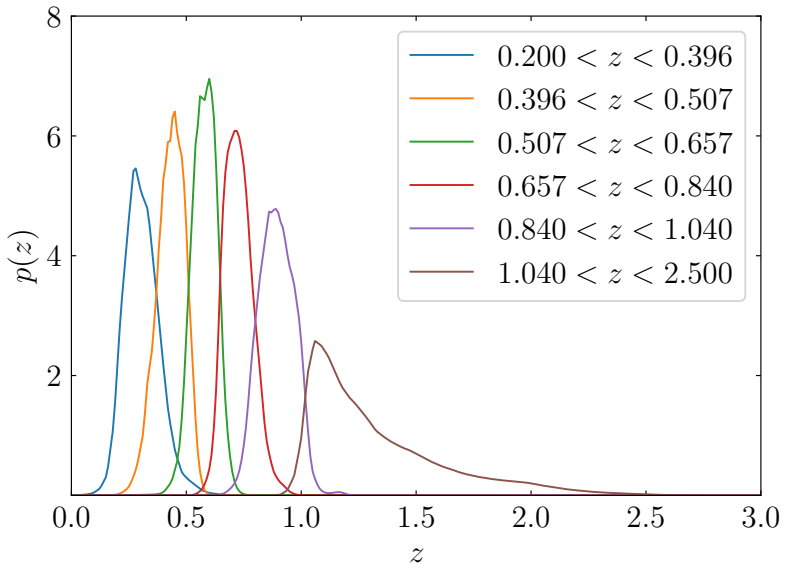


Figure 3.14. – Normalised redshift distributions of galaxies in Flagship 2.1.10. The sample is divided into 6 equipopulated photometric redshift bins.

3.4.3. Two-point angular correlation function with a DR1 setting

We also consider a DR1-like setting, using 6 redshift bins instead of 13 and a brighter magnitude cut at $I_E \leq 23.5$. The redshift distribution is shown in Fig. 3.14. Each redshift bin counts about 10.8×10^6 galaxies. We provide the measurement of $w(\theta)$, shown in Fig. 3.15 in blue, with the associated errors from the jackknife covariance and the same scale cuts as grey areas. Apart from bins 3 and 6 where the BAO signal appears more clearly, the statistical fluctuations of $w(\theta)$ tend to hide its peak. With this sample, the galaxy bias fit, obtained with the same method as before, yields the following parameters for Eq. (3.11) : $b_3 = -0.556$, $b_2 = 1.546$, $b_1 = -0.606$, and $b_0 = 1.22$.

3.4.4. Effect of the photometric redshift choice

In this section, we show the effect of using different definitions of the photo-z. Indeed, within the Photometric Galaxy Clustering Work Package (GCph WP), part of the Galaxy Clustering Science Working Group (GC SWG) in the *Euclid* collaboration, the choice made is to use the first mode of the photo-z PDF. However, the Flaghip galaxy mock catalogue provides also the median photo-z computed from the same PDF. Figure 3.16 illustrates the effect of using the median or the first mode in a DR1-like setting where the survey area is limited to 2500 deg^2 and a stricter quality cut is done at a brighter magnitude of $I_E \leq 22.25$ in the VIS I_E band. With the different photo-z, the limits of the redshift bins vary by no more than 0.001. However, we find that there is more power at small scales with the median photo-z in bins 0, 2, 4, and 5 and less in bins 1 and 3. The difference in $w(\theta)$ normalized to its error is shown in

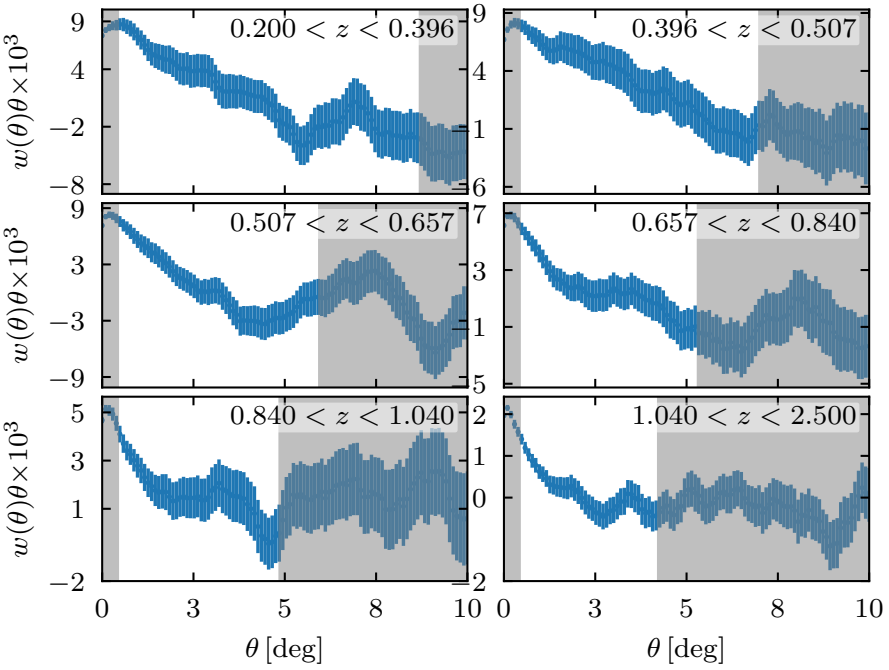


Figure 3.15. – Two-point angular correlation function measured on the Flagship simulation in 6 equipopulated redshift bins with $I_E \leq 23.5$.

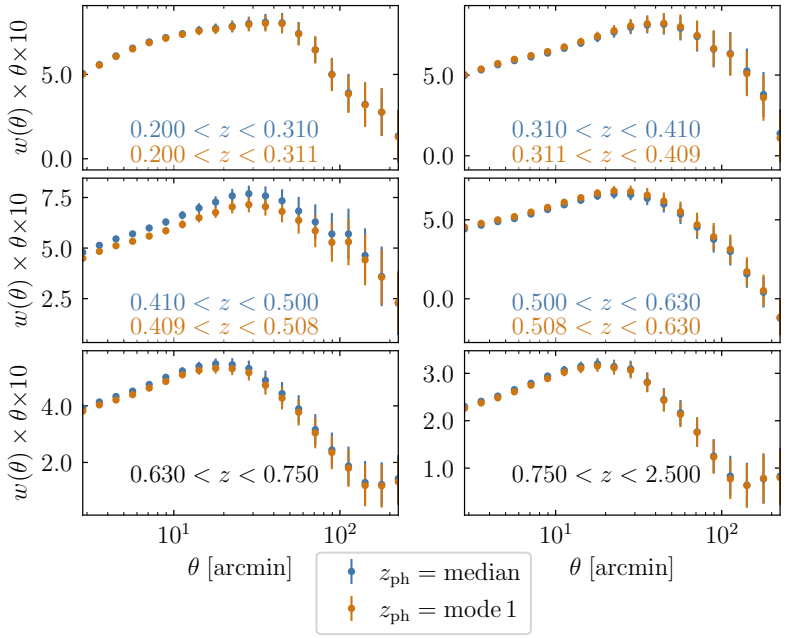


Figure 3.16. – Two-point angular correlation function measured on the 2500 deg^2 of the Flagship simulation in 6 equipopulated redshift bins with a DR1-like setting where the sample selection is done with $I_E \leq 22.25$.

Fig. 3.17. The effect reaches up to $3.5\,\sigma(w_{\rm median})$ in bin 3 and at $\theta = 2.5'$.

The Flaghip galaxy mock catalogue also provides a different point-estimate computed with the DeepZ machine learning algorithm instead of the photo-z first mode computed with NNPZ. The associated $w(\theta)$ measurement is shown in Fig. 3.18. As the DeepZ photo-z were available earlier than the other ones, the measurement was performed before and with slightly different settings than in the baseline analysis. Here, we divided the sample into 12 equidistant redshift bins between $z = 0.2$ and $z = 2.36$ with a cut at a magnitude of $I_{\rm E} \leq 24.5$ in the VIS $I_{\rm E}$ band. In this case, we find even larger shifts than when comparing median and first mode, up to $4\,\sigma$ at small angular separations in the bin $1.280 < z < 1.460$. This is not negligible, which is why the measurement was updated once the photo-z from the official OU-PHZ pipeline with NNPZ were made available.

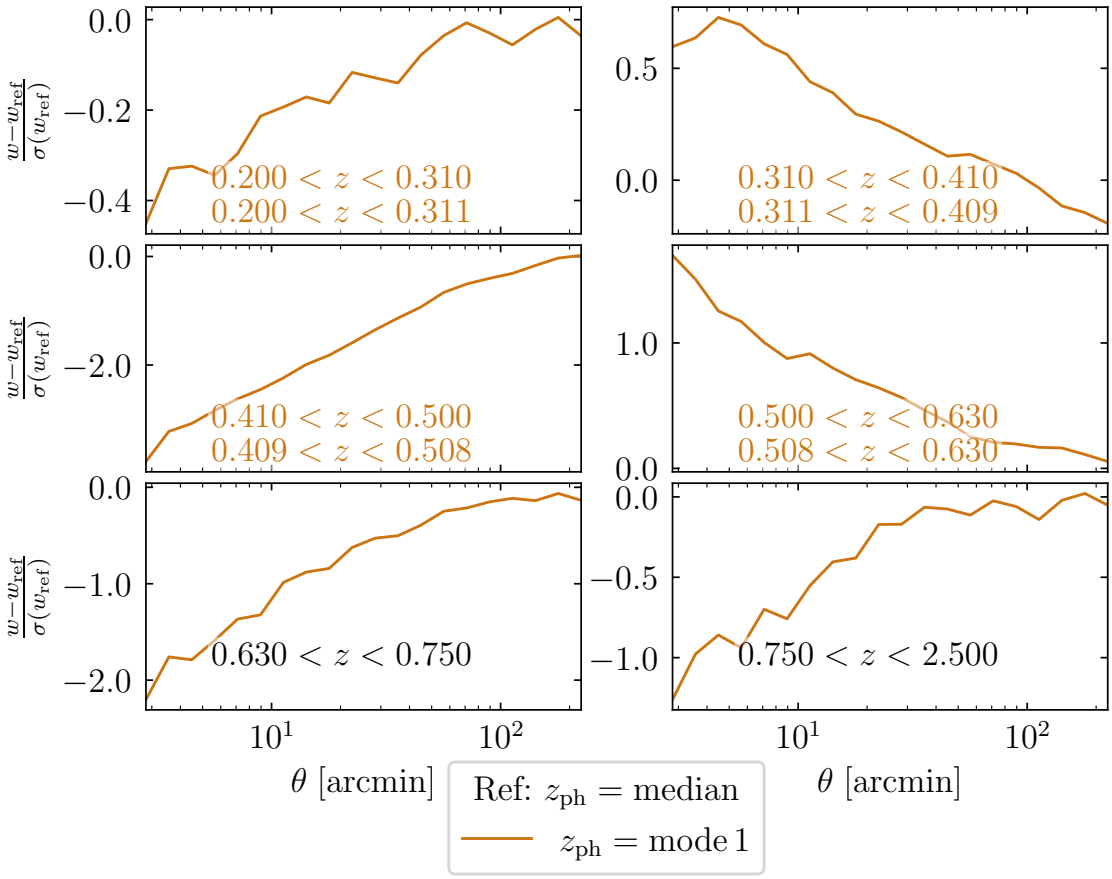


Figure 3.17. – Shift of $w(\theta)$ measured with the first mode photo-z with respect to the reference $w(\theta)$ measured with the median photo-z (subscript "ref" in the labels) in the same setting as Fig. 3.16.

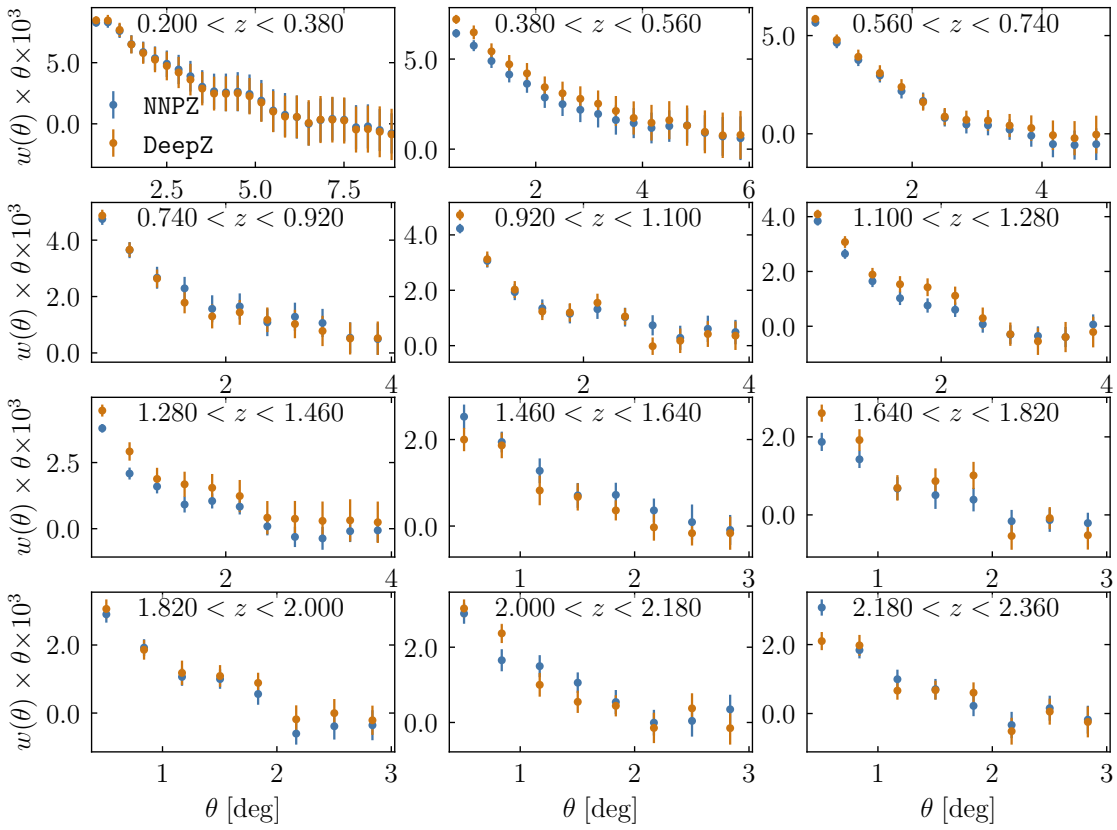


Figure 3.18. – Two-point angular correlation function measured with photo-z either computed with `NNPZ` or `DeepZ` on the full Flagship simulation in 12 equidistant redshift bins between $z = 0.2$ and $z = 2.36$ with a cut at a magnitude of $I_E \leq 24.5$ in the VIS I_E band. The errors come from a jackknife resampling of 60 patches.

3.4.5. Effect of the random sample angular resolution $N_{\rm side}$

The angular resolution used to build the random sample is important to match the mask of a survey with its eventual holes or other geometrical features. A mismatch between the resolution of the angular mask and the features of the survey will lead to variations of the clustering amplitude. To this effect, we use the DES Year 1 data for which we compute a new set of random samples with various angular resolutions called $N_{\rm side}$ in the HealPix system. Indeed, this survey presents a non uniform mask ideal for this test, unlike the Flagship simulation which is an octant of the sky and presents no specific geometrical feature nor masking. In Fig. 3.19 is depicted the influence of $N_{\rm side}$ on $w(\theta)$. We find that in this case, increasing $N_{\rm side}$ from 4096 to 8192

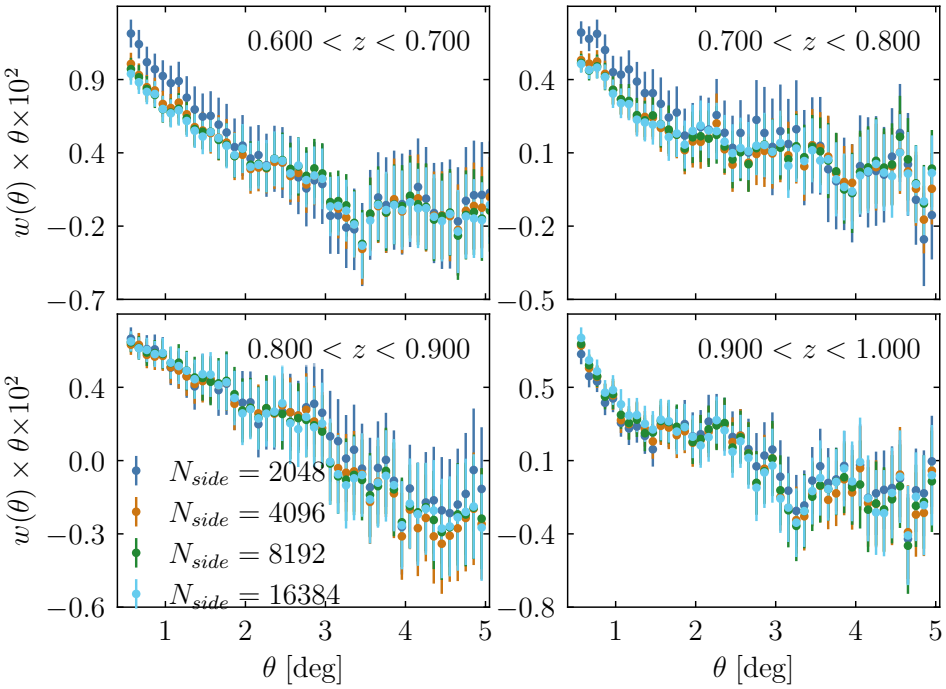


Figure 3.19. – Influence of the angular resolution of the HealPix mask $N_{\rm side}$ used to compute the catalogue of random points. For the DES photometric survey, as there are many fine structures or holes in the survey footprint, values of 2048 or 4096 are not high enough to reach a convergence of $w(\theta)$.

(from an angular resolution of 0.014°to 0.007°) changes $w(\theta)$ moderately, compared to the variation from 2048 to 4096. Averaged over all redshift bins and angular scales, the differences in $w(\theta)$ with respect to $N_{\rm side} = 16384$ amount to 0.5σ, 0.2σ, and 0.1σ for $N_{\rm side}$ varying between 2048, 4096 and 8192 respectively. If we consider the maximum difference with respect to $N_{\rm side} = 16384$ instead of the average, we find that with $N_{\rm side} = 2048$, differences as large as 6σ can be seen between $w(\theta)$. In the case of DES, $N_{\rm side} = 4096$ still yields shifts larger than 1σ at small scales $\theta < 0.5°$ in three redshift bins out of four while $N_{\rm side} = 8192$ shifts don't exceed 0.5σ. For this reason, using

at least $N_{\rm side} = 8192$ seems necessary. Apart from the amplitude of the clustering itself, the jackknife errors are also affected by $N_{\rm side}$, with variations with respect to $N_{\rm side} = 16384$ which are smaller than 50%, 20%, and 10% with $N_{\rm side} = 2048$, 4096 and 8192 respectively.

However, in the context of the Flagship simulation, since it covers one octant with a regular footprint and without any specific angular feature, we chose a smaller value of $N_{\rm side} = 4096$ which is sufficient to allow the $w(\theta)$ measurements to converge as shown in Fig. 3.20, with variations which do not exceed $0.15\,\sigma$ at most between $N_{\rm side} = 4096$ and $N_{\rm side} = 8192$.

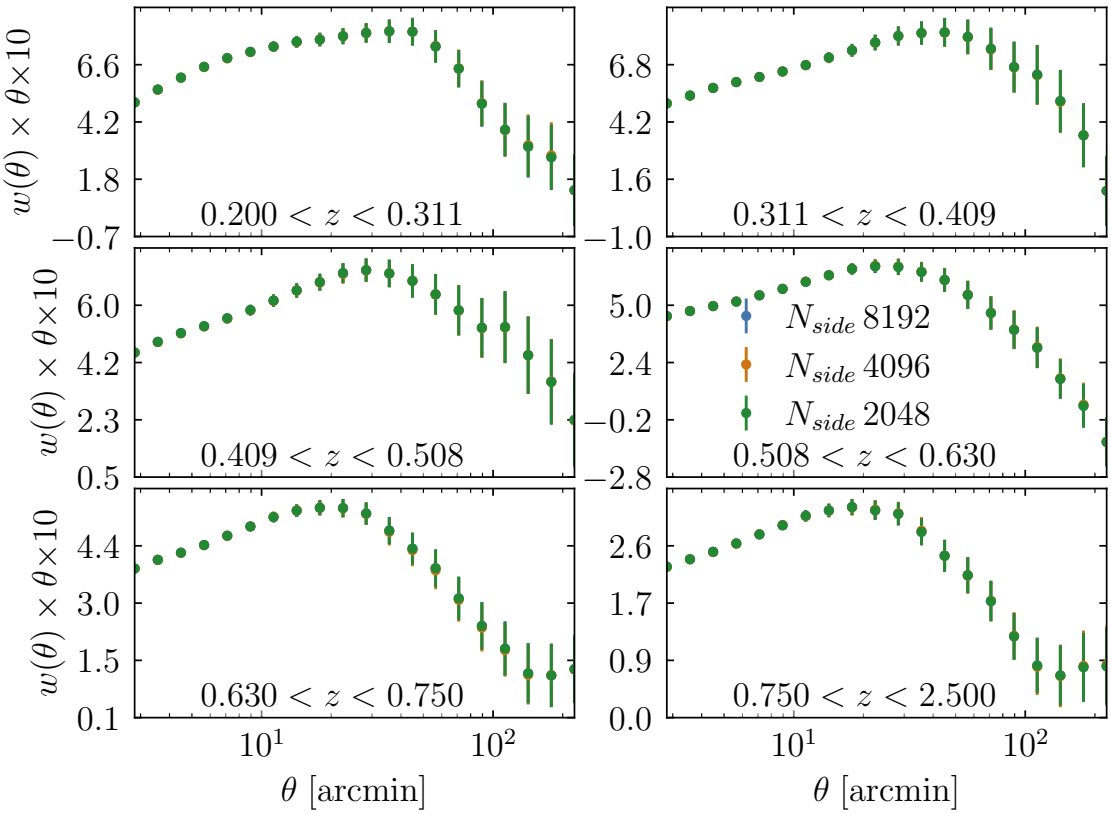


Figure 3.20. – Influence of the angular resolution of the HealPix mask $N_{\rm side}$ used to compute the catalogue of random points. For the Flagship simulation, since there are no simulated effect of completeness like missing of masked observations, stripes or other artificial clustering effects, $N_{\rm side} = 4096$ seems to be a high enough value to reach a convergence of $w(\theta)$.

3.4.6. The `TreeCorr` *bin_slop* approximation

The *bin_slop* parameter ($b_{\rm s}$ from now on) defined in `TreeCorr` and introduced in M. Jarvis et al., 2004 is the fraction of an angular bin width by which it is accepted to

let the pairs miss the correct bin, the pairs being either galaxy-galaxy, galaxy-random point, or random point-random point. This can otherwise be seen as adding a slope to the angular bin edge, making each bin trapezoidal rather than rectangular. If $b_s = 0.01$ with bins of width 0.1°, it means that pairs can be misplaced if they are within $\pm 0.001°$ around the edge of the bin.The b_s parameter enables faster computations of $w(\theta)$, with an important speed-up, which will be quantified later in this section. Indeed, this allows the KD-tree to be stopped at an earlier stage, without having to continue splitting cells into smaller cells. Statistically, as many pairs should fall on each side of the angular bin edge and so, with a sufficient enough number of pairs, this approximation is supposed to be negligible. However, this depends on the definition of how close a pair is from the edge of the bin. The larger the slope is, the bigger the approximation is and the faster the computation will be. However, there is a limit to what is reasonable depending on the application of the result. The following definition of the default maximum acceptable value of b_s, $b_{s,max}$ is used in `TreeCorr` under the name max_good_slop:

$$b_{s,max} = \min\left(1, \frac{0.1\ (\theta_{min} + 0.5\,\Delta\theta)}{\Delta\theta}\right), \tag{3.12}$$

where θ_{min} is the minimum angular separation considered and $\Delta\theta$ is the width of the angular bin. This definition yields a maximum recommended value of $b_{s,max} = 0.17$ for $\theta_{min} = 0.12°$ and $\Delta\theta = 0.1°$. However, two changes in how b_s is handled with a linear angular binning were introduced in version 4.3.3 of `TreeCorr`, leading to a measurement of $w(\theta)$ which is so noisy that the signal cannot be recognized if the same value of $b_s = 1$ is used. As a matter of fact, even with $b_s = 0.05$, the measurement is still incorrect, which explains why measurements made after this update have been done with $b_s = 0.01$. The first change is the removal of a factor θ_{max} between the input value of b_s and the value used internally, where θ_{max} is the maximum angular separation, following a change of the definition of b_s for the linear binning case. The second change is the introduction of a bug: b_s no longer took into account the unit of the angular separation. As a consequence, there was a ratio $\pi/180$ between the value of b_s given in input and the value used internally. With these two changes, there is a ratio $b_{s,4.3.3}/b_{s,4.3.2} = 180\,\theta_{max}/\pi$ between the values used internally, for the same input. The bug was fixed in version 5.0.2 of the `TreeCorr`, leading to the ratios $b_{s,5.0.2}/b_{s,4.3.3} = \pi/180$ and $b_{s,5.0.2}/b_{s,4.3.2} = \theta_{max}$ between the values used internally.

In Fig. 3.21, following the recommendation of the `TreeCorr` code documentation to decrease b_s to check if $w(\theta)$ is changed, we see that with version 4.3.2, using $b_s = 1$ doesn't seem to be an issue, apart from the first angular bin at small scales. If the application includes small scales then it is necessary to use a lower value of b_s. Given that this was not initially the case, the rest of the measurement was performed with $b_s = 1$ given the large speed increase enabled by this value of b_s. However, with version 4.3.3, we made a new measurement of $w(\theta)$ for the BAO analysis with a thinner angular binning $\Delta\theta = 0.1°$ and including scales up to $\theta_{max} = 10.5°$, previously shown in Fig. 3.8 and now shown in blue in Fig. 3.22, the orange $w(\theta)$ being measured with version 4.3.2,

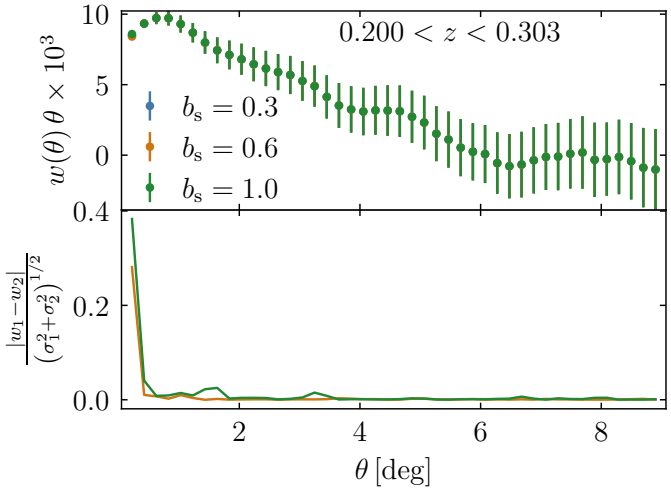


Figure 3.21. – Comparison of $w(\theta)$ measured in the first redshift bin of the Flagship simulation with $b_s \in [0.3, 0.6, 1.0]$. Apart from the first angular bin, the difference between all values is negligible.

$b_s = 1$, $\Delta\theta = 0.2°$, and $\theta_{max} = 4°$. We find that the different definition of b_s between versions 4.3.2 and 4.3.3 of `TreeCorr` can change the measurement quite significantly. The measurement in blue (version 4.3.3) used a much smaller value of $b_s = 0.01$, needed following the introduction of the bug, which is inferior to the recommended $b_{s,max}$. We find that the two measurements are in good agreement with shifts that are smaller than $0.5\,\sigma$ at all scales and redshifts up to $z = 0.8$. Beyond this redshift, we find discrepancies which are more frequent and closer to $0.5\,\sigma$. This is expected, given that the previous value of 1 is slightly larger than the $b_{s,max} = 0.68$ which should have been used in this version (corresponding to $b_{s,max} = 0.17$ in the 5.0.2 version). This illustrates the fact that a careful analysis of the effect of b_s is necessary. Because it is intrinsically a statistical effect which depends on the distribution of the data itself, using a value of b_s which is too large could either pass as a small (Fig. 3.21) or important effect (Fig. 3.22, last panel). Moreover, pairs being allowed to fall on either one side or the other at the edge of the angular bin, the statistical nature of the compensation of the effect of b_s when there are many pairs make it dependent on the size of the sample.

The advantage of this approximation resides in the speed-up it allows when we measure $w(\theta)$. We show in blue in Fig. 3.23 the computation time for each of the 13 redshift bins of the equidistant binning þmeasurement. An estimate of this time is shown in orange, adapted from the formula proposed in M. Jarvis et al., 2004 to yield:

$$t_{\text{computation}} = \left(6.5 \times \frac{N_{\text{tot}}}{10^8}\right)^{0.9} \left(\frac{b}{0.1}\right)^{-1.7} N_{\text{threads}}^{-1}, \tag{3.13}$$

where N_{threads} is the number of threads used in parallel, $b = \Delta\theta\, b_s$ and N_{tot} is the total number of objects considered in the computation of the Landy–Szalay estimator

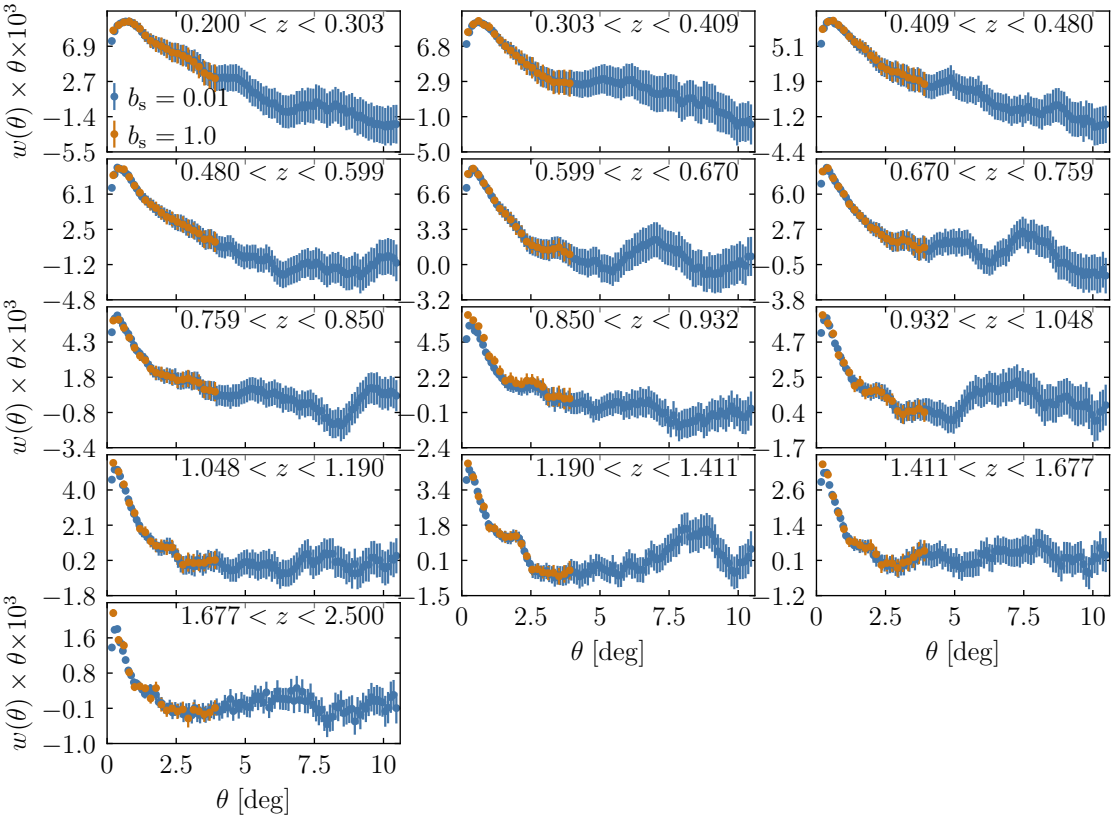


Figure 3.22. – Comparison of the effect of b_s in all redshift bins for $b_s = 1$ (version 4.3.2) and $b_s = 0.01$ (version 4.3.3). We find no significant effect at $z < 0.8$ but more frequent and larger shifts of $w(\theta)$ at $z > 0.8$.

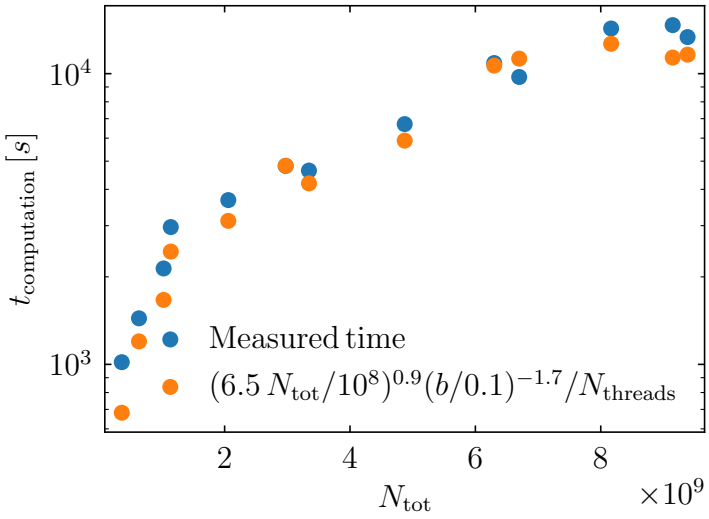


Figure 3.23. – Computation time as a function of the number of galaxies and random points for $w(\theta)$ on the Flagship simulation 13 equidistant bins.

between two samples of $N_{\rm gal,1}$ and $N_{\rm gal,2}$ galaxies with a factor $N_{\rm r}$ times as many random points as galaxies:

$$N_{\rm tot} = \left(N_{\rm gal,1} + N_{\rm gal,2}\right) + \left(N_{\rm gal,1} + N_{\rm gal,2}\, N_{\rm r}\right) + \left(N_{\rm gal,1}\, N_{\rm r} + N_{\rm gal,2}\right) + \left(N_{\rm gal,1}\, N_{\rm r} + N_{\rm gal,2}\, N_{\rm r}\right), \tag{3.14}$$

which becomes $4\,(N_{\rm r}+1)\,N_{\rm gal,1}$ for autocorrelations. The size of the sample used with Flagship with $N_{\rm gal} = 34.8 \times 10^8$ in each of the 13 equipopulated bins makes this scaling in $b^{-1.7}$ is very interesting. Since b is proportional to $b_{\rm s}$, we find that doubling $b_{\rm s}$ divides the computation time by 3.2. Given that the computation of $w(\theta)$ with $b_{\rm s} = 0.01$ (version 4.3.3) takes 2060 CPU-hours for the autocorrelations alone and 32 232 CPU-hours with the cross-correlations, the increase in speed due to this approximation becomes very substantial in terms of resources.

3.4.7. Jackknife resampling, effect of $N_{\rm jack}$

In this section, we check how the jackknife error $\sigma\left(w_{\rm Njack}\right)$ evolves as a function of the number of jackknife patches, varying $N_{\rm jack} \in [30, 60, 90, 210, 500]$. The jackknife errors are derived from the covariance estimated with Eq. (3.15). We represent the relative difference in $\sigma(w(\theta))$ as a function of θ and $N_{\rm jack}$ in Fig. 3.24, taking $N_{\rm jack} = 500$ as a reference. In the first redshift bin, we see that the errors $\sigma\left(w_{90}\right)$ or $\sigma\left(w_{210}\right)$ are consistent with the $\sigma\left(w_{500}\right)$ within 30%, unlike the $\sigma\left(w_{60}\right)$ and $\sigma\left(w_{30}\right)$ which differs by more than 40 % and 70 % at $\theta > 10^\circ$. With less than 200 patches, the error has larger fluctuations and has not converged. However, we find that even when increasing $N_{\rm jack}$ to 210, the measurement still yields larger errors beyond $\theta = 4^\circ$, the difference increasing with separation angles to reach about 20 % at $\theta = 10^\circ$. For this reason, we confirm whether the error has converged at $N_{\rm jack} = 500$ in Fig. 3.25 by comparing $\sigma\left(w_{500}\right)$ with the jackknife error for $N_{\rm jack} = 1000$. We find that in this case, the difference between the errors is about 5 % with a maximum of 10 %. This motivated the use of $N_{\rm jack} = 500$ for the baseline measurements of $w(\theta)$.

3.4.8. Effect of the ratio $N_{\rm rand}/N_{\rm galaxies}$

We evaluate the influence of the number density of the random sample by varying the ratio $N_{\rm r} := N_{\rm rand}/N_{\rm galaxies} \in [10, 20, 30, 40, 50]$. This mainly affects the shot noise of the measurement. This is visible in Fig. 3.26 which describes, for the first redshift bin, the relative difference in $\sigma(w(\theta))$ as a function of θ and $N_{\rm r}$ and where we see that with respect to $N_{\rm r} = 50$, using $N_{\rm r} \in [10, 20, 30, 40]$ increases the shot noise error by 16 %, 5.7 %, 2.3 %, and 0.7 %.

In all cases, the shot noise error stays negligible when compared to the error estimated from jackknife resampling. We check that $N_{\rm r}$ does not affect $w(\theta)$ significantly in Fig. 3.27. The top panel shows $w(\theta)$ with its associated jackknife errors measured with various $N_{\rm r}$ values in the first redshift bin. The bottom panel shows the level of agreement of these different measurements, which barely exceeds $0.3\,\sigma$ and stays within $0.15\,\sigma$ for the majority of $N_{\rm r}$ values and scales.

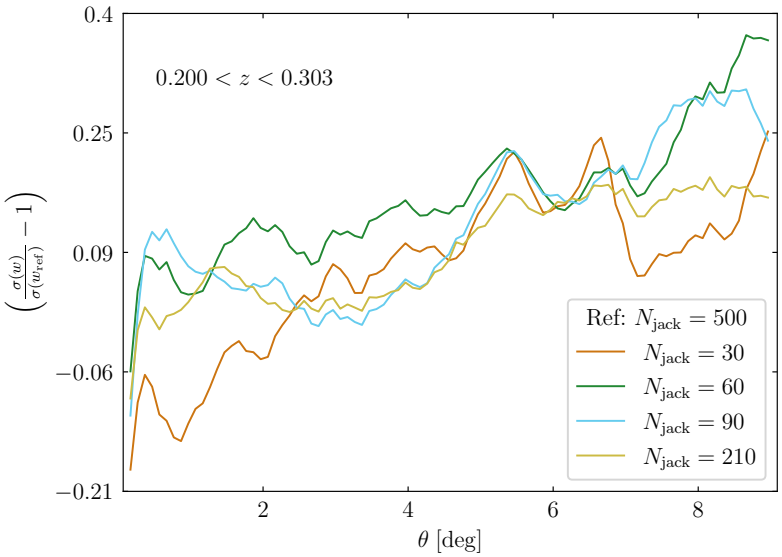


Figure 3.24. – Comparison of the jackknife error measured on the Flagship simulation with a resampling of $w(\theta)$ in $N_{\rm jack} \in [30, 60, 90, 210, 500]$ patches. We find that the variations with respect to $N_{\rm jack} = 500$ reach 20 % at large scales even with $N_{\rm jack} = 210$.

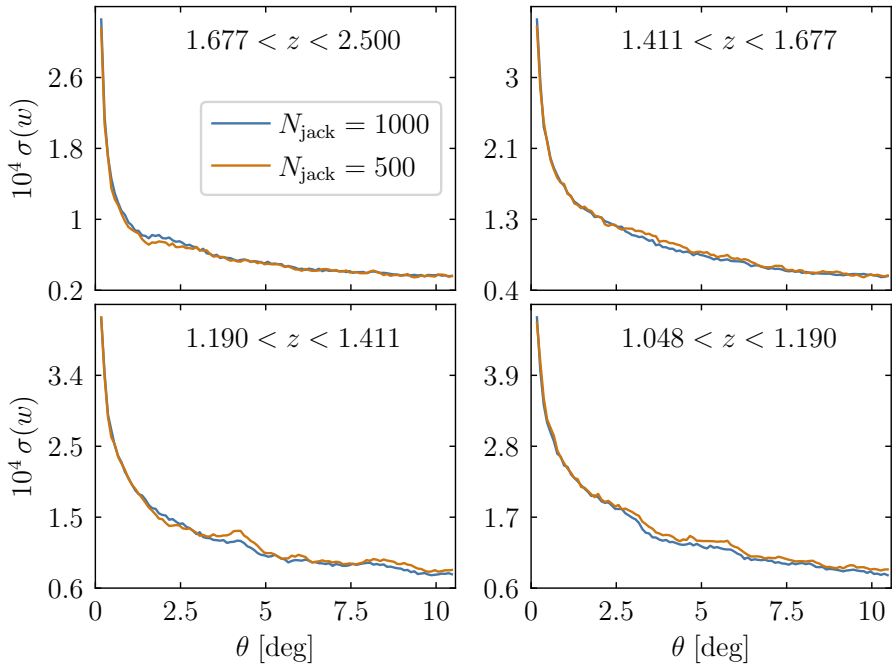


Figure 3.25. – Comparison of the jackknife error measured in the last four redshift bins on the Flagship simulation with a resampling of $w(\theta)$ in 500 or 1000 patches. We find that the variations of $\sigma\,(w_{500})$ with respect to $\sigma\,(w_{1000})$ are smaller than 10 % and close to 5 % on average.

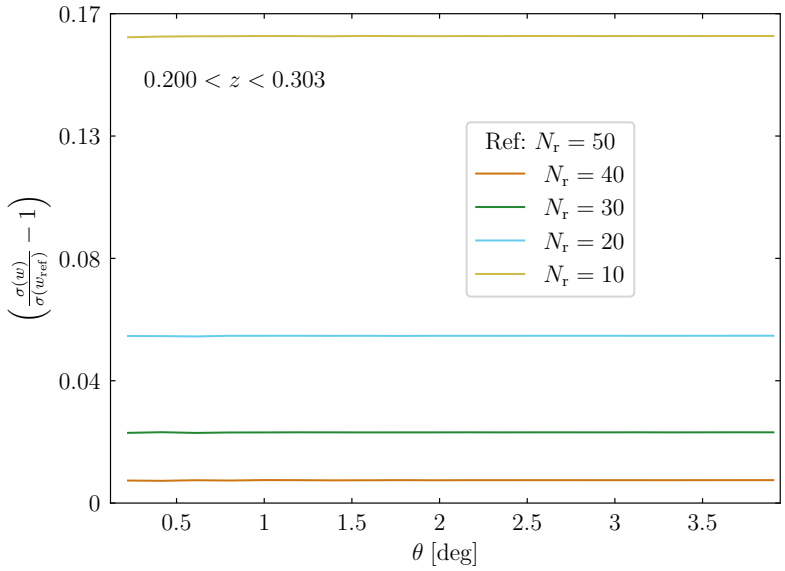


Figure 3.26. – Comparison of the shot noise measured on the Flagship simulation in the first redshift bin for $N_{\rm rand}/N_{\rm galaxies} \in [10, 20, 30, 40, 50]$.

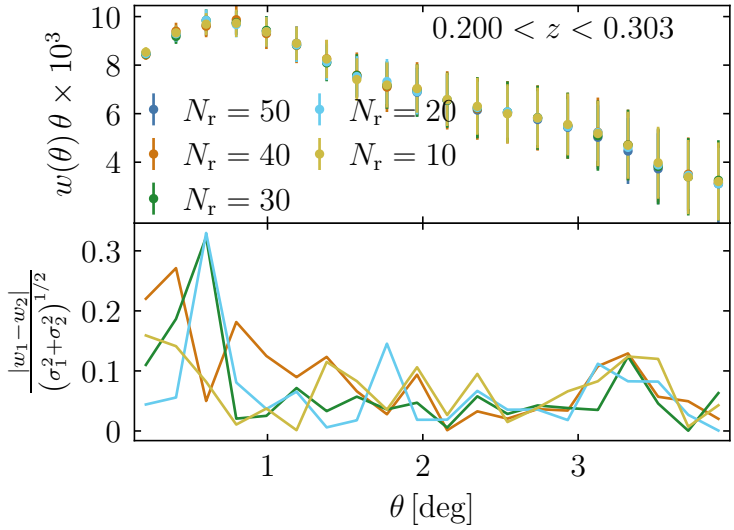


Figure 3.27. – Comparison of $w(\theta)$ measured on the Flagship simulation in the first redshift bin for $N_{\rm rand}/N_{\rm galaxies} \in [10, 20, 30, 40, 50]$.

3.5. Covariances

Two approaches are considered to compute the covariance of the two-point angular correlation function. For individual bins analyses, in which we fit one value of the α parameter for each redshift bin, we use the jackknife covariance matrix built from the data vector measured with `TreeCorr` while joint analyses use an analytical covariance computed with `CosmoCov` (Krause et al., 2017). The use of an analytical covariance is made necessary by the noise in the covariance of the 13 redshift bins,

even with 500 jackknife patches. Increasing to larger number of patches yields very little improvement in that regard.

The jackknife covariance matrix is computed with the following formula:

$$\mathrm{Cov}^{\mathrm{JK}}(w_{ij}(\theta), w_{kl}(\theta')) = \frac{N_{\mathrm{jack}}-1}{N_{\mathrm{jack}}} \sum_{n=1}^{N_{\mathrm{jack}}} \left(w_{ij}^{(n)}(\theta) - \overline{w}_{ij}(\theta)\right)^{\mathrm{T}} \left(w_{kl}^{(n)}(\theta') - \overline{w}_{kl}(\theta')\right), \quad (3.15)$$

where n is the index of the jackknife realization, $w_{ij}(\theta)$ is the correlation of redshift bins i and j at angular separation θ, and $\overline{w}_{ij}$ stands for the mean over all jackknife realizations for each angular separation $\overline{w}_{ij}(\theta) = \frac{1}{N_{\mathrm{jack}}} \sum_{n=1}^{N_{\mathrm{jack}}} w_{ij}^{(n)}(\theta)$. The full jackknife covariance matrix of $w(\theta)$ in the 13 redshift bins, cross-correlations included is shown in Fig. 3.28 where the covariance has been normalized to compute the correlation matrix

$$\mathrm{Cov}_{i,j,\mathrm{norm}} = \frac{\mathrm{Cov}_{i,j}}{\sqrt{\mathrm{Cov}_{i,i}\mathrm{Cov}_{j,j}}}. \quad (3.16)$$

Its size is 9464×9464 as it is computed from 91 auto- and cross-correlations of 104 angular bins between $\theta = 0.12°$ and $\theta = 10.5°$, the large scales being necessary for the BAO analysis. However, most analyses use only autocorrelations which lead to a covariance of a more reasonable size of 1352×1352 and scale cuts which decrease it further to 690×690 in the case of BAO analyses where $\theta_{\mathrm{min}} = 0.6°$ and $\theta_{\mathrm{max}} = \theta_{\mathrm{BAO}} + 2.5°$. If cross-correlations were to be included in the BAO analysis then the covariance size would reach 5522×5522 with scale cuts. In the case of the full-shape analysis where only small scales $\theta \in [0.12°, 1.7°]$ are considered, its size is 195×195 for autocorrelations alone or 1365×1365 with cross-correlations.

We checked that the jackknife covariance matrix of individual redshift bins is numerically stable with conditioning numbers ranging from 2.3×10^4 for the covariance of the last redshift bin to 2.2×10^5 for the first bin. Multiplying each of the jackknife covariances by its inverse yields the identity matrix, as expected from a numerically stable matrix, with a ratio between the diagonal and off-diagonal terms larger than 10^{13}. The inverse jackknife covariance of individual redshift bins is corrected by the Hartlap multiplicative factor (Hartlap et al., 2007)

$$\Psi = \frac{N_{\mathrm{jack}} - N_{\mathrm{b}} - 2}{N_{\mathrm{jack}} - 1}, \quad (3.17)$$

where N_{b} is the number of angular bins in the data vector.

The analytical covariance is defined as the sum of the Gaussian and super-sample contributions, leaving aside the connected non-Gaussian term from modes within the footprint. The Gaussian covariance is computed using `CosmoCov` as in Krause et al., 2017 and Fang, Eifler, et al., 2020, with a correction for the survey footprint like in Troxel et al., 2018 and without considering the Limber approximation (Fang, Krause,

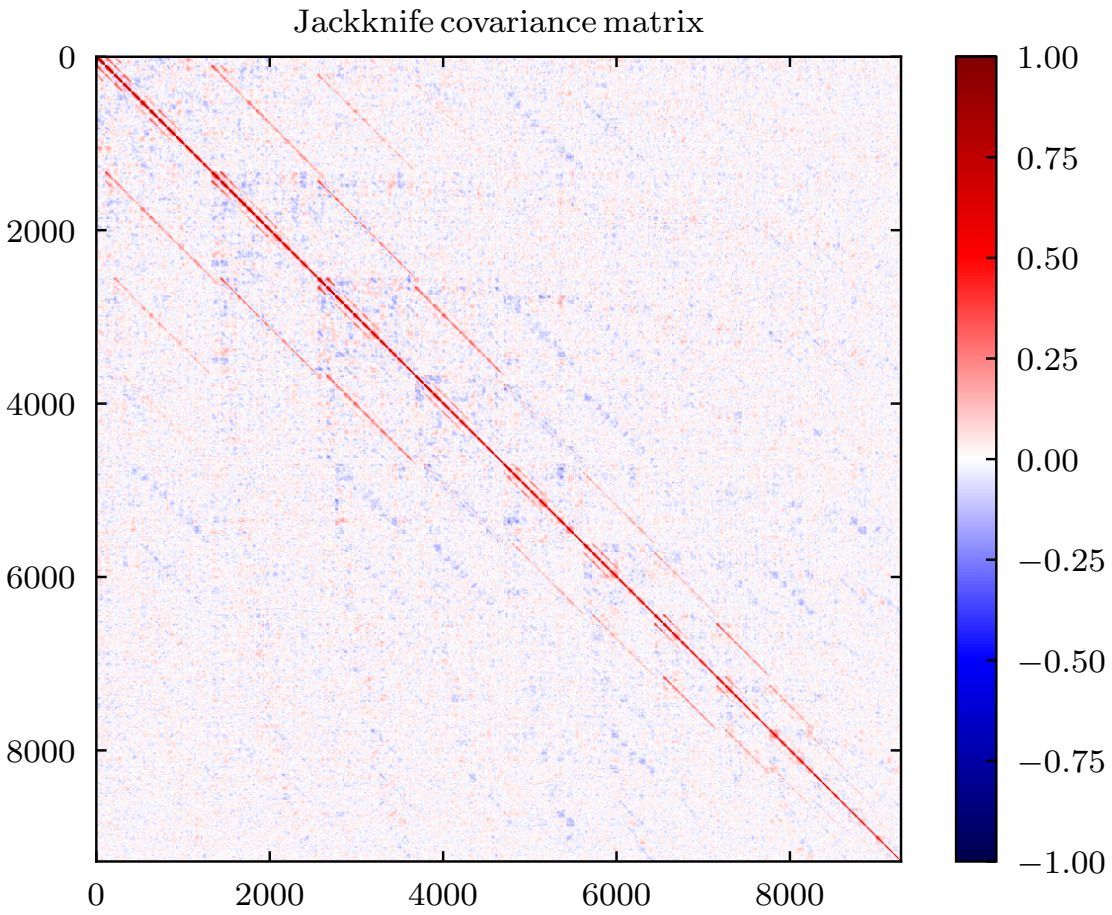


Figure 3.28. – Full jackknife covariance matrix of $w(\theta)$ in the 13 redshift bins, cross-correlations included. Its size is 9464 × 9464 as it is computed from 91 auto- and cross-correlations of 104 angular bins between $\theta = 0.12°$ and $\theta = 10.5°$, the large scales being necessary for the BAO analysis. However, most analyses use only autocorrelations which lead to a covariance of a more reasonable size of 1352 × 1352 and scale cuts which decrease it further to 690 × 690 in the case of BAO analyses.

et al., 2020)

$$\mathrm{Cov}^{\mathrm{G}}\left[C_{ij}(\ell), C_{kl}(\ell')\right] = \frac{4\pi\delta^{\mathrm{K}}_{\ell\ell'}}{\Omega_{\mathrm{s}}(2\ell+1)}\left[\left(C_{ik}(\ell)+\frac{\delta^{\mathrm{K}}_{ik}}{\bar{n}^i}\right)\times\left(C_{jl}(\ell')+\frac{\delta^{\mathrm{K}}_{jl}}{\bar{n}^j}\right)\right.$$
$$\left.+\left(C_{il}(\ell)+\frac{\delta^{\mathrm{K}}_{il}}{\bar{n}^i}\right)\left(C_{jk}(\ell')+\frac{\delta^{\mathrm{K}}_{jk}}{\bar{n}^j}\right)\right], \quad (3.18)$$

with C_{ij} the angular power spectrum of redshift bins i and j, Ω_{s} the survey area, $\bar{n}$ the effective number density of galaxies and i, j, k, and l are the indices of the redshift bins. The two-point angular correlation function is then computed from angular power spectra with the following relation (Abbott, Adamow, et al., 2024):

$$\mathrm{Cov}^{\mathrm{G}}\left[w_{ij}(\theta), w_{kl}(\theta')\right] = \sum_{\ell,\ell'}\frac{(2\ell+1)(2\ell'+1)}{(4\pi)^2}\overline{\mathrm{P}_\ell}(\theta)\,\overline{\mathrm{P}_{\ell'}}(\theta')\,\mathrm{Cov}^{\mathrm{G}}\left[C_{ij}(\ell), C_{kl}(\ell')\right], \quad (3.19)$$

with $\overline{\mathrm{P}_\ell}$ the Legendre polynomial averaged over angular bins

$$\overline{\mathrm{P}_\ell} := \frac{\int_{x_{\min}}^{x_{\max}}\mathrm{d}x\,P_\ell(x)}{x_{\max}-x_{\min}} = \frac{[P_{\ell+1}(x)-P_{\ell-1}(x)]_{x_{\min}}^{x_{\max}}}{(2\ell+1)(x_{\max}-x_{\min})} \quad (3.20)$$

in which $x=\cos(\theta)$ with $\theta_{\min},\theta_{\max}$ the lower and upper limits of each angular bins.

As for the super-sample covariance (SSC) contribution to the covariance, it was computed following the fast approximation from Lacasa et al., 2019 extended to partial-sky in Gouyou Beauchamps et al., 2022 to go beyond the full-sky approximation by taking into account the footprint of the survey

$$\mathrm{Cov}^{\mathrm{SSC}}\left[w_{ij}(\theta), w_{kl}(\theta')\right] \approx \tilde{w}_{ij}(\theta)\;\tilde{w}_{kl}(\theta')\,S_{ijkl}, \quad (3.21)$$

where $\tilde{w}_{ij}(\theta)$ is computed as

$$\tilde{w}_{ij}(\theta) = \sum_\ell \frac{2\ell+1}{4\pi}\,R_\ell\;C_{ij}(\ell)\;P_\ell(\cos\theta) =: (R * w_{ij})(\theta), \quad (3.22)$$

with R_ℓ the response of the galaxy power spectrum to variations of the background density $\frac{\partial P_{\mathrm{gal}}(k,z)}{\partial\delta_{\mathrm{b}}}$. The S_{ijkl} matrix element is computed using the implementation from `PySSC`[3] as

$$S_{ijkl} = \int \mathrm{d}V_1\,\mathrm{d}V_2\,\frac{W_i(z_1)\,W_j(z_1)\,W_k(z_2)\,W_l(z_2)\,\sigma^2(z_1,z_2)}{\int\mathrm{d}V_1\;W_i(z_1)\;W_j(z_1)\int\mathrm{d}V_2\;W_k(z_2)\;W_l(z_2)}, \quad (3.23)$$

where W_i is the kernel of the observable in redshift bin i, the kernel being the normalized redshift distribution $p_i(z)$ in the case of photometric galaxy clustering. The comoving volume element $\mathrm{d}V = r^2(z)\,(\mathrm{d}r/\mathrm{d}z)\,\mathrm{d}z$ is integrated between $z=0$ and

3. https://github.com/fabienlacasa/PySSC

$z = z_{\rm max} = 3$. The variance of the background density σ^2 is, for a survey with a window function $\mathcal{W}$ of angular power spectrum $C^{\mathcal{W}}$

$$\sigma^2(z_1, z_2) = \frac{1}{\Omega_{\rm s}^2} \sum_{\ell} (2\ell + 1)\, C^{\mathcal{W}}(\ell)\, C(\ell, z_1, z_2)\,, \tag{3.24}$$

where the angular matter power spectrum between redshifts z_1 and z_2 is obtained from the 3D matter cross-spectrum $P_{\rm m}(k\,|\,z_{12}) = D(z_1)\, D(z_2)\, P_{\rm m}(k, z = 0)$ with

$$C(\ell, z_1, z_2) = \frac{2}{\pi} \int_{k_{\rm min}}^{k_{\rm max}} k^2\, {\rm d}k\, P_{\rm m}(k\,|\,z_{12})\, j_\ell(kr_1)\, j_\ell(kr_2)\,, \tag{3.25}$$

where $D(z)$ is the linear scale-independent growth factor from `CLASS`, $r_i = r(z_i)$ is the comoving radial distance, $k_{\rm min} = 0.1/r(z_{\rm max})$, and $k_{\rm max} = 10/r(z_{\rm min})$.

We use the `anafast` routine from the `HEALPix`[4] library (Zonca et al., 2019; Górski et al., 2005) to compute $C^{\mathcal{W}}$. We make the approximation of a constant $R_\ell = 5$, which reduces the convolution product to a multiplication. A detailed discussion on the response of the SSC can be found in Euclid Collaboration: Sciotti et al., 2024. The approximation on R_ℓ used in this work has an impact which does not exceed 0.5% on α and 3% on its uncertainty in all redshift bins, which is expected given the angular scales and redshifts considered.

We show the $S_{i,j,k,l}$ matrix and the associated SSC covariance matrix in Fig. 3.29 and Fig. 3.30.

The resulting analytical covariance is shown in Fig. 3.31 where it was normalized following Eq. (3.16) as it was done for the jackknife covariance matrix. The structure of the covariance is identical to the jackknife one, with the exception of the noise of the jakknife covariance present in off-diagonal terms. However, there is a clear overestimation of the error $\sigma(w)$ with the jackknife method in all redshift bins except for the first one, as shown in Fig. 3.32 of the ratio of the Gaussian and jackknife errors $\sigma(w_i) = \sqrt{{\rm Cov}_{i,i}}$ where i is the index of the angular bin. The difference is close to 20 % at most scales. On the other hand, the difference between Gaussian error and Gaussian+SSC error is minimal at the considered redshifts and scales. SSC, as a non-linear effect, is non-negligible at low redshifts, especially at small scales. This is why the gap in $\sigma(w)$ reaches 30 % at $\theta = 0.3°$ when the SSC is added to the covariance of the first redshift bin. The effect drops to 2 % at $\theta = 2°$ and it drops to 15 % and 3 % at $\theta = 0.3°$ when we consider the second and third redshift bins. This small influence of the SSC over the scales considered in the BAO analysis is directly reflected in the results from Sect. 4.4.6.

4. http://healpix.sf.net

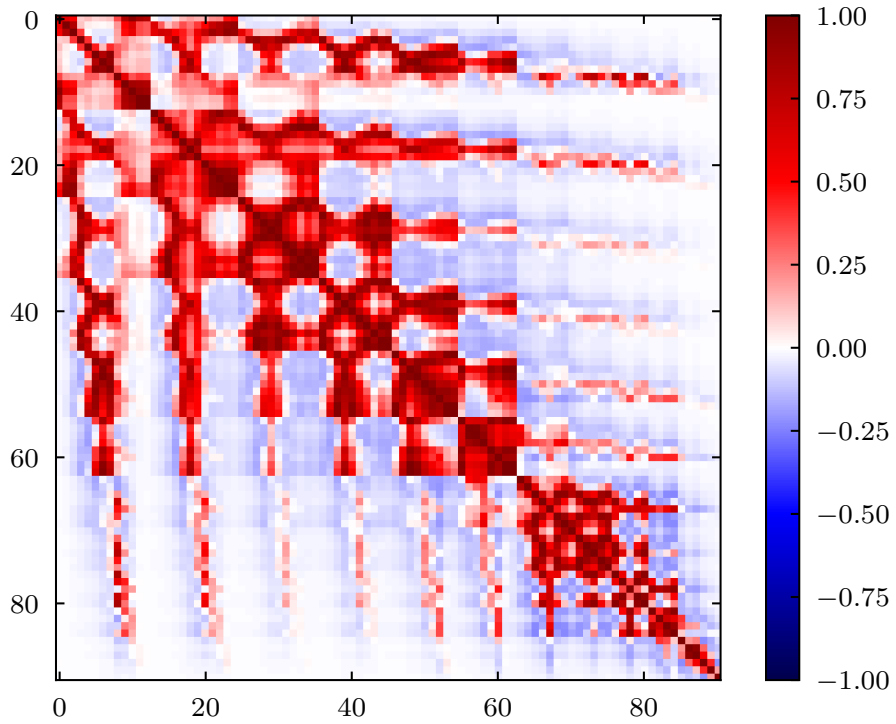


Figure 3.29. – $S_{i,j,k,l}$ matrix computed with the PySSC code and the $p_i(z)$ measured on Flagship 2.1.10.

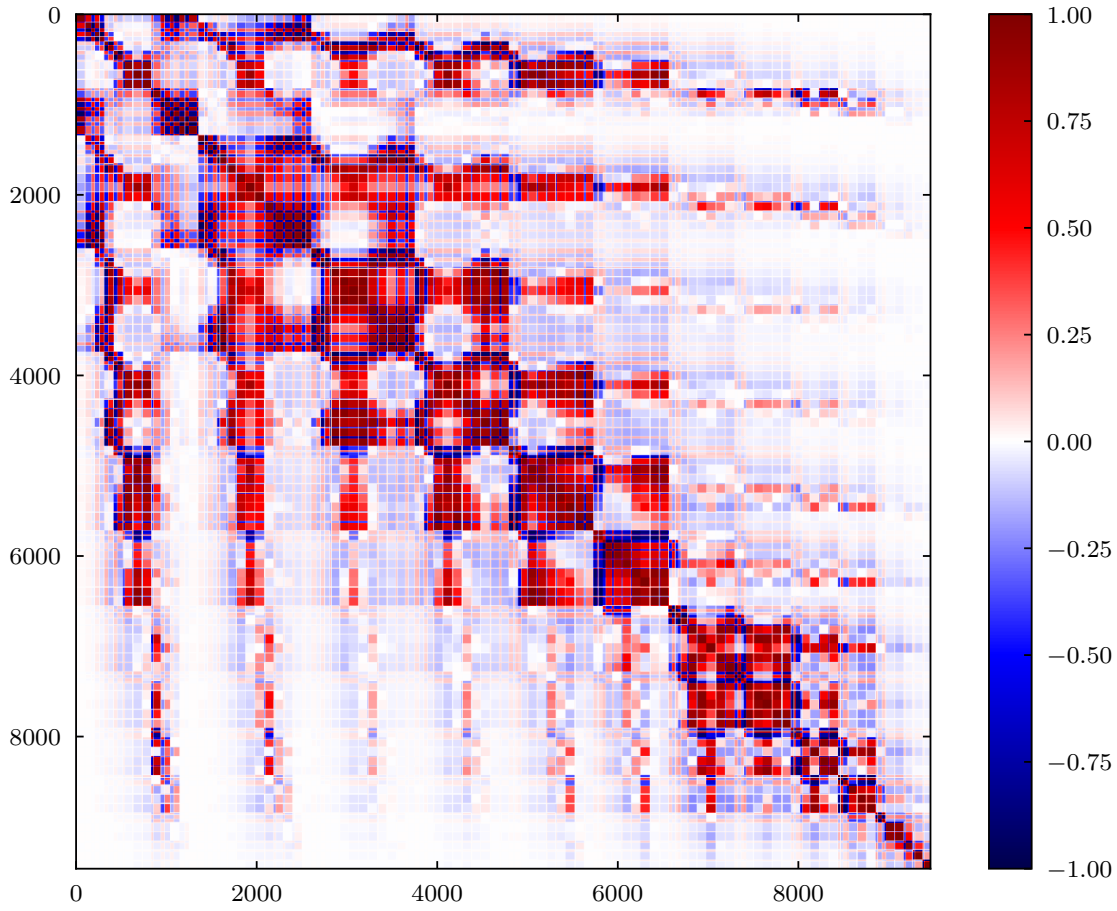


Figure 3.30. – SSC covariance matrix computed with the PySSC code and the $p_i(z)$ measured on Flagship 2.1.10.

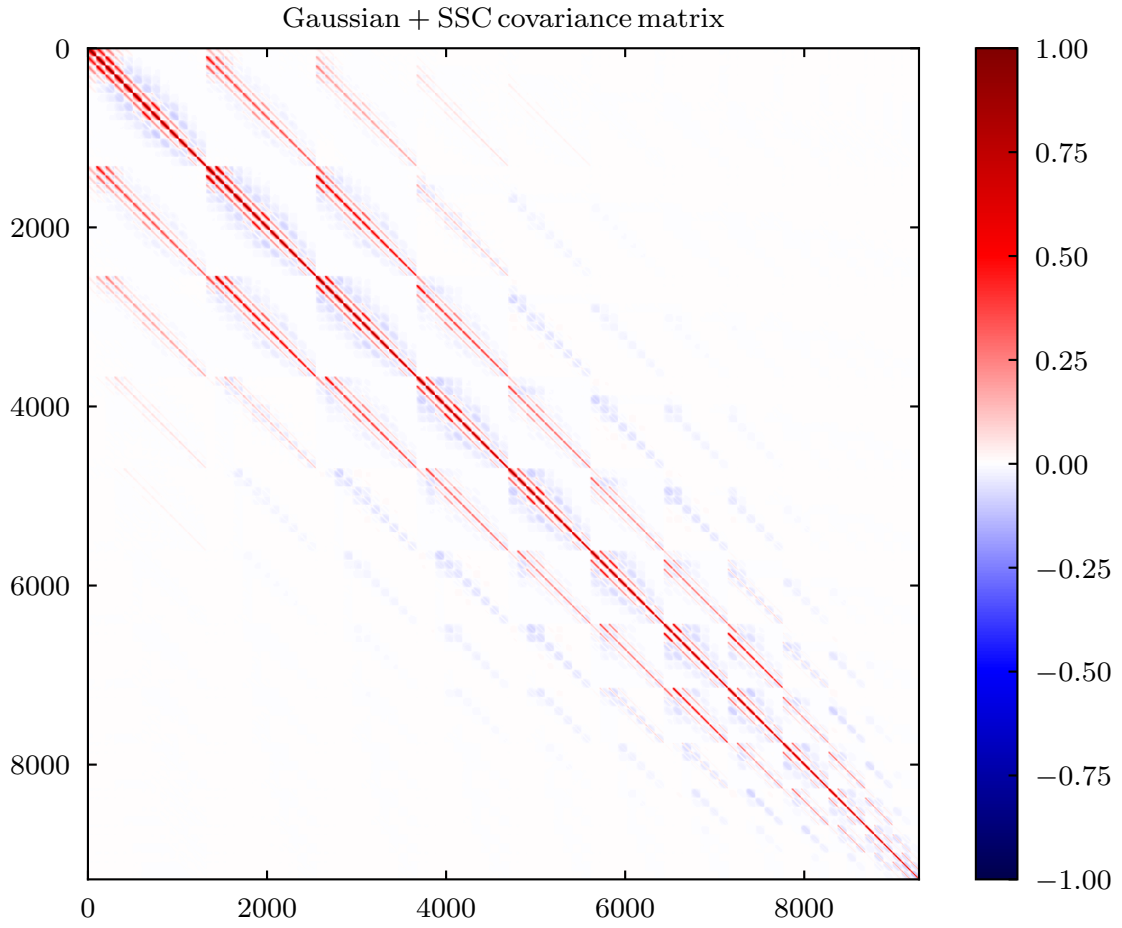


Figure 3.31. – Full Gaussian+SSC analytical covariance matrix $w(\theta)$ of the 13 redshift bins, cross-correlations included. The comparison with Fig. 3.28 shows a very good agreement in the structure of off-diagonal terms, at the difference of the noise present in the jackknife covariance due to the limited number of jackknife patches.

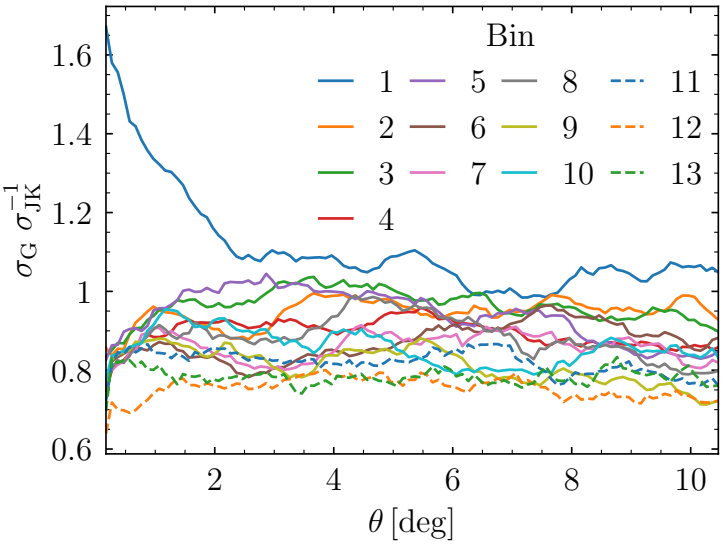


Figure 3.32. – Ratio of the diagonal terms of the autocorrelations blocks of the Gaussian and jackknife covariance matrices.

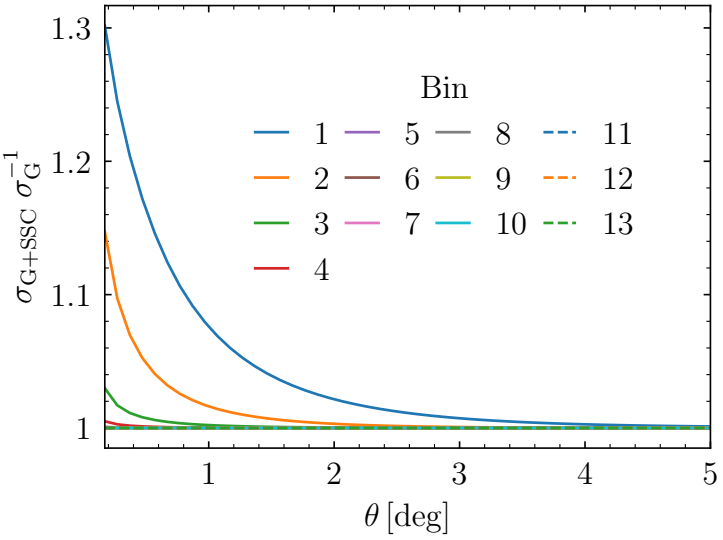


Figure 3.33. – Ratio of the diagonal terms of the autocorrelations blocks of the Gaussian+SSC and Gaussian covariance matrices.

4. A tomographic BAO analysis of photometric galaxy clustering

Summary

4.1. Constraints on the BAO scale as a function of redshift 113
4.1.1. Methodology for the analysis of individual redshift bins 113
4.1.2. Results of the individual redshift bins baseline analysis 115
4.2. Cosmological constraints from BAO 121
4.2.1. Methodology of the inference of cosmological parameters from BAO 121
4.2.2. Cosmological parameters infered from BAO 123
4.3. Constraints on alpha from a joint analysis 127
4.3.1. Methodology for the joint analysis 127
4.3.2. Results with the baseline joint analysis 127
4.4. BAO, a robust probe 130
4.4.1. Influence of the fiducial cosmology 130
4.4.2. Influence of the template 130
4.4.3. Influence of redshift space distortions 132
4.4.4. Influence of the scale cuts 133
4.4.5. Influence of the redshift binning scheme 136
4.4.6. Influence of the covariance 140
4.4.7. Optimization of the sample selection and redshift binning scheme 146

In this chapter, we present our analyses of BAO with photometric galaxy clustering using the observable $w(\theta)$ presented in the previous chapter. Three main analyses are conducted. The first one consists in extracting the BAO signal in each redshift bin to estimate the variation of the position of the BAO peak with respect to a fiducial cosmology as a function of redshift. The second analysis, enabled by the first one, consists in constraining cosmological parameters through the Universe expansion history, caracterized by the evolution of the size of the BAO scale as a function of redshift. The third analysis is a joint analysis of all redshift bins to constrain the BAO scale at one single effective redshift of the whole sample rather than in each redshift bin. The work done in this chapter is published in Euclid Collaboration: Duret et al. (2025).

4.1. Constraints on the BAO scale as a function of redshift

In this section, we present how the extraction of the BAO signal is performed in each redshift bin, before reporting the results obtained. A comparison of two statistical methods, MCMC and profile likelihood is provided and we estimate the strength of the detection of the BAO signal as a function of redshift. We give these results for the measured $w(\theta)$ but also with a synthetic $w(\theta)$ as a comparison to compare our constraints obtained from a realistic simulation to an optimistic noise-free data vector.

4.1.1. Methodology for the analysis of individual redshift bins

To extract the BAO feature in the photometric samples, we perform the fitting between the measured $w(\theta)$ and a template derived from the theoretical two-point angular correlation function $w_{\rm fid}(\theta)$ computed for the fiducial cosmology described by Eq. (4.5). The template is defined as in Abbott, Abdalla, Alarcon, et al. (2019)

$$T(\alpha,\theta) = B\, w(\alpha\theta) + A_0 + \frac{A_1}{\theta} + \frac{A_2}{\theta^2} \tag{4.1}$$

where α is the transverse Alcock-Paczynski parameter quantifying an eventual shift of the BAO peak between the measured $w(\theta)$ and the model $w_{\rm fid}(\theta)$. The parameter α is defined as

$$\alpha = \frac{D_{\rm A}}{r_{\rm d}} \frac{r_{\rm d,fid}}{D_{\rm A,fid}} \tag{4.2}$$

The nuisance parameters B, A_0, A_1, and A_2 are needed to absorb residual effects like non-linear galaxy bias or redshift-space distortions which do not affect the position of the BAO peak. Alternatives to this template exist, with the example of the fully empirical functional form used in Carvalho et al. (2020), composed of a power law to model the general shape of the correlation function, summed with a gaussian to model the BAO peak. This thesis is focused on the template from Eq. (4.1). The best fit is obtained by maximization of the logarithm of the likelihood $\mathscr{L}$

$$\mathscr{L} \propto e^{-\frac{\chi^2}{2}}, \tag{4.3}$$

where

$$\chi^2 = \sum_{i,j} \left(T_i(\alpha,\theta) - w_i(\theta)\right)^T C_{i,j}^{-1} \left(T_j(\alpha,\theta) - w_j(\theta)\right) \tag{4.4}$$

The maximization is performed with the `lmfit` implementation (Newville et al., 2024) of the quasi-Newton BFGS algorithm, named after Charles George Broyden, Roger Fletcher, Donald Goldfarb, and David Shanno who proposed it (Broyden, 1970a; Broyden, 1970b; Fletcher, 1970; Goldfarb, 1970; Shanno, 1970). The α parameter is the quantity of interest in BAO analyses and since the fiducial cosmology used to compute $w_{\rm fid}(\theta)$ is the same as the one used in the simulation, we expect to recover $\alpha = 1$. On

Table 4.1. – Priors used for the template fitting parameters. With the first template, defined in Eq. (4.1), the A_i parameters have a unit of deg^i. For the other templates, defined in Sect. 4.4.2, the units should be adapted to have a template $T(\alpha,\theta)$ of unit consistent with $w(\theta)$.

α	$A_0 \times 10^3$	$A_i \times 10^3$ $(i \neq 0)$	B
[0.8,1.2]	[-1,1]	[-5,5]	[0.2,6]

the contrary, using a different fiducial cosmology to compute $w_{\rm fid}(\theta)$ should result in $\alpha \neq 1$. The fiducial cosmology used in this work unless specified otherwise is a flat ΛCDM cosmology, described by the following set of parameters

$$\begin{aligned} \lambda &= \{\Omega_{\rm m}, \Omega_{\rm b}, {\rm h}, n_{\rm s}, A_{\rm s}\} \\ &= \left\{0.319, 0.049, 0.67, 0.96, 2.1 \times 10^{-9}\right\} \end{aligned} \tag{4.5}$$

Different template parametrisations can be used, and we will verify in Sect. 4.4.2 that the choice of polynomial has minimal impact on the α parameter. Unless specified otherwise, the template of Eq. (4.1) is used in all analyses.The jackknife covariance is used to compute the likelihood in individual bin analyses. Scale cuts are $\theta_{\rm min} = 0.60°$, $\theta_{\rm max} = \theta_{\rm BAO} + 2.50°$, visible as the grey bands in Fig. 3.8. We will study the impact of a different choice of scale cuts in Sect. 4.4.4. We will consider one set of nuisance parameter per redshift bin, since these parameters are expected to vary with redshift. Markov Chain Monte-Carlo (MCMC) is used to quantify the uncertainty on α marginalized over the nuisance parameters. The `emcee` sampler introduced in Foreman-Mackey et al., 2013 is used with the Gelman–Rubin convergence stopping criterion described in Gelman et al., 1992 with a threshold $R_{\rm GR} - 1 = 0.005$ for analyses on individual redshift bins. This threshold was chosen to stop chains when parameter values and uncertainties reached a plateau. We run 48 parallel chains (walkers) initialized in a small ball around the expected true value of the parameters with a dispersion of 10^{-4} which spreads to explore the space delimited by the priors in a few tens of steps. Uniform priors applied to the template parameters are presented in Table 4.1.

As a comparison to MCMC, the frequentist technique of profile likelihood (Ade, Aghanim, Arnaud, Ashdown, Aumont, Baccigalupi, Banday, Barreiro, Bartlett, Battaner, et al., 2014) is also used by computing $\Delta\chi^2(\alpha)$, the one sigma uncertainty on α being given by $\Delta\chi^2 = 1$. The profile $\Delta\chi^2(\alpha)$ is obtained by computing the best fit χ^2 for each value of α between 0.8 and 1.2 by steps of 0.001. An 8th-order polynomial is fitted to this profile to then compute $\Delta\chi^2 = \chi^2 - \chi^2(\alpha_{\rm min})$ where $\alpha_{\rm min}$ is the value minimizing the polynomial. A polynomial fit of the χ^2 profile is performed because of its oscillations which perturb the determination of its minimum. The order 8 was chosen so as to reach a plateau in the evolution of residuals of the fit as a function of the order of the polynomial. The profile likelihood is also used to quantify the significance of the BAO detection. The detection level $\Delta_{\rm det}$ is defined for each individual redshift bin as

follows

$$\Delta_{\rm det} := \left| \chi^2_{\rm w}(\alpha_{\rm min}) - \chi^2_{\rm no\,wiggle}(\alpha_{\rm min}) \right|^{1/2}, \tag{4.6}$$

evaluated at the $\alpha_{\rm min}$ value minimizing $\chi^2_{\rm w}(\alpha)$, computed with the model described in Eq. (3.2) to Eq. (3.6). On the other hand, $\chi_{\rm no\,wiggle}$ is computed in a similar manner, replacing the transfer function of `CAMB` by the one from Eisenstein and Hu, 1998 where the wiggles of the BAO feature are removed. As a consequence, we expect $\Delta\chi_{\rm no\,wiggle}$ to be constant when α varies, unlike $\Delta\chi_{\rm w}$. A non-detection of the BAO signal is then defined as $\Delta_{\rm det} < 1$. The code `iminuit` based on the MINUIT algorithm is used to compute the likelihood profiles (Dembinski et al., 2020; James et al., 1975).

We also compare the results from `emcee` to the importance nested sampler `nautilus` (Lange, 2023; Feroz et al., 2019), used in its default configuration. Importance nested sampling (INS) consists in drawing samples from the prior following a uniform distribution, computing the likelihood values of these points, and identifying a region defined by a bound where points of high likelihood cluster. Then, this new region is sampled instead of the prior and iteratively, the region of highest likelihood is determined. The posterior is then computed by sampling each shell defined as a difference between successive bounds and by weighting these samples by the ratio between their likelihood and the sampling density. This sampler does not run several chains at once like `emcee` and so the value of $R_{\rm GR} - 1$ can't be computed. We check the convergence with the evolution of the parameters and their uncertainties but also by ensuring that the shell-bound occupation fraction is 1 for all shells and bounds, meaning that in the iterative process described previously, each new shell is contained within the previous bound. If it is not 1 for some shell and bounds, it means that a part of the high-likelihood space was not entirely explored during the corresponding iteration, in which case it would be necessary to further investigate this.

4.1.2. Results of the individual redshift bins baseline analysis

We now present the constraints obtained for α in all thirteen redshift bins of the Flagship galaxy mock catalogue, their associated uncertainties and $\Delta_{\rm det}$ are grouped in Table 4.2.

We first notice that the one sigma uncertainty is larger at low redshift. This is due to the smearing of the BAO signal by the non linear evolution of the large scale structures under the effect of gravitation. This is clearly visible in Fig. 3.8 where the BAO is much more peaked at higher redshift. α is compatible with $\alpha = 1$ within one sigma in all redshift bins but bin 11 at $z_{\rm eff} = 1.245$ for which we find a 1.3 σ shift. Note that this shift is not worrying from a statistical point of view given that the constraints given correspond to the uncertainty at 68 %. This bin is also the one with the strongest constraining power, explained by the high redshift and small scatter of photometric redshifts $\sigma_{\rm NMAD} = 0.024$. As for the level of detection of the BAO signal, we find three redshift bins with no significant detection, bins 1, 4, and 6. Otherwise, $\Delta_{\rm det}$ ranges between 1.1 and 4.0 σ, with a maximum at $z_{\rm eff} = 1.245$ and the one sigma uncertainty on α decreases from ± 0.13 to ± 0.024 as $\Delta_{\rm det}$ increases, as expected. Note that the

Table 4.2. – α with its uncertainty at 68 % extracted from the MCMC analysis in each redshift bin. The detection level $\Delta_{\rm det}$ is defined in Eq. (4.6). When $\Delta_{\rm det} < 1$, the result is considered as a non detection.

Bin	$z_{\rm eff}$	α	$\Delta_{\rm det}\,(\sigma)$
1	0.290	$1.026^{+0.122}_{-0.140}$	no detection
2	0.374	$1.044^{+0.097}_{-0.107}$	1.2
3	0.436	$0.957^{+0.112}_{-0.093}$	1.1
4	0.527	$1.003^{+0.146}_{-0.123}$	no detection
5	0.613	$1.002^{+0.079}_{-0.095}$	1.1
6	0.705	$0.985^{+0.087}_{-0.096}$	no detection
7	0.802	$0.932^{+0.072}_{-0.054}$	1.5
8	0.858	$1.052^{+0.067}_{-0.067}$	1.7
9	0.972	$1.037^{+0.057}_{-0.048}$	1.5
10	1.090	$1.015^{+0.029}_{-0.028}$	2.7
11	1.245	$1.031^{+0.024}_{-0.024}$	4.0
12	1.488	$0.996^{+0.040}_{-0.038}$	2.4
13	1.922	$0.991^{+0.036}_{-0.037}$	2.9

uniform prior $\alpha \in [0.8, 1.2]$ is informative in the first redshift bins, which is necessary to limit biases if there are only 13 redshift bins. Other possibilities for subsequent analyses would be to either use smaller bins at low redshift, where $\theta_{\rm BAO}$ varies quickly or to completely discard these redshift bins. We find that in our case, discarding or keeping bins with $\Delta_{\rm det} < 1$ has no significant impact when constraining cosmological parameters (Sect. 4.2.2) or when a unique α parameter is constrained in a joint analysis (Sect. 4.3.2).

Table 4.3 groups all values for α, its positive and negative uncertainties determined by the $16^{\rm th}$ and $84^{\rm th}$ quantiles for MCMC and INS, and the positive and negative roots of $\Delta\chi^2(\alpha) - 1 = 0$ for profile likelihood.

We find that in the first redshift bin where the BAO signal is very weak, the profile likelihood technique fails and find a minimum at $\alpha = 1.2$ which is the bound of the grid used to compute the $\Delta\chi^2(\alpha)$. This is explained by the fact that $\Delta\chi^2(\alpha)$ is monotonically decreasing in the [0.8,1.2] interval and never reaches 1. As a consequence, the associated confidence level is not reliable. For this reason, we only use profile likelihood as a mean to quantify $\Delta_{\rm det}$ as described in Sect. 4.1.1. However, as shown in Fig. 4.1, it is interesting to find that it yields values of α which are consistent with MCMC in higher redshfit bins, where the BAO signal is stronger. The confidence level associated is always smaller than the uncertainty computed from the MCMC analysis beyond $z > 0.6$ while it is sometimes larger at lower redshifts. This has to be kept in

Table 4.3. – Measurement of α in the 13 redshift bins, its positive and negative uncertainties determined by the 16$^{\text{th}}$ and 84$^{\text{th}}$ quantiles for MCMC and INS, and the positive and negative roots of $\Delta\chi^2(\alpha) - 1 = 0$ for profile likelihood (PL).

	Method	Bin 1	Bin 2	Bin 3	Bin 4	Bin 5	Bin 6	Bin 7	Bin 8	Bin 9	Bin 10	Bin 11	Bin 12	Bin 13
	MCMC	1.026	1.044	0.957	1.003	1.002	0.985	0.932	1.052	1.037	1.015	1.031	0.996	0.991
α	PL	1.200	1.027	0.934	1.200	1.007	0.987	0.925	1.050	1.035	1.016	1.031	0.996	0.989
	INS	1.024	1.043	0.954	1.009	1.005	0.985	0.933	1.061	1.044	1.016	1.030	0.995	0.991
	MCMC	0.122	0.097	0.112	0.146	0.079	0.087	0.072	0.067	0.057	0.029	0.024	0.040	0.036
σ_+	PL	0.058	0.140	0.108	0.068	0.067	0.063	0.045	0.063	0.050	0.027	0.024	0.036	0.033
	INS	0.122	0.097	0.113	0.143	0.080	0.085	0.062	0.068	0.058	0.028	0.024	0.041	0.036
	MCMC	0.140	0.107	0.093	0.123	0.095	0.096	0.054	0.067	0.048	0.028	0.024	0.038	0.037
σ_-	PL	0.378	0.110	0.129	0.196	0.072	0.068	0.044	0.058	0.043	0.027	0.022	0.034	0.033
	INS	0.138	0.108	0.093	0.125	0.095	0.096	0.051	0.067	0.048	0.028	0.024	0.039	0.038

mind when comparing our constraints from the MCMC analysis to other results like DES Y6 which used profile likelihood instead and discarded redshift bins where the BAO was only weakly detected. Regarding INS, we find very good agreement with MCMC, with shifts of the median α smaller than 0.9 % at all redshifts, a maximum variation of the uncertainty of 11.5 % in bin 7 and otherwise smaller than 2.5 %.

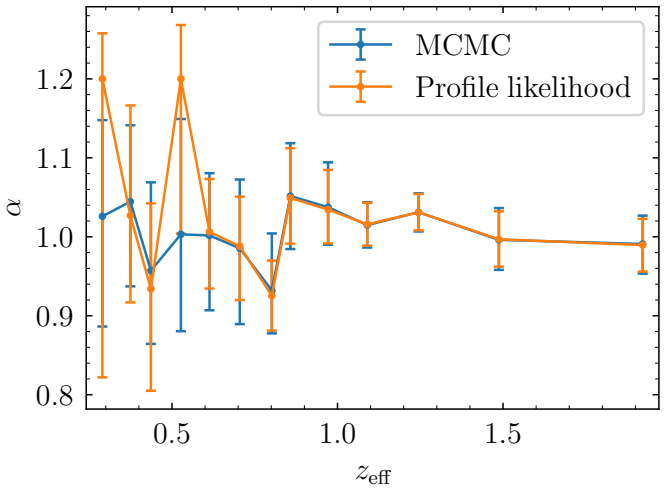


Figure 4.1. – Comparison of the α_i obtained by MCMC analysis and profile likelihood on the data vector measured in the 13 redshift bins of Flagship.

We show in Fig. 4.2 a comparison of our results to the ones from BOSS DR12 (Wang et al., 2017) and DES Y6. As explained before, this is not a one-to-one comparison since Flagship is a simulation, while observations are always subject to contamination by systematic effects and the methodology used to constrain α differs but given our observation of larger uncertainties with MCMC than profile likelihood at the redshifts considered, this is very promising. With *Euclid*, the expected performance of the photometric sample to constrain α as a function of redshift improves by a factor 2 to 4 with respect to BOSS DR12 at low redshift while it improves by up to a factor 3 with respect to DES Y6.

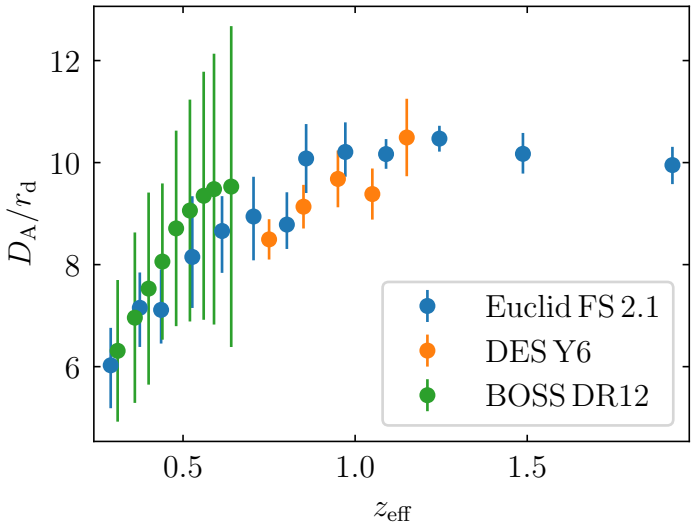


Figure 4.2. – Comparison of the constraints on the ratio D_A/r_d obtained with BOSS DR12, DES Y6, and Flagship 2.1. *Euclid* will provide better constraints on this ratio in a larger range of redshifts, up to $z = 2.0$. The first two bins of DES Y6 are the only constraints from a photometric survey which are stronger than the ones obtained in this analysis.

As we observe shifts on some α_i with respect to the expected value of 1, we check if this is explained by our measurement of the two-point angular correlation function on Flagship. The analysis is repeated while replacing the measured $w(\theta)$ by a noise-free synthetic data vector computed similarly to the theoretical model with the fiducial cosmological parameters of the Flagship simulation and $\alpha_i = 1$, $B = 0$, $A_0 = 0$, $A_1 = 0$, and $A_2 = 0$. This is an ideal case used for validation, where the data vector and model fully agree. The results are given in Table 4.4. We find that all α_i values are consistent with 1 within 0.2σ. As shown in Fig. 4.3, the uncertainties follow loosely the ones obtained with the measured data vector, about 17 % smaller before $z = 0.9$, and 56 % larger after, ranging from ± 0.107 in the first bin to ± 0.037 in the last one. We find no detection of the BAO signal at more than 1σ is the first four redshift bins, while it grows from $\Delta_{det} = 1.2\sigma$ to 3.1σ in the next bins. The comparison with the results from the measured data vector indicates that the strength of the BAO signal measured in Flagship is larger, especially in bin 11 where Δ_{det} is 1.6 times as large as the one from the synthetic data vector, which explains the difference in the uncertainties of α.

In Fig. 4.4, we check how the profile likelihood fares with this cleaner, synthetic data vector with respect to the measured one. The detail of the results can be found in Table 4.5. We find that profile likelihood still fails to estimate a coherent confidence level for α in the first redshift bin simply because the $\Delta\chi^2(\alpha)$ profiles never reach 1 in the [0.8,1.2] interval. However, the best fit value is properly estimated as the profile, similar to an inverted Bell curve, shows a clear minimum, unlike the previously monotonically decreasing profile with the measured data vector. As a matter of fact, the best fit value shows an even smaller bias than what is obtained with MCMC with a maximum bias of

Table 4.4. – α with its uncertainty extracted from the MCMC analysis in each redshift bin using a noise-free synthetic data vector.

Bin	$z_{\rm eff}$	α	$\Delta_{\rm det}\,(\sigma)$
1	0.290	$1.019^{+0.104}_{-0.110}$	no detection
2	0.374	$1.018^{+0.097}_{-0.103}$	no detection
3	0.436	$1.013^{+0.089}_{-0.089}$	no detection
4	0.527	$1.010^{+0.075}_{-0.073}$	no detection
5	0.613	$1.008^{+0.069}_{-0.066}$	1.2
6	0.705	$1.009^{+0.069}_{-0.064}$	1.4
7	0.802	$1.010^{+0.067}_{-0.059}$	1.6
8	0.858	$1.006^{+0.061}_{-0.054}$	1.7
9	0.972	$1.004^{+0.053}_{-0.048}$	1.7
10	1.090	$1.005^{+0.052}_{-0.048}$	2.1
11	1.245	$1.003^{+0.041}_{-0.039}$	2.4
12	1.488	$1.005^{+0.050}_{-0.045}$	2.5
13	1.922	$1.002^{+0.038}_{-0.035}$	3.1

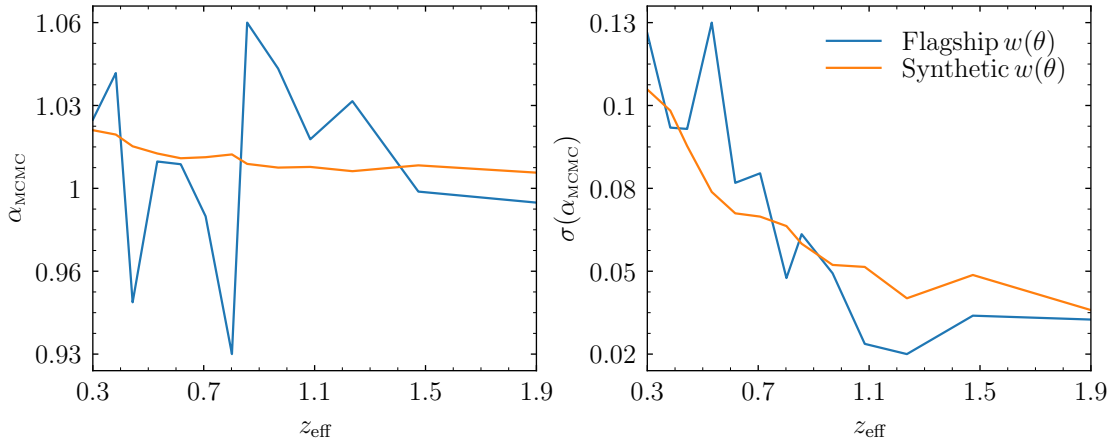


Figure 4.3. – Comparison of the α_i obtained by MCMC analysis with template fitting of $w(\theta)$ measured on Flagship and computed as a synthetic noise-free data vector. We find that the biases observed with the measured data vector are no longer present with the synthetic data vector.

0.002. As for the comparison as a function of redshift, confidence intervals are larger than uncertainties at redshifts $z < 0.8$ and slightly smaller at $z > 0.8$.

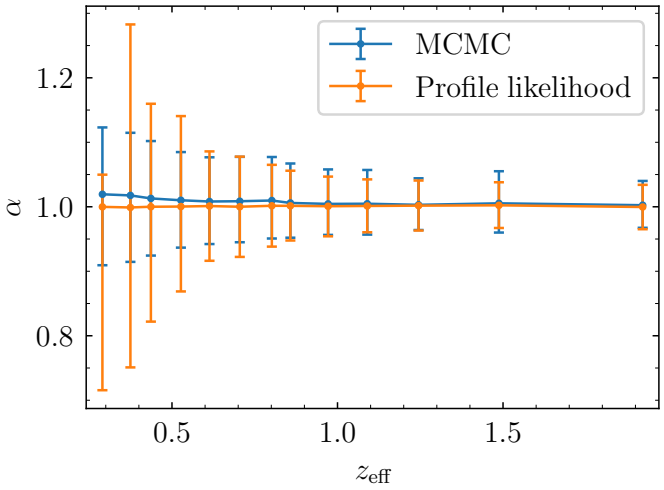


Figure 4.4. – Comparison of the α_i obtained by MCMC analysis and profile likelihood on the synthetic data vector computed in the 13 redshift bins.

Table 4.5. – Measurement of α in the 13 redshift bins as in Table 4.3 for the validation synthetic data vector.

	Method	Bin 1	Bin 2	Bin 3	Bin 4	Bin 5	Bin 6	Bin 7	Bin 8	Bin 9	Bin 10	Bin 11	Bin 12	Bin 13
α	MCMC	1.019	1.018	1.013	1.010	1.008	1.009	1.010	1.006	1.004	1.005	1.003	1.005	1.002
	Likelihood profile	1.000	0.999	1.000	1.000	1.001	1.000	1.002	1.001	1.001	1.001	1.002	1.002	1.000
σ_+	MCMC	0.104	0.097	0.089	0.075	0.069	0.069	0.067	0.061	0.053	0.052	0.041	0.050	0.038
	Likelihood profile	0.050	0.284	0.160	0.140	0.085	0.078	0.064	0.054	0.046	0.041	0.039	0.036	0.034
σ_-	MCMC	0.110	0.103	0.089	0.073	0.066	0.064	0.059	0.054	0.048	0.048	0.039	0.045	0.035
	Likelihood profile	0.284	0.248	0.178	0.132	0.085	0.078	0.063	0.054	0.047	0.041	0.039	0.035	0.034

We also provide the results in a DR1-like setting in Table 4.6, with 6 equipopulated redshift bins with a selection at $I_{\rm E} \leq 23.5$, keeping the same analysis choices as in the baseline of 13 redshift bins (scale cuts, template, etc). When we compare bins of similar effective redshifts, the constraints on α are about 20% weaker than with 13 bins in Table 4.2 in the first bins but significantly worse in the last two bins. We find no significant detection of the BAO signal in the first, second and fifth redshift bins and the $\Delta_{\rm det}$ values in the three remaining bins don't exceed 1.2. This is expected from the larger redshift bins : the intra-bin variation of the BAO scale is more important and dilutes the peak. Combined with the larger uncertainties on $w(\theta)$ from the smaller DR1-like sample, this explains the constraints obtained. A caveat of this analysis is that at the time of the *Euclid* DR1, LSST photometry won't be available, DES photometry will be used instead. For this reason, the results presented in Table 4.6 are optimistic. Using a sample which is optimized for BAO will be necessary and different scale cuts may improve these constraints. A new study would be helpful in that regard.

Table 4.6. – α extracted from the MCMC analysis in a DR1-like setting in each equidistant redshift bin. The detection level $\Delta_{\rm det}$ is defined in Eq. (4.6). The detection of the BAO signal is overall weaker than with 13 redshift bins, which is expected from the larger bins and larger $w(\theta)$ uncertainties.

Bin	$z_{\rm min}$	$z_{\rm eff}$	$z_{\rm max}$	α	$\Delta_{\rm det}\,(\sigma)$
1	0.200	0.307	0.396	$1.055^{+0.102}_{-0.148}$	no detection
2	0.396	0.432	0.507	$1.021^{+0.118}_{-0.131}$	no detection
3	0.507	0.578	0.657	$1.086^{+0.068}_{-0.106}$	1.2
4	0.657	0.727	0.840	$0.909^{+0.113}_{-0.070}$	1.2
5	0.840	0.893	1.040	$1.016^{+0.120}_{-0.155}$	no detection
6	1.040	1.325	2.500	$1.045^{+0.079}_{-0.089}$	1.1

4.2. Cosmological constraints from BAO

The redshit-dependent constraints obtained allow us to infer cosmological parameters through the angular diameter distance $D_{\rm A}(z)$ by comparing the size of the BAO scale measured in $w(\theta)$ against the expected $D_{\rm A}(z)$ for a given cosmology. After a presentation of the method used, the constraints are given for the baseline analysis. The robustness of the analysis with respect to the exclusion of one or several redshift bin is studied, along with the influence of the priors used in the inference.

4.2.1. Methodology of the inference of cosmological parameters from BAO

Checking the definition of α given in (4.2), we can actually see that the BAO analysis can only provide a constraint on the ratio $D_{\rm A}/r_{\rm d}$, not on $D_{\rm A}$ itself. To proceed with the inference of cosmological parameters, we can then use a very tight prior on $r_{\rm d}$ derived from the *Planck* measurement (Ade, Aghanim, Arnaud, Ashdown, Aumont, Baccigalupi, Banday, Barreiro, Bartlett, Bartolo, et al., 2016) to obtain $D_{\rm A}$. In order to have an analysis which is as model-independent as possible, we can also choose to constrain cosmological parameters by constraining the Universe expansion history, comparing the ratio $D_{\rm A}/r_{\rm d}$ obtained at various redshifts. This explains importance of the tomographic approach used in this work, where the galaxy sample is divided into thirteen redshift bins. In spectroscopic galaxy clustering of BAO, the correlation function is measured in three dimensions. This allows the comparison of both the transverse and radial component of the BAO scale which is isotropic. While the transverse component constrains $D_{\rm A}(z)/r_{\rm d}$, the radial one constrains $D_{\rm H}(z)/r_{\rm d}$ where $D_{\rm H}$ is the Hubble distance defined as

$$D_{\rm H}(z) = \frac{c}{H(z)} \tag{4.7}$$

The combination of both ratios D_A/r_d and D_H/r_d is very powerful in constraining the expansion history. However, in photometric galaxy clustering, the radial component of correlation measurement is plagued by the photometric redshift uncertainty. For this reason, we will see in the following subsection that the constraints obtained from D_A/r_d with *Euclid* photometric sample alone do not provide very strong constraints. However, we find that this is no longer the case with a prior from the *Planck* measurement of $\Omega_b h^2 = 0.0220 \pm 0.0004$ and $D_A(1+z_{Planck})/r_{s,drag} = 83.197 \pm 0.065$ where $z_{Planck} = 1090$. The priors from Ade, Aghanim, Arnaud, Ashdown, Aumont, Baccigalupi, Banday, Barreiro, Bartlett, Bartolo, et al. (2016) were adapted to match the Flagship simulation cosmological parameters so that the ratios between the uncertainties and fiducial values stay the same.

In our definition of α in Eq. (4.2), all quantities are evaluated at the effective redshift of the samples, i.e. of each redshift bin. As a reminder, the effective redshift of bin i is defined as:

$$z_{\mathrm{eff},i} = \int_0^3 \mathrm{d}z\, z\, p_i(z)\,, \tag{4.8}$$

where $p_i(z)$ is the normalized distribution of photometric redshifts shown in Fig. 3.6. We checked that using the median redshift z_{med} of each redshift bin instead did not affect the constraints on h, Ω_b, and Ω_{cdm} obtained in Sect. 4.2.2 (shift smaller than $0.03\,\sigma$). This is expected from the small difference between z_{eff} and z_{med} in most redshift bins. Note that with observations, galaxy weights will be introduced and this definition should be adapted to include them as in Abbott, Adamow, et al. (2024)

$$z_{\mathrm{eff},i} = \frac{\sum_j^N w_{j,\mathrm{sys}}\, w_{j,\mathrm{FKP}}\, z_{\mathrm{ph}}}{\sum_j^N w_{j,\mathrm{sys}}\, w_{j,\mathrm{FKP}}} \tag{4.9}$$

with N the number of galaxies in redshift bin i, $w_{j,\mathrm{sys}}$ the weights computed to take into account systematic effects, and $w_{j,\mathrm{FKP}}$ the Feldman–Kaiser–Peacock weights (Feldman et al., 1994). Fig. 4.5 shows the evolution of the ratio D_A/r_d as a function of z and so it is akin to the sensitivity of the results to z. The maximum shift of D_A/r_d when changing from z_{eff} to z_{med} is in the first bin, where the ratio increases abruptly with z. This shift represents 25.1% of the uncertainty on α measured in this bin. The second largest shift is in the last bin with 4.9% of the uncertainty. The width of the last bin explains this shift. It is worth noting that comparing D_A/r_d at z_{max} and z_{min} instead, the shift reaches 193%, 165%, 78%, 71% and 157%, in bins 1, 2, 3, 4 and 13, respectively. This intra-bin variation dilutes the BAO signal and, combined with the smearing of the non-linear evolution of large-scale structures at low z, explains the low values of Δ_{det} in these bins. For this reason, the BAO analysis could benefit from using more redshift bins as we will see in Sect. 4.4.7.

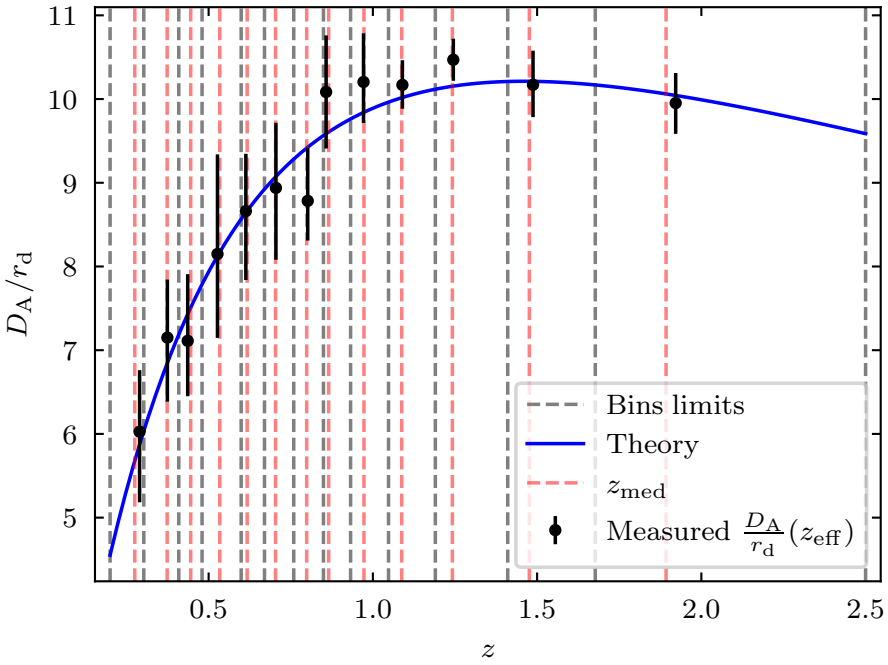


Figure 4.5. – Evolution of the ratio D_A/r_d as a function of redshift. The theoretical expectation is shown in blue, the constraints on the α_i from Table 4.2 are shown in black as shifts of the theory and at the effective redshift of the bins. The red dashed line is at the median redshift of the bins delimited by the grey dashed lines. We can see that the difference between median and effective redshifts is small with respect to the variations of D_A/r_d and the uncertainties.

4.2.2. Cosmological parameters infered from BAO

One can sample over h, Ω_b, and Ω_{cdm} to constrain these parameters by comparing the expected α_i (Eq. (4.2), Eq. (1.38) and Eq. (1.49)) to the measured α_i, $i \in [1,13]$ obtained by template fitting in each individual bins. We list in Table 4.2 the values of α_i and the associated uncertainties obtained by template fitting. In Fig. 4.6, we show the constraints on h, Ω_b, and Ω_{cdm}. We obtain $h = 0.669 \pm 0.003$, $\Omega_b \times 10^2 = 4.921^{+0.044}_{-0.046}$, and $\Omega_{cdm} = 0.293^{+0.023}_{-0.022}$, which is in agreement with the simulation cosmology, though Ω_{cdm} is at the 1σ limit. Using a noise-free synthetic $w(\theta)$ computed like the theoretical model instead of the measured $w(\theta)$ to extract the $\alpha_i, i \in [1,13]$ and then obtain cosmological constraints with the same analysis, we check that the bias on Ω_{cdm} decreases from 1 to 0.3σ.

We studied how cosmological constraints are affected by the exclusion of some redshift bins from this analysis. Figure 4.7 groups all results for h, Ω_b, and Ω_{cdm} with *Planck* priors as inferred from α_i, $i \in [1,13]$ obtained by template fitting on $w(\theta)$ measured on Flagship in blue or on the noise-free synthetic $w(\theta)$ in orange. We performed 13 estimations removing each of the 13 redshift bins alone. We then observed that redshift bin 11 seems to have a large weight in shifting h towards smaller

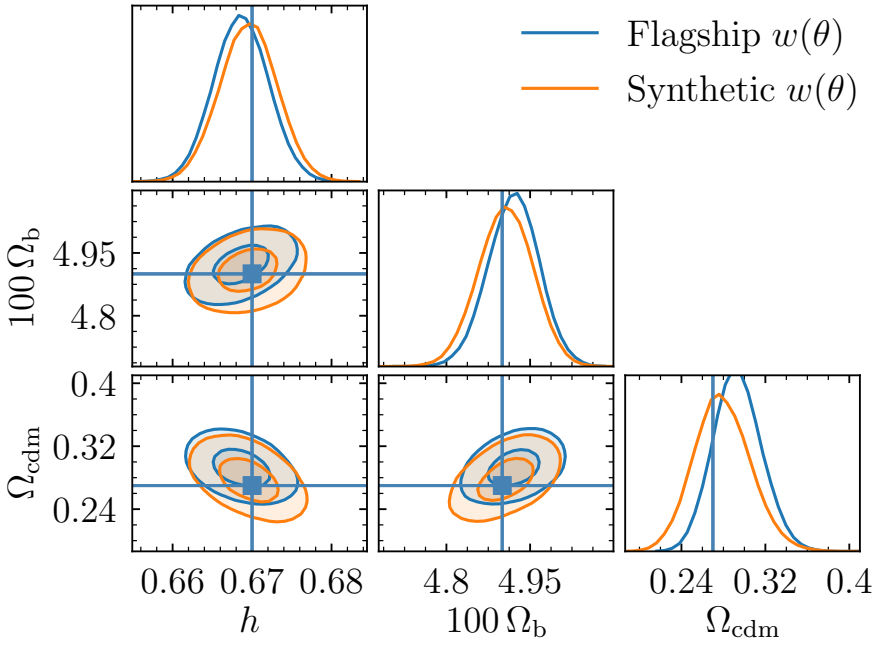


Figure 4.6. – Constraints on h, Ω_b, and Ω_{cdm} with *Planck* priors.

values : when this bin is excluded, we obtain a lower bias on h, Ω_b, and Ω_{cdm} with a shift with respect to the true cosmology of about 0.3, 0.2, and 0.4 σ respectively. Removing the other bins has a much smaller effect. In the same Fig. 4.7, results are also shown when removing redshift bins with no BAO detection (bins 1, 4, and 6), low redshift bins (1 to 8), high redshift bins (9 to 13). Apart from the effect seen from removing bin 11, we find that high redshift bins tend to bias h towards lower values while Ω_b and Ω_{cdm} are biased towards larger values. However, high redshift bins also provide the tighest constraints, with an increase of the uncertainty of h, Ω_b, and Ω_{cdm} by 23 %, 30 %, and 87 % respectively when they are removed. This is explained by the large amount of cosmological information contained in these bins which have a combined effective volume 6 times as large as low redshift bins as shown in Table 3.1. The BAO peak is also better defined at high redshift due to the smearing which occurs at low redshift with the non-linear evolution of large scale structures, to the point where the BAO signal is detected with a significance which is up to 3.6 times as large as in low redshift bins Table. 4.2.

As for the results obtained from the synthetic $w(\theta)$, we find that shifts of h, Ω_b, and Ω_{cdm} shown in orange in Fig. 4.7 with respect to their fiducial values is on average decreasing from 0.4, 0.4, and 0.9 σ with the measured data vector to 0.1, 0.1, and 0.3 σ with the synthetic one. The constraining power is also robust with respect to the bins when excluded one by one, with an average variation smaller than 2 % for h and Ω_b, 7 % for Ω_{cdm}. With the synthetic data vector, the increase of the uncertainties when removing high redshift bin is smaller with 16 %, 17 %, and 63 % respectively.

As a comparison, we also show the constraints obtained from the same α_i values ($\alpha_i \in [0.8, 1.2]$, see Table 4.1) without *Planck* prior and either broad uniform priors

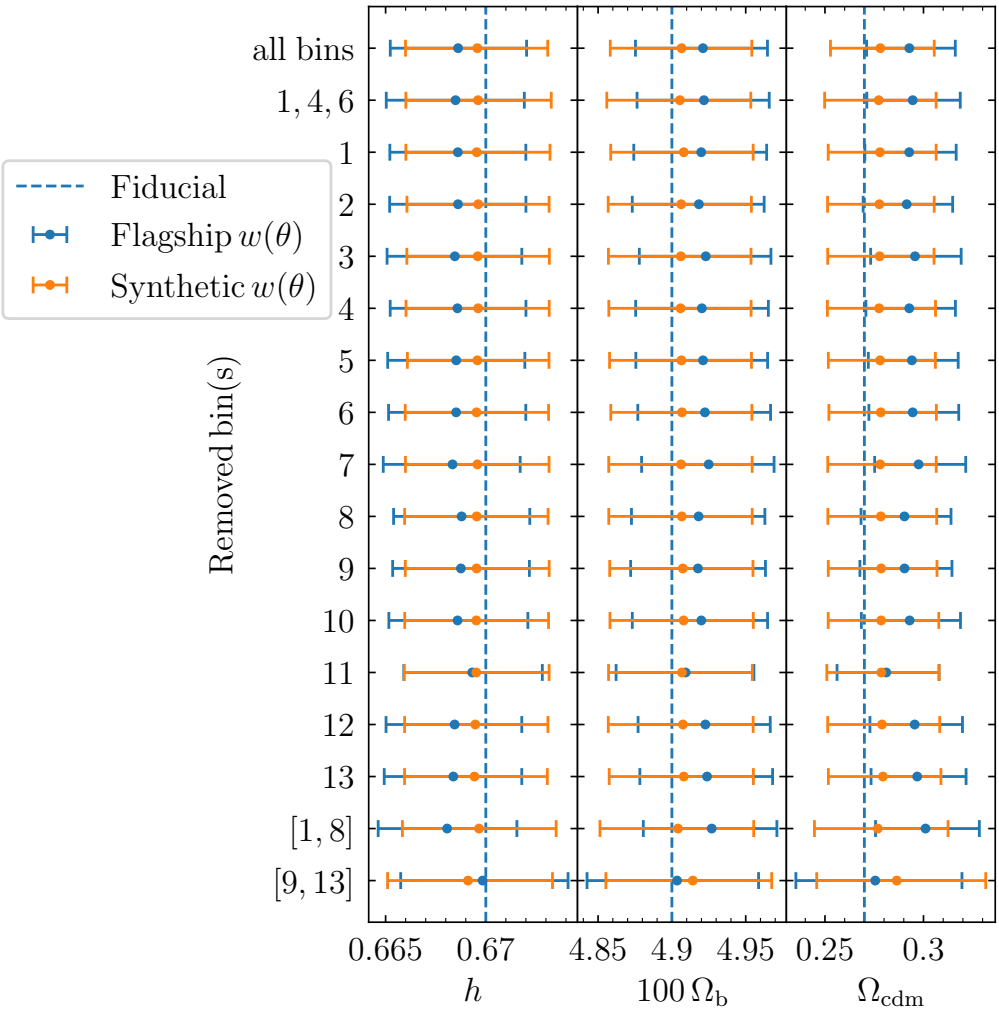


Figure 4.7. – Comparison of cosmological parameters obtained when one or several redshift bins are removed from the analysis. The fiducial values of the simulation is highlighted as a vertical dashed line. The baseline including all bins is shown at the top as a reference. The results in blue and orange are respectively obtained from the α_i extracted by template fitting of the $w(\theta)$ measured on Flagship and a noise-free synthetic $w(\theta)$.

in Fig. 4.8 or smaller ones in Fig. 4.9. In the former case, we use $h \in [0.2, 1.0]$, $\Omega_\mathrm{b} \in [0.0002, 0.1]$, and $\Omega_\mathrm{cdm} \in [0.00004, 0.99]$ while in the latter case, we use $h \in [0.6, 0.8]$, $\Omega_\mathrm{b} \in [0.039, 0.059]$, and $\Omega_\mathrm{cdm} \in [0.17, 0.37]$. The goal of this comparison is to show that *Euclid* photometric galaxy clustering will not provide competitive constraints alone, without *Planck* prior and very large priors. However, we see that with reasonable assumptions on the value of the parameters, we can still constrain h, Ω_b, and Ω_cdm at 8.5 %, 10.8 %, and 19.3 %.

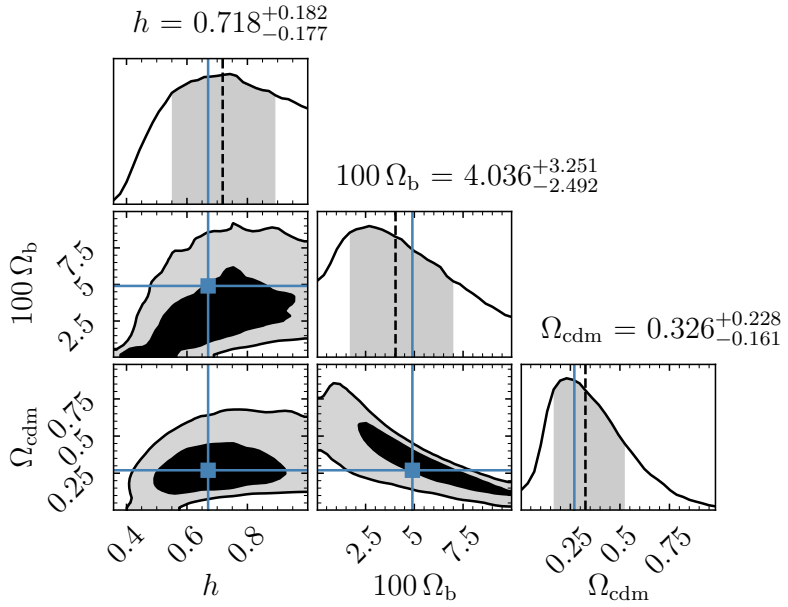


Figure 4.8. – Constraints on h, Ω_b, and Ω_cdm without *Planck* priors and large uniform priors are used with $h \in [0.2, 1.0]$, $\Omega_\mathrm{b} \in [0.0002, 0.1]$, and $\Omega_\mathrm{cdm} \in [0.00004, 0.99]$. In this case, the three cosmological parameters are poorly constrained.

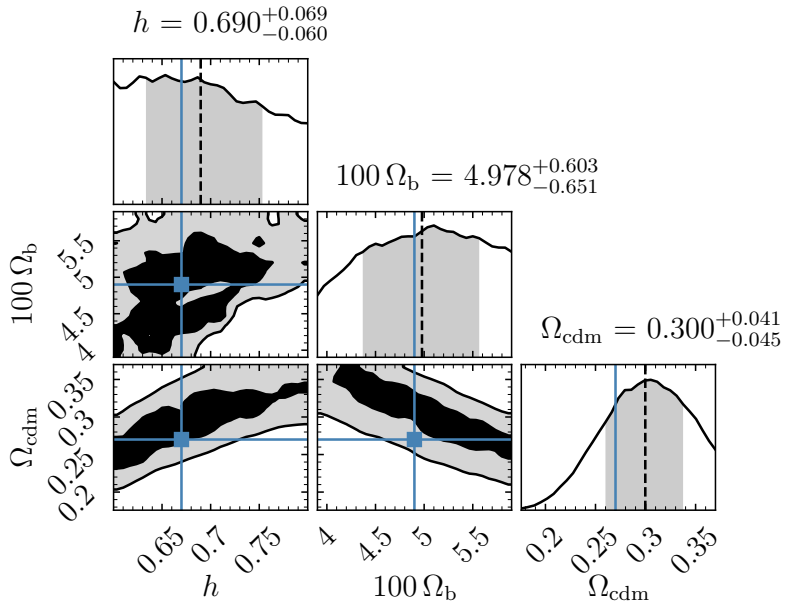


Figure 4.9. – Constraints on h, Ω_b, and Ω_cdm without *Planck* priors and smaller uniform priors $h \in [0.6, 0.8]$, $\Omega_\mathrm{b} \in [0.039, 0.059]$, and $\Omega_\mathrm{cdm} \in [0.17, 0.37]$.

4.3. Constraints on α from a joint analysis

This section aims at providing a joint constraint on α, with a single value using all redshift bins. This is the approach traditionally used in previous surveys and the robustness of this analysis is verified by excluding redshift bins successively. However, we will also explain why this approach reaches the limits of its theoretical approximations with *Euclid*.

4.3.1. Methodology for the joint analysis

In this subsection, we use the same template 1, defined in Eq. (4.1) which we extend to account for specific nuisance parameters B_i, $A_{0,i}$, $A_{1,i}$, and $A_{2,i}$ with $i \in [1,13]$ for a total of 53 parameters. Following the increase of the dimensionality, we now use 130 walkers, still initialized with a small ball around the expected true value of the parameters with a dispersion of 10^{-4}. However, we also test a larger initialization with a dispersion of 10^{-2} in Sect. 4.4.6. Scale cuts are unchanged with respect to the individual bin analysis : $\theta_{\rm min} = 0.60°$, $\theta_{\rm max} = \theta_{\rm BAO} + 2.50°$. We use the analytical covariance (Gaussian and SSC) for this joint analysis.

We explain the use of profile likelihood instead of MCMC for this joint analysis in Sect. 4.4.6. When the MCMC technique is used, the Gelman–Rubin convergence criterion is adapted to $R_{\rm GR} - 1 = 0.02$ to ensure convergence of the parameters and their uncertainties without running unnecessarily long chains. The resolution of the grid of α on which this polynomial is evaluated is increased to use steps of 0.0001 to match the increased constraining power (against 0.001 for the analyses of individual bins).

4.3.2. Results with the baseline joint analysis

For this joint analysis with all redshift bins, we report a constraint of $\alpha = 1.0011^{+0.0078}_{-0.0079}$ which represents a constraint at the sub-percent level, obtained with a profile likelihood approach shown in Fig. 4.10. This might seem optimistic given that it represents an improvement by a factor 3 with respect to the latest results from Abbott, Adamow, et al. (2024) (DES Y6) which yield a constraint of α at 2.4 % with the two-point angular correlation function. The investigations presented in Sect. 4.4.6 suggest that the improvement could even reach a factor 4.4. However, several factors are to be taken into account in this comparison. The first one is that this work uses data from a simulation and so it is inherently optimistic since it is free from systematic effects while DES Y6 uses observations and has to correct them. In DES Y6, 5 redshift bins between $0.7 < z < 1.2$ are used whereas the Flagship sample is here divided into 13 redshift bins between $0.2 < z < 2.5$, which increases significantly the constraining power of the joint analysis. We quantified the significance of the BAO detection $\Delta_{\rm det}$ defined in Eq. (4.6) to be $\Delta_{\rm det} = 10.3\,\sigma$ with a profile likelihood approach with our data compared to $3.5\,\sigma$

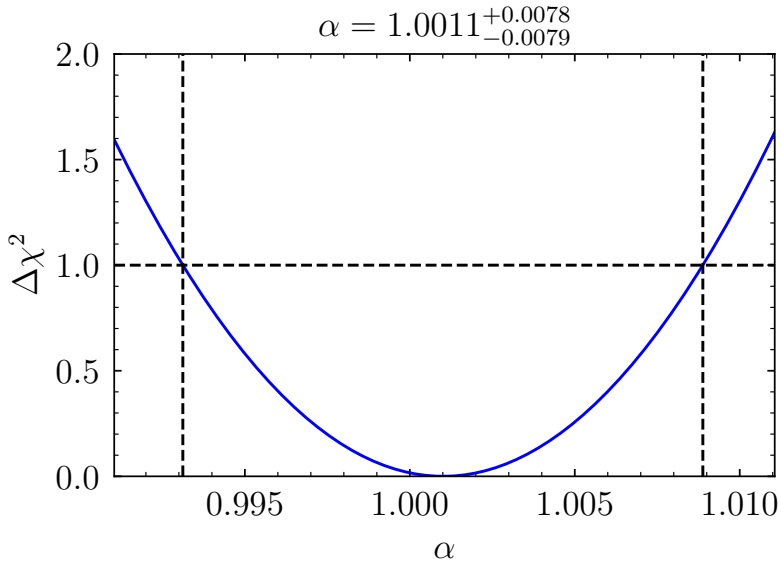


Figure 4.10. – Profile likelihood of α from a joint analysis. The $\Delta\chi^2 = 1$ determines the one sigma uncertainty with $\alpha = 1.0011^{+0.0078}_{-0.0079}$.

in DES Y6. We also find significantly tighter constraints in each individual redshift bins, contributing to this result.

We further investigate this result by using a similar approach to DES Y6 by excluding redshift bins in which the BAO signal is not detected with sufficient strength. After excluding the redshift bins with no significant detection (bins 1, 4, and 6), we report a value $\alpha = 1.0023^{+0.0080}_{-0.0084}$, almost identical to the result obtained by including all the redshift bins. The fact that the increase of the uncertainty is as small as 4.5 % despite removing three out of 13 bins can be understood by the fact that if redshift bins have no significant detection of the BAO signal then they provide very little constraining power on α.

We continue to validate this constraint by evaluating the impact of the different redshift bins in the joint analysis. This is done by removing each of the thirteen redshift bin one at a time. The constraints on α of all these cases are shown in Fig. 4.11. While most bins have very little effect over the constraints, removing the redshift bin 11 at $z_{\rm eff} = 1.245$ from the joint analysis decreases α by $1\,\sigma_{\rm all\,bins}$. It also increases uncertainties by 11 %, which is expected given that we remove one bin out of 13. Moreover, this is the redshift bin with the most constraining power so this is perfectly normal. This constraining power can be understood by studying the properties of the photometric redshifts computed for the Flagship galaxy mock catalogue. Indeed, comparing them to the true redshifts of the simulation using the same binning, we find that with a measure of the scatter $\sigma_{\rm NMAD}$ robust to outliers and defined as

$$\sigma_{\rm NMAD} = 1.4826 \times \text{median}\left(\frac{\Delta z - \text{median}(\Delta z)}{1 + z_{\rm true}}\right) \tag{4.10}$$

where $\Delta z = z_{\rm ph} - z_{\rm true}$, bin 11 has a scatter which is about 25 % smaller than bins 12

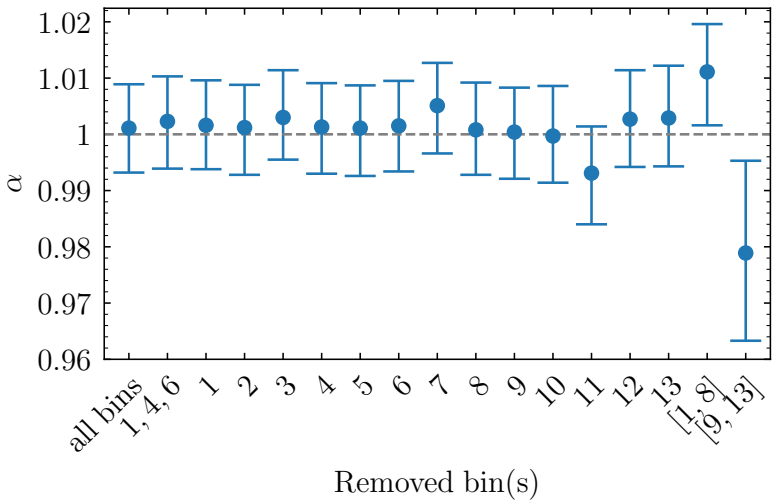


Figure 4.11. – Comparison of α from a joint analysis in which redshift bins are successively removed. Bin 11 of effective redshift $z_{\rm eff} = 1.245$ has a larger effect over the joint constraints compared to other bins, as one can see from the shift and increase of the uncertainty when it is not included. Selecting high or low redshift bins induces respectively a 1.3 or 2.8 $\sigma_{\rm all\,bins}$ shift towards higher or lower values for α.

and 13. The combination of good photometric redshifts and high redshift explains the importance of this bin.

Bin 7 also creates an important shift of 0.6σ when removed but towards larger values of α, due to the very low $\alpha = 0.932^{+0.072}_{-0.054}$ measured in this bin. If we compare constraints from bins with redshift $z_{\rm eff} < 0.9$ to the baseline with all bins, we find that α is shifted by $2.8\sigma_{\rm all\,bins}$ towards smaller values and its uncertainty is increased by a factor of two. On the contrary, including high redshift bins $z_{\rm eff} > 0.9$ and removing low redshift bins, the shift towards a larger value of α is limited to $1.3\sigma_{\rm all\,bins}$. The uncertainty is only increased by 14.6 %, in this case. These results can be understood in light of the constraints from individual bins detailed in Table 4.2. Bins at $z_{\rm eff} < 0.9$ with the largest $\Delta_{\rm det}$ are biased towards low values of α_i, which explains why the joint value of α increases when they are removed. On the other hand, bins at $z_{\rm eff} > 0.9$ are overall biased towards larger values of α_i, which explains why removing them decreases the value of the joint α. The large difference in the uncertainties of these last two cases (1.3 against $2.8\sigma_{\rm all\,bins}$) can be explained by the much tighter constraints obtained at high redshift, where the BAO peak is not smeared.

An important caveat to fitting a unique α to all redshift bins is that it assumes a perfect match between the fiducial cosmology and the true cosmology of the Universe which is unknown. Any mismatch will lead to a variation of α which depends on redshift. This effect can be quantified thanks to the definition of α in Eq. (4.2) in which $D_{\rm A}$ and $r_{\rm s,\,drag}$ are computed for different cosmologies while $D_{\rm A,\,fid}$ and $r_{\rm s,\,drag,\,fid}$ are constant at the fiducial cosmology of the Flagship simulation. We check that varying $\Omega_{\rm cdm}$, $\Omega_{\rm b}$, and h by 5 % leads to a maximum expected variation of α of 1 %

between the first and last redshift bin. This maximum variation of α scales linearly as $\alpha(z_{\rm eff}=1.922)/\alpha(z_{\rm eff}=0.290) \propto 0.2\,\Delta(\Omega_{\rm cdm},\Omega_{\rm b},h)$. Given the constraint obtained on α, this effect is non negligible and is a limit to this joint analysis. This is one of the reasons motivating the analysis in individual redshift bins presented in Sect. 4.1.

4.4. BAO, a robust probe

In this section, we repeat our individual bin analyses with variations of the baseline choices to quantify the effect of the fiducial cosmology, template, RSD, scale cuts, redshift binning and covariance matrix over our constraint both at the level of α and cosmological parameters. We also provide a study of the constraints as a function of the number of redshift bins, their type (equipopulated or equidistant) and the magnitude cut used as a guide for future analyses.

4.4.1. Influence of the fiducial cosmology

The impact of the choice of fiducial cosmology is investigated by varying h from 0.67 to 0.73. Galaxy bias is fitted again before repeating the MCMC analysis bin by bin. We expect a shift of α by a factor

$$\frac{D_{\rm A}(h=0.73,\Omega_{\rm b},\Omega_{\rm cdm})}{r_{\rm s,\,drag}(h=0.73,\Omega_{\rm b},\Omega_{\rm cdm})}\,\frac{r_{\rm s,\,drag}(h=0.67,\Omega_{\rm b},\Omega_{\rm cdm})}{D_{\rm A}(h=0.67,\Omega_{\rm b},\Omega_{\rm cdm})}=0.982\,. \tag{4.11}$$

After correction by this shift, we measure a remaining maximum relative difference $|\Delta\alpha|/\alpha$ of 0.5 %, the average over all redshift bins being 0.12 %. This is illustrated in Fig. 4.12. As an additional test, we vary $\Omega_{\rm cdm}$ by $\pm 5\,\sigma_{Planck}$, keeping $h=0.67$ and $\Omega_{\rm b}=0.049$. With $\Omega_{\rm cdm}=0.281$ and $\Omega_{\rm cdm}=0.259$, we respectively find a remaining maximum relative difference $|\Delta\alpha|/\alpha$ of 0.9 % and 0.4 %, the average over all redshift bins being 0.31 % and 0.13 %. These variations are negligible when compared to the uncertainties on α, which shows that the analysis is robust against the choice of fiducial cosmology.

4.4.2. Influence of the template

The polynomial correction applied in the template is defined arbitrarily and different choices can be found in the literature. It is important to check whether the polynomial includes enough orders to absorb eventual non-linearities of the galaxy bias. In this context, we explore ten different combinations of orders leading to the ten templates using the same scale cuts and fiducial cosmology as for the analysis of the individual bins. The templates considered in this analysis are the following:

— template 1: $B\,w_{\rm fid}(\alpha\theta)+A_0+\frac{A_1}{\theta}+\frac{A_2}{\theta^2}$
— template 2: $B\,w_{\rm fid}(\alpha\theta)+A_0+A_1\theta+\frac{A_2}{\theta}$
— template 3: $B\,w_{\rm fid}(\alpha\theta)+A_0+A_1\theta+\frac{A_2}{\theta^2}$

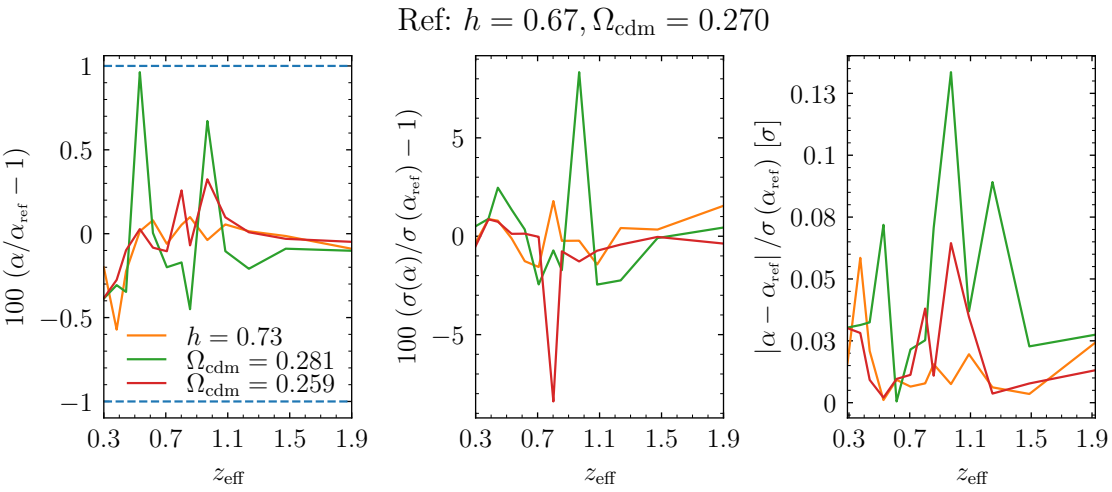


Figure 4.12. – Effect of the fiducial cosmology on α in all redshift bins for three variations replacing $h = 0.67$ by $h = 0.73$, $\Omega_{\rm cdm} = 0.270$ by $\Omega_{\rm cdm} = 0.281$, and $\Omega_{\rm cdm} = 0.259$. The dashed line in the first panel shows a relative difference of 1 % which is not exceeded at all redshifts. The effect of the fiducial cosmology on α is negligible with respect to the uncertainties varying between ± 0.13 and ± 0.024 and the effect on its uncertainty is smaller than 3 % except for redshift bins 6 and 8 with respectively $-5\,\sigma_{Planck}$ and $+5\,\sigma_{Planck}$ on $\Omega_{\rm cdm}$, as can be seen in the second panel. The last panel represents the shift of the various measurements computed in sigmas as $\frac{|\alpha-\alpha_{\rm ref}|}{\sigma_{ref}}$.

— template 4: $B\,w_{\rm fid}(\alpha\theta) + A_0 + A_1\theta + A_2\theta^2$
— template 5: $B\,w_{\rm fid}(\alpha\theta) + A_0 + \frac{A_1}{\theta} + A_2\theta^2$
— template 6: $B\,w_{\rm fid}(\alpha\theta) + A_0 + \frac{A_1}{\theta}$
— template 7: $B\,w_{\rm fid}(\alpha\theta) + A_0 + \frac{A_1}{\theta} + \frac{A_2}{\theta^2} + \frac{A_3}{\theta^3}$
— template 8: $B\,w_{\rm fid}(\alpha\theta) + A_0 + \frac{A_1}{\theta} + \frac{A_2}{\theta^2} + \frac{A_3}{\theta^3} + \frac{A_4}{\theta^4}$
— template 9: $B\,w_{\rm fid}(\alpha\theta) + A_0 + \frac{A_1}{\theta} + \frac{A_2}{\theta^2} + A_3\theta$
— template 10: $B\,w_{\rm fid}(\alpha\theta) + A_0 + \frac{A_1}{\theta} + \frac{A_2}{\theta^2} + A_3\theta + A_4\theta^2$

The comparison of the resulting α for each template with respect to the fiducial template 1 is shown in Fig. 4.13. Constraints from templates 2, 4, 5, and 6 are highlighted because they are consistent with each other and quite different from the reference at low redshift. These templates do not have a term in $1/\theta^2$. From this observation, it seems that this order is needed. We find that the one sigma uncertainty on α is systematically underestimated by 10 % with templates 2, 4, 5, and 6. This result is still observed when a noise-free synthetic data vector is used instead of the measured two-point correlation function. On the contrary, we see almost no variation of the results between the other templates with additional orders $\theta^{-3}, \theta^{-4}, \theta, \theta^2$. The shifts on α are smaller than $0.15\,\sigma$. This trend is also observed when cosmological constraints are inferred, with a small but very clear shift in the posterior distributions of $\Omega_{\rm cdm}$ for

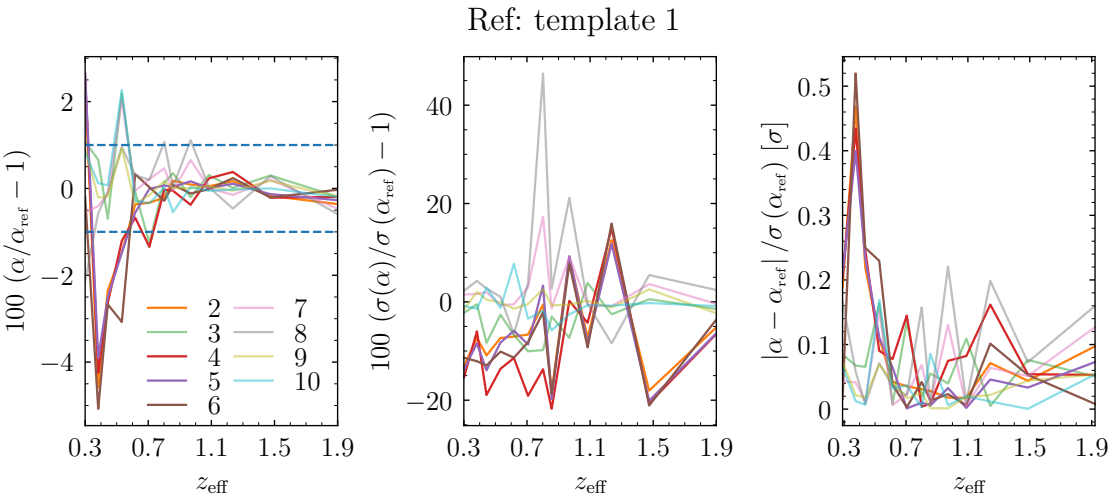


Figure 4.13. – Comparison of templates for BAO fitting as a function of redshift bin. The first panel represents the shift of α with respect to the reference (template 1). We highlight by transparency templates 2, 4, 5, and 6 which do not include a term in θ^{-2} to showcase the fact that they all have larger shifts at low redshift. The 1% dashed blue line is a reference to guide the eye rather than a goal, given that the uncertainty on α is much larger in the first bins. In the second panel, we see that the highlighted templates underestimate the uncertainty while the last panel represents the agreement of the various measurements computed in sigmas as $\frac{|\alpha-\alpha_{\rm ref}|}{\sqrt{\sigma^2+\sigma^2_{ref}}}$.

templates 2, 4, 5, and 6, as shown in Fig. 4.14. Given the similar constraints between the other templates, template 1 was chosen for the main analysis.

Another important aspect of the robustness of the template is to be able to handle shifts of the fiducial cosmology with respect to the true cosmology. As such, the previous comparison was repeated in a setup where the fiducial cosmology was altered to differ from the cosmology from the Flagship simulation, using $h = 0.73$ instead of $h = 0.67$. In this case, we find that the absolute shift of α with respect to the expected value of 1 averaged over all redshift bins $\langle|1-\alpha|\rangle$ for templates 1, 3, 7, 8, 9, 10 (we exclude templates without order θ^{-2}) is respectively 0.030, 0.033, 0.030, 0.030, 0.031, and 0.032. Table 4.7 groups all the results of this analysis, showing no preference for including higher orders in the template polynomial when it comes to robustness with respect to the choice of fiducial cosmology.

4.4.3. Influence of redshift space distortions

In this section, we check whether including RSD in the theoretical model described in Sect. 3.2.1 affects the constraints on α. The effect of RSD over the two-point angular correlation function is illustrated in Fig. 3.1. The correlation function amplitude is

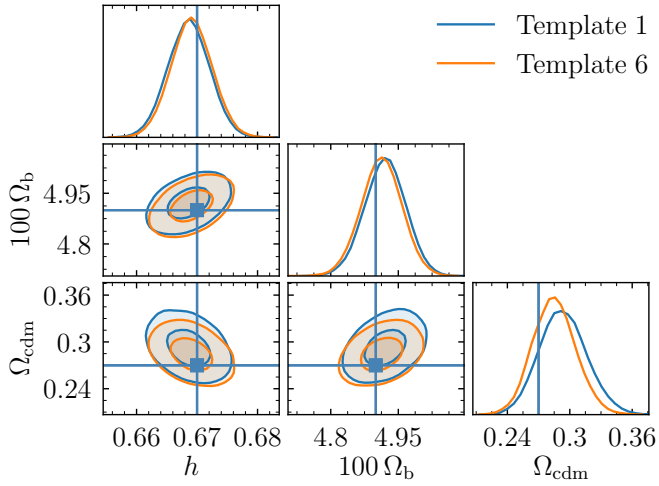


Figure 4.14. – Comparison of templates 1 and 6 for BAO fitting at the level of cosmological parameters. Templates 3, 7, 8, 9 and 10 show contours that are similar to the reference template 1. Templates 2, 4, and 5 have similarly biased contours like template 6. The shift seen most clearly on the posterior distribution of Ω_{cdm} is the effect of omitting the polynomial term in θ^{-2}.

increased at large scales and low redshift. However, the actual position of the BAO scale remains unchanged and we see in Fig. 4.15 that this is reflected in the constraints obtained from the MCMC analysis. The template nuisance parameters compensate for the effect of RSD with a significant decrease of A_1, while A_0 and A_2 are slightly increased. This trend holds in all redshift bins except the last one where the amplitude of these shifts becomes negligible. The relative difference $|\Delta\alpha|/\alpha$ averaged over all redshift bins is 0.25 %, the maximum being 0.5 %. As for the uncertainty of α, its variations do not exceed 3.7 % and are on average 1.4 %. Thanks to the freedom in the broadband of the template fitting approach, the analysis is robust with respect to redshift space distortions. In any case, as explained in Sect. 3.2.1, RSD are included in the analysis.

4.4.4. Influence of the scale cuts

The large redshift range $0.2 \leq z \leq 2.5$ included in this configuration space analysis entails that θ_{BAO} varies between 1.6°and 7.0°. In this situation, using a single scale cut for all bins or a redshift-dependent one is not an obvious decision to make. A first study of how α varies as a function of θ_{min} and θ_{max} was performed with a fitting approach on a grid defined by $\theta_{min} \in [0.2°, \theta_{BAO} - 1.0°]$ and $\theta_{max} \in [\theta_{BAO} + 1.0°, \theta_{BAO} + 3.0°]$ by steps of 0.1°. The smallest data vector considered is $\theta_{BAO} \pm 1.0°$ with 20 points.

The results of this study are shown in Fig. 4.16. The bias $\alpha - 1$ varies with θ_{min}, with a clear cut-off at $\theta = 1.0°$. Increasing θ_{min} beyond this cut-off tends to bias α, especially at low redshift, where the BAO signal is smeared by the non-linear evolution of large

Table 4.7. – α obtained with the reference template 1 and templates including higher polynomial orders using a fiducial cosmology which differs from the simulation cosmology (h=0.73 against h=0.67). $\langle|1-\alpha|\rangle$ and $\langle\sigma_{68}\rangle$ are respectively the bias and the uncertainty of α averaged over all redshift bins. We find that template 1 has the smallest $\langle\sigma_{68}\rangle$ among templates of minimum bias $\langle|1-\alpha|\rangle = 0.030$.

T	Bin 1	2	3	4	5	6	7	8	9	10	11	12	13	$\langle\lvert1-\alpha\rvert\rangle$	$\langle\sigma_{68}\rangle$
1	1.013	1.046	0.969	1.011	1.012	0.996	0.949	1.069	1.047	1.032	1.049	1.011	1.010	0.030	0.068
3	1.038	1.057	0.956	1.014	1.003	0.979	0.949	1.066	1.038	1.033	1.048	1.012	1.009	0.033	0.064
7	1.010	1.042	0.970	1.027	1.010	0.996	0.952	1.068	1.056	1.032	1.047	1.013	1.007	0.030	0.070
8	0.992	1.052	0.969	1.017	1.015	1.000	0.956	1.070	1.059	1.032	1.045	1.015	1.005	0.030	0.070
9	1.034	1.052	0.970	1.016	1.005	0.994	0.949	1.067	1.049	1.032	1.048	1.012	1.009	0.031	0.067
10	1.026	1.052	0.967	1.016	1.012	0.993	0.947	1.063	1.048	1.032	1.048	1.012	1.010	0.032	0.062

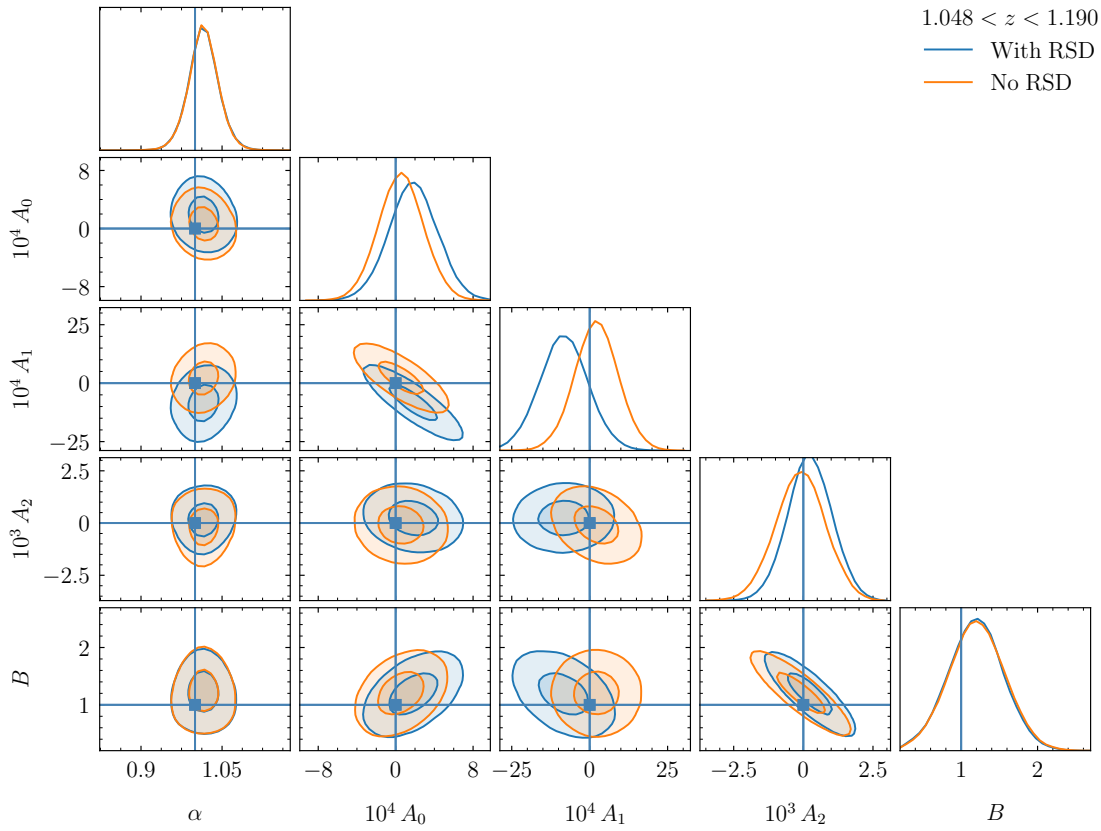


Figure 4.15. – Comparison of the constraints on α with and without RSD in the theoretical model for the redshift bin 1.048 < z < 1.190. The posterior distribution of α is visually identical, the effect of RSD is completely absorbed by nuisance parameters.

scale structures. While a pronounced evolution of α with $\theta_{\rm max} - \theta_{\rm BAO}$ is visible at low

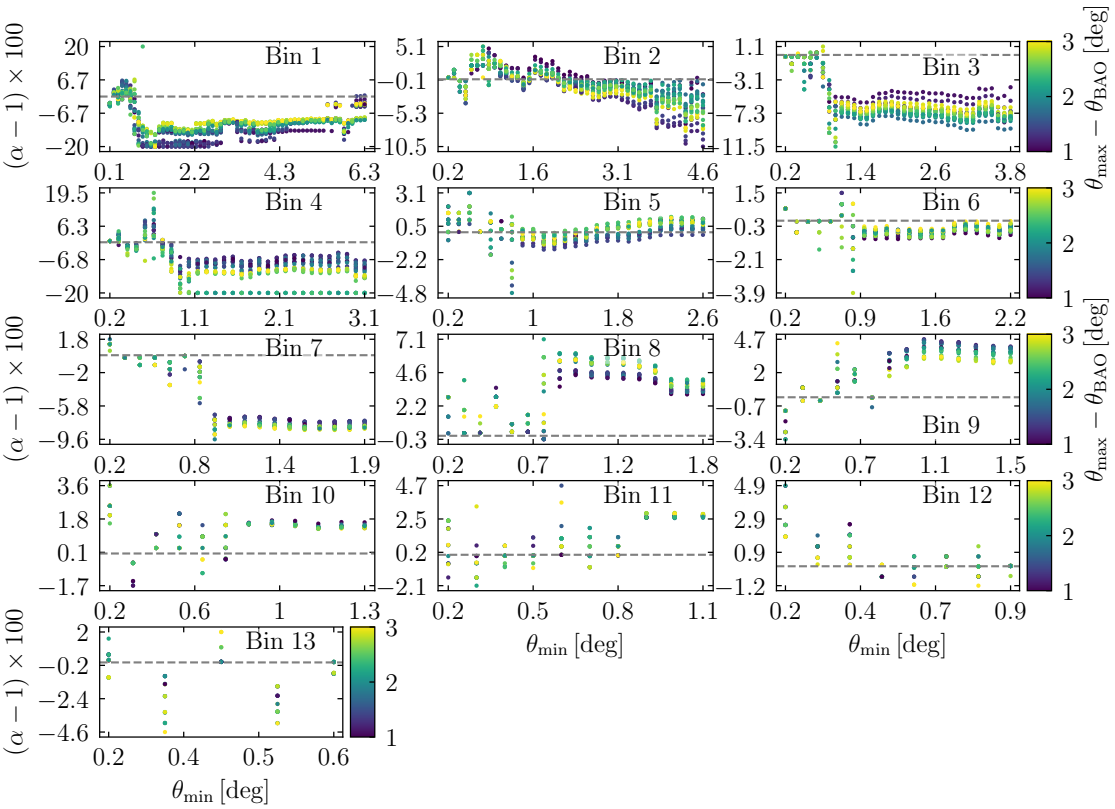


Figure 4.16. – Bias $(\alpha-1)\times 100$ as a function of $\theta_{\rm min}$ and $\theta_{\rm max}$ (colour) in the 13 redshift bins of the analysis. The dashed line corresponds to $\alpha-1=0$. In this analysis, α is obtained by best fit rather than MCMC. In almost all redshift bins, including small scales helps in recovering an unbiased estimate of α.

redshift when $\theta_{\rm min}\geq 1.0°$, no clear trend can be found when $\theta_{\rm min}\leq 1.0°$, where the bias is the smallest.

Following these observations, a MCMC study was then carried out on a smaller grid defined as $\theta_{\rm min}\in[0.5°,0.7°]$ with the same $0.1°$ resolution and $\theta_{\rm max}\in[\theta_{\rm BAO}+1.0°,\theta_{\rm BAO}+2.5°]$ with steps of $0.5°$. On this grid, no significant variation of α was observed with both $\theta_{\rm min}$ and $\theta_{\rm max}-\theta_{\rm BAO}$. The same observations were made when the analytical Gaussian covariance was used instead of the jackknife covariance. The final scale cut chosen was then $\theta_{\rm min}=0.6°,\theta_{\rm max}=\theta_{\rm BAO}+2.5°$ as it yielded the most robust results across all redshift bins. In the $\theta_{\rm min},\theta_{\rm max}$ grid used for the MCMC, the α_i extracted in all bins are in agreement within $0.06\,\sigma$ on average and at most $0.25\,\sigma$. We can see two example of the results in bin 2 and 12 in Fig. 4.17 and Fig. 4.18 respectively. There is a very clear effect of the minimum scale cut $\theta_{\rm min}$ on nuisance parameters B and A_2 in bin 3 and mostly A_2 in bin 13. However, the value of α is mostly unaffected thanks to the template. The effect on h, $\Omega_{\rm b}$, and $\Omega_{\rm cdm}$ inferred from the α_i shown in Fig. 4.19 and is on average $0.05\,\sigma$ while never exceeding $0.14\,\sigma$. The largest difference is seen on $\Omega_{\rm cdm}$ with $\theta_{\rm min}=0.5°$.

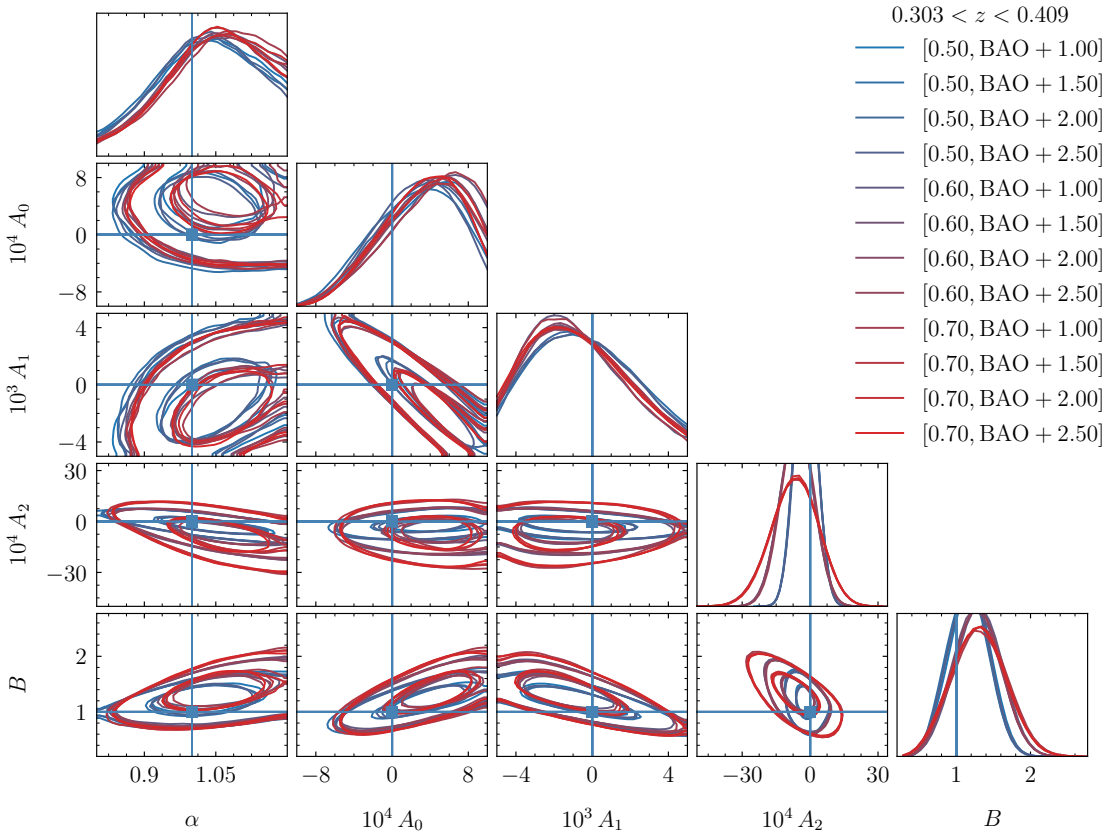


Figure 4.17. – Comparison of the constraints obtained for α in bin 2 when the scale cuts applied to the data vector are varied in a grid $\theta_{\rm min} \in [0.5°, 0.7°]$ by steps of 0.1° and $\theta_{\rm max} \in [\theta_{\rm BAO} + 1.0°, \theta_{\rm BAO} + 3.0°]$ by steps of 0.5°. A strong dependance with $\theta_{\rm min}$ is visible in the nuisance parameters B and A_2 but the effect over α is limited, especially when the very large uncertainty is taken intot account.

4.4.5. Influence of the redshift binning scheme

In this subsection, we show the effect of the choice of using equidistant redshift bins compared to the constraints obtained with equipopulated bins while keeping the same fiducial choice of template and scale cuts. This choice results in bins of width $\mathrm{d}z = 0.177$. For this analysis, the two-point correlation function and galaxy bias are measured in the same way as described in Sect. 3.4 for the equipopulated binning scheme. The rest of the analysis is carried out in an identical way. Using this binning scheme, we get equivalent constraints for redshift bins of similar $z_{\rm eff}$, as reported in Table 4.8 and shown in Fig. 4.20. Note that the equidistant binning does not entail regularly spaced $z_{\rm eff}$, it is still computed with Eq. (3.9). By construction, we have more bins with high $z_{\rm eff}$ where the BAO signal is not smeared by the non-linear evolution of structures due to gravitation. Simultaneously, thinner redshift bins present a BAO signal which is less diluted by intra-bin variations of the BAO scale. However, the

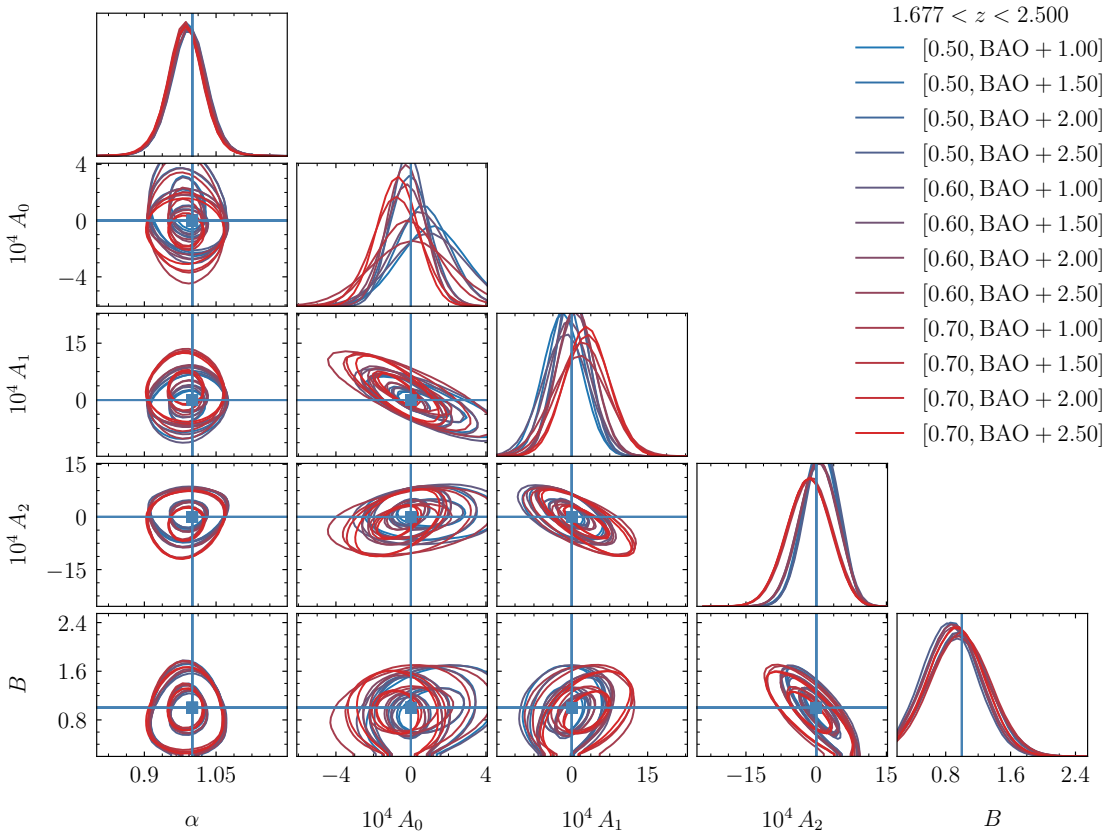


Figure 4.18. – Comparison of the constraints obtained for α in bin 13 when the scale cuts applied to the data vector are varied in a grid $\theta_{\rm min} \in [0.5°, 0.7°]$ by steps of 0.1° and $\theta_{\rm max} \in [\theta_{\rm BAO} + 1.0°, \theta_{\rm BAO} + 3.0°]$ by steps of 0.5°. The dependance with $\theta_{\rm min}$ seen in bin 2 is still found in an attenuated way, due to the better defined BAO peak.

decrease in number density entails that the error bars of the measured two-point correlation function are larger at high redshift. In our case, this compromise yields more bins with large $\Delta_{\rm det}$ and tight constraints on α. We also find several bins with low values of α, two of them being more than $1\,\sigma$ away from $\alpha = 1$, at $z_{\rm eff} = 1.993$ and 2.174.

Propagating these results to the cosmological parameters, we find $h = 0.670^{+0.003}_{-0.003}$, $\Omega_{\rm b} \times 10^2 = 4.895^{+0.044}_{-0.045}$, and $\Omega_{\rm cdm} = 0.266^{+0.017}_{-0.016}$, shown in Fig. 4.21 against the results obtained with the equipopulated redshift bins. This represents shifts of +0.1 %, −0.5 %, and +9.2 % respectively with respect to the equipopulated binning scheme, and a 36.4 % improvement in the constraining power for $\Omega_{\rm cdm}$ with respect to the equipopulated binning results. The biases we observed with respect to the fiducial cosmological parameters h, $\Omega_{\rm b}$, and $\Omega_{\rm cdm}$ are significantly smaller with $0.09\,\sigma$, $0.1\,\sigma$, and $0.24\,\sigma$ against $0.3\,\sigma$, $0.5\,\sigma$, and $1.0\,\sigma$ with the equipopulated binning scheme . The variations in the parameter values are driven by the low α value and tight constraints of bin 11 in the equidistant binning. Bin 12 has an even lower value $\alpha = 0.937$ and participates to

Table 4.8. – α extracted from the MCMC analysis in each equidistant redshift bin. The detection level $\Delta_{\rm det}$ is defined in Eq. (4.6). The detection of the BAO signal is overall stronger than with equipopulated bins, increasing the constraining power over cosmological parameters.

Bin	$z_{\rm eff}$	α	$\Delta_{\rm det}\,(\sigma)$
1	0.311	$1.076^{+0.090}_{-0.145}$	no detection
2	0.442	$0.974^{+0.145}_{-0.114}$	1.0
3	0.63	$0.971^{+0.086}_{-0.089}$	no detection
4	0.806	$0.946^{+0.076}_{-0.063}$	1.2
5	0.961	$1.033^{+0.056}_{-0.060}$	1.3
6	1.126	$1.007^{+0.052}_{-0.049}$	2.0
7	1.286	$1.022^{+0.022}_{-0.022}$	4.1
8	1.474	$1.005^{+0.035}_{-0.032}$	2.5
9	1.641	$0.955^{+0.050}_{-0.042}$	2.2
10	1.82	$0.996^{+0.028}_{-0.028}$	3.4
11	1.993	$0.962^{+0.028}_{-0.025}$	3.3
12	2.174	$0.937^{+0.057}_{-0.045}$	2.0
13	2.365	$1.001^{+0.018}_{-0.018}$	4.6

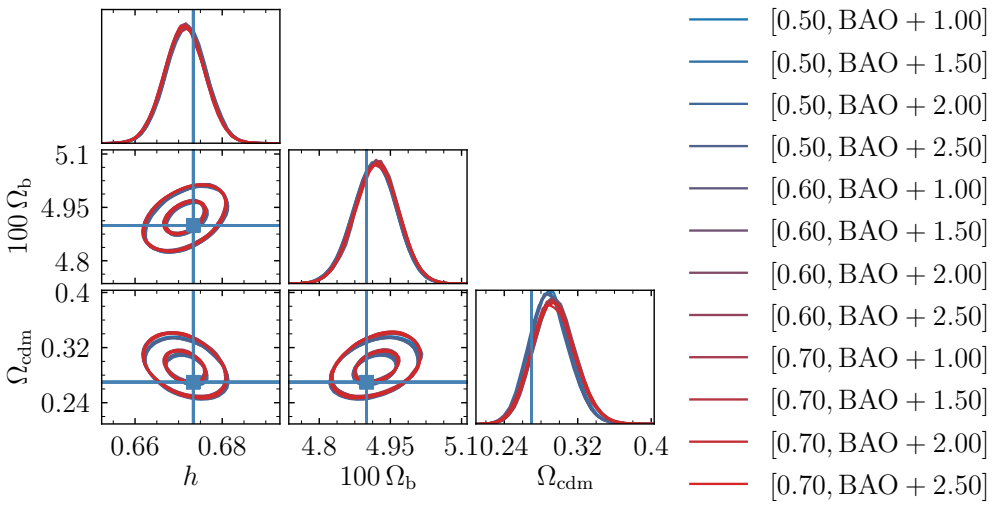


Figure 4.19. – Comparison of the constraints on h, Ω_b, and Ω_{cdm} obtained from BAO when the scale cuts applied to the data vector are varied in a grid $\theta_{min} \in [0.5°, 0.7°]$ by steps of 0.1° and $\theta_{max} \in [\theta_{BAO} + 1.0°, \theta_{BAO} + 3.0°]$ by steps of 0.5°. At the exception of Ω_{cdm} with $\theta_{min} = 0.5°$, we find that all scale cuts are visually equivalent, with an effect of $0.05\,\sigma$ on average.

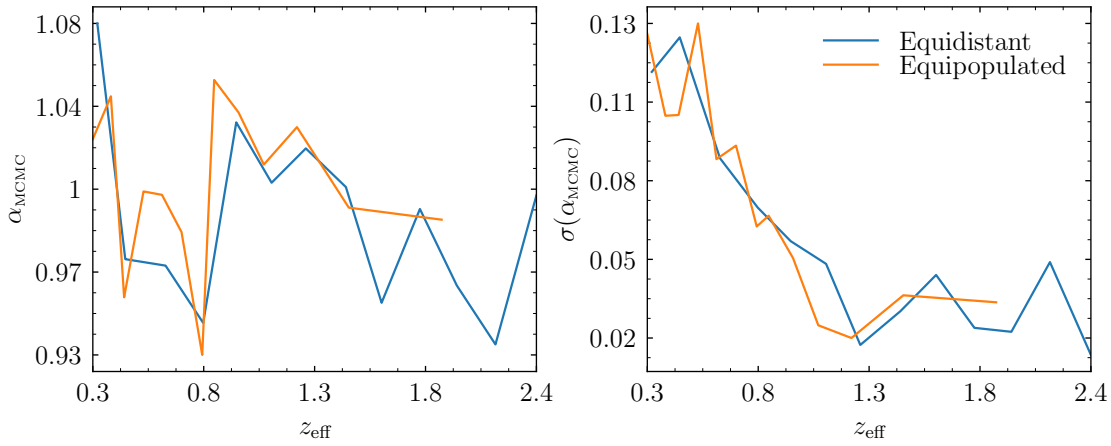


Figure 4.20. – Comparison of the constraints on α_i for the equidistant and equipopulated redshift binning schemes, in blue and orange respectively.

these variations but in a weaker way due to its uncertainty, larger than in bin 11 by a factor 2.1. Given these results, it seems that the equidistant scheme may be more suitable for the BAO analysis than the equipopulated scheme initially chosen to match the choice that maximizes the dark energy figure of merit of the 3×2-point analysis for *Euclid*. In future *Euclid* BAO analyses, an optimization of the photometric sample selection will by necessary.

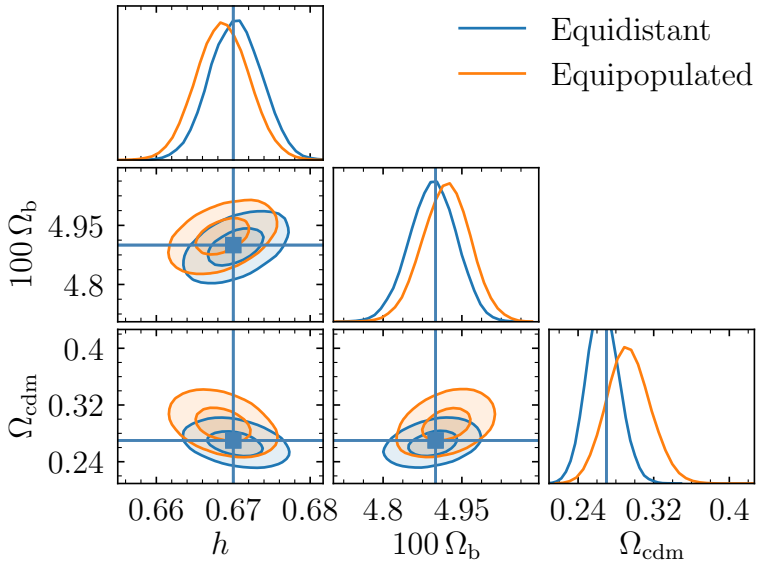


Figure 4.21. – Comparison of the constraints on cosmological parameters obtained with an equidistant and equipopulated redshift binning schemes, in blue and orange respectively.

4.4.6. Influence of the covariance

The covariance is a key component of the inference of α for both the individual bins or joint analysis. In this section, we first show how jackknife or analytical covariances influence α in individual bins with MCMC, before tackling the effect over the joint analysis with both MCMC and profile likelihood approaches. First, we compare jackknife and analytical covariances where the analytical encompasses both Gaussian and SSC contributions. As one can see in Fig. 4.22, the Gaussian+SSC covariance often yields lower values of α_i and are less biased with respect to the expected value of $\alpha = 1$. The uncertainty of α is larger at almost all redshifts. This is due to the overestimation of the $w(\theta)$ errors by the jackknife resampling with respect to the Gaussian errors shown in Fig. 3.32, especially large at high redshift. Given that the SSC contribution is much smaller than the Gaussian one at the BAO scale (see Fig. 3.33), the overestimation is as large when comparing jackknife and Gaussian+SSC. As a consequence, defining $\Delta\alpha = \alpha_{\rm G+SSC} - \alpha_{\rm jackknife}$, we find that averaging over all redshift bins, the mean relative difference $|\Delta\alpha/\alpha_{\rm jackknife}|$, mean variation of the uncertainty $|\Delta\sigma(\alpha)/\sigma(\alpha_{\rm jackknife})|$, and mean shift $|\Delta\alpha/\sigma(\alpha_{\rm jackknife})|$ are 1.5 %, 39 %, and $0.3\,\sigma$ with a maximum of 4.7 %, 99 %, and $1.4\,\sigma$.

Checking this result with a synthetic data vector, we find that the Gaussian+SSC covariance yields systematically lower values of α_i which are less biased with respect to 1. Regarding the uncertainty, it is slightly larger in the first 3 redshift bins and much smaller at higher redshift for the same reason. With the same definition as before, we find that averaging over all redshift bins, the mean relative difference, mean variation of the uncertainty, and mean shift are 0.5 %, 28 %, and $0.08\,\sigma$ with a maximum of 0.8 %,

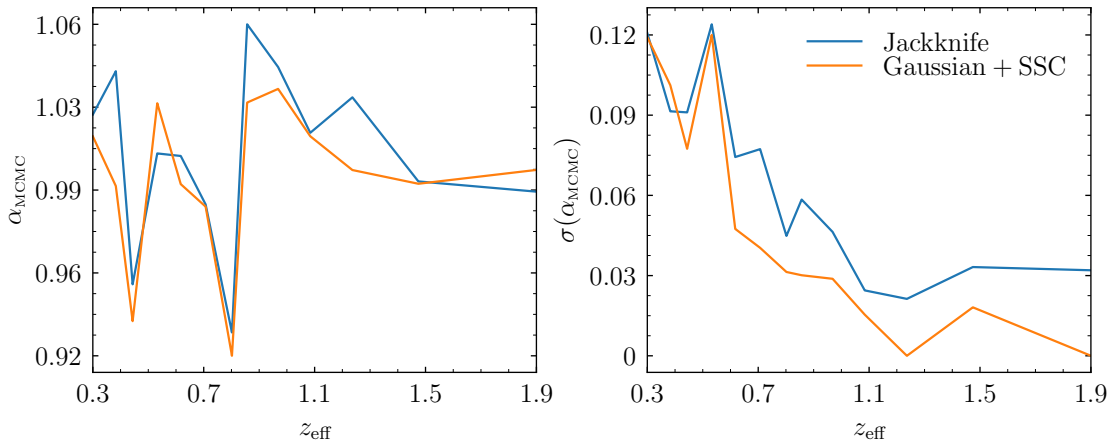


Figure 4.22. – Comparison of the constraints on α_i changing the covariance from jackknife to Gaussian+SSC.

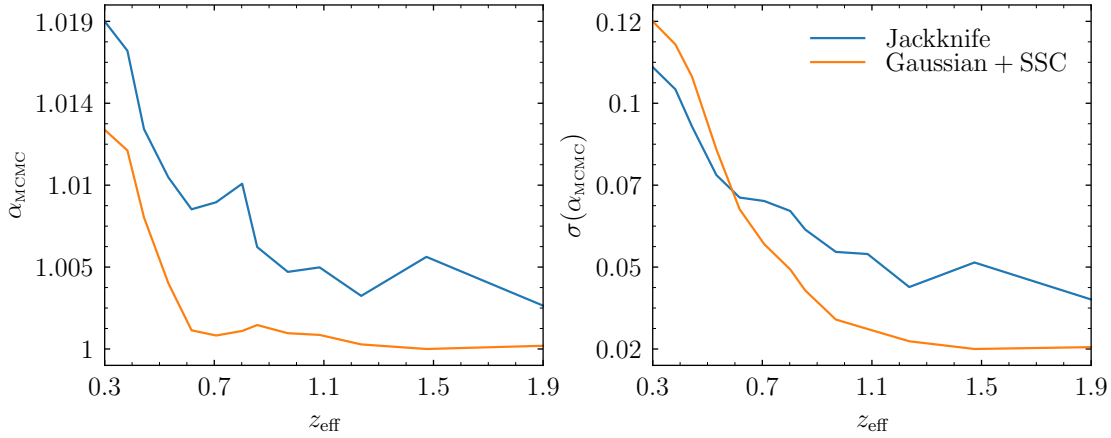


Figure 4.23. – Comparison of the constraints on α_i changing the covariance from jackknife to Gaussian+SSC, with a synthetic data vector.

55 %, and $0.13\,\sigma$.

Then, we compare Gaussian and Gaussian+SSC covariances. Given the nature of SSC, with its predominance at low redshifts and small scales, we expect a limited effect in our BAO analysis. This is indeed what is observed in our statistics. Averaging over all redshift bins, the mean relative difference $|\Delta\alpha/\alpha_{\rm G}|$, mean variation of the uncertainty $|\Delta\sigma(\alpha)/\sigma(\alpha_{\rm G})|$, and mean shift $|\Delta\alpha/\sigma(\alpha_{\rm G})|$ are 0.08 %, 0.7 %, and $0.01\,\sigma$ with a maximum of 0.4 %, 1.9 %, and $0.04\,\sigma$. These very small variations are similar with a synthetic data vector, the results being shown in Fig. 4.24. The associated averaged statistics are respectively 0.06 %, 1.5 %, and $0.009\,\sigma$.

For the joint analysis, the full jackknife covariance cannot be used because of the noise it contains, making its inversion numerically unstable. For this reason, we only report constraints using the jackknife diagonal covariance, where all off-diagonal terms are neglected. This is not a small approximation because of the strongly cor-

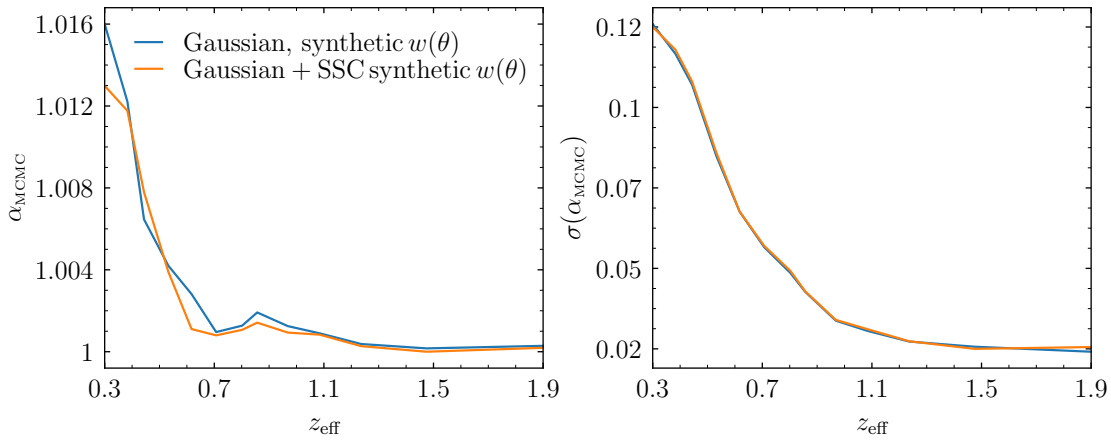


Figure 4.24. – Comparison of the constraints on α_i changing the covariance from Gaussian to Gaussian+SSC, with a synthetic data vector.

related angular scales visible in Fig. 3.8, but it allows us to derive constraints from this empirical covariance and compare them to the analytical one. The option of covariance cleaning methods like tapering was not explored but could definitely be considered in future analyses. With the diagonal jackknife covariance, we report a joint value of $\alpha = 1.0095^{+0.0108}_{-0.0108}$. This is a factor 2.2 of improvement with respect to the result of DES Y6 which constrained α at the 2.4 % level with the same observable. However, this neglects the full covariance of $w(\theta)$.

Results from the joint analyses are grouped in Table 4.9. Using the analytical covariance Gaussian+SSC, the MCMC technique yields a very optimistic $\alpha = 0.9997^{+0.0003}_{-0.0002}$, a factor 95 better with respect to DES Y6. While investigating this result, we reported larger constraints but still very optimistic $\alpha = 1.0000 \pm 0.0005$ when a noise-free synthetic $w(\theta)$ computed as the model is used instead of the measured one. Alternatively, keeping the measured data vector but neglecting off-diagonal terms of the covariance, we find about 34 times larger constraints $\alpha = 1.0096^{+0.0085}_{-0.0087}$, which is of the same order of magnitude as the result obtained with the jackknife covariance. This represents a 27 % decrease of the uncertainty which is explained by the larger amplitude of the jackknife errors $\sigma_i^{\rm jack}$ when compared to the analytical ones $\sigma_i^{\rm G+SSC}$. We checked that the bias observed with the measured $w(\theta)$ is no longer present with the noise-free synthetic $w(\theta)$ which yields $\alpha = 1.0008^{+0.0085}_{-0.0083}$. We also note that the constraint is almost unchanged between the two, which was not the case with the full covariance (factor 2). At this point, we used the profile likelihood approach instead of the MCMC technique and we report $\alpha = 1.0011^{+0.0078}_{-0.0079}$ with the Gaussian+SSC full covariance and $\alpha = 0.9925^{+0.0098}_{-0.0095}$ when neglecting off-diagonal terms. This represents a 22.2 % decrease of the uncertainty on α when the covariance is taken into account.

The large difference between some of these results is explained by failures of the exploration of the α parameter space with the MCMC technique. The profile likelihood technique reveals a noisy profile for α, with numerous local minima. This is visible in Fig. 4.25. The fit of the $\Delta\chi^2(\alpha)$ profile shown in green prevents the issue encountered

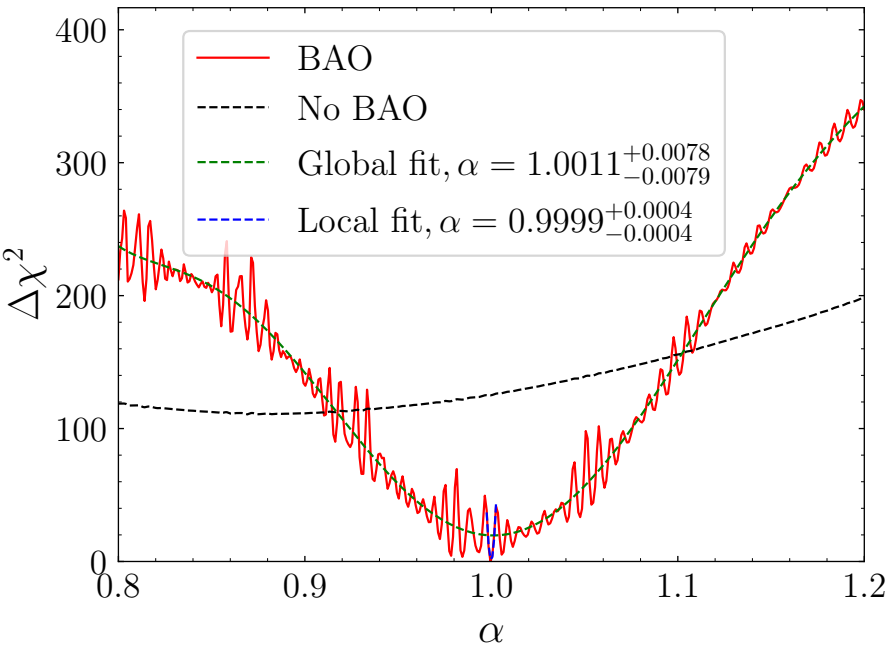


Figure 4.25. – Result of the profile likelihood $\Delta\chi^2(\alpha)$ for the joint analysis with BAO in red and without BAO wiggles in the model in black dashed line. The green dashed line is the polynomial fit performed to smooth the local variations. The blue dashed line is the polynomial fit of the restricted range of α values between the two local maxima found around the global minimum. The reported values of $\alpha = 1.0011^{+0.0078}_{-0.0079}$ and $\alpha = 0.9999 \pm 0.0004$ are the respective $\Delta\chi^2 = 1$ constraints from the global and local fits.

with MCMC. The green fit shown at the level of $\Delta\chi^2(\alpha)$ in this figure is properly shifted by its own minimum value to compute the $\Delta\chi^2_{\rm fit}(\alpha) = 1$ $1\,\sigma$ limits. We check that restricting the fitting range to the interval between the two local maxima found around the global minimum, the profile likelihood technique fit shown in blue yields 0.9999 ± 0.0004. The MCMC technique doesn't fully explore the red profile and so the resulting uncertainty is much smaller than it should. This issue arises despite the use of the `emcee` recommended move strategy in case of multimodal posterior, replacing the default stretch move strategy by a 80%/20% combination of two differential evolution moves, dubbed DEMove and DESnookerMove in `emcee` and fully described in (Nelson et al., 2014; ter Braak et al., 2008). The principle behind differential evolution is to use information from the past evolution of the walkers to generate the next sample proposals, resulting in a much more efficient sampling. Given the results, this is apparently not enough to deal with the multimodal posterior distribution, at least with the default values of the proposal vector stretch parameters in the various move strategies. Increasing the standard deviation of the initialization values of the walkers from 10^{-4} to 10^{-2} enables the exploration of three modes of the posterior, at the cost of a slower convergence. Moreover, it seems that this can also cause a bias, with the

constraint $\alpha = 0.9845^{+0.0005}_{-0.0003}$ shown in Fig. 4.26. This figure shows the 1 to 5σ contours of α against the first nuisance parameter B_0 with the $\Delta\chi^2$ profile in red. We see the match between the widths of minima and various contours but also that maximum of the explored posterior distribution differs from the global minimum of the Δchi^2 profile.

If the constraining power is decreased with respect to the covariance of the 13 bins, for example by removing bin 11 from the joint analysis, then we recover $\alpha = 0.9993^{+0.0067}_{-0.0065}$, with two modes around this median value in the posterior distribution if the large initialization is used. Without the large initialization and without bin 11, we find $\alpha = 0.9992^{+0.0005}_{-0.0008}$. This is explained by the strong constraining power of bin 11. When it is included, the depth of the local minima is more than doubled. This is also observed with bin 13. The multimodal posterior and exploration issue is still observed with the noise-free synthetic $w(\theta)$ but also with a noisy $w(\theta)$ sampled from the analytical covariance. With and without the large initialization, this noisy data vector yields $\alpha = 0.9989^{+0.0003}_{-0.0003}$ and $1.0060^{+0.0010}_{-0.0009}$, respectively. When the constraining power is decreased by removing off-diagonal terms of the analytical or jackknife covariance, the modes of the posterior widen and merge into one.

We also report the constraints from nested sampling with `nautilus`. With the analytical covariance and the measured $w(\theta)$, we find $\alpha = 0.9997^{+0.0004}_{-0.0003}$. If the noisy $w(\theta)$ sampled from the covariance is used, then $\alpha = 1.0060^{+0.0057}_{-0.0053}$. Finally, applying an eigenvalue decomposition (EVD) of the jackknife covariance, removing eigenvalues smaller than 5×10^{-10} and computing a cleaned version of the covariance from the remaining eigenvalues, we obtain an invertible jackknife covariance. The threshold was determined from the histogram of the eigenvalues as to remove small outliers. The structure of the covariance shown in Fig. 3.28 is preserved by this cleaning. The jackknife covariance cleaned by EVD yields $\alpha = 1.0117^{+0.0025}_{-0.0065}$ with the MCMC analysis and $1.0115^{+0.0064}_{-0.0071}$ with nested sampling. This median value corresponds to the second local minimum to the right of the global minimum in the profile from Fig. 4.25. The asymetrical uncertainty is explained by the smaller amplitude of the next local minimum at the right, with respect to the left. The constraint from `nautilus` shows a larger overlap of the three modes in the posterior distribution and a stronger amplitude in the adjacent modes, showing a better exploration than with the MCMC technique. However, since no study was done to check the influence of the EVD cleaning of the covariance at the level of the constraints, these results should be considered with caution.

From these results, we could consider the result $1.0060^{+0.0057}_{-0.0053}$ as representative of the uncertainty that could be reached with this joint analysis and the MCMC technique, with an improvement by a factor 4.4 with respect to DES Y6. However, given that this was not the result obtained with the measured data vector and the exploration issues in the other MCMC joint analyses, we report the result of the profile likelihood technique as the main one, with an improvement by a factor 3.

Table 4.9. – Constraints on α from various joint analyses, varying the covariance used, data vector, analysis method, initialization of the MCMC walkers or removing one redshift bin.

Chain	α
MCMC, jackknife errors	$1.0095^{+0.0108}_{-0.0108}$
MCMC, Gaussian+SSC covariance	$0.9997^{+0.0003}_{-0.0002}$
MCMC, Gaussian+SSC covariance, synthetic DV	$1.0000^{+0.0005}_{-0.0005}$
MCMC, Gaussian+SSC errors	$1.0096^{+0.0085}_{-0.0087}$
MCMC, Gaussian+SSC errors, synthetic DV	$1.0008^{+0.0085}_{-0.0083}$
Profile likelihood, Gaussian+SSC covariance	$1.0011^{+0.0078}_{-0.0079}$
Profile likelihood, Gaussian+SSC errors	$0.9925^{+0.0098}_{-0.0095}$
MCMC, Gaussian+SSC covariance, large ini	$0.9845^{+0.0005}_{-0.0003}$
MCMC, Gaussian+SSC covariance, large ini, remove bin 11	$0.9993^{+0.0067}_{-0.0065}$
MCMC, Gaussian+SSC covariance, remove bin 11	$0.9992^{+0.0005}_{-0.0008}$
MCMC, Gaussian+SSC covariance, noisy DV	$0.9989^{+0.0003}_{-0.0003}$
MCMC, Gaussian+SSC covariance, noisy DV, large ini	$1.0060^{+0.0010}_{-0.0009}$
Nested sampling, Gaussian+SSC covariance	$0.9997^{+0.0004}_{-0.0003}$
Nested sampling, Gaussian+SSC covariance, noisy DV	$1.0060^{+0.0057}_{-0.0053}$
Nested sampling, jackknife covariance (EVD)	$1.0115^{+0.0064}_{-0.0071}$
MCMC, jackknife covariance (EVD)	$1.0117^{+0.0025}_{-0.0065}$

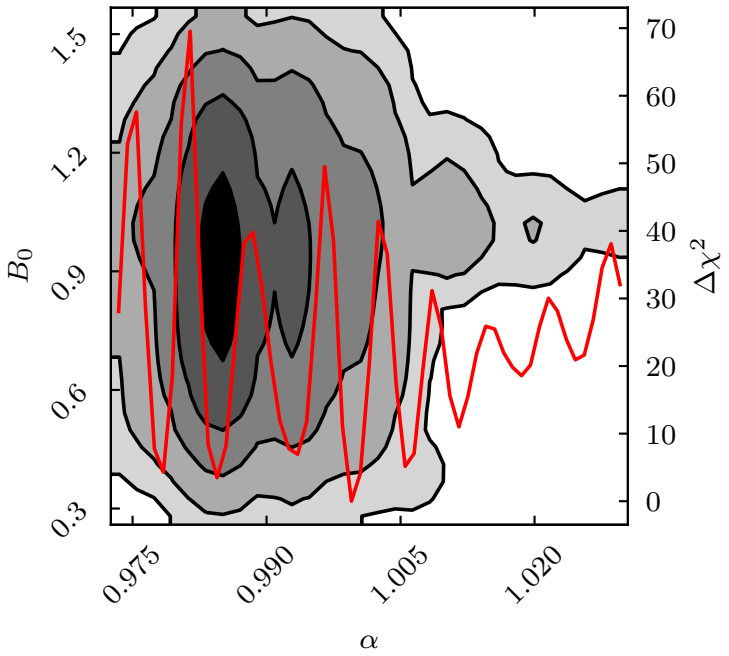


Figure 4.26. – In black and grey, 1 to 5σ contours of α against the first nuisance parameter B_0 obtained with the MCMC analysis of the measured $w(\theta)$, analytical covariance and with a large initialization. The result from profile likelihood is shown as the $\Delta\chi^2$ profile in red, restricted to the range of α values in the 5σ contours. The fact the MCMC analysis failed to identify the global minimum as the maximum of its posterior is an indication of the poor exploration.

4.4.7. Optimization of the sample selection and redshift binning scheme

In this subsection, we propose a preliminary study to improve upon the sample selection initially proposed in the context of the *Euclid* Photometric Galaxy Clustering Work Package. As a reminder, the selection chosen was $I_E \leq 24.5$ and `phz_flags = 0`, with 13 equipopulated redshift bins between $z = 0.2$ and $z = 2.5$. We have seen in Sect. 4.4.5 that the equidistant redshift binning scheme might be better suited to the BAO analysis than the equipopulated one, unlike what was found for 3×2-pt analyses. In this study, we make a number of approximations to compute the figure of merit of h, Ω_b, Ω_{cdm} in a reasonable amount of time. The first and main one is to use a synthetic data vector rather than a measured $w(\theta)$. Indeed, given the very long computation time of $w(\theta)$ discussed in Sect. 3.4.6, it would take an unreasonable amount of resources to perform many measurement of $w(\theta)$ with varied sample selection criteria, number of redshift bins and redshift binning scheme. The second approximation made is to use a gaussian covariance matrix, without SSC contribution. We have shown in Sect. 4.4.6 that ignoring the SSC part of the covariance has a negligible effect, even at low redshift. The next choice, rather than approximation,

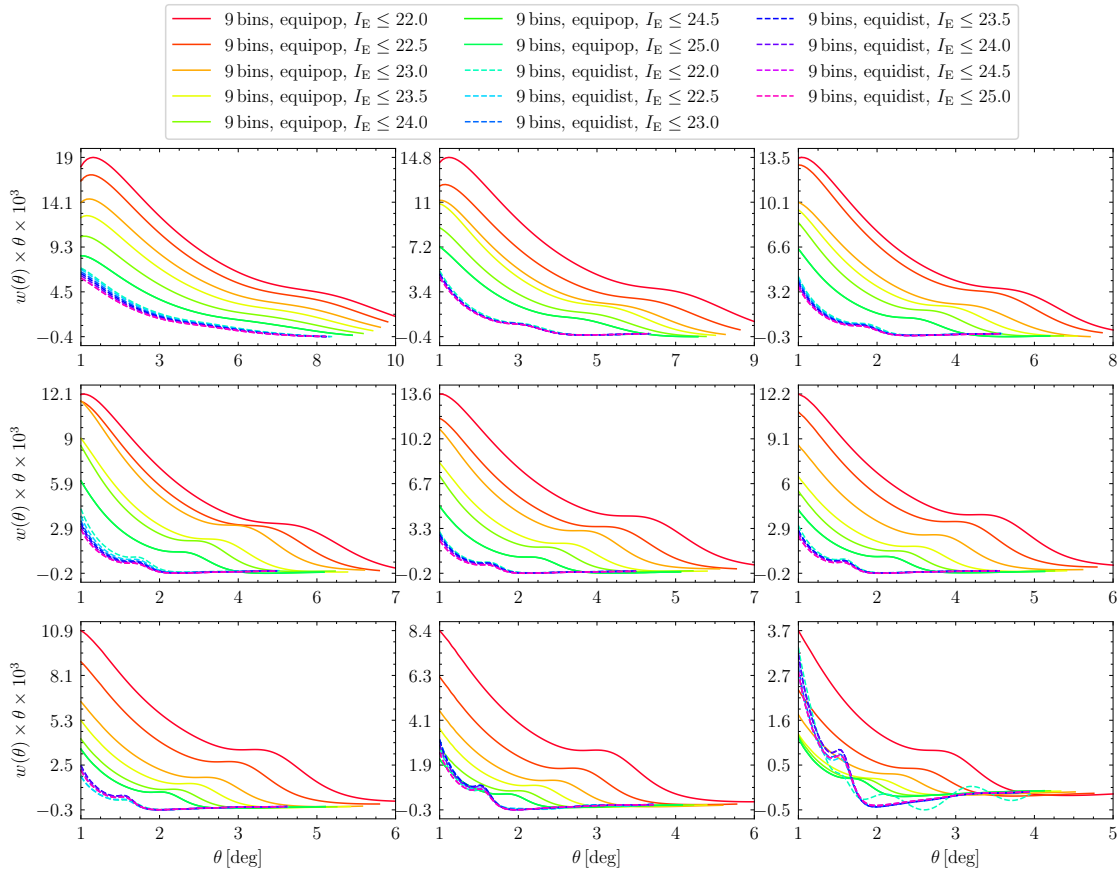


Figure 4.27. – Evolution of the synthetic $w(\theta)$ with 9 redshift bins as a function of the binning scheme and magnitude cut in the I_E band. The equipopulated binning scheme is shown in full lines while the equidistant scheme is in dashed lines. The colour is indicative of the magnitude cut.

is to use the likelihood profile approach to obtain the constraints on the α_i parameters, as running chains to obtain them is the slowest part of this optimization process if a synthetic $w(\theta)$ is used. We have discussed the implications of this choice in Sect. 4.1.2, this might result in slightly tighter constraints than what MCMC provides. The fourth choice made for this optimization was to use all bins without discarding the ones with a non significant detection of the BAO signal. This choice is motivated by the small effect of these bins over the final cosmological constraints, as seen in Sect. 4.2.2. To summarize the method used, we first compute the bin edges given the number of bins, the binning scheme, and the sample selection cut, we extract the redshift distributions $p_i(z)$ for each bin, we compute the synthetic $w(\theta)$ and the analytical gaussian covariance associated. We then use profile likelihood to obtain the α_i values in each redshift bins and use the MCMC technique to infer cosmological constraints on h, Ω_b and Ω_{cdm}.

In this optimization, we vary the sample selection cut in the I_E band in [22,25] by steps of 0.5, we change the number of redshift bins between 9 and 15 by steps of 2

and we switch the redshift binning scheme to either equipopulated or equidistant. The $w(\theta)$ computed from the associated redshift distributions is shown in Fig. 4.27 for a fixed number of 9 bins. The colour is indicative of the magnitude cut in the I_E band while the line style is used to distinguish equipopulated and equidistant binning schemes. The differences in sample selection and bining scheme lead to sometimes very different redshift bin limits and $z_{\rm eff}$, which explains the difference both in the ampitude of $w(\theta)$ and in the position of the BAO peak. The oscillatory behaviour of $w(\theta)$ in the last panel for the equidistant binning at $I_E \leq 22$ (cyan dashed line) is explained by the fact that this magnitude cut leaves only a few hundreds of galaxies in the last equidistant bins. For this reason, the results for $I_E \leq 22$ and $I_E \leq 22.5$ should be considered with caution and are only given as an indication of the evolution of the results. When the number density drops with these strong magnitude cuts, the associated error on $w(\theta)$ increases a lot and the cosmological constraints worsen as a consequence. This is also what explains the fact that the profile likelihood failed to converge in the last redshift bins when more bins than 15 were used. The results are reported in Table B.1 and are visually ranked in Fig. 4.28 through the ratio of the FoM of h, $\Omega_{\rm b}$, and $\Omega_{\rm cdm}$ of the various configurations on the FoM obtained for the baseline choice of 13 equipopulated bins with $I_E \leq 24.5$. We find that the configuration yielding the highest FoM is 15 equidistant bins with $I_E \leq 24.5$, with $h = 0.670^{+0.003}_{-0.003}$, $100\,\Omega_{\rm b} = 4.901^{+0.042}_{-0.041}$, and $\Omega_{\rm cdm} = 0.273^{+0.011}_{-0.010}$. This corresponds to an improvement by 32 % for the constraint on $\Omega_{\rm cdm}$ with respect to the baseline. In terms of FoM, there is a factor 1.5 between the reference and best configurations.

In Fig. 4.28, we see that the FoM reaches a maximum for 15 redshift bins regardless of the binning scheme, equipopulated or equidistant. The evolution as a function of the number of redshift bins is linear in both cases. The cut of $I_E \leq 24.5$ maximizes the FoM for almost all binning schemes and bin numbers. 9 and 13 equipopulated bins are the exceptions, with a FoM maximized for $I_E \leq 25$ instead. For the reason explained before about the size of the sample, the performance of the equidistant binning scheme is inferior to the equipopulated binning scheme when the magnitude cut is at a threshold strictly smaller than $I_E = 23.5$. On the contrary, the ratio between the FoM of the equidistant and equipopulated binning schemes increases when the threshold increases, until $I_E = 24.5$.

These results will have to be taken into account in future analyses of BAO with photometric galaxy clustering with *Euclid*. A complete optimization of the sample selection with redshift-dependent colour cuts would be even more profitable, as it will allow the use of the best sample possible for BAO analyses.

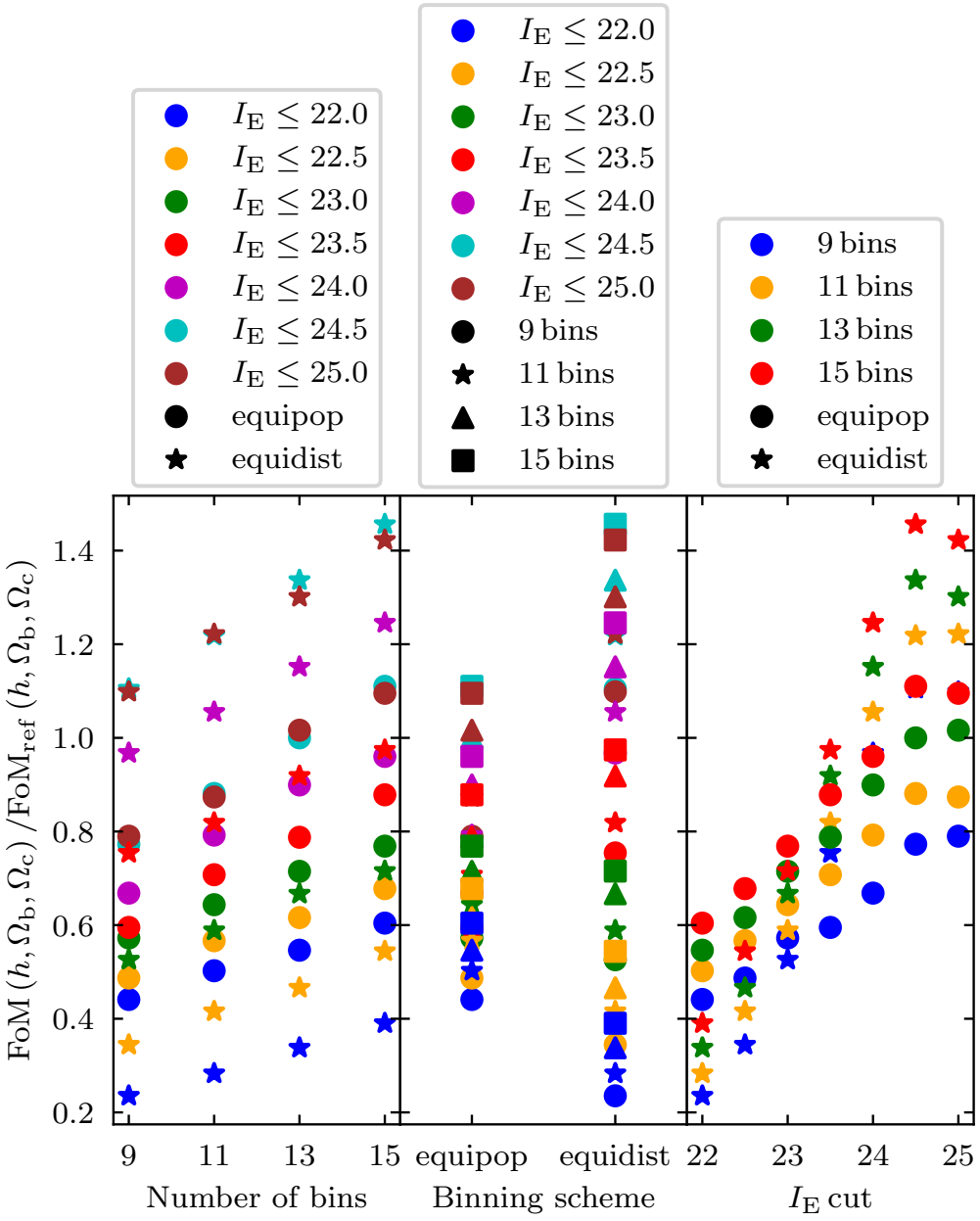


Figure 4.28. – For various numbers of bins, I_E magnitude cuts and binning schemes, ratio of the FoM of h, Ω_b, and Ω_{cdm} over the FoM of the baseline with 13 equipopulated bins with $I_E \leq 24.5$.

5. A tomographic full-shape analysis of photometric galaxy clustering

In this chapter, we present a full-shape analysis of $w(\theta)$. Unlike the BAO analysis which uses the information condensed in the position of the BAO peak, here, the entire shape of $w(\theta)$ is used. Instead of the template introduced in Eq. (4.1), the theoretical $w(\theta)$ computed from Eq. (3.2) is the model used in the likelihood analysis. We directly sample the cosmological parameters of the ΛCDM model h, $\Omega_{\rm b}$, $\Omega_{\rm cdm}$, $A_{\rm s}$, and $n_{\rm s}$ instead of α, B, A_0, A_1, and A_2. The methodology of this analysis is presented in Sect. 5.1. The first goal of this work is to estimate in Sect. 5.2 the constraints from photometric galaxy clustering alone available at the time of *Euclid* DR1, with a survey area of about 2500 deg^2. This sample uses 6 equipopulated redshift bins and a selection at $I_{\rm E} \leq 22.25$. Note that this threshold was chosen before the decision was made to use $I_{\rm E} \leq 23.5$ for the DR1 *Euclid* sample. For this reason, this analysis is slightly conservative with respect to DR1. The second goal is to estimate the effect of redshift distributions uncertainties over these constraints in Sect. 5.3. This work was done in the context of the GCph WP from the *Euclid* GC SWG in collaboration with Klara Bertmann who studied these constraints using synthetic data vectors for a 3×2-point analysis (Bertmann et al., in prep) while I focused my work on the constraining power of photometric galaxy clustering alone with measured data vectors. The measurements are performed on the Flagship simulation following the same procedure as in Sect. 3.2.2.

Summary

5.1. Methodology of the full-shape analysis 150
5.2. Constraints on the ΛCDM model 152
5.3. Impact of redshift uncertainties on cosmological constraints 154

5.1. Methodology of the full-shape analysis

In this section, we present the differences in the methodology used with respect to the BAO analysis. The `CosmoSIS` environment is used for this analysis (Zuntz et

Table 5.1. – Galaxy bias measured by fitting $w(\theta)$ following the approach detailed in Sect. 3.4.1 with two different choice of scale cuts.

Scale cuts	$b_{g,1}$	$b_{g,2}$	$b_{g,3}$	$b_{g,4}$	$b_{g,5}$	$b_{g,6}$
$6' \leq \theta \leq 60'$	1.144	1.259	1.292	1.407	1.455	1.720
$30' \leq \theta \leq 240'$	1.067	1.229	1.245	1.408	1.407	1.774

al., 2014). The `CAMB` module of `CosmoSIS` is used with the Takahashi halofit model (Takahashi et al., 2012), with $\ell_{\rm max} = 2500$, $k \in [10^{-4}, 50]$ extrapolated up to $k = 500$ with 700 bins, and with an accuracy boost parameter of 1.1. The `pk_to_cl_gg` module is used to project the 3D power spectrum to the galaxy angular power spectrum including RSD using $\ell \in [5, 10^5]$ with 80 log-spaced bins, using the Limber approximation beyond $\ell = 200$. The two-point angular correlation function model is then computed with $\ell_{\rm max} = 40\,000$. As for the galaxy bias of the model, we will consider two cases depending on the choice of scales used to fit the galaxy bias. The first case uses the same scales as the BAO analysis with $30' \leq \theta \leq 240'$ while the second case uses the same scale cuts as the analysis from Bertmann et al., $6' \leq \theta \leq 60'$. The resulting bias values for the six redshift bins are given in Table 5.1. We find slightly larger values of $b_{\rm g}$ when it is fitted on smaller scales, except in the last redshift bin.

The posterior is obtained with the `nautilus` sampler. The number of live points is doubled from the default 2000 to 4000. The batch size of likelihood evaluations is 512 and 4 neural networks are used to estimate the bounds. The model considered is no longer the BAO template but the ΛCDM model. We use the full shape of $w(\theta)$ and sample over h, $A_{\rm s}$, $n_{\rm s}$, $\Omega_{\rm b}$, $\Omega_{\rm m}$ while we keep the galaxy bias fixed. We then derive the parameters σ_8 and $S_8 = \sigma_8 \sqrt{\Omega_{\rm m}/0.3}$. Note that our analysis differs slightly from Bertmann et al. by including the contribution of neutrinos with $m_\nu = 0.06$ eV, by using the redshift distribution measured and the galaxy bias fitted on the 2500 deg^2 area rather than the 400 deg^2 area used in the SPV3 exercise. Otherwise, the analytical covariance is computed as in Sect. 3.5 with `CosmoCov`, with 6 redshift bins and without SSC contribution. The jackknife covariance is estimated with 500 patches. We use large uniform priors with $\Omega_{\rm m} \in [0.1, 0.9]$, $\Omega_{\rm b} \in [0.03, 0.07]$, $h \in [0.55, 0.91]$, $n_{\rm s} \in [0.87, 1.07]$, and $A_{\rm s} \times 10^9 \in [0.5, 5]$ from the DES Y3 analysis (Porredon et al., 2022). As for the scale cuts of the full-shape analysis, we adopt the redshift-dependent minimum scale cut defined in the DES Y3 analysis by

$$\theta_{{\rm min},i} = \frac{R}{r\left(z_{{\rm mean},i}\right)}, \tag{5.1}$$

where $R = 8\ h^{-1}\,$Mpc, r is the comoving distance, and $z_{{\rm mean},i}$ is the mean redshift of each redshift bin i : $z_{{\rm mean},i} = 0.272$, 0.370 , 0.457, 0.568, 0.677, and 0.905. A fixed maximum angular scale of $\theta_{\rm max} = 100'$ is also applied to the data vectors. The scales considered in full-shape analyses are smaller than in BAO analyses. As a comparison, $\theta_{\rm BAO}$ varies from $446'$ in the first redshift bin to $160'$ in the last one. The fiducial

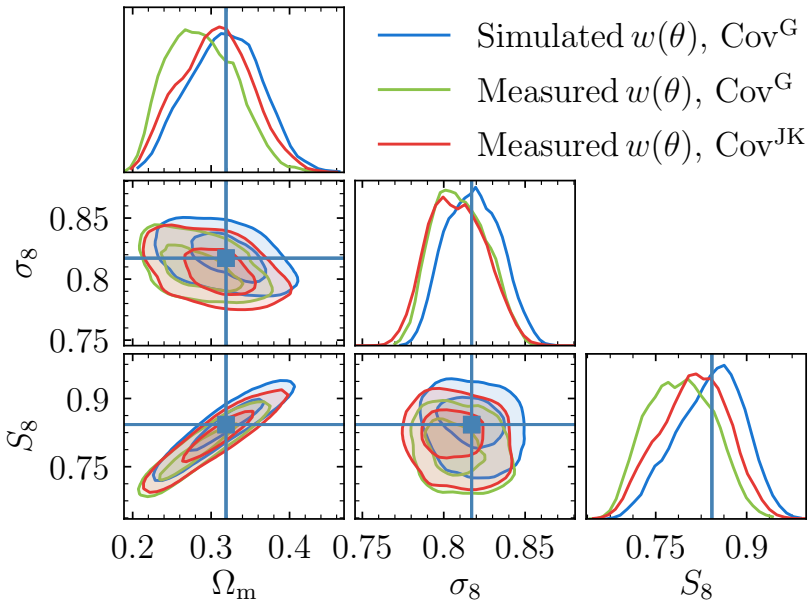


Figure 5.1. – Comparison of the constraints on Ω_{m}, σ_8 and S_8 for the simulated and measured $w(\theta)$ with the full-shape analysis in a DR1-like setting.

cosmology is unchanged with respect to Sect. 3.3 and the three parameters we will focus on are $\Omega_{\mathrm{m}} = 0.319$, $\sigma_8 = 0.817$, $S_8 = 0.843$.

5.2. Constraints on the ΛCDM model

In this section, we first present the constraints obtained on the ΛCDM model in this DR1-like configuration. We then quantify the influence of several choices made in this analysis, like scale cuts. We show the constraints obtained in Fig. 5.1 with the simulated $w(\theta)$ computed as the theoretical model by `CosmoSIS`, with the measured $w(\theta)$ and with either the analytical or jackknife covariance. The results from the measured and simulated data vectors are in agreement. Indeed, we measure $S_8 = 0.844^{+0.051}_{-0.064}$ with the simulated $w(\theta)$ and analytical covariance against $0.791^{+0.058}_{-0.057}$ with the measured $w(\theta)$, while the jackknife covariance yields $0.815^{+0.055}_{-0.062}$ with the measured $w(\theta)$. All constraints on parameters from the ΛCDM model and derived parameters can be found in Table 5.2. The bias of $-0.7\,\sigma$ observed on Ω_{m} with the measured $w(\theta)$ is limited to $0.01\,\sigma$ with the simulated $w(\theta)$ and $-0.3\,\sigma$ with the jackknife covariance.

We found that this bias is partially explained by the scales used to fit the galaxy bias, between $30'$ and $240'$. Using scales between $6'$ and $60'$, we find overall larger values of b_{g} which lead to a better agreement between the measured $w(\theta)$ and the theoretical model. As a consequence, the amplitude of this bias decreases from $-0.9\,\sigma$ to $0.1\,\sigma$ with a new constraint of $S_8 = 0.848^{+0.050}_{-0.062}$

The measurement of $w(\theta)$ is shown in blue in Fig. 5.2 with the associated uncertainty from the Gaussian covariance. The scale cuts are shown as grey areas. We justify

Table 5.2. – Constraints on the parameters of the ΛCDM model with the full-shape analysis in a DR1-like setting. The first setting uses the simulated $w(\theta)$ and the analytical covariance while setting 2 uses the measured $w(\theta)$ and the analytical covariance and setting 3 uses the measured $w(\theta)$ and jackknife covariance.

Parameter	Setting 1	Setting 2	Setting 3
Ω_m	$0.318^{+0.045}_{-0.049}$	$0.286^{+0.048}_{-0.043}$	$0.306^{+0.045}_{-0.049}$
σ_8	$0.818^{+0.017}_{-0.017}$	$0.809^{+0.019}_{-0.016}$	$0.808^{+0.019}_{-0.017}$
S_8	$0.844^{+0.051}_{-0.064}$	$0.791^{+0.058}_{-0.057}$	$0.815^{+0.055}_{-0.062}$
h	$0.669^{+0.114}_{-0.084}$	$0.740^{+0.109}_{-0.114}$	$0.694^{+0.117}_{-0.098}$
$100\,\Omega_\mathrm{b}$	$4.894^{+1.369}_{-1.250}$	$4.246^{+1.278}_{-0.899}$	$4.551^{+1.393}_{-1.070}$
n_s	$0.972^{+0.065}_{-0.068}$	$0.955^{+0.072}_{-0.060}$	$0.961^{+0.071}_{-0.063}$
$10^9 A_\mathrm{s}$	$2.123^{+0.381}_{-0.359}$	$1.871^{+0.380}_{-0.282}$	$1.997^{+0.398}_{-0.333}$

the different changes to the analysis choices detailed in Sect. 5.1 by comparing the corresponding theoretical models of $w(\theta)$ computed with `CosmoSIS`. The most obvious one is the difference in redshift distribution and galaxy bias measured on the SPV3 area against the area used for the measurement, as they lead to an overestimation of the clustering by several times the uncertainty of $w(\theta)$. Comparing the model in green and purple, we find that the angular scales used to fit b_g also matter since it creates a shift in the model which exceeds $1\,\sigma$ in most redshift bins, with the exception of bin 4 where the two models are perfectly superimposed. Finally, the addition of neutrinos with $m_\nu = 0.06$ eV is important to better match the Flagship simulation by decreasing the amplitude of the clustering.

All of these changes affect the constraints on the ΛCDM parameters, shown in Fig. 5.3 and listed in Table 5.3. The setting 1 is the one used in Bertmann et al., where the redshift distribution and galaxy bias are measured on the SPV3 area, the scales used to fit b_g are $6' \leq \theta \leq 60'$ and neutrinos are not included in the analysis, with $m_\nu = 0$ eV. This setting is not adapted to the measured data vector and creates large biases with respect to the fiducial cosmology, $-0.6\,\sigma$ on Ω_m and $-2.0\,\sigma$ on σ_8. The second setting uses the redshift distribution and galaxy bias from the 2500 deg^2 area, with the same fitting scales and $m_\nu = 0.06$ eV. In this case, Ω_m and σ_8 are consistent with the fiducial cosmology with 0.3 and $-0.7\,\sigma$ biases, respectively. The third and fourth cases differ from the second one by the scales used to fit b_g, between $30' \leq \theta \leq 240'$, and also by the use of $m_\nu = 0$ eV for case 3. We find that the impact of the scales is significant on Ω_m, with $0.7\,\sigma$ shifts towards lower values for the two cases with respect to the fiducial value. However, the neutrino mass has a much smaller effect when ignored. This is consistent with the variations of the data vector seen in Fig. 5.2.

The choice of scale cuts for the full-shape analysis is important with the measured $w(\theta)$. In Fig. 3.16 where the data vector is shown in blue, we find an excess of clustering

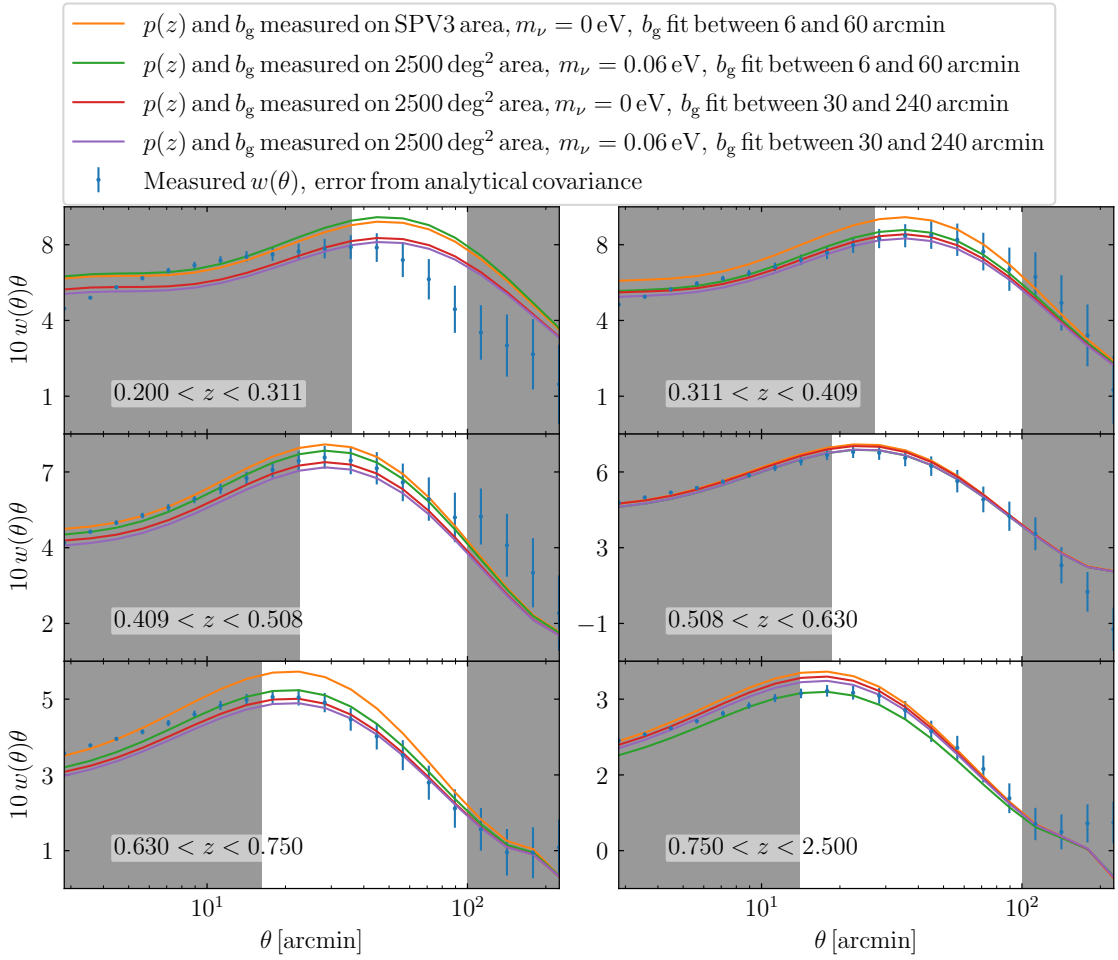


Figure 5.2. – Measurement of $w(\theta)$ on the Flagship simulation with 6 redshift bins and comparison with the theoretical model simulated while varying the redshift distribution, galaxy bias and neutrino mass.

at $\theta \geq 100'$ in bins 2, 3 and 6 with respect to the theoretical model. On the contrary, bins 1 and 4 have a lack of clustering at large scales. We find that including these scales at $\theta \geq 100'$ creates biases larger than $2\,\sigma$ on Ω_m, h, Ω_b, and A_s, while we recover an agreement within $1\,\sigma$ for all parameters when these scales are excluded.

5.3. Impact of redshift uncertainties on cosmological constraints

In this section, we consider the effect of model misspecifications with the redshift distribution. Since this component of the theoretical model described in Eq. (3.5) is unknown and can only be estimated from observations, it can be biased. We use a bias parameter B to quantify the shift of the mean of each redshift distribution with

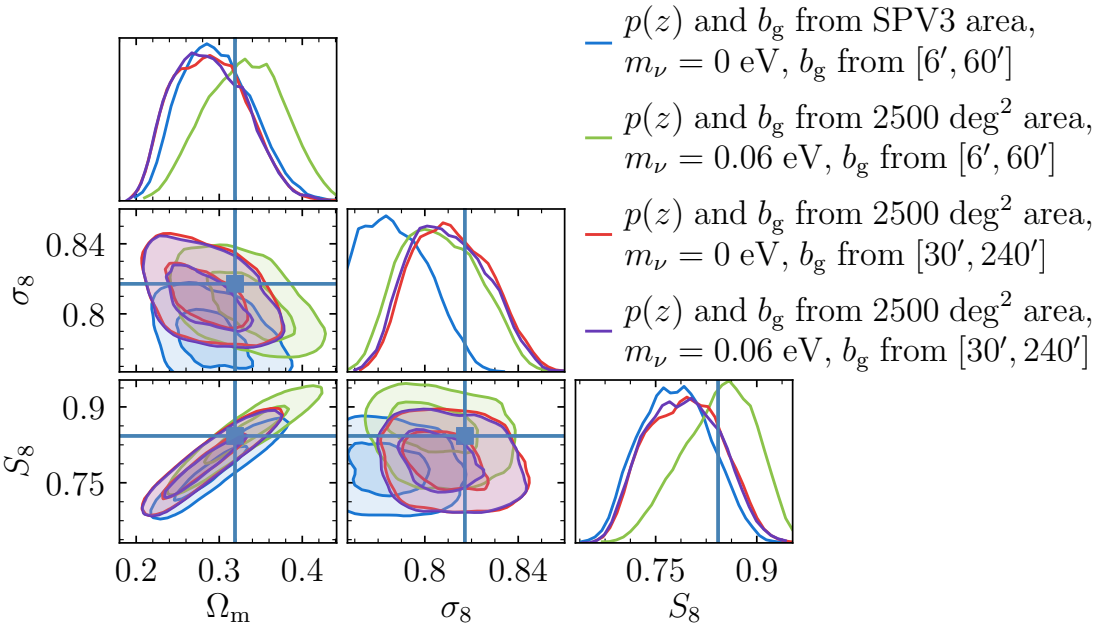


Figure 5.3. – Comparison of the constraints on Ω_m, σ_8 and S_8 for the full-shape analysis, varying the redshift distribution, galaxy bias and neutrino mass used to compute the theoretical model.

respect to the true one such that

$$p^{\text{true}}(z) = p\,(z - \text{B})\,. \tag{5.2}$$

The width of the redshift distribution can also be affected, which is why a second parameter, W, is introduced for the stretch

$$p^{\text{true}}(z) = \frac{1}{\text{W}(1+z)}\, p\left(z_{\text{mean}} + \frac{z - z_{\text{mean}}}{\text{W}(1+z)}\right). \tag{5.3}$$

We show in Fig. 5.4 the effect of the multiplicative bias B on the redshift distributions with $B = 0.002\,(1 + z_{\text{mean},i})$ with i the index of the bin. This corresponds to the maximum bias allowed by the *Euclid* scientific requirements. The left panel shows $p(z)$ with and without bias, illustrating the fact that we are considering very small effects. The difference between both distributions $\Delta p(z)$ is visible in the right panel, with an underestimation of the distribution at the start of each redshift bin and an overestimation after the bin, as expected from the bias.

The effect of the stretch by 2% with W = 1.02 is presented in Fig. 5.5. The stretch leads to an underestimation of $p(z)$ within each redshift bin and an overestimation before and after. The amplitude of the effect on $\Delta p(z) \sim 0.2$ is similar to the bias but positive and no longer centered around 0. The consequence of both effects and their combination on $w(\theta)$ is shown in Fig. 5.6. We find that with respect to the baseline, the multiplicative bias shown in purple affects $w(\theta)$ the least in the 3 first bins, the

Table 5.3. – Constraints on the parameters of the ΛCDM model with the full-shape analysis in a DR1-like setting, varying the redshift distribution, galaxy bias and neutrino mass used to compute the theoretical model. The settings correspond the 4 cases considered in Fig. 5.2 and Fig. 5.3.

Parameter	Setting 1	Setting 2	Setting 3	Setting 4
Ω_m	$0.294^{+0.046}_{-0.041}$	$0.331^{+0.046}_{-0.049}$	$0.288^{+0.046}_{-0.044}$	$0.286^{+0.048}_{-0.043}$
σ_8	$0.785^{+0.017}_{-0.015}$	$0.806^{+0.018}_{-0.017}$	$0.811^{+0.018}_{-0.016}$	$0.809^{+0.019}_{-0.016}$
S_8	$0.779^{+0.054}_{-0.053}$	$0.848^{+0.050}_{-0.062}$	$0.794^{+0.056}_{-0.059}$	$0.791^{+0.058}_{-0.057}$
h	$0.712^{+0.112}_{-0.107}$	$0.645^{+0.117}_{-0.071}$	$0.732^{+0.115}_{-0.110}$	$0.740^{+0.109}_{-0.114}$
$100\Omega_\mathrm{b}$	$4.476^{+1.325}_{-1.007}$	$5.088^{+1.302}_{-1.343}$	$4.271^{+1.282}_{-0.909}$	$4.246^{+1.278}_{-0.899}$
n_s	$0.957^{+0.071}_{-0.059}$	$0.958^{+0.072}_{-0.062}$	$0.957^{+0.071}_{-0.062}$	$0.955^{+0.072}_{-0.060}$
$10^9 A_\mathrm{s}$	$1.810^{+0.365}_{-0.298}$	$2.124^{+0.348}_{-0.353}$	$1.850^{+0.376}_{-0.283}$	$1.871^{+0.380}_{-0.282}$

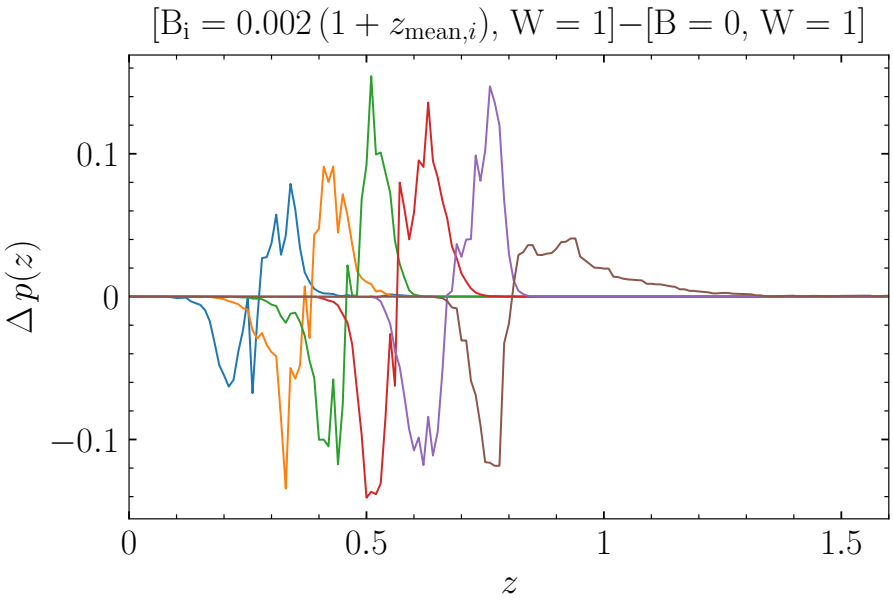


Figure 5.4. – Comparison of the redshift distributions used in the full-shape analysis with and without multiplicative bias in a DR1-like setting.

constant additive bias taking over in the 3 last bins. Both only represent sub-percent effects at $\theta \leq 100'$ and increase slightly beyond 1% at $\theta \in [100', 250']$. The effect of the stretch on $w(\theta)$ is larger, with a shift of 2% below $\theta \sim 60'$ and an increasing shift beyond. We observe that the combined effect of the bias (additive or multiplicative) and stretch on $w(\theta)$ is the sum of both effects within 1% in the first 3 redshift bins, within 14% in bin 4, and within 3% in the last 2 bins.

The constraints obtained with `nautilus` are grouped in Table 5.4 and shown in Fig. 5.7. In the first case considered, we use the galaxy bias obtained using scales

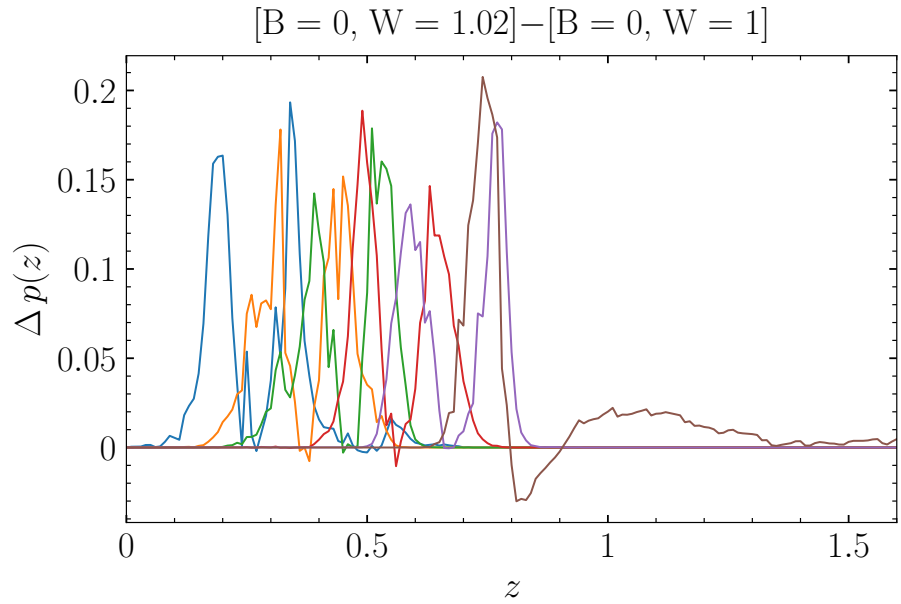


Figure 5.5. – Comparison of the redshift distributions used in the full-shape analysis with and without stretch in a DR1-like setting.

between 30′ and 240′, with the analytical covariance and measured data vector. With the baseline analysis where $B = 0$, $W = 0$, we find a bias on Ω_m and σ_8 with respect to the simulation cosmology towards low values, with $\Omega_m = 0.286^{+0.048}_{-0.043}$, $\sigma_8 = 0.809^{+0.019}_{-0.016}$, and $S_8 = 0.791^{+0.058}_{-0.057}$. With a multiplicative bias $B = 0.002\,(1+z)$, we find that the $\sim 1\%$ effect seen on $w(\theta)$ shifts Ω_m and σ_8 by a negligible amount, 0.03 and $0.1\,\sigma$, respectively. As we have seen in Fig. 5.6, the stretch applied on $p(z)$ had a marginally larger effect on $w(\theta)$ but it is significantly more noticeable with σ_8 : it is shifted by $0.50\,\sigma$. This is explained by the fact that the stretch decreases the amplitude of the theoretical model of $w(\theta)$ by at least 2% at all scales, which is compensated by an increase of σ_8. The shift is also much larger with the stretch than with the bias because the effect of the bias is even weaker at high redshift whereas the signal-to-noise ratio increases. As for the combination of bias and stretch, the shift of σ_8 reaches $0.59\,\sigma$.

We also provide in Table 5.5 the results with the galaxy bias obtained using scales between 6′ and 60′ and considering a variable additive bias of amplitude $B = 0.002(1 + z_{\mathrm{mean},i})$, slightly different from the previous multiplicative bias. Fig. 5.8 shows the constraints of Ω_m, σ_8 and S_8 as before. The decrease of the bias on Ω_m with respect to the fiducial value of $\Omega_m = 0.319$ already mentioned is clear in this figure. We now find that adding the $0.002\,(1 + z_{\mathrm{mean},i})$ bias on $p(z)$, the shift on Ω_m is almost unchanged with respect to the baseline value ($0.04\,\sigma$) while the bias on σ_8 decreases from 0.1 to $0.03\,\sigma$. The stretch of 2% induces shifts of $0.02\,\sigma$ and $0.44\,\sigma$ on Ω_m and σ_8, while the combination of bias and stretch has a slightly larger impact on σ_8 with $0.49\,\sigma$. The amplitude of these biases is in agreement with the previous results obtained with the galaxy bias fitted on larger scales.

While all of these results remain compatible within $1\,\sigma$, the amplitude of the shifts

Table 5.4. – Constraints on the parameters of the ΛCDM model with the full-shape analysis in a DR1-like setting, varying the multiplicative bias B= 0.002(1 + z) and stretch W = 1.02 of the redshift distributions. The galaxy bias is fitted with $30' \leq \theta \leq 240'$.

Parameter	Baseline	Biased	Stretched	Both
Ω_m	$0.286^{+0.048}_{-0.043}$	$0.287^{+0.046}_{-0.044}$	$0.284^{+0.048}_{-0.042}$	$0.283^{+0.049}_{-0.041}$
σ_8	$0.809^{+0.019}_{-0.016}$	$0.811^{+0.018}_{-0.016}$	$0.818^{+0.019}_{-0.016}$	$0.819^{+0.018}_{-0.016}$
S_8	$0.791^{+0.058}_{-0.057}$	$0.794^{+0.057}_{-0.059}$	$0.797^{+0.058}_{-0.056}$	$0.797^{+0.060}_{-0.055}$
h	$0.740^{+0.109}_{-0.114}$	$0.737^{+0.112}_{-0.114}$	$0.742^{+0.108}_{-0.116}$	$0.741^{+0.108}_{-0.115}$
$100\Omega_\mathrm{b}$	$4.246^{+1.278}_{-0.899}$	$4.282^{+1.306}_{-0.911}$	$4.209^{+1.262}_{-0.855}$	$4.219^{+1.289}_{-0.861}$
n_s	$0.955^{+0.072}_{-0.060}$	$0.957^{+0.072}_{-0.060}$	$0.957^{+0.070}_{-0.061}$	$0.957^{+0.071}_{-0.061}$
$10^9 A_\mathrm{s}$	$1.871^{+0.380}_{-0.282}$	$1.896^{+0.405}_{-0.299}$	$1.914^{+0.389}_{-0.292}$	$1.927^{+0.394}_{-0.295}$

Table 5.5. – Constraints on the parameters of the ΛCDM model with the full-shape analysis in a DR1-like setting, varying the redshift-dependent additive bias B = $0.002\left(1 + z_{\mathrm{mean},i}\right)$ and stretch W = 1.02 of the redshift distributions. The galaxy bias is fitted with $6' \leq \theta \leq 60'$.

Parameter	Baseline	Biased	Stretched	Both
Ω_m	$0.331^{+0.046}_{-0.049}$	$0.333^{+0.045}_{-0.048}$	$0.330^{+0.049}_{-0.049}$	$0.331^{+0.048}_{-0.049}$
σ_8	$0.806^{+0.018}_{-0.017}$	$0.806^{+0.019}_{-0.016}$	$0.813^{+0.020}_{-0.016}$	$0.814^{+0.020}_{-0.016}$
S_8	$0.848^{+0.050}_{-0.062}$	$0.850^{+0.048}_{-0.059}$	$0.855^{+0.053}_{-0.061}$	$0.857^{+0.051}_{-0.061}$
h	$0.645^{+0.117}_{-0.071}$	$0.644^{+0.111}_{-0.070}$	$0.646^{+0.117}_{-0.071}$	$0.644^{+0.119}_{-0.070}$
$100\Omega_\mathrm{b}$	$5.088^{+1.302}_{-1.343}$	$5.144^{+1.232}_{-1.323}$	$5.118^{+1.239}_{-1.349}$	$5.124^{+1.237}_{-1.322}$
n_s	$0.958^{+0.072}_{-0.062}$	$0.956^{+0.072}_{-0.059}$	$0.955^{+0.074}_{-0.060}$	$0.954^{+0.075}_{-0.059}$
$10^9 A_\mathrm{s}$	$2.124^{+0.348}_{-0.353}$	$2.135^{+0.342}_{-0.341}$	$2.165^{+0.350}_{-0.353}$	$2.175^{+0.349}_{-0.354}$

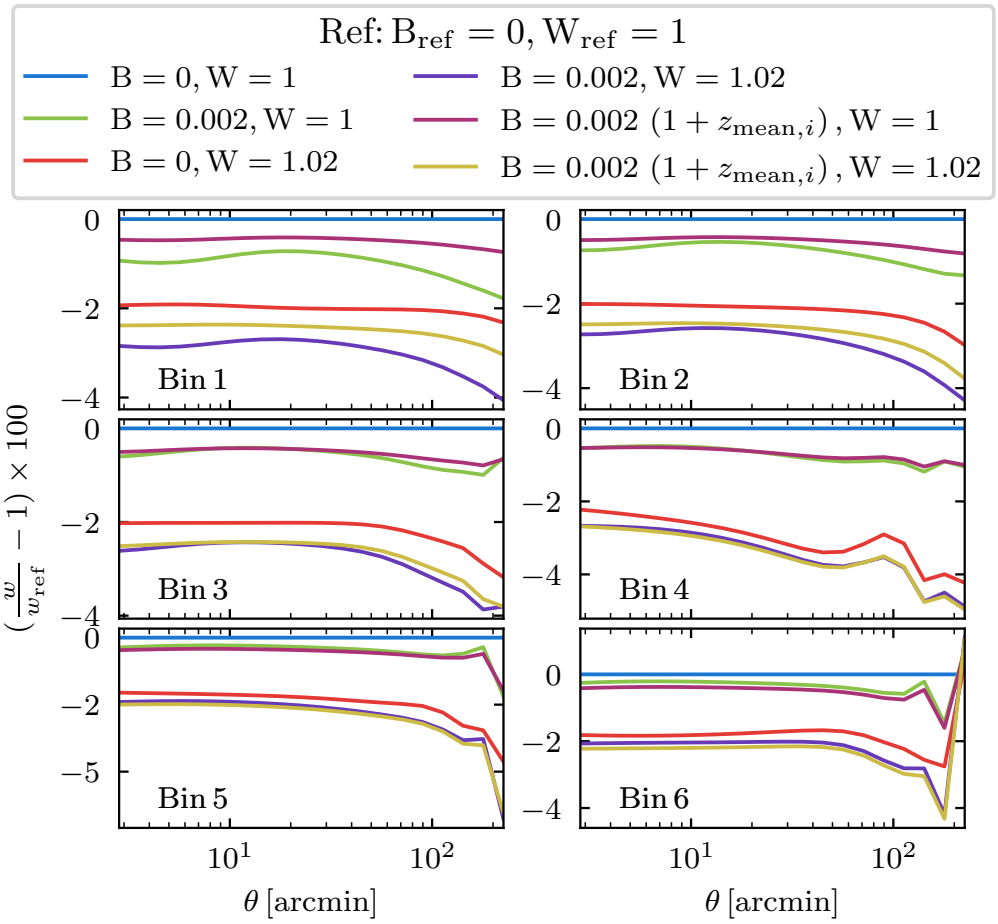


Figure 5.6. – Comparison of the theoretical model of $w(\theta)$ used in the full-shape analysis with and without bias and stretch in a DR1-like setting.

observed is not negligible when we consider the fact that it is caused by a 2% misspecification of the $p(z)$ stretch, especially when there is no specific *Euclid* requirement on our knowledge of this stretch. The fact that the sample used in this study is more conservative than what was finally decided for *Euclid* DR1 may lead to changes in these conclusions. With a larger sample and more constraining power, the uncertainty on the cosmological parameters will decrease and the biases observed will become more considerable if the redshift distribution bias and stretch are not better controlled. However, as explained in Sect. 3.3, the photometry used to derive the photo-z of the Flagship simulation are optimistic (LSST-like). As a consequence, it will be important to assess this effect again once the size and properties of the *Euclid* DR1 sample are better known, in order to provide a more realistic analysis.

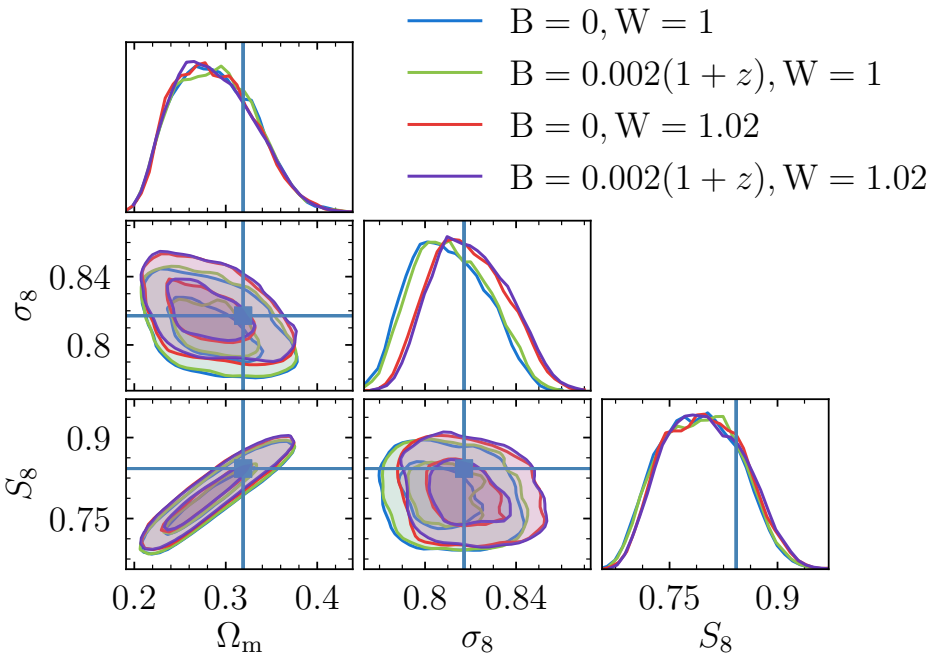


Figure 5.7. – Comparison of the constraints on Ω_m, σ_8 and S_8 for the full-shape analysis with and without bias and stretch in a DR1-like setting.

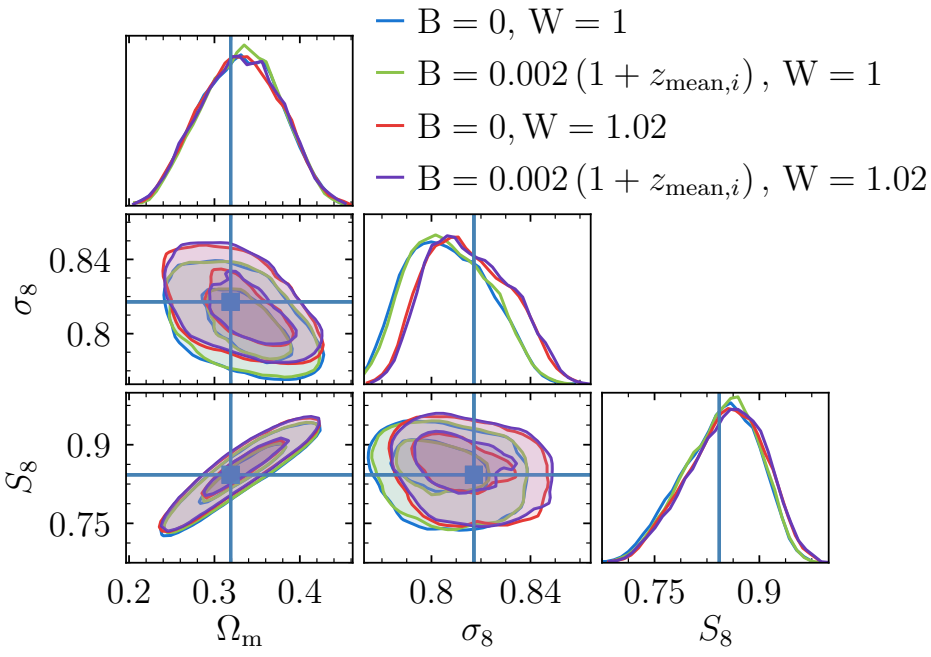


Figure 5.8. – Comparison of the constraints on Ω_m, σ_8 and S_8 for the full-shape analysis with and without bias and stretch in a DR1-like setting with b_g fitted between $6'$ and $60'$.

Conclusion

In the last two decades, Cosmology has known a large progress thanks to galaxy surveys. The statistical study of large scale structures is slowly revealing the properties of our Universe through observables like the two-point angular correlation function used in this work which can be compared to a theoretical framework introduced in Chapter 1 thanks to the development of the theory of general relativity and the work of many researchers in the last century. Similarly, it is through the work of many researchers, professors, engineers, technicians of all ages invested in *Euclid* or other collaborations that we are entering the era of stage IV surveys, an era of precision cosmology to answer questions such as the nature of dark energy or dark matter with an amount of observations and data never seen before. This goal of this work was not to study the main probes of the *Euclid* mission which are spectroscopic galaxy clustering for BAO and weak gravitational lensing. Instead, we studied photometric galaxy clustering, a secondary probe often only seen as one of the component of the 3×2-point analysis. Photometric redshifts are the central element of this probe, which is why I studied in Chapter 2 recent approaches in deep learning to estimate photo-z directly from images rather than photometry. Convolutional neural network and in particular the inception architecture and residual network were studied to predict photo-z. I found that on data observed and released in SDSS DR12, the use of deep neural networks and galaxy images can provide very significant improvements, with 1.5 times less outliers with respect to a naive approach using only magnitude with a MLP. I also showed that it is possible to adapt these architectures to predict photo-z PDF to quantify the uncertainty while keeping performances on the bias, dispersion and fraction of outliers which are similar or even better than with point-estimates of photo-z. I then used simulated data from the *Euclid* SC8 exercise to study whether these results found with SDSS data held with the *Euclid* photometry alone, in the $H_{\rm E}$, $Y_{\rm E}$, $J_{\rm E}$, and $I_{\rm E}$ passbands. Following the issues of the SC8 $z_{\rm spec}$ extraction, I simulated mock spectroscopic redshifts to create a training sample. Because of the poor quality of this sample, the results on photo-z estimates obtained from this sample are not representative of the actual performance of *Euclid* photo-z but I found that even in this pessimistic scenario, the improvement on the outlier fraction observed between MLP and inception CNN is also a factor 1.5. Most importantly, it is the combination of both inception CNN and MLP models into one multi-input model (images and magnitudes) which provides the best performances by far, with an improvement by a factor 4 on the outlier fraction, more than 2 on the NMAD, and 1.5 on the bias. Whether such performances are linked to the quality of the training set and whether this improvement is as impressive on a pure training sample remains be tested. This can either be done by artificially decreasing the fraction of

noise and line interlopers in the spectroscopic redshift model or with the future pixel-level simulations for *Euclid*. It will also be important to see how the performance of the various models scale with the addition of ground-based photometry, which will be crucial for photo-z estimates. Lastly, further investigations of the photo-z PDF produced by the classification approach will be useful, especially in light of variations of the input magnitudes or images, given their own uncertainties.

In Chapter 3, I provided the measurements of the two-point angular correlation function in 13 redshift bins on the latest version 2.1.10 of the Flagship simulation, with the setting of future DR3 analyses. This work was done with both equipopulated and equidistant redshift binning schemes and in the first case, all cross-correlations where also measured. The measurement was also performed in a DR1-like setting, with 6 bins, 2500 deg^2 and a brighter magnitude cut. In addition, I provide results on the influence of the photo-z type, median or first mode, computed with `NNPZ` or `DeepZ`, showing that this is absolutely not negligible, with variations of the amplitude of $w(\theta)$ by several times its uncertainty. The influence of the angular resolution of the random samples on $w(\theta)$ with both the Flagship simulation and observations from the Dark Energy Survey with a complex mask is studied, showing that $N_{\rm side} = 4096$ can be used on the simulation but a minimum of 8192 is necessary with observations like the ones from DES. Though it is specific to the `TreeCorr` code, the study of the $b_{\rm s}$ approximation remains important in light of its impact on $w(\theta)$, especially at small angular separations, and the very significant speed-up that it provides on long computations. I also studied the influence of the number of jackknife samples to compute its jackknife covariance and evaluate the uncertainty on $w(\theta)$. This jackknife covariance was then presented along analytical Gaussian and SSC covariances.

The tomographic BAO analysis of Flagship photometric galaxy clustering presented in Chapter 4 resulted in a publication (Euclid Collaboration: Duret et al., 2025). Several approaches were considered : analysis on individual redshift bins and joint analysis, empirical or analytical covariance, measured or synthetic data vector, MCMC or profile likelihood. With the joint analysis, I obtained an improvement by a factor 3 on the constraint of the α parameter with respect to the current best constraints from photometric galaxy clustering, with DES Y6. Results obtained from individual bins will be useful to constrain the expansion history of the Universe between $z = 2.5$ and $z = 0.2$. Constraints at 0.4 %, 0.9 %, and 7.7 % are obtained on h, $\Omega_{\rm b}$ and $\Omega_{\rm cdm}$. I also provide detailed results on the robustness of the constraints both at the level of α and cosmological parameters, robustness with respect to the choice of fiducial cosmology (effect smaller than $0.1\,\sigma$). Different functional forms of the template used to fit α are tested, showing that biases can appear at low redshift when θ^{-2} is not included, along with an underestimation of the uncertainty. The fact that the template is robust with respect to RSD is checked successfully while on the contrary, the scale cuts applied to the data vector seem important, at least on the best-fit α since the bias with respect to the expected value can exceed $1\,\sigma$. It would be interesting to check if this bias is as strong with a MCMC approach on a large grid of scale cuts, since the bias observed on the small grid was negligible. Another element one should keep in mind for future analyses of the same kind : the weight of each redshift bin on the

global result can be crucial, either in the joint analysis or in the cosmological analysis, with the example of the bin 11 In Flagship which shifts constraints on $\Omega_{\rm cdm}$ by 1σ. Finally a preliminary study indicates that using equidistant bins and more redshift bins (if the number of galaxies allows it) tightens the cosmological constraints we obtained, with an improvement by 32% of the constrains on $\Omega_{\rm cdm}$. This will have to be taken into account in future analyses of this probe with *Euclid*. Ultimately, a complete optimization of the sample selection with redshift-dependant colour cuts would be even more profitable, as it will allow the use of the best sample tailored for the BAO analysis.

The full-shape analysis of Chapter 5 provides an estimate of the constraints on the ΛCDM model cosmological parameters one could expect from photometric galaxy clustering in a DR1-like setting with a slightly more conservative sample selection than the future DR1 sample. In order to complete this analysis, it would be useful to extend the constraints on the ΛCDM model to the $w_0 w_{\rm a} CDM$ model. Including a non-linear bias and baryonic feedback in the theoretical model of $w(\theta)$ may allow the use of smaller angular scales and improve the constraints. However, these results are subject to the contamination of effects like a bias or a broadening of the redshift distributions used to compute the theoretical model of $w(\theta)$. The stretch is especially harmful to σ_8 since a small stretch of 2% can create a 0.44σ bias alone and 0.49σ when combined with a multiplicative bias of $0.002\,(1+z)$. Marginalizing over redshift bin-dependent bias and stretch nuisance parameters is a way to alleviate these biases on cosmological parameters but it comes at the price of degraded constraints. This degradation decreases when the width of the prior of these nuisance parameters shrink, which is another argument as to why it is very important to improve photo-z estimates as much as possible to obtain accurate and precise redshift distributions for photometric galaxy clustering analyses. When new complete pixel-level simulations or when enough data will be available, the work done during this thesis will enable a complete study starting from the production of photo-z from galaxy images and magnitudes with deep learning models down to cosmological constraints with both BAO and full-shape analyses of tomographic photometric galaxy clustering.

Bibliography

[1] Abadi, M., Agarwal, A., Barham, P., et al. *TensorFlow: Large-Scale Machine Learning on Heterogeneous Systems*. Software available from tensorflow.org. 2015. URL: https://www.tensorflow.org/ (cit. on p. 57).

[2] Abbott, T. M. C., Abdalla, F. B., Alarcon, A., et al. "Dark Energy Survey Year 1 Results: Measurement of the Baryon Acoustic Oscillation scale in the distribution of galaxies to redshift 1". In: *MNRAS* 483.4 (Mar. 2019), p. 4866. DOI: 10.1093/mnras/sty3351. arXiv: 1712.06209 [astro-ph.CO] (cit. on p. 113).

[3] Abbott, T. M. C., Abdalla, F. B., and Allam, S. "The Dark Energy Survey: Data Release 1". In: *ApJS* 239.2, 18 (Dec. 2018), p. 18. DOI: 10.3847/1538-4365/aae9f0. arXiv: 1801.03181 [astro-ph.IM] (cit. on p. 46).

[4] Abbott, T. M. C., Adamow, M., Aguena, M., et al. "Dark Energy Survey: A 2.1% measurement of the angular baryonic acoustic oscillation scale at redshift z=0.85 from the final dataset". In: *Phys. Rev. D* 110.6, 063515 (Sept. 2024), p. 063515. DOI: 10.1103/PhysRevD.110.063515. arXiv: 2402.10696 [astro-ph.CO] (cit. on pp. 76, 106, 122, 127).

[5] Abdalla, F. B., Banerji, M., Lahav, O., et al. "A comparison of six photometric redshift methods applied to 1.5 million luminous red galaxies". In: *MNRAS* 417.3 (Nov. 2011), p. 1891. DOI: 10.1111/j.1365-2966.2011.19375.x. arXiv: 0812.3831 [astro-ph] (cit. on p. 52).

[6] Ade, P. A. R., Aghanim, N., Arnaud, M., Ashdown, M., Aumont, J., Baccigalupi, C., Banday, A. J., Barreiro, R. B., Bartlett, J. G., Bartolo, N., et al. "Planck2015 results: XIII. Cosmological parameters". In: *A&A* 594 (Sept. 2016), A13. ISSN: 1432-0746. DOI: 10.1051/0004-6361/201525830. URL: http://dx.doi.org/10.1051/0004-6361/201525830 (cit. on pp. 121, 122).

[7] Ade, P. A. R., Aghanim, N., Arnaud, M., Ashdown, M., Aumont, J., Baccigalupi, C., Banday, A. J., Barreiro, R. B., Bartlett, J. G., Battaner, E., et al. "Planckintermediate results: XVI. Profile likelihoods for cosmological parameters". In: *A&A* 566 (June 2014), A54. ISSN: 1432-0746. DOI: 10.1051/0004-6361/201323003. URL: http://dx.doi.org/10.1051/0004-6361/201323003 (cit. on p. 114).

[8] Agarwal, V., Singal, J., and Gyure, C. "SpyderZ: An Efficient Support Vector Machine Library for Photometric Redshift Estimation and Redshift Probability Information". In: *RNAAS* 8.5 (May 2024), p. 126. DOI: 10.3847/2515-5172/ad47fb. URL: https://dx.doi.org/10.3847/2515-5172/ad47fb (cit. on p. 54).

[9] Aihara, H., Arimoto, N., Armstrong, R., et al. "The Hyper Suprime-Cam SSP Survey: Overview and survey design". In: *PASJ* 70, S4 (Jan. 2018), S4. DOI: 10.1093/pasj/psx066. arXiv: 1704.05858 [astro-ph.IM] (cit. on p. 46).

[10] Alam, S., Albareti, F. D., Allende Prieto, C., et al. "The Eleventh and Twelfth Data Releases of the Sloan Digital Sky Survey: Final Data from SDSS-III". In: *ApJS* 219.1, 12 (July 2015), p. 12. DOI: 10.1088/0067-0049/219/1/12. arXiv: 1501.00963 [astro-ph.IM] (cit. on p. 59).

[11] Alam, S., Aubert, M., and Avila, S. "Completed SDSS-IV extended Baryon Oscillation Spectroscopic Survey: Cosmological implications from two decades of spectroscopic surveys at the Apache Point Observatory". In: *Physical Review D* 103.8 (Apr. 2021). ISSN: 2470-0029. DOI: 10.1103/physrevd.103.083533. URL: http://dx.doi.org/10.1103/PhysRevD.103.083533 (cit. on pp. 36, 38, 45).

[12] Almosallam, I. A., Jarvis, M. J., and Roberts, S. J. "GPZ: non-stationary sparse Gaussian processes for heteroscedastic uncertainty estimation in photometric redshifts". In: *MNRAS* 462.1 (Oct. 2016), p. 726. DOI: 10.1093/mnras/stw1618. arXiv: 1604.03593 [astro-ph.IM] (cit. on p. 53).

[13] Almosallam, I. A., Lindsay, S. N., Jarvis, M. J., et al. "A sparse Gaussian process framework for photometric redshift estimation". In: *MNRAS* 455.3 (Jan. 2016), p. 2387. DOI: 10.1093/mnras/stv2425. arXiv: 1505.05489 [astro-ph.IM] (cit. on p. 53).

[14] Alonso, D., Bull, P., Ferreira, P. G., et al. "Ultra-large scale cosmology in next-generation experiments with single tracers". In: *ApJ* 814.2 (Nov. 2015), p. 145. ISSN: 1538-4357. DOI: 10.1088/0004-637x/814/2/145. URL: http://dx.doi.org/10.1088/0004-637X/814/2/145 (cit. on p. 79).

[15] Amaro, V., Cavuoti, S., Brescia, M., et al. "Statistical analysis of probability density functions for photometric redshifts through the KiDS-ESO-DR3 galaxies". In: *MNRAS* 482.3 (Jan. 2019), pp. 3116–3134. DOI: 10.1093/mnras/sty2922. arXiv: 1810.09777 [astro-ph.IM] (cit. on p. 54).

[16] Armendariz-Picon, C., Mukhanov, V., and Steinhardt, Paul J. "Dynamical Solution to the Problem of a Small Cosmological Constant and Late-Time Cosmic Acceleration". In: *Phys. Rev. Lett.* 85.21 (Nov. 2000), p. 4438. DOI: 10.1103/PhysRevLett.85.4438. arXiv: astro-ph/0004134 [astro-ph] (cit. on p. 44).

[17] Armendariz-Picon, C., Mukhanov, V., and Steinhardt, Paul J. "Essentials of k-essence". In: *Phys. Rev. D* 63.10, 103510 (May 2001), p. 103510. DOI: 10.1103/PhysRevD.63.103510. arXiv: astro-ph/0006373 [astro-ph] (cit. on p. 44).

[18] Arnouts, S., Moscardini, L., Vanzella, E., et al. "Measuring the redshift evolution of clustering: the Hubble Deep Field South". In: *MNRAS* 329.2 (Jan. 2002), p. 355. DOI: 10.1046/j.1365-8711.2002.04988.x. arXiv: astro-ph/0109453 [astro-ph] (cit. on p. 51).

[19] Assef, R. J., Kochanek, C. S., Brodwin, M., et al. "Low-Resolution Spectral Templates for Active Galactic Nuclei and Galaxies from 0.03 to 30 μm". In: *ApJ* 713.2 (Apr. 2010), p. 970. DOI: 10.1088/0004-637X/713/2/970. arXiv: 0909.3849 [astro-ph.CO] (cit. on p. 51).

[20] Beck, R., Dobos, L., Budavári, T., Szalay, A. S., et al. "Photometric redshifts for the SDSS Data Release 12". In: *MNRAS* 460.2 (Aug. 2016), p. 1371. DOI: 10.1093/mnras/stw1009. arXiv: 1603.09708 [astro-ph.GA] (cit. on p. 60).

[21] Beck, R., Dobos, L., Budavári, T., Szalay, A.S., et al. "Photo-z-SQL: Integrated, flexible photometric redshift computation in a database". In: *Astronomy and Computing* 19 (Apr. 2017), p. 34. ISSN: 2213-1337. DOI: 10.1016/j.ascom.2017.03.002. URL: http://dx.doi.org/10.1016/j.ascom.2017.03.002 (cit. on p. 51).

[22] Behroozi, P. S., Wechsler, R. H., and Wu, H.-Y. "The ROCKSTAR Phase-space Temporal Halo Finder and the Velocity Offsets of Cluster Cores". In: *ApJ* 762.2, 109 (Jan. 2013), p. 109. DOI: 10.1088/0004-637X/762/2/109. arXiv: 1110.4372 [astro-ph.CO] (cit. on p. 83).

[23] Benitez, N. "Bayesian Photometric Redshift Estimation". In: *ApJ* 536.2 (June 2000), p. 571. ISSN: 1538-4357. DOI: 10.1086/308947. URL: http://dx.doi.org/10.1086/308947 (cit. on p. 51).

[24] Benítez, N., Ford, H., Bouwens, R., et al. "Faint Galaxies in Deep Advanced Camera for Surveys Observations". In: *ApJS* 150.1 (Jan. 2004), p. 1. DOI: 10.1086/380120. arXiv: astro-ph/0309077 [astro-ph] (cit. on p. 51).

[25] Blanton, M. R., Hogg, D. W., Bahcall, N. A., et al. "The Galaxy Luminosity Function and Luminosity Density at Redshift z = 0.1". In: *ApJ* 592.2 (Aug. 2003), p. 819. DOI: 10.1086/375776. arXiv: astro-ph/0210215 [astro-ph] (cit. on p. 83).

[26] Blanton, M. R., Lupton, R. H., Schlegel, David J., et al. "The Properties and Luminosity Function of Extremely Low Luminosity Galaxies". In: *ApJ* 631.1 (Sept. 2005), p. 208. DOI: 10.1086/431416. arXiv: astro-ph/0410164 [astro-ph] (cit. on p. 83).

[27] Blas, D., Lesgourgues, J., and Tram, T. "The Cosmic Linear Anisotropy Solving System (CLASS). Part II: Approximation schemes". In: *JCAP* 07.7, 034 (July 2011), p. 034. DOI: 10.1088/1475-7516/2011/07/034. arXiv: 1104.2933 [astro-ph.CO] (cit. on p. 48).

[28] Boisseau, B., Esposito-Farèse, G., Polarski, D., et al. "Reconstruction of a Scalar-Tensor Theory of Gravity in an Accelerating Universe". In: *Phys. Rev. Lett.* 85.11 (Sept. 2000), pp. 2236–2239. DOI: 10.1103/PhysRevLett.85.2236. arXiv: gr-qc/0001066 [gr-qc] (cit. on p. 44).

[29] Bolzonella, M., Miralles, J. -M., and Pelló, R. "Photometric redshifts based on standard SED fitting procedures". In: *A&A* 363 (Nov. 2000), p. 476. DOI: 10.48550/arXiv.astro-ph/0003380. arXiv: astro-ph/0003380 [astro-ph] (cit. on p. 51).

[30] Brammer, G. B., van Dokkum, P. G., and Coppi, P. "EAZY: A Fast, Public Photometric Redshift Code". In: *ApJ* 686.2 (Oct. 2008), p. 1503. DOI: 10.1086/591786. arXiv: 0807.1533 [astro-ph] (cit. on p. 51).

[31] Brans, C. and Dicke, R. H. "Mach's Principle and a Relativistic Theory of Gravitation". In: *Physical Review* 124.3 (Nov. 1961), p. 925. DOI: 10.1103/PhysRev.124.925 (cit. on p. 44).

[32] Broyden, C. G. "The Convergence of a Class of Double-rank Minimization Algorithms 1. General Considerations". In: *IMA Journal of Applied Mathematics* 6.1 (Mar. 1970), p. 76. ISSN: 0272-4960. DOI: 10.1093/imamat/6.1.76. eprint: https://academic.oup.com/imamat/article-pdf/6/1/76/2233756/6-1-76.pdf. URL: https://doi.org/10.1093/imamat/6.1.76 (cit. on p. 113).

[33] Broyden, C. G. "The Convergence of a Class of Double-rank Minimization Algorithms: 2. The New Algorithm". In: *IMA Journal of Applied Mathematics* 6.3 (Sept. 1970), p. 222. ISSN: 0272-4960. DOI: 10.1093/imamat/6.3.222. eprint: https://academic.oup.com/imamat/article-pdf/6/3/222/1848059/6-3-222.pdf. URL: https://doi.org/10.1093/imamat/6.3.222 (cit. on p. 113).

[34] Caldwell, R. R., Dave, R., and Steinhardt, P. J. "Cosmological Imprint of an Energy Component with General Equation of State". In: *Phys. Rev. Lett.* 80.8 (Feb. 1998), p. 1582. DOI: 10.1103/PhysRevLett.80.1582. arXiv: astro-ph/9708069 [astro-ph] (cit. on p. 44).

[35] Carrasco Kind, M. and Brunner, R. J. "TPZ: photometric redshift PDFs and ancillary information by using prediction trees and random forests". In: *MNRAS* 432.2 (May 2013), p. 1483. ISSN: 1365-2966. DOI: 10.1093/mnras/stt574. URL: http://dx.doi.org/10.1093/mnras/stt574 (cit. on p. 53).

[36] Carrasco Kind, M. and Brunner, R. J. "SOMz: photometric redshift PDFs with self-organizing maps and random atlas". In: *MNRAS* 438.4 (Jan. 2014), p. 3409. ISSN: 0035-8711. DOI: 10.1093/mnras/stt2456. eprint: https://academic.oup.com/mnras/article-pdf/438/4/3409/3868167/stt2456.pdf. URL: https://doi.org/10.1093/mnras/stt2456 (cit. on p. 54).

[37] Carretero, J., Castander, F. J., Gaztañaga, E., et al. "An algorithm to build mock galaxy catalogues using MICE simulations". In: *MNRAS* 447.1 (Feb. 2015), p. 646. ISSN: 0035-8711. DOI: 10.1093/mnras/stu2402. eprint: https://academic.oup.com/mnras/article-pdf/447/1/646/4911622/stu2402.pdf. URL: https://doi.org/10.1093/mnras/stu2402 (cit. on p. 83).

[38] Carretero, J., Tallada, P., Casals, J., et al. "CosmoHub and SciPIC: Massive cosmological data analysis, distribution and generation using a Big Data platform". In: *Proceedings of the European Physical Society Conference on High Energy Physics. 5-12 July*. July 2017, 488, p. 488 (cit. on p. 82).

[39] Carroll, S. M., de Felice, A., Duvvuri, V., et al. "Cosmology of generalized modified gravity models". In: *Phys. Rev. D* 71.6, 063513 (Mar. 2005), p. 063513. DOI: 10.1103/PhysRevD.71.063513. arXiv: astro-ph/0410031 [astro-ph] (cit. on p. 44).

[40] Carvalho, G. C., Bernui, A., Benetti, M., et al. "The transverse baryonic acoustic scale from the SDSS DR11 galaxies". In: *Astroparticle Physics* 119, 102432 (May 2020), p. 102432. DOI: 10.1016/j.astropartphys.2020.102432. arXiv: 1709.00271 [astro-ph.CO] (cit. on p. 113).

[41] Cavuoti, S., Amaro, V., Brescia, M., et al. "METAPHOR: a machine-learning-based method for the probability density estimation of photometric redshifts". In: *MNRAS* 465 (Feb. 2017), p. 1959. DOI: 10.1093/mnras/stw2930. arXiv: 1611.02162 [astro-ph.IM] (cit. on p. 54).

[42] Challinor, A. and Lewis, A. "Linear power spectrum of observed source number counts". In: *Phys. Rev. D* 84 (4 Aug. 2011), p. 043516. DOI: 10.1103/PhysRevD.84.043516. URL: https://link.aps.org/doi/10.1103/PhysRevD.84.043516 (cit. on p. 77).

[43] Chambers, K. C., Magnier, E. A., Metcalfe, N., et al. "The Pan-STARRS1 Surveys". In: *arXiv e-prints*, arXiv:1612.05560 (Dec. 2016), arXiv:1612.05560. DOI: 10.48550/arXiv.1612.05560. arXiv: 1612.05560 [astro-ph.IM] (cit. on p. 46).

[44] Chevallier, M. and Polarski, D. "Accelerating Universes with Scaling Dark Matter". In: *International Journal of Modern Physics D* 10.2 (Jan. 2001), p. 213. DOI: 10.1142/S0218271801000822. arXiv: gr-qc/0009008 [gr-qc] (cit. on p. 43).

[45] Chisari, N. E., Alonso, D., Krause, E., et al. "Core Cosmology Library: Precision Cosmological Predictions for LSST". In: *ApJS* 242.1 (May 2019), p. 2. ISSN: 1538-4365. DOI: 10.3847/1538-4365/ab1658. URL: http://dx.doi.org/10.3847/1538-4365/ab1658 (cit. on pp. 78–80).

[46] Chollet, F. et al. *Keras*. https://keras.io. 2015 (cit. on p. 57).

[47] Chow, N. and Khoury, J. "Galileon cosmology". In: *Phys. Rev. D* 80.2, 024037 (July 2009), p. 024037. DOI: 10.1103/PhysRevD.80.024037. arXiv: 0905.1325 [hep-th] (cit. on p. 44).

[48] Cole, S., Percival, W. J., Peacock, J. A., et al. "The 2dF Galaxy Redshift Survey: power-spectrum analysis of the final data set and cosmological implications". In: *MNRAS* 362.2 (Sept. 2005), p. 505. ISSN: 1365-2966. DOI: 10.1111/j.1365-2966.2005.09318.x. URL: http://dx.doi.org/10.1111/j.1365-2966.2005.09318.x (cit. on p. 35).

[49] Crocce, M., Cabré, A., and Gaztañaga, E. "Modelling the angular correlation function and its full covariance in photometric galaxy surveys: Angular clustering in photometric surveys". In: *MNRAS* 414.1 (Mar. 2011), p. 329. ISSN: 0035-8711. DOI: 10.1111/j.1365-2966.2011.18393.x. URL: http://dx.doi.org/10.1111/j.1365-2966.2011.18393.x (cit. on p. 77).

[50] D'Isanto, A. and Polsterer, K. L. "Photometric redshift estimation via deep learning - Generalized and pre-classification-less, image based, fully probabilistic redshifts". In: *A&A* 609 (2018), A111. DOI: 10.1051/0004-6361/201731326. URL: https://doi.org/10.1051/0004-6361/201731326 (cit. on p. 55).

[51] Dahlen, T., Mobasher, B., Somerville, R. S., et al. "The Evolution of the Optical and Near-Infrared Galaxy Luminosity Functions and Luminosity Densities to z~2". In: *ApJ* 631.1 (Sept. 2005), p. 126. DOI: 10.1086/432027. arXiv: astro-ph/0505297 [astro-ph] (cit. on p. 83).

[52] de Felice, A., Mota, D. F., and Tsujikawa, S. "Matter Instabilities in General Gauss-Bonnet Gravity". In: *Modern Physics Letters A* 25.11-12 (Jan. 2010), p. 885. DOI: 10.1142/S0217732310000046. arXiv: 0911.1811 [gr-qc] (cit. on p. 44).

[53] De Vicente, J., Sánchez, E., and Sevilla-Noarbe, I. "DNF – Galaxy photometric redshift by Directional Neighbourhood Fitting". In: *MNRAS* 459.3 (Apr. 2016), p. 3078. ISSN: 0035-8711. DOI: 10.1093/mnras/stw857. eprint: https://academic.oup.com/mnras/article-pdf/459/3/3078/8109193/stw857.pdf. URL: https://doi.org/10.1093/mnras/stw857 (cit. on p. 53).

[54] Deffayet, C., Pujolàs, O., Sawicki, I., et al. "Imperfect dark energy from kinetic gravity braiding". In: *J. Cosmology Astropart. Phys.* 2010.10, 026 (Oct. 2010), p. 026. DOI: 10.1088/1475-7516/2010/10/026. arXiv: 1008.0048 [hep-th] (cit. on p. 44).

[55] Dembinski, H., Ongmongkolkul, P., Deil, C., et al. *Zenodo, 10.5281/zenodo.3949207*. Dec. 2020. DOI: 10.5281/zenodo.3949207. URL: https://doi.org/10.5281/zenodo.3949207 (cit. on p. 115).

[56] DESI Collaboration: Adame, A. G., Aguilar, J., Ahlen, S., et al. "DESI 2024 III: Baryon Acoustic Oscillations from Galaxies and Quasars". In: arXiv:2404.03000 (2024), arXiv:2404.03000. DOI: 10.48550/arXiv.2404.03000. arXiv: 2404.03000 [astro-ph.CO]. URL: https://arxiv.org/abs/2404.03000 (cit. on p. 36).

[57] Einstein, A. "Die Feldgleichungen der Gravitation". In: *Sitzungsberichte der Königlich Preussischen Akademie der Wissenschaften* (Jan. 1915), p. 844 (cit. on p. 36).

[58] Einstein, A. "Kosmologische Betrachtungen zur allgemeinen Relativitätstheorie". In: *Sitzungsberichte der Königlich Preussischen Akademie der Wissenschaften* (Jan. 1917), p. 142 (cit. on p. 38).

[59] Eisenstein, D. J. and Hu, W. "Baryonic Features in the Matter Transfer Function". In: *ApJ* 496.2 (Apr. 1998), p. 605. ISSN: 1538-4357. DOI: 10.1086/305424. URL: http://dx.doi.org/10.1086/305424 (cit. on pp. 47, 48, 115).

[60] Eisenstein, D. J., Zehavi, I., Hogg, D. W., et al. "Detection of the Baryon Acoustic Peak in the Large-Scale Correlation Function of SDSS Luminous Red Galaxies". In: *ApJ* 633.2 (Nov. 2005), p. 560. ISSN: 1538-4357. DOI: 10.1086/466512. URL: http://dx.doi.org/10.1086/466512 (cit. on p. 35).

[61] Elliott, J., Souza, R.S. de, Krone-Martins, A., et al. "The overlooked potential of Generalized Linear Models in astronomy-II: Gamma regression and photometric redshifts". In: *Astronomy and Computing* 10 (Apr. 2015), p. 61. ISSN: 2213-1337. DOI: 10.1016/j.ascom.2015.01.002. URL: http://dx.doi.org/10.1016/j.ascom.2015.01.002 (cit. on p. 53).

[62] Eriksen, M, Alarcon, A, Gaztanaga, E, et al. "The PAU Survey: early demonstration of photometric redshift performance in the COSMOS field". In: *Monthly Notices of the Royal Astronomical Society* 484.3 (Jan. 2019), p. 4200. ISSN: 1365-2966. DOI: 10.1093/mnras/stz204. URL: http://dx.doi.org/10.1093/mnras/stz204 (cit. on p. 51).

[63] Euclid Collaboration: Blanchard, A., Camera, S., Carbone, C., et al. "Euclid preparation: VII. Forecast validation for Euclid cosmological probes". In: *A&A* 642 (Oct. 2020), A191. ISSN: 1432-0746. DOI: 10.1051/0004-6361/202038071. URL: http://dx.doi.org/10.1051/0004-6361/202038071 (cit. on pp. 44, 76).

[64] Euclid Collaboration: Castander, F. J., Fosalba, P., Stadel, J., et al. "Euclid. V. The Flagship galaxy mock catalogue: a comprehensive simulation for the Euclid mission". In: arXiv:2405.13495 (May 2024), arXiv:2405.13495. DOI: 10.48550/arXiv.2405.13495. arXiv: 2405.13495 [astro-ph.CO] (cit. on pp. 48, 82).

[65] Euclid Collaboration: Cropper, M., Al-Bahlawan, A., Amiaux, J., et al. "Euclid. II. The VIS Instrument". In: arXiv:2405.13492 (May 2024), arXiv:2405.13492. DOI: 10.48550/arXiv.2405.13492. arXiv: 2405.13492 [astro-ph.IM] (cit. on pp. 44, 46).

[66] Euclid Collaboration: Desprez, G., Paltani, S., Coupon, J., et al. "Euclid preparation - X. The Euclid photometric-redshift challenge". In: *A&A* 644 (2020), A31. DOI: 10.1051/0004-6361/202039403. URL: https://doi.org/10.1051/0004-6361/202039403 (cit. on pp. 52, 53).

[67] Euclid Collaboration: Duret, V., Escoffier, S., Gillard, W., et al. "Euclid preparation. BAO analysis of photometric galaxy clustering in configuration space". In: *arXiv e-prints*, arXiv:2503.11621 (Mar. 2025), arXiv:2503.11621. DOI: 10.48550/arXiv.2503.11621. arXiv: 2503.11621 [astro-ph.CO] (cit. on pp. 3, 112, 162).

[68] Euclid Collaboration: Enia, A., Bolzonella, M., Pozzetti, L., et al. "Euclid preparation: LI. Forecasting the recovery of galaxy physical properties and their relations with template-fitting and machine-learning methods". In: *A&A* 691, A175 (Nov. 2024), A175. DOI: 10.1051/0004-6361/202451425. arXiv: 2407.07940 [astro-ph.GA] (cit. on p. 52).

[69] Euclid Collaboration: Jahnke, K., Gillard, W., Schirmer, M., et al. "Euclid. III. The NISP Instrument". In: arXiv:2405.13493 (May 2024), arXiv:2405.13493. DOI: 10.48550/arXiv.2405.13493. arXiv: 2405.13493 [astro-ph.IM] (cit. on pp. 44–46, 75).

[70] Euclid Collaboration: Mellier, Y., Abdurro'uf, Acevedo Barroso, J. A., et al. "Euclid. I. Overview of the Euclid mission". In: arXiv:2405.13491 (May 2024), arXiv:2405.13491. DOI: 10.48550/arXiv.2405.13491. arXiv: 2405.13491 [astro-ph.CO] (cit. on pp. 44–46, 76, 83).

[71] Euclid Collaboration: Scaramella, R., Amiaux, J., Mellier, Y., et al. "Euclid preparation. I. The Euclid Wide Survey". In: *A&A* 662, A112 (June 2022), A112. DOI: 10.1051/0004-6361/202141938. arXiv: 2108.01201 [astro-ph.CO] (cit. on p. 44).

[72] Euclid Collaboration: Sciotti, D., Gouyou Beauchamps, S., Cardone, V. F., et al. "Euclid preparation: LII. Forecast impact of super-sample covariance on 3×2pt analysis with Euclid". In: *A&A* 691, A318 (Nov. 2024), A318. DOI: 10.1051/0004-6361/202348389. arXiv: 2310.15731 [astro-ph.CO] (cit. on p. 107).

[73] Euclid Collaboration: Serrano, S., Hudelot, P., Seidel, G., et al. "Euclid preparation - XLVIII. The pre-launch Science Ground Segment simulation framework". In: *A&A* 690 (2024), A103. DOI: 10.1051/0004-6361/202349128. URL: https://doi.org/10.1051/0004-6361/202349128 (cit. on p. 66).

[74] Euclid Collaboration: Tucci, M., Paltani, S., Hartley, W. G., et al. "Euclid Quick Data Release (Q1). Photometric redshifts and physical properties of galaxies through the PHZ processing function". In: *arXiv e-prints*, arXiv:2503.15306 (Mar. 2025), arXiv:2503.15306. DOI: 10.48550/arXiv.2503.15306. arXiv: 2503.15306 [astro-ph.GA] (cit. on pp. 51, 84).

[75] Fang, X., Eifler, T., and Krause, E. "2D-FFTLog: efficient computation of real-space covariance matrices for galaxy clustering and weak lensing". In: *MNRAS* 497.3 (June 2020), p. 2699. ISSN: 1365-2966. DOI: 10.1093/mnras/staa1726. URL: http://dx.doi.org/10.1093/mnras/staa1726 (cit. on p. 104).

[76] Fang, X., Krause, E., Eifler, T., et al. "Beyond Limber: efficient computation of angular power spectra for galaxy clustering and weak lensing". In: *JCAP* 05.05, 010 (May 2020), p. 010. DOI: 10.1088/1475-7516/2020/05/010. arXiv: 1911.11947 [astro-ph.CO]. URL: https://dx.doi.org/10.1088/1475-7516/2020/05/010 (cit. on pp. 80, 104).

[77] Feldman, Hume A., Kaiser, Nick, and Peacock, John A. "Power-Spectrum Analysis of Three-dimensional Redshift Surveys". In: *ApJ* 426 (May 1994), p. 23. DOI: 10.1086/174036. arXiv: astro-ph/9304022 [astro-ph] (cit. on p. 122).

[78] Feldmann, R., Carollo, C. M., Porciani, C., et al. "The Zurich Extragalactic Bayesian Redshift Analyzer and its first application: COSMOS". In: *MNRAS* 372.2 (Oct. 2006), p. 565. DOI: 10.1111/j.1365-2966.2006.10930.x. arXiv: astro-ph/0609044 [astro-ph] (cit. on p. 51).

[79] Feroz, F., Hobson, M. P., Cameron, E., et al. "Importance Nested Sampling and the MultiNest Algorithm". In: *The Open Journal of Astrophysics* 2.1, 10 (Nov. 2019), p. 10. DOI: 10.21105/astro.1306.2144. arXiv: 1306.2144 [astro-ph.IM] (cit. on p. 115).

[80] Fixsen, D. J. "The temperature of the Cosmic Microwave Background". In: *ApJ* 707.2 (Nov. 2009), p. 916. ISSN: 1538-4357. DOI: 10.1088/0004-637x/707/2/916. URL: http://dx.doi.org/10.1088/0004-637X/707/2/916 (cit. on p. 42).

[81] Fletcher, R. "A new approach to variable metric algorithms". In: *The Computer Journal* 13.3 (Jan. 1970), p. 317. ISSN: 0010-4620. DOI: 10.1093/comjnl/13.3.317. eprint: https://academic.oup.com/comjnl/article-pdf/13/3/317/988678/130317.pdf. URL: https://doi.org/10.1093/comjnl/13.3.317 (cit. on p. 113).

[82] Foreman-Mackey, D., Hogg, D. W., Lang, D., et al. "<tt>emcee</tt>: The MCMC Hammer". In: *PASP* 125.925 (Mar. 2013), p. 306. ISSN: 1538-3873. DOI: 10.1086/670067. URL: http://dx.doi.org/10.1086/670067 (cit. on p. 114).

[83] Fotopoulou, S. and Paltani, S. "CPz: Classification-aided photometric-redshift estimation". In: *ApJ* 619 (Oct. 2018), A14. ISSN: 1432-0746. DOI: 10.1051/0004-6361/201730763. URL: http://dx.doi.org/10.1051/0004-6361/201730763 (cit. on p. 51).

[84] Freund, Y. and Schapire, R. E. "A Decision-Theoretic Generalization of On-Line Learning and an Application to Boosting". In: *Journal of Computer and System Sciences* 55.1 (1997), p. 119. ISSN: 0022-0000. DOI: https://doi.org/10.1006/jcss.1997.1504. URL: https://www.sciencedirect.com/science/article/pii/S002200009791504X (cit. on p. 53).

[85] Friedmann, A. "Über die Krümmung des Raumes". In: *Zeitschrift fur Physik* 10 (Jan. 1922), p. 377. DOI: 10.1007/BF01332580 (cit. on p. 39).

[86] Friedmann, A. "Über die Möglichkeit einer Welt mit konstanter negativer Krümmung des Raumes". In: *Zeitschrift fur Physik* 21.1 (Dec. 1924), p. 326. DOI: 10.1007/BF01328280 (cit. on p. 39).

[87] Gelman, A. and Rubin, D. B. "Inference from Iterative Simulation Using Multiple Sequences". In: *Statistical Science* 7 (Jan. 1992), p. 457. DOI: 10.1214/ss/1177011136 (cit. on p. 114).

[88] Gerdes, D. W., Sypniewski, A. J., McKay, T. A., et al. "ArborZ: Photometric Redshifts Using Boosted Decision Trees". In: *ApJ* 715.2 (May 2010), p. 823. ISSN: 1538-4357. DOI: 10.1088/0004-637x/715/2/823. URL: http://dx.doi.org/10.1088/0004-637X/715/2/823 (cit. on p. 53).

[89] Gini, C. "Measurement of Inequality of Incomes". In: *The Economic Journal* 31.121 (Mar. 1921), p. 124. ISSN: 0013-0133. DOI: 10.2307/2223319. eprint: https://academic.oup.com/ej/article-pdf/31/121/124/27606330/ej0124.pdf. URL: https://doi.org/10.2307/2223319 (cit. on p. 53).

[90] Goldfarb, D. "A Family of Variable-Metric Methods Derived by Variational Means". In: *Mathematics of Computation* 24.109 (1970), p. 23. ISSN: 00255718, 10886842. URL: https://www.ams.org/journals/mcom/1970-24-109/S0025-5718-1970-0258249-6/S0025-5718-1970-0258249-6.pdf (cit. on p. 113).

[91] Górski, K. M., Hivon, E., Banday, A. J., et al. "HEALPix: A Framework for High-Resolution Discretization and Fast Analysis of Data Distributed on the Sphere". In: *ApJ* 622 (Apr. 2005), p. 759. DOI: 10.1086/427976. eprint: arXiv:astro-ph/0409513 (cit. on p. 107).

[92] Gouyou Beauchamps, S., Lacasa, F., Tutusaus, I., et al. "Impact of survey geometry and super-sample covariance on future photometric galaxy surveys". In: *A&A* 659 (Mar. 2022), A128. ISSN: 1432-0746. DOI: 10.1051/0004-6361/202142052. URL: http://dx.doi.org/10.1051/0004-6361/202142052 (cit. on p. 106).

[93] Guth, A. H. "Inflationary universe: A possible solution to the horizon and flatness problems". In: *Phys. Rev. D* 23.2 (Jan. 1981), p. 347. DOI: 10.1103/PhysRevD.23.347 (cit. on p. 43).

[94] Hartlap, J., Simon, P., and Schneider, P. "Why your model parameter confidences might be too optimistic. Unbiased estimation of the inverse covariance matrix". In: *A&A* 464.1 (Mar. 2007), p. 399. DOI: 10.1051/0004-6361:20066170. arXiv: astro-ph/0608064 [astro-ph] (cit. on p. 104).

[95] He, K., Zhang, X., Ren, S., et al. "Deep Residual Learning for Image Recognition". In: *2016 IEEE Conference on Computer Vision and Pattern Recognition (CVPR*. June 2016, 1, p. 1. DOI: 10.1109/CVPR.2016.90. arXiv: 1512.03385 [cs.CV] (cit. on p. 57).

[96] Henghes, B., Thiyagalingam, J., Pettitt, C., et al. "Deep learning methods for obtaining photometric redshift estimations from images". In: *MNRAS* 512.2 (Feb. 2022), p. 1696. ISSN: 0035-8711. DOI: 10.1093/mnras/stac480. eprint: https://academic.oup.com/mnras/article-pdf/512/2/1696/48229843/stac480.pdf. URL: https://doi.org/10.1093/mnras/stac480 (cit. on p. 59).

[97] Hill, J. M. "The History of Multiobject Fiber Spectroscopy". In: *Fiber Optics in Astronomy*. Ed. by Samuel C. Barden. Vol. 3. Astronomical Society of the Pacific Conference Series. Jan. 1988, p. 77 (cit. on p. 45).

[98] Hill, J. M., Angel, J. R. P., Scott, J. S., et al. "Multiple object spectroscopy: the medusa spectrograph." In: *ApJ* 242 (Dec. 1980), p. L69. DOI: 10.1086/183405 (cit. on p. 45).

[99] Hoyle, B. "Measuring photometric redshifts using galaxy images and Deep Neural Networks". In: *Astronomy and Computing* 16 (2016), p. 34. ISSN: 2213-1337. DOI: https://doi.org/10.1016/j.ascom.2016.03.006. URL: https://www.sciencedirect.com/science/article/pii/S221313371630021X (cit. on p. 55).

[100] Hoyle, B., Rau, M. M., Paech, K., et al. "Anomaly detection for machine learning redshifts applied to SDSS galaxies". In: *MNRAS* 452.4 (Aug. 2015), p. 4183. ISSN: 1365-2966. DOI: 10.1093/mnras/stv1551. URL: http://dx.doi.org/10.1093/mnras/stv1551 (cit. on p. 53).

[101] Hu, W. and Sugiyama, N. "Small-Scale Cosmological Perturbations: An Analytic Approach". In: *ApJ* 471.2 (Nov. 1996), p. 542. ISSN: 1538-4357. DOI: 10.1086/177989. URL: http://dx.doi.org/10.1086/177989 (cit. on p. 48).

[102] Hubbard, E. N., Angel, J. R. P., and Gresham, M. S. "Operation of a long fused silica fiber as a link between telescope and spectrograph." In: *ApJ* 229 (May 1979), p. 1074. DOI: 10.1086/157041 (cit. on p. 45).

[103] Hubble, E. "A Relation between Distance and Radial Velocity among Extra-Galactic Nebulae". In: *Proceedings of the National Academy of Science* 15.3 (Mar. 1929), p. 168. DOI: 10.1073/pnas.15.3.168 (cit. on pp. 34, 35).

[104] Ibata, R. A., McConnachie, A., Cuillandre, J-C., et al. "The Canada-France Imaging Survey: First Results from the u-Band Component". In: *ApJ* 848.2, 128 (Oct. 2017), p. 128. DOI: 10.3847/1538-4357/aa855c. arXiv: 1708.06356 [astro-ph.GA] (cit. on p. 46).

[105] Ilbert, O., Arnouts, S., McCracken, H. J., et al. "Accurate photometric redshifts for the CFHT legacy survey calibrated using the VIMOS VLT deep survey". In: *A&A* 457.3 (Oct. 2006), p. 841. DOI: 10.1051/0004-6361:20065138. arXiv: astro-ph/0603217 [astro-ph] (cit. on p. 51).

[106] Ioffe, S. and Szegedy, C. "Batch normalization: accelerating deep network training by reducing internal covariate shift". In: *Proceedings of the 32nd International Conference on International Conference on Machine Learning - Volume 37*. ICML'15. Lille, France: JMLR.org, 2015, p. 448. URL: https://arxiv.org/abs/1502.03167 (cit. on p. 56).

[107] Ivezić, Ž., Kahn, S. M., Tyson, J. A., et al. "LSST: From Science Drivers to Reference Design and Anticipated Data Products". In: *ApJ* 873.2, 111 (Mar. 2019), p. 111. DOI: 10.3847/1538-4357/ab042c. arXiv: 0805.2366 [astro-ph] (cit. on p. 46).

[108] James, F. and Roos, M. "Minuit: A System for Function Minimization and Analysis of the Parameter Errors and Correlations". In: *Comput. Phys. Commun.* 10 (1975), p. 343. DOI: 10.1016/0010-4655(75)90039-9 (cit. on p. 115).

[109] Jarvis, M., Bernstein, G., and Jain, B. "The skewness of the aperture mass statistic". In: *MNRAS* 352.1 (July 2004), p. 338. ISSN: 0035-8711. DOI: 10.1111/j.1365-2966.2004.07926.x. eprint: https://academic.oup.com/mnras/article-pdf/352/1/338/3195813/352-1-338.pdf. URL: https://doi.org/10.1111/j.1365-2966.2004.07926.x (cit. on pp. 82, 97, 99).

[110] Jones, E. and Singal, J. "Analysis of a custom support vector machine for photometric redshift estimation and the inclusion of galaxy shape information". In: *A&A* 600 (2017), A113. DOI: 10.1051/0004-6361/201629558. URL: https://doi.org/10.1051/0004-6361/201629558 (cit. on p. 54).

[111] Kaiser, N. "Clustering in real space and in redshift space". In: *MNRAS* 227 (July 1987), p. 1. DOI: 10.1093/mnras/227.1.1 (cit. on p. 78).

[112] Kaiser, N. "Weak Gravitational Lensing of Distant Galaxies". In: *ApJ* 388 (Apr. 1992), p. 272. DOI: 10.1086/171151 (cit. on p. 79).

[113] Kobayashi, T., Yamaguchi, M., and Yokoyama, J. "Inflation Driven by the Galileon Field". In: *Phys. Rev. Lett.* 105.23, 231302 (Dec. 2010), p. 231302. DOI: 10.1103/PhysRevLett.105.231302. arXiv: 1008.0603 [hep-th] (cit. on p. 44).

[114] Kobayashi, T., Yamaguchi, M., and Yokoyama, J. "Generalized G-Inflation — Inflation with the Most General Second-Order Field Equations —". In: *Progress of Theoretical Physics* 126.3 (Sept. 2011), p. 511. DOI: 10.1143/PTP.126.511. arXiv: 1105.5723 [hep-th] (cit. on p. 44).

[115] Kohonen, T. "Self-organized formation of topologically correct feature maps". In: *Biological Cybernetics* 43.1 (Jan. 1982), p. 59. ISSN: 0340-1200. DOI: 10.1007/BF00337288. URL: http://dx.doi.org/10.1007/BF00337288 (cit. on p. 54).

[116] Krause, E. and Eifler, T. "cosmolike - cosmological likelihood analyses for photometric galaxy surveys". In: *MNRAS* 470.2 (Sept. 2017), p. 2100. DOI: 10.1093/mnras/stx1261. arXiv: 1601.05779 [astro-ph.CO] (cit. on pp. 103, 104).

[117] Lacasa, F. and Grain, J. "Fast and easy super-sample covariance of large-scale structure observables". In: *A&A* 624 (Apr. 2019), A61. ISSN: 1432-0746. DOI: 10.1051/0004-6361/201834343. URL: http://dx.doi.org/10.1051/0004-6361/201834343 (cit. on p. 106).

[118] Landy, S. D. and Szalay, A. S. "Bias and Variance of Angular Correlation Functions". In: *ApJ* 412 (July 1993), p. 64. DOI: 10.1086/172900 (cit. on p. 82).

[119] Lange, J. U. "nautilus: boosting Bayesian importance nested sampling with deep learning". In: *MNRAS* 525.2 (Aug. 2023), p. 3181. DOI: 10.1093/mnras/stad2441. eprint: https://academic.oup.com/mnras/article-pdf/525/2/3181/51331635/stad2441.pdf. URL: https://doi.org/10.1093/mnras/stad2441 (cit. on p. 115).

[120] Le Borgne, D. and Rocca-Volmerange, B. "Photometric redshifts from evolutionary synthesis with PÉGASE: The code Z-PEG and the $z = 0$ age constraint". In: *ApJ* 386.2 (May 2002), p. 446. ISSN: 1432-0746. DOI: 10.1051/0004-6361:20020259. URL: http://dx.doi.org/10.1051/0004-6361:20020259 (cit. on p. 51).

[121] Leavitt, H. S. and Pickering, E. C. "Periods of 25 Variable Stars in the Small Magellanic Cloud." In: *Harvard College Observatory Circular* 173 (Mar. 1912), p. 1 (cit. on p. 34).

[122] Lecun, Y., Bottou, L., Bengio, Y., et al. "Gradient-based learning applied to document recognition". In: *Proceedings of the IEEE* 86.11 (1998), p. 2278. DOI: 10.1109/5.726791 (cit. on p. 55).

[123] Lemaître, G. "Un Univers homogène de masse constante et de rayon croissant rendant compte de la vitesse radiale des nébuleuses extra-galactiques". In: *Annales de la Société Scientifique de Bruxelles* 47 (Jan. 1927), p. 49 (cit. on pp. 34, 39).

[124] Lemaître, G. "Evolution of the Expanding Universe". In: *Proceedings of the National Academy of Science* 20.1 (Jan. 1934), pp. 12–17. DOI: 10.1073/pnas.20.1.12 (cit. on p. 38).

[125] Lepori, F., Tutusaus, I., Viglione, C., et al. "Euclid preparation: XIX. Impact of magnification on photometric galaxy clustering". In: *A&A* 662 (June 2022), A93. ISSN: 1432-0746. DOI: 10.1051/0004-6361/202142419. URL: http://dx.doi.org/10.1051/0004-6361/202142419 (cit. on p. 79).

[126] Lewis, A., Challinor, A., and Lasenby, A. "Efficient Computation of Cosmic Microwave Background Anisotropies in Closed Friedmann-Robertson-Walker Models". In: *ApJ* 538.2 (Aug. 2000), p. 473. ISSN: 1538-4357. DOI: 10.1086/309179. URL: http://dx.doi.org/10.1086/309179 (cit. on p. 48).

[127] Linder, E. V. and Jenkins, A. "Cosmic structure growth and dark energy". In: *MNRAS* 346.2 (Dec. 2003), p. 573. DOI: 10.1046/j.1365-2966.2003.07112.x. arXiv: astro-ph/0305286 [astro-ph] (cit. on p. 43).

[128] Mather, J. C., Fixsen, D. J., Shafer, R. A., et al. "Calibrator Design for the COBE Far-Infrared Absolute Spectrophotometer (FIRAS)". In: *ApJ* 512.2 (Feb. 1999), p. 511. DOI: 10.1086/306805. arXiv: astro-ph/9810373 [astro-ph] (cit. on pp. 34, 47).

[129] Mead, A. J., Brieden, S., Tröster, T., et al. "hmcode-2020: improved modelling of non-linear cosmological power spectra with baryonic feedback". In: *MNRAS* 502.1 (Jan. 2021), p. 1401. ISSN: 0035-8711. DOI: 10.1093/mnras/stab082. eprint: https://academic.oup.com/mnras/article-pdf/502/1/1401/42438464/stab082.pdf. URL: https://doi.org/10.1093/mnras/stab082 (cit. on p. 77).

[130] Miyazaki, S., Komiyama, Y., Kawanomoto, S., et al. "Hyper Suprime-Cam: System design and verification of image quality". In: *PASJ* 70, S1 (Jan. 2018), S1. DOI: 10.1093/pasj/psx063 (cit. on p. 46).

[131] Nelder, J. A. and Wedderburn, R. W. M. "Generalized Linear Models". In: *Journal of the Royal Statistical Society: Series A (General)* 135.3 (1972), p. 370. DOI: https://doi.org/10.2307/2344614. URL: https://rss.onlinelibrary.wiley.com/doi/abs/10.2307/2344614 (cit. on p. 53).

[132] Nelson, B., Ford, E. B., and Payne, M. J. "RUN DMC: An Efficient, Parallel Code for Analyzing Radial Velocity Observations Using N-body Integrations and Differential Evolution Markov Chain Monte Carlo". In: *ApJS* 210.1, 11 (Jan. 2014), p. 11. DOI: 10.1088/0067-0049/210/1/11. arXiv: 1311.5229 [astro-ph.EP] (cit. on p. 143).

[133] Newton, I. *Philosophiae Naturalis Principia Mathematica*. 1687. DOI: 10.3931/e-rara-440 (cit. on p. 36).

[134] Newville, M., Otten, R., Nelson, A., et al. *lmfit/lmfit-py: 1.3.1*. Version 1.3.1. Apr. 2024. DOI: 10.5281/zenodo.10998841 (cit. on p. 113).

[135] Nojiri, S. and Odintsov, S. D. "Modified Gauss Bonnet theory as gravitational alternative for dark energy". In: *Physics Letters B* 631.1-2 (Dec. 2005), p. 1. DOI: 10.1016/j.physletb.2005.10.010. arXiv: hep-th/0508049 [astro-ph] (cit. on p. 44).

[136] Pasquet, J., Bertin, E., Treyer, M., et al. "Photometric redshifts from SDSS images using a convolutional neural network". In: *A&A* 621 (2019), A26. DOI: 10.1051/0004-6361/201833617. URL: https://doi.org/10.1051/0004-6361/201833617 (cit. on pp. 55, 58, 64).

[137] Peebles, P. J. E. and Ratra, B. "Cosmology with a Time-Variable Cosmological "Constant"". In: *ApJ* 325 (Feb. 1988), p. L17. DOI: 10.1086/185100 (cit. on p. 44).

[138] Percival, W. J., Baugh, C. M., Bland-Hawthorn, J., et al. "The 2dF Galaxy Redshift Survey: the power spectrum and the matter content of the Universe". In: *MNRAS* 327.4 (Nov. 2001), p. 1297. ISSN: 1365-2966. DOI: 10.1046/j.1365-8711.2001.04827.x. URL: http://dx.doi.org/10.1046/j.1365-8711.2001.04827.x (cit. on p. 35).

[139] Perlmutter, S., Aldering, G., Goldhaber, G., et al. "Measurements of Ω and Λ from 42 High-Redshift Supernovae". In: *ApJ* 517.2 (June 1999), p. 565. DOI: 10.1086/307221. arXiv: astro-ph/9812133 [astro-ph] (cit. on p. 43).

[140] Planck Collaboration : Aghanim, N., Akrami, Y., Ashdown, M., et al. "Planck 2018 results. VI. Cosmological parameters". In: *A&A* 641, A6 (Sept. 2020), A6. DOI: 10.1051/0004-6361/201833910. arXiv: 1807.06209 [astro-ph.CO] (cit. on p. 40).

[141] Porredon, A., Crocce, M., Elvin-Poole, J., et al. "Dark Energy Survey Year 3 results: Cosmological constraints from galaxy clustering and galaxy-galaxy lensing using the MagLim lens sample". In: *Phys. Rev. D* 106 (10 Nov. 2022), p. 103530. DOI: 10.1103/PhysRevD.106.103530. URL: https://link.aps.org/doi/10.1103/PhysRevD.106.103530 (cit. on p. 151).

[142] Potter, D., Stadel, J., and Teyssier, R. "PKDGRAV3: beyond trillion particle cosmological simulations for the next era of galaxy surveys". In: *CompAC* 4.1, 2 (May 2017), p. 2. DOI: 10.1186/s40668-017-0021-1. arXiv: 1609.08621 [astro-ph.IM] (cit. on p. 82).

[143] Pujolàs, O., Sawicki, I., and Vikman, A. "The imperfect fluid behind kinetic gravity braiding". In: *Journal of High Energy Physics* 2011, 156 (Nov. 2011), p. 156. DOI: 10.1007/JHEP11(2011)156. arXiv: 1103.5360 [hep-th] (cit. on p. 44).

[144] Riess, A. G., Filippenko, A. V., Challis, P., et al. "Observational Evidence from Supernovae for an Accelerating Universe and a Cosmological Constant". In: *AJ* 116.3 (Sept. 1998), p. 1009. DOI: 10.1086/300499. arXiv: astro-ph/9805201 [astro-ph] (cit. on p. 43).

[145] Sadeh, I., Abdalla, F. B., and Lahav, O. "ANNz2: Photometric Redshift and Probability Distribution Function Estimation using Machine Learning". In: *PASP* 128.968 (Oct. 2016), p. 104502. DOI: 10.1088/1538-3873/128/968/104502. arXiv: 1507.00490 [astro-ph.CO] (cit. on p. 55).

[146] Sahni, V. and Starobinsky, A. "The Case for a Positive Cosmological Λ-Term". In: *International Journal of Modern Physics D* 9.4 (Jan. 2000), p. 373. DOI: 10.1142/S0218271800000542. arXiv: astro-ph/9904398 [astro-ph] (cit. on p. 44).

[147] Shanno, D. F. "Conditioning of Quasi-Newton Methods for Function Minimization". In: *Mathematics of Computation* 24.111 (1970), p. 647. ISSN: 00255718, 10886842. URL: https://www.ams.org/journals/mcom/1970-24-111/S0025-5718-1970-0274029-X/S0025-5718-1970-0274029-X.pdf (cit. on p. 113).

[148] Silber, J. H., Fagrelius, P., Fanning, K., et al. "The Robotic Multiobject Focal Plane System of the Dark Energy Spectroscopic Instrument (DESI)". In: *AJ* 165.1, 9 (Jan. 2023), p. 9. DOI: 10.3847/1538-3881/ac9ab1. arXiv: 2205.09014 [astro-ph.IM] (cit. on p. 45).

[149] Smith, L. N. "Cyclical Learning Rates for Training Neural Networks". In: *2017 IEEE Winter Conference on Applications of Computer Vision (WACV)*. 2017, p. 464. DOI: 10.1109/WACV.2017.58 (cit. on p. 62).

[150] Szegedy, C., L., Wei, J., Yangqing, et al. "Going deeper with convolutions". In: *2015 IEEE Conference on Computer Vision and Pattern Recognition (CVPR)*. 2015, p. 1. DOI: 10.1109/CVPR.2015.7298594. URL: https://doi.org/10.1109/CVPR.2015.7298594 (cit. on p. 57).

[151] Takahashi, R., Sato, M., Nishimichi, T., et al. "Revising the Halofit Model for the Nonlinear Matter Power Spectrum". In: *ApJ* 761.2, 152 (Dec. 2012), p. 152. DOI: 10.1088/0004-637X/761/2/152. arXiv: 1208.2701 [astro-ph.CO] (cit. on p. 151).

[152] Tallada, P., Carretero, J., Casals, J., et al. "CosmoHub: Interactive exploration and distribution of astronomical data on Hadoop". In: *Astronomy and Computing* 32 (2020), p. 100391. ISSN: 2213-1337. DOI: https://doi.org/10.1016/j.ascom.2020.100391. URL: http://www.sciencedirect.com/science/article/pii/S2213133720300457 (cit. on p. 82).

[153] Tanaka, M., Coupon, J., Hsieh, B.-C., et al. "Photometric redshifts for Hyper Suprime-Cam Subaru Strategic Program Data Release 1". In: *PASJ* 70, S9 (Jan. 2018), S9. DOI: 10.1093/pasj/psx077. arXiv: 1704.05988 [astro-ph.GA] (cit. on pp. 53, 84).

[154] ter Braak, C. J. F. and Vrugt, J. A. "Differential Evolution Markov Chain with snooker updater and fewer chains". English. In: *Statistics and Computing* 18.4 (2008), p. 435. ISSN: 0960-3174. DOI: 10.1007/s11222-008-9104-9 (cit. on p. 143).

[155] Tristram, M., Banday, A. J., Douspis, M., et al. "Cosmological parameters derived from the final Planck data release (PR4)". In: *A&A* 682, A37 (Feb. 2024), A37. DOI: 10.1051/0004-6361/202348015. arXiv: 2309.10034 [astro-ph.CO] (cit. on p. 42).

[156] Troxel, M. A., Krause, E., Chang, C., et al. "Survey geometry and the internal consistency of recent cosmic shear measurements". In: *MNRAS* 479.4 (Oct. 2018), p. 4998. DOI: 10.1093/mnras/sty1889. arXiv: 1804.10663 [astro-ph.CO] (cit. on p. 104).

[157] Tutusaus, I., Martinelli, M., Cardone, V. F., et al. "Euclid: The importance of galaxy clustering and weak lensing cross-correlations within the photometric Euclid survey". In: *A&A* 643, A70 (Nov. 2020), A70. DOI: 10.1051/0004-6361/202038313. arXiv: 2005.00055 [astro-ph.CO] (cit. on p. 44).

[158] Vainshtein, A. I. "To the problem of nonvanishing gravitation mass". In: *Physics Letters B* 39.3 (May 1972), p. 393. DOI: 10.1016/0370-2693(72)90147-5 (cit. on p. 44).

[159] Wang, Y., Zhao, G.-B., Chuang, C.-H., et al. "The clustering of galaxies in the completed SDSS-III Baryon Oscillation Spectroscopic Survey: tomographic BAO analysis of DR12 combined sample in configuration space". In: *MNRAS* 469.3 (Aug. 2017), p. 3762. DOI: 10.1093/mnras/stx1090. arXiv: 1607.03154 [astro-ph.CO] (cit. on p. 117).

[160] Webb, N., Hello, P., Lamine, B., et al. *Gravitation*. ISTE editions, 2023 (cit. on p. 36).

[161] Wetterich, C. "Cosmology and the fate of dilatation symmetry". In: *Nuclear Physics B* 302.4 (June 1988), p. 668. DOI: 10.1016/0550-3213(88)90193-9. arXiv: 1711.03844 [hep-th] (cit. on p. 44).

[162] Zehavi, I., Zheng, Z., Weinberg, D. H., et al. "Galaxy Clustering in the Completed SDSS Redshift Survey: The Dependence on Color and Luminosity". In: *ApJ* 736.1, 59 (July 2011), p. 59. DOI: 10.1088/0004-637X/736/1/59. arXiv: 1005.2413 [astro-ph.CO] (cit. on p. 83).

[163] Zonca, A., Singer, L., Lenz, D., et al. "healpy: equal area pixelization and spherical harmonics transforms for data on the sphere in Python". In: *Journal of Open Source Software* 4.35 (Mar. 2019), p. 1298. DOI: 10.21105/joss.01298. URL: https://doi.org/10.21105/joss.01298 (cit. on p. 107).

[164] Zuntz, J., Paterno, M., Jennings, E., et al. "CosmoSIS: Modular cosmological parameter estimation". In: *Astronomy and Computing* 12 (Sept. 2014). DOI: 10.1016/j.ascom.2015.05.005 (cit. on p. 150).

[165] Zwicky, F. "Die Rotverschiebung von extragalaktischen Nebeln". In: *Helvetica Physica Acta* 6 (Jan. 1933), p. 110 (cit. on p. 39).

[166] Zwicky, F. "Republication of: The redshift of extragalactic nebulae". In: *General Relativity and Gravitation* 41.1 (Jan. 2009), p. 207. DOI: 10.1007/s10714-008-0707-4 (cit. on p. 40).

Appendices

A. Architectures of deep learning models

In this appendix, I present the architecture of the various deep learning models used in Chapter 2. We group the successions of layers of the models in tables, listing for each layer its type and name, the name of the previous layer, the kernel and input size if it is relevant, the number of feature maps (depth) or equivalently, the number of neurons for full-connected layers, and the number of parameters associated with the layer (weights and biases).

A.1. Multi-layer perceptron

This section introduces the architecture of the multi-layer perceptron, made of a succession of fully-connected layers.

Table A.1. – Properties of the layers of the MLP model (1 314 561 parameters): name of the layer, input layer, size of the convolution kernel (in pixels), size (height×width in pixels), number of neurons, and number of parameters. "I" stands for input layer and "FC" for fully connected layer.

Layer	Inputs	Kernel size	$h \times w$	# neurons	Parameters
I1	-	-	-	4	0
FC1	I1	-	-	256	1280
FC2	FC1	-	-	512	131584
FC3	FC2	-	-	1024	525312
FC4	FC3	-	-	512	524800
FC5	FC4	-	-	256	131328
FC6	FC5	-	-	1	257

A.2. Sequential CNN

This section introduces the architecture of the sequential CNN, based on 3 convolutional layers which decrease the spatial extent of the input images while the depth (number of filters) is increased. A flattening layer is then used before using 5 full-connected layers.

Table A.2. – Properties of the layers of the sequential CNN model (529 409 parameters): name of the layer, input layer, size of the convolution kernel (in pixels), size (height×width in pixels), number of the resulting feature maps which becomes the number of neurons after the flattening layer, and number of parameters. "I" stands for input layer, "C" stands for convolutional layer, "B" for batch normalization, "SD" for 2D spatial dropout, "P" for max pooling, "F" for flattening layer, "D" for dropout, and "FC" for fully connected.

Layer	Inputs	Kernel size	$h \times w$	# feature maps	Parameters
I1	-	-	32×32	4	0
C1	I1	3×3	32×32	32	1152
B1	C1	-	32×32	32	128
SD1	B1	-	32×32	32	0
P1	SD1	-	11×11	32	0
C2	P1	3×3	11×11	64	18432
B2	C2	-	11×11	64	256
SD2	B2	-	11×11	64	0
P2	SD2	-	4×4	64	0
C3	P2	3×3	4×4	128	73728
B3	C3	-	4×4	128	512
SD3	B3	-	4×4	128	0
P3	SD3	-	2×2	128	0
F1	P3	-	-	512	0
D1	F1	-	-	512	0
FC1	D1	-	-	512	262656
FC2	FC1	-	-	256	131328
FC3	FC2	-	-	128	32896
FC4	FC3	-	-	64	8256
FC5	FC4	-	-	1	65

A.3. Inception CNN

This section introduces the architecture of the inception CNN, based on inception blocks which apply efficiently 5×5 and 3×3 convolutions to extract the information from input images.

Table A.3. – Properties of the layers of the inception CNN model (1 451 001 parameters): name of the layer, input layer, size of the convolution kernel (in pixels), size (height×width in pixels), number of the resulting feature maps which becomes the number of neurons after the flattening layer, and number of parameters. "I" stands for input layer, "C" stands for convolutional layer, "B" for batch normalization, "SD" for 2D spatial dropout, "P" for max pooling, "F" for flattening layer, "Co" for concatenation layer, and "FC" for fully connected.

Layer	Inputs	Kernel size	$h \times w$	# feature maps	Parameters
I1	-	-	32×32	4	0
C1	I1	5×5	32×32	32	3232
A1	C1	-	16×16	32	0
C2	A1	1×1	16×16	16	528
C3	A1	1×1	16×16	16	528
A2	A1	-	16×16	32	0
C4	C2	5×5	16×16	16	6416
C5	C3	3×3	16×16	16	2320
C6	A2	1×1	16×16	16	528
C7	A1	1×1	16×16	16	528
C8	C4,C5,C6,C7	-	16×16	64	0
C9	C8	1×1	16×16	16	1040
C10	C8	1×1	16×16	16	1040
A3	C8	-	16×16	64	0
C11	C9	5×5	16×16	16	6416
C12	C10	3×3	16×16	16	2320
C13	A3	1×1	16×16	16	1040
C14	C8	1×1	16×16	16	1040
C15	C11,C12,C13,C14	-	16×16	64	0
A4	C15	-	8×8	64	0
C16	A4	1×1	8×8	8	520
C17	A4	1×1	8×8	8	520
A5	A4	-	8×8	64	0
C18	C16	5×5	8×8	8	1608
C19	C17	3×3	8×8	8	584
C20	A5	1×1	8×8	8	520
C21	A4	1×1	8×8	8	520
C22	C18,C19,C20,C21	-	8×8	32	0

C23	C22	1×1	8×8	8	264
C24	C22	1×1	8×8	8	264
A6	C22	-	8×8	32	0
C25	C23	5×5	8×8	8	1608
C26	C24	3×3	8×8	8	584
C27	A6	1×1	8×8	8	264
C28	C22	1×1	8×8	8	264
C29	C25,C26,C27,C28	-	8×8	32	0
A7	C29	-	4×4	32	0
C30	A7	3×3	4×4	4	1156
A8	A7	-	4×4	32	0
C31	C30	3×3	4×4	4	148
C32	A8	1×1	4×4	4	132
C33	A7	1×1	4×4	4	132
C34	C31,C32,C33	-	4×4	12	0
F1	C34	-	-	192	0
FC1	F1	-	-	1096	211528
FC2	FC1	-	-	1096	1202312
FC3	FC2	-	-	1	1097

A.4. Multi-input inception CNN+MLP

This section introduces the architecture of the multi-input inception CNN+MLP, based on the inception architecture to extract the information from input images and completed by a MLP to process magnitudes as additional input to the neural network. This compensates for the imperfect processing by the inception branch and improves significantly the model performances.

Table A.4. – Properties of the layers of the inception CNN+MLP model (7 826 353 parameters): name of the layer, input layer, size of the convolution kernel (in pixels), size (height×width in pixels), number of the resulting feature maps which becomes the number of neurons after the flattening layer, and number of parameters. "I" stands for input layer, "C" stands for convolutional layer, "B" for batch normalization, "SD" for 2D spatial dropout, "P" for max pooling, "F" for flattening layer, "Co" for concatenation layer, and "FC" for fully connected.

Layer	Inputs	Kernel size	$h \times w$	# feature maps	Parameters
I1	-	-	32×32	4	0
C1	I1	5×5	32×32	32	3232
A1	C1	-	16×16	32	0
C2	A1	1×1	16×16	16	528
C3	A1	1×1	16×16	16	528
A2	A1	-	16×16	32	0
C4	C2	5×5	16×16	16	6416
C5	C3	3×3	16×16	16	2320
C6	A2	1×1	16×16	16	528
C7	A1	1×1	16×16	16	528
C8	C4,C5,C6,C7	-	16×16	64	0
C9	C8	1×1	16×16	16	1040
C10	C8	1×1	16×16	16	1040
A3	C8	-	16×16	64	0
C11	C9	5×5	16×16	16	6416
C12	C10	3×3	16×16	16	2320
C13	A3	1×1	16×16	16	1040
C14	C8	1×1	16×16	16	1040
C15	C11,C12,C13,C14	-	16×16	64	0
A4	C15	-	8×8	64	0
C16	A4	1×1	8×8	8	520
C17	A4	1×1	8×8	8	520
A5	A4	-	8×8	64	0
C18	C16	5×5	8×8	8	1608
C19	C17	3×3	8×8	8	584
C20	A5	1×1	8×8	8	520

C21	A4	1×1	8×8	8	520
C22	C18,C19,C20,C21	-	8×8	32	0
C23	C22	1×1	8×8	8	264
C24	C22	1×1	8×8	8	264
A6	C22	-	8×8	32	0
C25	C23	5×5	8×8	8	1608
C26	C24	3×3	8×8	8	584
C27	A6	1×1	8×8	8	264
C28	C22	1×1	8×8	8	264
C29	C25,C26,C27,C28	-	8×8	32	0
A7	C29	-	4×4	32	0
C30	A7	3×3	4×4	4	1156
A8	A7	-	4×4	32	0
I2	-	-	-	4	0
C31	C30	3×3	4×4	4	148
C32	A8	1×1	4×4	4	132
C33	A7	1×1	4×4	4	132
FC1	I2	-	-	1024	5120
FC2	C31,C32,C33	-	4×4	12	0
FC3	FC1	-	-	1024	1049600
F1	FC2	-	-	192	0
FC4	FC3	-	-	1024	1049600
FC5	F1	-	-	1096	211528
FC6	FC4	-	-	1024	1049600
FC7	FC5	-	-	1096	1202312
FC8	FC6	-	-	1024	1049600
FC9	FC7,FC8	-	-	2120	0
FC10	FC9	-	-	1024	2171904
FC11	FC10	-	-	1	1025

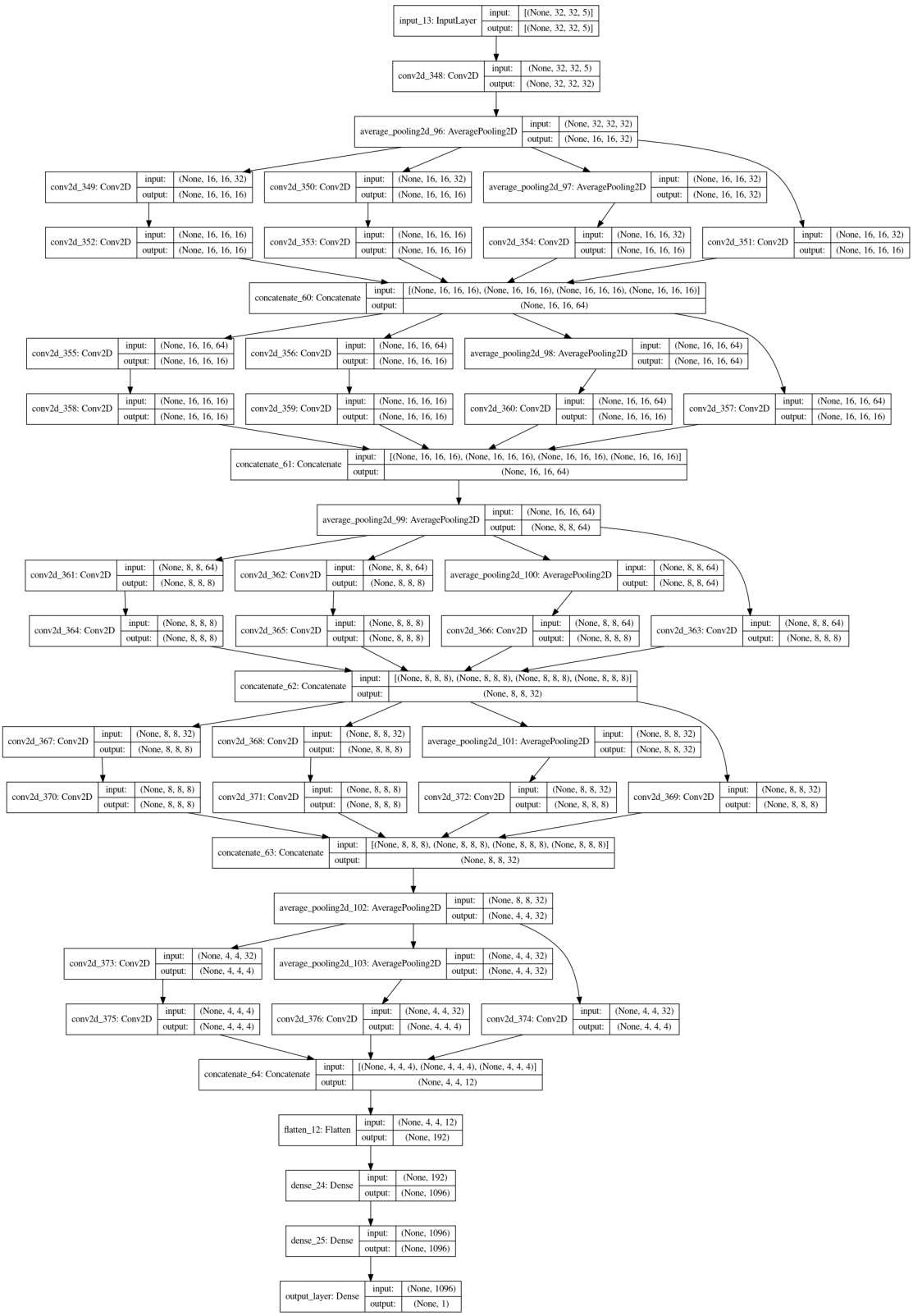


Figure A.1. – Inception CNN architecture.

A.5. ResNet34

This section introduces the architecture of the ResNet34, a residual network based on skip connections which helps deepening the architecture by adding more layers without encountering issues like vanishing gradients.

Table A.5. – Properties of the layers of the ResNet model (21 576 065 parameters): name of the layer, input layer, size of the convolution kernel (in pixels), size (height×width in pixels), number of the resulting feature maps which becomes the number of neurons after the flattening layer, and number of parameters. "I" stands for input layer, "C" stands for convolutional layer, "B" for batch normalization, "SD" for 2D spatial dropout, "P" for max pooling, "F" for flattening layer, "Co" for concatenation layer, and "FC" for fully connected.

Layer	Inputs	Kernel size	$h \times w$	# feature maps	Parameters
I1	-	-	32×32	5	0
Zpad1	I1	-	38×38	5	0
C1	Zpad1	7×7	19×19	64	15744
B1	C1	-	19×19	64	256
Act1	B1	-	19×19	64	0
P1	Act1	-	10×10	64	0
C2	P1	3×3	10×10	64	36928
B2	C2	-	10×10	64	256
Act2	B2	-	10×10	64	0
C3	Act2	3×3	10×10	64	36928
B3	C3	-	10×10	64	256
Add1	B3,P1	-	10×10	64	0
Act3	Add1	-	10×10	64	0
C4	Act3	3×3	10×10	64	36928
B4	C4	-	10×10	64	256
Act4	B4	-	10×10	64	0
C5	Act4	3×3	10×10	64	36928
B5	C5	-	10×10	64	256
Add2	B5,Act3	-	10×10	64	0
Act5	Add2	-	10×10	64	0
C6	Act5	3×3	10×10	64	36928
B6	C6	-	10×10	64	256
Act6	B6	-	10×10	64	0
C7	Act6	3×3	10×10	64	36928
B7	C7	-	10×10	64	256
Add3	B7,Act5	-	10×10	64	0
Act7	Add3	-	10×10	64	0
C8	Act7	3×3	5×5	128	73856

B8	C8	-	5 × 5	128	512
Act8	B8	-	5 × 5	128	0
C9	Act8	3 × 3	5 × 5	128	147584
B9	C9	-	5 × 5	128	512
C10	Act7	1 × 1	5 × 5	128	8320
Add4	B9,C10	-	5 × 5	128	0
Act9	Add4	-	5 × 5	128	0
C11	Act9	3 × 3	5 × 5	128	147584
B10	C11	-	5 × 5	128	512
Act10	B10	-	5 × 5	128	0
C12	Act10	3 × 3	5 × 5	128	147584
B11	C12	-	5 × 5	128	512
Add5	B11,Act9	-	5 × 5	128	0
Act11	Add5	-	5 × 5	128	0
C13	Act11	3 × 3	5 × 5	128	147584
B12	C13	-	5 × 5	128	512
Act12	B12	-	5 × 5	128	0
C14	Act12	3 × 3	5 × 5	128	147584
B13	C14	-	5 × 5	128	512
Add6	B13,Act11	-	5 × 5	128	0
Act13	Add6	-	5 × 5	128	0
C15	Act13	3 × 3	5 × 5	128	147584
B14	C15	-	5 × 5	128	512
Act14	B14	-	5 × 5	128	0
C16	Act14	3 × 3	5 × 5	128	147584
B15	C16	-	5 × 5	128	512
Add7	B15,Act13	-	5 × 5	128	0
Act15	Add7	-	5 × 5	128	0
C17	Act15	3 × 3	3 × 3	256	295168
B16	C17	-	3 × 3	256	1024
Act16	B16	-	3 × 3	256	0
C18	Act16	3 × 3	3 × 3	256	590080
B17	C18	-	3 × 3	256	1024
C19	Act15	1 × 1	3 × 3	256	33024
Add8	B17,C19	-	3 × 3	256	0
Act17	Add8	-	3 × 3	256	0
C20	Act17	3 × 3	3 × 3	256	590080
B18	C20	-	3 × 3	256	1024
Act18	B18	-	3 × 3	256	0
C21	Act18	3 × 3	3 × 3	256	590080
B19	C21	-	3 × 3	256	1024
Add9	B19,Act17	-	3 × 3	256	0
Act19	Add9	-	3 × 3	256	0
C22	Act19	3 × 3	3 × 3	256	590080

B20	C22	-	3 × 3	256	1024
Act20	B20	-	3 × 3	256	0
C23	Act20	3 × 3	3 × 3	256	590080
B21	C23	-	3 × 3	256	1024
Add10	B21,Act19	-	3 × 3	256	0
Act21	Add10	-	3 × 3	256	0
C24	Act21	3 × 3	3 × 3	256	590080
B22	C24	-	3 × 3	256	1024
Act22	B22	-	3 × 3	256	0
C25	Act22	3 × 3	3 × 3	256	590080
B23	C25	-	3 × 3	256	1024
Add11	B23,Act21	-	3 × 3	256	0
Act23	Add11	-	3 × 3	256	0
C26	Act23	3 × 3	3 × 3	256	590080
B24	C26	-	3 × 3	256	1024
Act24	B24	-	3 × 3	256	0
C27	Act24	3 × 3	3 × 3	256	590080
B25	C27	-	3 × 3	256	1024
Add12	B25,Act23	-	3 × 3	256	0
Act25	Add12	-	3 × 3	256	0
C28	Act25	3 × 3	3 × 3	256	590080
B26	C28	-	3 × 3	256	1024
Act26	B26	-	3 × 3	256	0
C29	Act26	3 × 3	3 × 3	256	590080
B27	C29	-	3 × 3	256	1024
Add13	B27,Act25	-	3 × 3	256	0
Act27	Add13	-	3 × 3	256	0
C30	Act27	3 × 3	2 × 2	512	1180160
B28	C30	-	2 × 2	512	2048
Act28	B28	-	2 × 2	512	0
C31	Act28	3 × 3	2 × 2	512	2359808
B29	C31	-	2 × 2	512	2048
C32	Act27	1 × 1	2 × 2	512	131584
Add14	B29,C32	-	2 × 2	512	0
Act29	Add14	-	2 × 2	512	0
C33	Act29	3 × 3	2 × 2	512	2359808
B30	C33	-	2 × 2	512	2048
Act30	B30	-	2 × 2	512	0
C34	Act30	3 × 3	2 × 2	512	2359808
B31	C34	-	2 × 2	512	2048
Add15	B31,Act29	-	2 × 2	512	0
Act31	Add15	-	2 × 2	512	0
C35	Act31	3 × 3	2 × 2	512	2359808
B32	C35	-	2 × 2	512	2048

Act32	B32	-	2×2	512	0
C36	Act32	3×3	2×2	512	2359808
B33	C36	-	2×2	512	2048
Add16	B33,Act31	-	2×2	512	0
Act33	Add16	-	2×2	512	0
A1	Act33	-	1×1	512	0
F1	A1	-	-	512	0
FC1	F1	-	-	512	262656
FC2	FC1	-	-	1	513

B. Optimization for the BAO analysis

In this appendix, we list the constraints obtained on h, Ω_b and Ω_{cdm} from the MCMC analysis with the cosmological analysis of the BAO results. A total of 56 results are grouped by number of redshift bins, binning scheme, and magnitude cut in the I_E passband.

Table B.1. – Cosmological constraints on h, Ω_b, and Ω_{cdm} obtained from BAO with between 9 and 15 bins, a cut in the I_E band varying between 22 and 25, and an equipopulated or equidistant binning scheme.

Configuration	h	$100\,\Omega_b$	Ω_{cdm}
9 equipopulated bins, $I_E \leq 22.0$	$0.670^{+0.004}_{-0.004}$	$4.902^{+0.050}_{-0.054}$	$0.273^{+0.034}_{-0.031}$
9 equipopulated bins, $I_E \leq 22.5$	$0.670^{+0.004}_{-0.004}$	$4.902^{+0.049}_{-0.052}$	$0.274^{+0.031}_{-0.029}$
9 equipopulated bins, $I_E \leq 23.0$	$0.670^{+0.004}_{-0.003}$	$4.902^{+0.047}_{-0.050}$	$0.273^{+0.028}_{-0.026}$
9 equipopulated bins, $I_E \leq 23.5$	$0.670^{+0.004}_{-0.004}$	$4.902^{+0.046}_{-0.049}$	$0.273^{+0.025}_{-0.024}$
9 equipopulated bins, $I_E \leq 24.0$	$0.670^{+0.003}_{-0.003}$	$4.902^{+0.046}_{-0.047}$	$0.273^{+0.023}_{-0.022}$
9 equipopulated bins, $I_E \leq 24.5$	$0.670^{+0.003}_{-0.003}$	$4.901^{+0.044}_{-0.045}$	$0.272^{+0.020}_{-0.019}$
9 equipopulated bins, $I_E \leq 25.0$	$0.670^{+0.003}_{-0.003}$	$4.901^{+0.044}_{-0.045}$	$0.272^{+0.020}_{-0.019}$
9 equidistant bins, $I_E \leq 22.0$	$0.670^{+0.005}_{-0.004}$	$4.907^{+0.060}_{-0.067}$	$0.280^{+0.054}_{-0.049}$
9 equidistant bins, $I_E \leq 22.5$	$0.670^{+0.004}_{-0.004}$	$4.903^{+0.055}_{-0.057}$	$0.276^{+0.041}_{-0.037}$
9 equidistant bins, $I_E \leq 23.0$	$0.670^{+0.004}_{-0.004}$	$4.903^{+0.048}_{-0.050}$	$0.274^{+0.029}_{-0.027}$
9 equidistant bins, $I_E \leq 23.5$	$0.670^{+0.003}_{-0.003}$	$4.902^{+0.045}_{-0.046}$	$0.273^{+0.020}_{-0.020}$
9 equidistant bins, $I_E \leq 24.0$	$0.670^{+0.003}_{-0.003}$	$4.902^{+0.043}_{-0.044}$	$0.273^{+0.016}_{-0.015}$
9 equidistant bins, $I_E \leq 24.5$	$0.670^{+0.003}_{-0.003}$	$4.903^{+0.042}_{-0.043}$	$0.273^{+0.014}_{-0.013}$
9 equidistant bins, $I_E \leq 25.0$	$0.670^{+0.003}_{-0.003}$	$4.903^{+0.042}_{-0.043}$	$0.273^{+0.014}_{-0.014}$
11 equipopulated bins, $I_E \leq 22.0$	$0.670^{+0.004}_{-0.004}$	$4.902^{+0.049}_{-0.051}$	$0.273^{+0.030}_{-0.028}$
11 equipopulated bins, $I_E \leq 22.5$	$0.670^{+0.004}_{-0.004}$	$4.901^{+0.047}_{-0.050}$	$0.272^{+0.027}_{-0.025}$
11 equipopulated bins, $I_E \leq 23.0$	$0.670^{+0.004}_{-0.003}$	$4.901^{+0.046}_{-0.047}$	$0.273^{+0.024}_{-0.023}$
11 equipopulated bins, $I_E \leq 23.5$	$0.670^{+0.003}_{-0.003}$	$4.901^{+0.046}_{-0.046}$	$0.272^{+0.022}_{-0.021}$
11 equipopulated bins, $I_E \leq 24.0$	$0.670^{+0.003}_{-0.003}$	$4.902^{+0.044}_{-0.046}$	$0.273^{+0.020}_{-0.018}$
11 equipopulated bins, $I_E \leq 24.5$	$0.670^{+0.003}_{-0.003}$	$4.902^{+0.043}_{-0.044}$	$0.273^{+0.018}_{-0.017}$
11 equipopulated bins, $I_E \leq 25.0$	$0.670^{+0.003}_{-0.003}$	$4.902^{+0.044}_{-0.044}$	$0.273^{+0.018}_{-0.017}$
11 equidistant bins, $I_E \leq 22.0$	$0.670^{+0.004}_{-0.004}$	$4.905^{+0.057}_{-0.063}$	$0.277^{+0.049}_{-0.043}$
11 equidistant bins, $I_E \leq 22.5$	$0.670^{+0.004}_{-0.004}$	$4.904^{+0.050}_{-0.054}$	$0.275^{+0.036}_{-0.033}$
11 equidistant bins, $I_E \leq 23.0$	$0.670^{+0.004}_{-0.004}$	$4.902^{+0.046}_{-0.048}$	$0.273^{+0.026}_{-0.024}$
11 equidistant bins, $I_E \leq 23.5$	$0.670^{+0.003}_{-0.003}$	$4.901^{+0.045}_{-0.045}$	$0.272^{+0.019}_{-0.018}$

11 equidistant bins, $I_E \leq 24.0$	$0.670^{+0.003}_{-0.003}$	$4.903^{+0.042}_{-0.043}$	$0.273^{+0.015}_{-0.014}$
11 equidistant bins, $I_E \leq 24.5$	$0.670^{+0.003}_{-0.003}$	$4.902^{+0.042}_{-0.042}$	$0.272^{+0.013}_{-0.012}$
11 equidistant bins, $I_E \leq 25.0$	$0.670^{+0.003}_{-0.003}$	$4.902^{+0.042}_{-0.043}$	$0.273^{+0.013}_{-0.012}$
13 equipopulated bins, $I_E \leq 22.0$	$0.670^{+0.004}_{-0.004}$	$4.902^{+0.049}_{-0.050}$	$0.273^{+0.028}_{-0.026}$
13 equipopulated bins, $I_E \leq 22.5$	$0.670^{+0.004}_{-0.004}$	$4.901^{+0.047}_{-0.048}$	$0.272^{+0.025}_{-0.024}$
13 equipopulated bins, $I_E \leq 23.0$	$0.670^{+0.003}_{-0.003}$	$4.902^{+0.045}_{-0.046}$	$0.273^{+0.022}_{-0.021}$
13 equipopulated bins, $I_E \leq 23.5$	$0.670^{+0.003}_{-0.003}$	$4.901^{+0.044}_{-0.046}$	$0.272^{+0.020}_{-0.019}$
13 equipopulated bins, $I_E \leq 24.0$	$0.670^{+0.003}_{-0.003}$	$4.902^{+0.043}_{-0.045}$	$0.272^{+0.017}_{-0.017}$
13 equipopulated bins, $I_E \leq 24.5$	$0.670^{+0.003}_{-0.003}$	$4.902^{+0.043}_{-0.043}$	$0.272^{+0.016}_{-0.015}$
13 equipopulated bins, $I_E \leq 25.0$	$0.670^{+0.003}_{-0.003}$	$4.902^{+0.043}_{-0.043}$	$0.272^{+0.016}_{-0.015}$
13 equidistant bins, $I_E \leq 22.0$	$0.670^{+0.004}_{-0.004}$	$4.904^{+0.053}_{-0.058}$	$0.276^{+0.042}_{-0.038}$
13 equidistant bins, $I_E \leq 22.5$	$0.670^{+0.004}_{-0.004}$	$4.903^{+0.049}_{-0.053}$	$0.274^{+0.032}_{-0.030}$
13 equidistant bins, $I_E \leq 23.0$	$0.670^{+0.003}_{-0.003}$	$4.901^{+0.045}_{-0.046}$	$0.273^{+0.023}_{-0.022}$
13 equidistant bins, $I_E \leq 23.5$	$0.670^{+0.003}_{-0.003}$	$4.902^{+0.043}_{-0.045}$	$0.272^{+0.017}_{-0.016}$
13 equidistant bins, $I_E \leq 24.0$	$0.670^{+0.003}_{-0.003}$	$4.901^{+0.043}_{-0.043}$	$0.273^{+0.013}_{-0.013}$
13 equidistant bins, $I_E \leq 24.5$	$0.670^{+0.003}_{-0.003}$	$4.902^{+0.041}_{-0.042}$	$0.272^{+0.012}_{-0.011}$
13 equidistant bins, $I_E \leq 25.0$	$0.670^{+0.003}_{-0.003}$	$4.902^{+0.042}_{-0.042}$	$0.273^{+0.012}_{-0.011}$
15 equipopulated bins, $I_E \leq 22.0$	$0.670^{+0.004}_{-0.003}$	$4.901^{+0.046}_{-0.048}$	$0.272^{+0.026}_{-0.025}$
15 equipopulated bins, $I_E \leq 22.5$	$0.670^{+0.003}_{-0.004}$	$4.901^{+0.046}_{-0.047}$	$0.272^{+0.023}_{-0.022}$
15 equipopulated bins, $I_E \leq 23.0$	$0.670^{+0.003}_{-0.003}$	$4.901^{+0.044}_{-0.046}$	$0.272^{+0.020}_{-0.020}$
15 equipopulated bins, $I_E \leq 23.5$	$0.670^{+0.003}_{-0.003}$	$4.901^{+0.043}_{-0.046}$	$0.272^{+0.018}_{-0.017}$
15 equipopulated bins, $I_E \leq 24.0$	$0.670^{+0.003}_{-0.003}$	$4.901^{+0.044}_{-0.044}$	$0.272^{+0.016}_{-0.015}$
15 equipopulated bins, $I_E \leq 24.5$	$0.670^{+0.003}_{-0.003}$	$4.902^{+0.042}_{-0.043}$	$0.272^{+0.014}_{-0.014}$
15 equipopulated bins, $I_E \leq 25.0$	$0.670^{+0.003}_{-0.003}$	$4.902^{+0.042}_{-0.043}$	$0.273^{+0.014}_{-0.014}$
15 equidistant bins, $I_E \leq 22.0$	$0.670^{+0.004}_{-0.004}$	$4.903^{+0.052}_{-0.055}$	$0.276^{+0.037}_{-0.035}$
15 equidistant bins, $I_E \leq 22.5$	$0.670^{+0.004}_{-0.004}$	$4.902^{+0.048}_{-0.049}$	$0.273^{+0.028}_{-0.027}$
15 equidistant bins, $I_E \leq 23.0$	$0.670^{+0.003}_{-0.003}$	$4.901^{+0.045}_{-0.046}$	$0.272^{+0.021}_{-0.020}$
15 equidistant bins, $I_E \leq 23.5$	$0.670^{+0.003}_{-0.003}$	$4.902^{+0.043}_{-0.044}$	$0.272^{+0.016}_{-0.015}$
15 equidistant bins, $I_E \leq 24.0$	$0.670^{+0.003}_{-0.003}$	$4.901^{+0.042}_{-0.042}$	$0.272^{+0.013}_{-0.012}$
15 equidistant bins, $I_E \leq 24.5$	$0.670^{+0.003}_{-0.003}$	$4.901^{+0.042}_{-0.041}$	$0.273^{+0.011}_{-0.010}$
15 equidistant bins, $I_E \leq 25.0$	$0.670^{+0.003}_{-0.003}$	$4.901^{+0.041}_{-0.042}$	$0.272^{+0.011}_{-0.010}$